
Defects in earth-abundant photovoltaic materials:
spotlight on kesterites and copper oxides



Thomas Ratz

Academic year 2023-2024



FACULTY OF SCIENCES

QUANTUM MATERIALS RESEARCH UNIT

SOLID-STATE PHYSICS: INTERFACES AND NANOSTRUCTURES

**Defects in earth-abundant photovoltaic materials:
spotlight on kesterites and copper oxides**

AUTHOR:

Thomas Ratz

SUPERVISOR:

Ngoc Duy Nguyen

PHD. THESIS PRESENTED IN PARTIAL FULFILMENT OF THE
REQUIREMENTS FOR THE DEGREE OF DOCTOR IN SCIENCE

ACADEMIC YEAR 2023-2024

PhD. thesis committee

Chairman:

Prof. Dr. Alejandro SILHANEK, University of Liège (Liège, Belgium)

Secretary:

Prof. Dr. Benoit VANDERHEYDEN, University of Liège (Liège, Belgium)

Jury members:

Prof. Dr. Michel HOUSSA, KUL Leuven (Leuven, Belgium)

Prof. Dr. Bart VERMANG, University of Hasselt (Hasselt, Belgium)

Dr. Claudia MALERBA, ENAE (Roma, Italy)

Supervisor :

Prof. Dr. Ngoc Duy NGUYEN, University of Liège (Liège, Belgium)

Dissertation presented in partial fulfilment of the requirements for the degree of Doctor in Science. The manuscript was defended by **Thomas Ratz** during a public oral examination on the July, 9th 2024.

©Copyright by Université de Liège - Faculté des Sciences, Place du 20 Août, 7, B-4000 Liège, Belgium.

Tous droits réservés. Aucune partie de ce document ne peut être reproduite sous forme d'imprimé, photocopie ou par n'importe quel autre moyen, sans l'autorisation écrite de l'auteur ou d'un des promoteurs.

All rights reserved. No part of this publication may be reproduced in any form by print, photo print or any other means without permission in writing from the author or the supervisor.

This thesis explores the **physics of point defects**, conducting a comprehensive investigation through both **theoretical** and **experimental** approaches. In a **first part**, we emphasize the rich behaviour of defects, leading to their detailed classification. Non-radiative defect-mediated recombinations are described based on the Shockley-Read-Hall (SRH) statistics and detailed by explaining the microscopic origin of charge carrier capture coefficients. This discussion unravels the effects of lattice distortions caused by defect incorporation or changes in charge states. Furthermore, in solid-state matter, the rich physics introduced by these lattice imperfections can either enhance or degrade material properties and performances within the desired application. The results presented in this thesis highlight this ambivalent feature of point defects in absorber materials for photovoltaic (PV) applications.

On that basis, we aim to deepen the scientific community's understanding of defects in **earth-abundant photovoltaic materials: Copper oxides** Cu_2O and **kesterites** $\text{Cu}_2\text{ZnSnS}_4$. As part of the PV thin film technology, both are Cu-based p-type semiconductors featuring high absorption coefficients and including chalcogen elements (S, Se or O) in their crystalline structures. As such, they are used as absorber layers in solar cell architectures. However, their solar cell efficiencies are limited by low open circuit voltage V_{OC} values due to high charge carriers recombination rates, primarily attributed to defects and crystalline imperfections within the synthesised layers. Despite these similarities, their differing bandgap values determine their distinct applications. Copper oxide, as a transparent conducting oxide (TCO), is more suitable for transparent PV, whereas sulphur-based kesterites with their 1.5 eV bandgaps, can be efficiently used in single or tandem approaches with either perovskite or traditional bulk-Si. Furthermore, the complex quaternary chemical nature of kesterites significantly increases the number of possible point defects and secondary phases compared to *simpler* binary copper oxide materials.

In a **first research work**, using a first-principles approach, we highlight the impact of Sn cationic substitution on the structural, electrical and optical properties of kesterite compounds. By sequentially replacing Sn with two isoelectronic elements, Ge and Si, we report an increase in the kesterite bandgaps and high absorption absorption coefficients of the order of 10^4 cm^{-1} . Then, *ab initio* optical results are used as data input to model the electrical power conversion efficiency of kesterite-based solar cells thanks to an improved version of the Shockley-Queisser model. The variation of the solar cell maximum efficiency is studied as a function of the non-radiative recombination rate. We emphasise the suitability of $\text{Cu}_2\text{ZnSnS}_4$ in single or tandem (top cell) solar cells, with a potential efficiency improvement of nearly 10% compared to state-of-the-art values. In addition, $\text{Cu}_2\text{ZnGeS}_4$ appears as an interesting candidate for top cell absorber layers in tandem approaches, with room for an efficiency improvement of 5 points.

To pursue, based on the supercell approach, the **second phase of research** involves confirming and predicting possible recombination centres in both $\text{Cu}_2\text{ZnSnS}_4$ and $\text{Cu}_2\text{ZnGeS}_4$, respectively. This study is motivated by the previously underlined room for improvement concerning the efficiency of Sn,Ge-based kesterite solar cells. Using a first-principles approach, we investigate the physical behaviour of point defects both upon Ge doping and alloying of $\text{Cu}_2\text{ZnSnS}_4$. The p-type conductivity of both $\text{Cu}_2\text{ZnSnS}_4$ and $\text{Cu}_2\text{ZnGeS}_4$, attributed to V_{Cu} and Cu_{Zn} acceptor defects, is established. We also confirm the detrimental role of the substitutional defects X_{Zn} ($X=\text{Sn,Ge}$) acting as recombination centres. However, we emphasise that, in contrast to Sn, the substitution of Zn by Ge results in a defect that is less likely to facilitate pure non-radiative recombinations. This observation could be one potential source of V_{OC} improvement reported in the literature upon Ge incorporation.

Finally, the **last research work** aims at the experimental investigation of N and Mg doping in Cu_2O thin films deposited using RF magnetron sputtering at room temperature. Using a wide range of characterisation techniques (XRD, EDX, VdP-Hall, spectrophotometry, Raman), we correlate the variations of the thin film optoelectrical properties to both crystalline transitions and point defect formations. Starting from a CuO crystalline phase, we unveil a possible synthesis mechanism for a N-doped Cu_2O layers. Then, upon N-doping, we report an increased concentration of $(\text{N}_2)_{\text{Cu}}$ shallow acceptor defects explaining the probed enhancement of p-type majority charge carriers observed. Consistent with the established literature, we also confirm the improvement of the sample optoelectrical properties as Mg is introduced within split copper vacancy sites $V_{\text{Cu,split}}$. Conversely, we demonstrate that co-doping with Mg and N degrades the material crystallinity, leading to a reduction in thin film conductivity, likely due to high nitrogen incorporation.

We believe our results clarified the fundamental mechanisms that operate at the atomic scale via the formation of point defects in both kesterites and copper oxides.

Cette thèse de doctorat explore la **physique des défauts ponctuels** au travers d'une double approche, **théorique** et **expérimentale**. Dans une **première partie**, la nomenclature des différents types de défauts est présentée, mettant en lumière la richesse de la physique associée à ceux-ci dans la matière condensée. Ensuite, l'étude statistique de l'état d'occupation d'un défaut réalisée par Shockley-Read-Hall (SRH) est introduite et complétée par une discussion sur l'origine du coefficient de capture. Cette dernière permet de mettre en avant l'impact fondamental de la déformation de la maille cristalline lors de l'introduction d'un défaut ou lors de la variation de son état de charge sur la physique du processus de capture. De plus, ces déviations locales du caractère cristallin de la matière peuvent mener à une amélioration ou une dégradation des propriétés optiques et électriques du matériau, influençant dès lors les performances de l'application envisagée. Dans cette thèse, ce comportement ambivalent des défauts est mis en lumière au travers de l'étude de couches absorbantes pour des applications photovoltaïques.

Sur cette base, notre objectif est d'approfondir les connaissances de la communauté scientifique concernant la physique des défauts dans les **oxydes de cuivre** et les **kesterites**. Faisant partie de la technologie des films minces, ces matériaux sont constitués d'éléments accessibles et abondants dans la croûte terrestre. De plus, définis comme des matériaux semi-conducteurs de type p et caractérisés par d'important coefficients d'absorption, ces composés sont utilisés comme couches absorbantes dans l'architecture des cellules solaires. Concernant leur efficacité, l'abondance de centres de recombinaisons est identifiée comme origine des faibles valeurs de V_{OC} , facteur de limitation commun à ces deux types de matériaux. Cependant, les différences notables de valeurs de bandes interdites observées pour Cu_2O et $\text{Cu}_2\text{ZnSnS}_4$ divisent leurs champs d'applications photovoltaïques. L'oxyde de cuivre, faisant partie d'une classe de matériaux transparents et conducteurs, est plus adapté aux applications en électronique transparente tandis que les kesterites apparaissent comme des candidats intéressants pour des applications en jonctions simples ou multiples. De plus,

comparée aux oxydes de cuivres, la nature plus complexe de la structure cristalline quaternaire des kesterites induit un nombre plus important de phases secondaires et de défauts ponctuels distincts.

Dans un **premier travail de recherche**, sur base de la théorie de la densité fonctionnelle, nous présentons l'étude de l'impact de la substitution de l'étain sur les propriétés cristalline, électrique et optique de l'alliage $\text{Cu}_2\text{ZnSnS}_4$. A la suite du remplacement successif de Sn par deux éléments présentant une configuration d'électrons de valence similaire, Ge et Si, nous observons une augmentation de la valeur de la bande interdite ainsi que des valeurs de coefficients d'absorption de l'ordre de 10^4 cm^{-1} . Sur base des propriétés optiques obtenues, nous présentons, via une version améliorée du modèle de Shockley-Queisser, la modélisation des paramètres photovoltaïques en fonction du taux de recombinaison non radiative. Comparées aux valeurs reportées dans l'état de l'art, ce travail nous permet de mettre en évidence les marges d'améliorations importantes concernant l'efficacité de cellules solaire comprenant comme couches absorbantes $\text{Cu}_2\text{ZnSnS}_4$ ($\sim 10\%$) et $\text{Cu}_2\text{ZnGeS}_4$ ($\sim 5\%$).

De manière complémentaire au premier travail réalisé, une **seconde phase de recherche** est dédiée à l'identification de possibles défauts agissant comme centres de recombinaison dans les composés kesterite d'étain et de germanium. Sur base de calculs *ab initio*, le comportement physique de défauts ponctuels est étudié suivant le dopage et l'alliage au Ge. Premièrement, nous identifions V_{Cu} et Cu_{Zn} comme défauts de types accepteurs responsables de la conductivité de type p observée dans $\text{Cu}_2\text{ZnSnS}_4$ et $\text{Cu}_2\text{ZnGeS}_4$. Ensuite, nous mettons l'accent sur le comportement délétère de X_{Zn} ($X=\text{Sn,Ge}$) agissant comme centres de recombinaisons. Pour finir, nous proposons que l'amélioration des performances photovoltaïques observées dans la littérature suite à l'incorporation de Ge pourrait être attribuée au comportement de Ge_{Zn} qui, en opposition à Sn_{Zn} , donne lieu à une probabilité plus faible de recombinaison purement non-radiative.

Pour finir, dans un **dernier travail**, une stratégie de co-dopage à l'azote et au magnésium de films minces d'oxyde de cuivre déposés à température ambiante par pulvérisation cathodique est étudiée. Via la mise en place d'une batterie de mesures (XRD, EDX, VdP-Hall, spectrophotométrie, Raman), nous corrélons l'évolution des propriétés électriques et optiques aux transitions cristallines observées ainsi qu'aux variations de concentrations en défauts ponctuels. En commençant par la mise en évidence d'une possible voie de synthèse de films minces de Cu_2O dopés à l'azote à partir d'une cible de CuO , nous présentons également, suite à l'incorporation d'azote, une augmentation de la concentration en $(\text{N}_2)_{\text{Cu}}$. Ce défaut au comportement d'accepteur est responsable de l'augmentation, observée expérimentalement, en porteurs de charge majoritaires de type p. De plus, nous confirmons l'amélioration des propriétés électriques observées à la suite du dopage au Mg. Cependant, de manière contrastée, le co-dopage N,Mg d'échantillons de Cu_2O détériore le caractère cristallin des films minces et mène également à une dégradation des propriétés électriques possiblement

attribuable à l'importante incorporation d'azote mesurée.

Cette thèse apporte une contribution au travail de clarification des mécanismes fondamentaux qui opèrent à l'échelle atomique via la formation de défauts ponctuels dans les kesterites et les oxydes de cuivre.

ACKNOWLEDGEMENTS

First of all, I would like to express my gratitude to the members of the jury for taking the time to evaluate this thesis.

Completing this thesis has been a 6-years journey that, in my opinion, share many similarities with the climb of a challenging mountain pass. At the base, the summit appears barely reachable, and it is impossible to fully assess the road ahead. Then we begin, and thousands of pedal strokes later, we realise the journey is marked by ups and downs. Some kilometres are steeper than others, and it is during these moments that we understand how much the support of the environment and the people around us makes this endeavour achievable. Finally, with the final meters in sight, overwhelmed by a feeling of satisfaction, what remains are fond memories and the envy to tackle new challenges.

In that sense, I was particularly fortunate to have conducted my research in the SPIN research group. Foremost, I would like to express my gratitude to my supervisor Prof. Dr. Ngoc Duy Nguyen. Six years ago, he gave me the opportunity to initiate this work and its final achievement has only been possible thanks to his guidance. I am grateful for his availability, his enthusiasm as well as the energy and the time he dedicated to my research. Along these years, his commitment and accuracy in every task were truly sources of motivation. It was also a real pleasure to collaborate on various teaching activities. For all of this, thank you, Duy.

I would also like to warmly thank Prof. Dr. Jean-Yves Raty for his guidance and advice concerning *ab initio* calculations. Our discussions were truly appreciated.

Furthermore, I extend my thanks to Dr. Guy Brammertz and Prof. Dr. Bart Vermang for the collaboration and the work realised at Energyville. Thank you also Romain for our discussion on research and kesterites. I am also grateful to Prof. Dr. Edgardo Saucedo along with his entire research group at UPC for the few days spent

learning from them.

I would also like to acknowledge Prof. Dr. Alejandro Silhanek for his sympathy as well as for his trust concerning our shared teaching activities.

Of course, I would also like to express my gratitude to all my EPNM-SPIN colleagues and friends with whom I had the chance to work: Jérémy, Joseph, Sunil, Sylvain, Naama and Cyril. Specifically, thank you Stefan, Amaury and François for the great work atmosphere. A special mention to Nicolas for the day and night emotional support provided via these reels exchanges. In addition, I am particularly grateful to Emile for our discussions in and out of the lab as well as for the time we spent disassembling and reassembling EVA2. I will miss our debate sessions on physics, politics, ethics, energy, cycling, series, etc. I would also like to distinctly thank Simon for his support, his friendship and his "*coaching*" during all our cycling rides. These shared 7 am *sufferings* in the dark, sometimes under characteristic Belgian weather, only make the upcoming day more enjoyable. I cannot stress enough how much this research environment participated to the achievement of this work. Eventually, I hope I have given you some insight into the question "*What's a deep defect ?*"

I would also like to thank my family and friends for their support and love. I am forever grateful for their presence in my life.

Je voudrais tout particulièrement remercier mes parents ainsi que ma sœur Audrey. Maman, papa, votre amour ainsi que votre confiance m'ont toujours permis d'avancer au mieux dans la vie. Cette thèse est bien sûr en partie la vôtre.

Enfin, j'aimerais remercier Eloïse. Merci pour ta patience, tes attentions, tes encouragements et ton amour. Je ne suis pas toujours le plus démonstratif et je profite donc de ces quelques lignes pour te dire à quel point je suis chanceux de t'avoir à mes côtés. Je t'aime.

Liege, June 2nd, 2024

Dedication & consistency.

1. **Ratz, T.**, Brammertz, G., Caballero, R., León, M., Canulescu, S., Schou, J., ... & Vermang, B, *Physical routes for the synthesis of kesterite*, Journal of Physics: Energy, **1(4)**, 042003, (2019).
2. Pike, N. A., Dewandre, A., Chaltin, F., Gonzalez, L. G., Pillitteri, S., **Ratz, T.**, & Verstraete, M. J, *Spontaneous interlayer compression in commensurately stacked van der Waals heterostructures*, Physical Review B, **103(23)**, 235307, (2021).
3. **Ratz, T.**, Raty, J. Y., Brammertz, G., Vermang, B., & Nguyen, N. D., *Opto-electronic properties and solar cell efficiency modelling of Cu_2ZnXS_4 ($X= Sn, Ge, Si$) kesterites*, Journal of Physics: Energy, **3(3)**, 035005, (2021).
4. **Ratz, T.**, Nguyen, N. D., Brammertz, G., Vermang, B., & Raty, J. Y., *Relevance of Ge incorporation to control the physical behaviour of point defects in kesterite*, Journal of Materials Chemistry A, **10(8)**, 4355-4365, (2022)
5. Sliti, N., Fourneau, E., **Ratz, T.**, Touihri, S., & Nguyen, N. D. (2022), *Mg-doped Cu_2O thin films with enhanced functional properties grown by magnetron sputtering under optimized pressure conditions*, Ceramics International, **48(16)**, 23748-23754, (2022)
6. **Ratz, T.**, Fourneau E., Sliti N., Baret A., Malherbe C., Vertruyen B., Silhanek A. & Nguyen, N. D., *Correlation between material properties, crystalline transitions, and point defects in RF sputtered (N,Mg)-doped copper oxide thin films*, under submission process, (2024)

CONTENTS

1	Introduction	1
1.1	World energy context	2
1.2	Earth-abundant photovoltaic thin films	7
1.2.1	Cu ₂ O copper oxide, a transparent conducting material	10
1.2.2	Cu ₂ ZnSnS ₄ kesterite, a close relative of CIGS material	13
1.3	Outline and objectives	17
2	Physics of photovoltaic absorber materials	21
2.1	Fundamentals of solid-state physics	22
2.1.1	Crystalline structure	22
2.1.2	Energy band structure	25
2.2	Perfect semiconducting materials	34
2.2.1	Light absorption	34
2.2.2	Charge carriers	37
2.3	Defects in crystalline semiconductors	39
2.3.1	Point defects: definitions and notations	41
2.3.2	Recombination processes	45
2.3.3	Defect-mediated recombination	48
2.4	The photovoltaic effect	61
2.4.1	Physics of the photovoltaic effect	63
2.4.2	Modelling of the electrical power conversion efficiency	71
3	Defect formation energy using <i>Ab initio</i> calculations	75
3.1	Density functional theory	76
3.1.1	Many-body Schrödinger equation	76
3.1.2	One-electron Hartree-Fock equations	81
3.1.3	One-electron theory: Density Functional Theory (DFT)	86
3.2	Numerical implementation	92

3.2.1	Electron wavefunction	92
3.2.2	Brillouin zone meshing	95
3.3	Defect formation energy	98
3.3.1	Supercell approach	98
3.3.2	Material phase diagram	101
3.3.3	Corrections terms	103
4	Sn cationic substitution in kesterite	105
4.1	Introduction	107
4.2	Computational method	108
4.3	Cationic substitution in kesterite	109
4.3.1	Crystalline structure	109
4.3.2	Electronic properties	110
4.3.3	Optical properties	113
4.4	Conversion efficiency modelling	115
4.5	Conclusion	121
5	Physics of point defects in kesterite	123
5.1	Introduction	125
5.2	Computational method	127
5.3	Point defect landscape	128
5.3.1	Kesterite growth: chemical environment	128
5.3.2	Intrinsic point defect formation energies	130
5.3.3	Defect identification: ionisation levels	135
5.4	Atomic distortions	137
5.5	Conclusion	140
6	Phases and point defects in N,Mg doped copper oxide	143
6.1	Introduction	145
6.2	Experimental methodology	148
6.2.1	Thin film synthesis and characterisation	148
6.2.2	Sputtering target crystallinity and composition	149
6.2.3	Plasma pressure optimisation	150
6.3	N,Mg doping of copper oxide	152
6.3.1	Crystallographic investigation	152
6.3.2	Thin film elemental composition	154
6.3.3	Electrical and optical properties	156
6.3.4	Phase and defects correlation through Raman spectroscopy	160
6.3.5	Point defect discussion	162
6.3.6	Experimental reproducibility	162
6.4	Conclusion	164
7	Conclusion	167

A	Comments on <i>ab initio</i> calculations	173
A.1	VASP practical features	173
A.1.1	Ionic and electronic relaxations	173
A.1.2	Band structure and density of states (DOS)	175
A.1.3	Optical properties	175
A.2	Hartree energy	176
A.3	Kesterite secondary phases	177
B	Comments on the sulphurisation of kesterite samples	179
B.1	Physical routes for kesterite synthesis	179
B.2	Sulphurisation using Annealsys	181
B.3	Solution-based processes	185
C	Plasma pressure effect on (N,Mg)-doped copper oxide layers	187
C.1	Results and discussion	187
C.2	Deposition parameters	190
	Bibliography	207

INTRODUCTION

1.1	World energy context	2
1.2	Earth-abundant photovoltaic thin films	7
1.2.1	Cu ₂ O copper oxide, a transparent conducting material	10
1.2.2	Cu ₂ ZnSnS ₄ kesterite, a close relative of CIGS material	13
1.3	Outline and objectives	17

The scientific research presented in this thesis focuses on the fundamental behaviour of materials relevant to the field of **photovoltaic (PV) technologies** as energy production sources. Therefore, the description of the **world energy context** appears necessary to highlight the challenges that our modern society is facing and which consequently motivate further innovations. As it will be described, the share of photovoltaic-based energy is only a small ingredient to a large global picture. To start, an overview of the energetic landscape including the electricity generation sources and, more specifically, the solar production within the global energy mix is described. Then, we present the current status of the photovoltaic technology including the different solar cell generations to introduce thin film materials and more specifically **earth-abundant** materials. Finally, the state-of-the-art of **kesterites** and **copper oxides** are presented, highlighting the relevance of **defect** behaviours on the optoelectrical properties, as well as on the solar cell performances. Finally, in a last section, the objectives and content of this thesis are provided.

1.1 WORLD ENERGY CONTEXT

In this opening section, we provide an overview of the energetic landscape in which the solar energy production, the application field of this thesis, takes place:

1. First, the energy context to date (energy consumption, electricity production, share of renewables, and part of solar production) is presented.
2. Second, the 2050 goals established by the Intergovernmental Panel on Climate Change (IPCC) to limit global warming to 1.5° C are provided. Additionally, a roadmap from the International Renewable Energy Agency (IRENA) on the transition to an energy production composed mainly of renewable sources is discussed along with and some "local" action plans.
3. Third, the role of solar energy within the transition is highlighted in parallel to a comment concerning the material requirements from one energy source to another.

As presented in **Fig.1.1(a)**, since the beginning of the 20th century the world consumption of energy has been ramping up continuously. In 2021, a total amount of 159×10^3 TWh of energy consumed was recorded in all sectors (building, transport, industry, agriculture, heat, *etc.*) and generated via various production methods. As part of the increasing needs of energy required by our modern society, in 2021, the contribution from the electrical mix was of 27.8×10^3 TWh, representing $\sim 17.5\%$ of the global energy consumed. In particular, within this mix of electricity, the part that comes from solar production was equal to 1.4×10^3 TWh ($\sim 3.74\%$ of the total electricity produced and $\sim 0.65\%$ of the total energy consumed). These figures are the result of the industrialisation, the improved lifestyle and the technological blossoming of the last century, reinforcing the energy needs for which the consumption rates of fossil sources (oil, gas, and coal) are, over the last decades, drastically higher (one order of magnitude) with respect to "low-carbon" sources.

Furthermore, concerning the global electricity production mix, as presented in **Fig.1.1(b)**, it is interesting to observe that, since 1985, the worldwide share of low carbon production sources (solar, wind, hydro, nuclear, bio, *etc.*) with respect to the total electricity mix fluctuates between 32 and 38% ($\sim 15\%$ for the total energy consumption) with nearly a steady-state increase since 2012. This year also corresponds to a sharp increase for wind and solar energy sources. In addition, the low-carbon

share value fluctuates¹ from one continent, one country to another depending on the geographical, historical and economic situation in each specific part of the world.

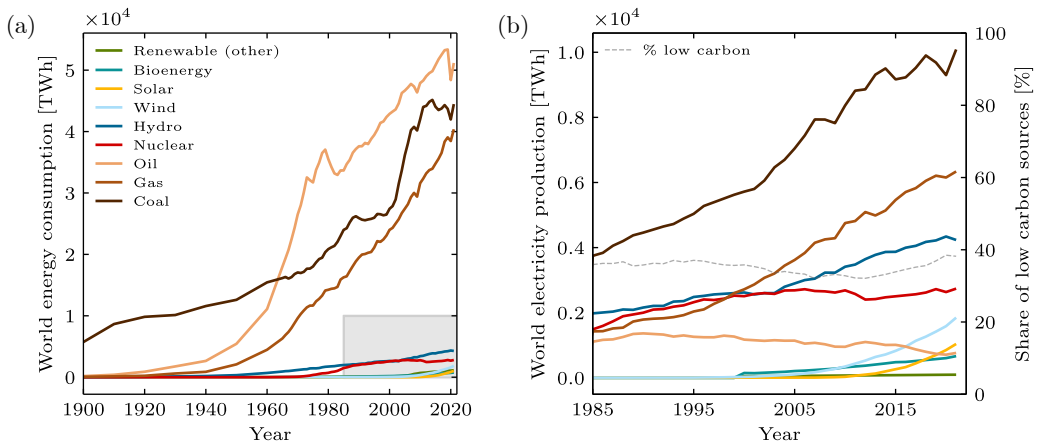


Figure 1.1: (a) Evolution of the world energy consumption in TWh from different energy sources taking into account inefficiencies of fossil fuel sources known as the "substitution method" as described in Ref. [1]. The grey-shaded area corresponds to the scale of the electricity production figure presented in (b). (b) Evolution of the world electricity production in TWh. The dashed line corresponds to the right axis presenting the evolution of the electricity share coming from "low-carbon" sources (bioenergy, solar, wind, hydro and nuclear). Raw data extracted from [1].

Within this context, in March 2023, the Intergovernmental Panel on Climate Change (IPCC) delivered its sixth assessment report on climate change with the following key headlines [2]:

"Human activities, principally through emissions of greenhouse gases, have unequivocally caused global warming"

"Limiting human-caused global warming requires net zero CO₂ emissions"

"There is sufficient global capital to close the global investment gaps but there are barriers to redirect capital to climate action. Enhancing technology innovation systems is key to accelerate the widespread adoption of technologies and practices"

To limit the global warming and to reduce the impact of the human activity on greenhouse gas emission, the decarbonisation has to be operated in each sector of our society and the proportion of the electricity from low-carbon sources in the actual electricity mix and with a higher extent in the total energy consumption, has to

¹57.92% in Europe and 73.78% in Belgium [1]

be increased while decreasing our dependence on fossil fuels (oil, gas, coal). While the "how" or practical implementation appears as a difficult question, efforts such as sobriety, time, money and research in renewable and nuclear energies appear as vital to achieve a sustainable society. To meet this goal, in 2022, the International Renewable Energy Agency (IRENA) published the "*World energy transitions outlook 2022*" [3] in which an energy transition pathway is provided to limit the global warming to 1.5° C through 6 technological avenues for 2050 while also providing direct actions to be taken before 2030. The main message of the IRENA plan is the **promotion of the electrification and the energy efficiency** as the spearhead of the energy transition enabled by renewable, hydrogen, and sustainable biomass. The reduction of emissions (36.9 Gt of CO₂), *i.e.* the transformation of our energy consumption and production methods is carried out via six main routes:

- (i) **25%**: The increase in the electricity generation from renewable sources,
- (ii) **25%**: The improvement of the energy efficiency,
- (iii) **20%**: The electrification of various sectors (transportation, heat, *etc.*),
- (iv) **14%**: The carbon capture and storage,
- (v) **10%**: The production of clean hydrogen (from low carbon electricity),
- (vi) **6%**: The efficient use of bioenergy.

As presented in **Fig.1.2**, following these routes to achieve the 2050 target, the electricity share in the final energy consumption should grow to 50% (17.5% in 2021) with a share of renewable production as high as 86% (electrification of transports, heat and hydrogen) [4]. As depicted in **Fig.1.2(a)**, the growth of the electricity production by sector is expected to occur along with an important electrification of the transport sector (from 2 to 22% of the total electricity produced) while reducing the share of industry and construction sectors by 8 to 9 points. Moreover, according to the IRENA, the electricity production via renewable sources is expected to become the main energy source in the coming decades. In addition, as presented in **Fig.1.2(b)**, the report also emphasises the dominance of solar and wind contributions. These two technologies are economically promising against fossil sources as they provide access to cheaper electricity. The electrification through renewable energies is also healthier, more efficient and should allow one to reduce the total energy consumption compared to the energy mix involving a large amount of fossil energies. The solar energy source is expected to grow from 1040.5 TWh (2021) to 14 437.5 TWh in 2050 (within the 1.5 °C scenario). Indeed, according to IRENA, solar PV is expected to become the second largest power source (behind wind) in 2050, representing approximately 25% of the total electricity generation by providing off grid and on grid possibilities [5]. This report provides a "big picture" of the transition that should be performed worldwide. Of course, taking into account the geopolitical and economic context as well as the available resources, this global transition has to

be applied with more "local" plans such as the *Shift* project in France [6, 7].

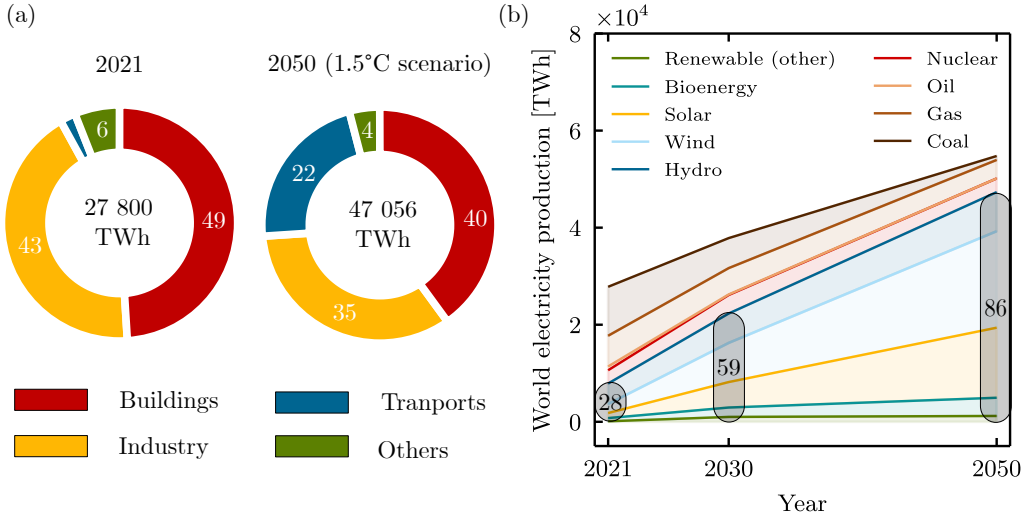


Figure 1.2: (a) Distribution of the electricity production in 2021 and the projected values for 2050 within the 1.5°C scenario according to the different sectors of use as established by the IRENA. In (b), the evolution of the electricity production is presented by source in order to meet the sector energy needs presented in (a). Two main milestones are presented: 2030 and 2050. The grey highlight represents the share of the renewable sources to the total electricity production (except nuclear). Raw data are extracted from [4].

Then, the investments required to transform our production methods in each sector will lead to inevitable consumption of material and energy resources. As presented in Ref. [8] and illustrated in **Fig.1.3**, renewable energy sources require more material, more minerals than their fossil-based counterpart. Focusing on metals, Gregoir *et al.* reported on "the demand, supply, and sustainability assessment of the EU Green Deal and its resource needs" [6, 9]. The authors state that the energy transition is metal intensive. With the electrification of transport, batteries, solar photovoltaic systems, wind turbines, and hydrogen technologies all these technologies require a significant amount of rare earth elements. Confirming this trend, in a 2021 report, the Internal Energy Agency (IEA) shows that the lowest demanding electricity sources by at least a factor of two are gas and coal. In contrast, solar photovoltaic requires around 7,500 tons per TW with roughly half of silicon and half of copper. However, these values depend on the chemical elements involved and on the technological efficiency. As a solar PV plant is composed of modules (solar cells), inverters, trackers and the structure, the differences in material consumption come mainly from the PV technology used (Si, thin film, perovskite, *etc.*). Moreover, as highlighted in **Fig.1.3**, crystalline bulk-Si is currently dominating the photovoltaic market (95% of the global capacity), with half of the material demand being Si. In contrast, thin film technologies require more glass but overall less minerals than Si

technology. However, the mineral accessibility levels might be lower.

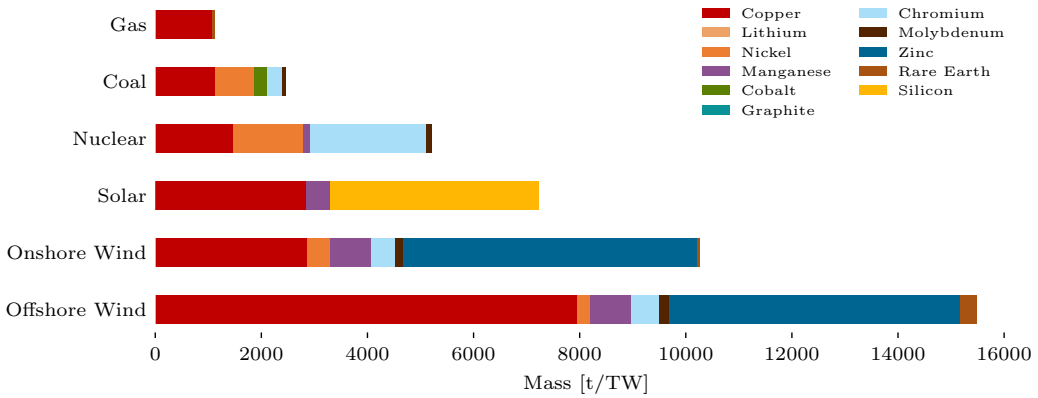


Figure 1.3: Representation of the mineral mass needed per TW of energy production rate as a function of the energy source in tons per TW. Raw data extracted from [8].

In the framework of the development that is necessary for a given technology, it is therefore required to assess its possible scaling up in terms of material availability. Regarding this matter, in 2012, Vesborg *et al.* [10] published a review evaluating the scalability of chemical elements to be incorporated in future technologies based on their accessibility. This point is specifically relevant for PV technologies. Of course, the amount of energy and materials required will also depend on the way our society will undergo this transition, keeping the same uses or evolving to more efficient and resilient lifestyles concerning materials and energy consumptions.

In the next section, the PV technologies which can contribute to fulfil the role of solar PV in the electrification of the energy production are discussed, leading to the introduction of the thin film solar cell technology and, more specifically, the presentation of two specific earth-abundant materials.

1.2 EARTH-ABUNDANT PHOTOVOLTAIC THIN FILMS

From the established outlook concerning the solar energy production within the global energy and electricity market, we focus the discussion on one particular photovoltaic technology and even more specifically on two earth-abundant PV materials which are at the heart of the research carried out in this thesis.

1. First, an overview of photovoltaic technologies is presented and the dominant place of bulk-Si PV for electricity production as well as the market niches for thin film technologies are highlighted (flexible substrate, transparent PV, tandem solar cells, *etc.*)
2. Then, **Kesterites**, promising absorber layers for PV application are introduced via a short state-of-the-art presenting the evolution of the efficiency as well as the improvements brought to kesterite-based solar cells. This description is given with a specific focus on the role of defects in kesterite compounds and their impact on the PV performances.
3. Finally, the second materials of interest for this thesis is presented, namely **Copper oxides**. The history of copper oxide in semiconductor research, first as a rectifier, then as a possible layer for photovoltaic application, as well as the evolution of the efficiency are provided. Then, in a similar way as for kesterite materials, the discussion is focused on defects and more specifically on doping strategies used to boost the material optoelectrical properties.

Solar cell technologies have evolved over the decades into four different generations defined by the type of materials, the absorber layer thickness, or the physical principle behind the energy conversion. Although the boundaries between these generations are not perfectly defined, one can distinguish the following classes :

1. **The crystalline silicon** technology is the most mature and by far the dominant technology on the PV market (with a share oscillating around 90% over the years). It is based on silicon wafers with manufactured absorber layers between 100 and 200 μm . Including monocrystalline and polycrystalline silicon, this technology provides commercial PV modules with an average efficiency of 21% [11] while the record efficiency for single bulk-Si cell is of 26.8% (the theoretical limit being around 32 % considering a 1.1 eV Si bandgap) [12].
2. **The thin film** technology is based on μm -thick thin film semiconductors such as amorphous silicon, GaAs, CdTe, CIGS, *etc.* deposited on various substrates

(glass, steel, polymer foils, *etc.*), broadening the range of applications (building-integrated, flexible, transparent, tandem, *etc.*). Since 2010, the thin film technology has been contributing between 5% to 10% to the PV market with commercialised module efficiency between 13% (CIGS) and 18% (CdTe). Moreover, single cell record efficiencies for CIGS, CdTe and GaAs are respectively of 23.3%, 21.0% and 29.1% [11,12].

3. **The third generation** includes thin film semiconductors with "novel" materials or architectures such as perovskite materials formed by a PbX_3 ($X = \text{halide}$) structure centred around an organic molecule (*e.g.* Methylammonium CH_3NH_3), quantum dot solar cells or dye-sensitised solar cells formed by a mesoporous medium covered with dye-sensitised molecules (active PV part) immersed into an electrolyte [13].

The robust efficiency of the current Si-bulk solar cells is the result of decades-long optimisation works since the first Si solar cell manufactured by Russell Ohl, a scientist from Bell's Laboratory in 1940 [13]. This technology has also benefited from intensive research and development on semiconductor processes in other domains such as Si transistors for logic devices. Silicon is also, by weight, the second most abundant element in the Earth's crust (after oxygen). However, Si material extracted from the Earth's crust is oxidised and most of it is present in the form of minerals made of a silicate group $\text{Si}_x\text{O}_y^{z+}$ and a metallic cation (Zn, Mg, Fe, *etc.*). The purification of Si from silicates requires high temperatures around 1000°C (10 to 12 MWh of energy per ton of silicon produced) as well as coal and wood to extract oxygen and form carbon oxides as a waste compounds. As a result, the main cost of bulk Si solar cells comes from the high Si purity required by this technology [14]. In contrast to the other PV technologies, the decades of experience and knowledge acquired in research and industrialisation for crystalline Si ultimately place this technology in first position for massive PV electricity production in the years to come. Indeed, as confirmed by the IEA, Si solar cells are expected to remain the strongest contender for some time and, as a result, the usage of stand-alone thin film solar cell might be limited to specific applications such as flexible, building-integrated PV or multijunction solar cells [8].

In addition, the thin film technology has emerged over the recent years as an interesting candidate for efficient energy production. Owing to their higher degree of versatility, thin film solar cells triggered the emergence of novel devices in the solar production market, complementary to the traditional solar panel. This technology offers various advantages such as a low material consumption via the reduction of the absorber layer thickness down to the μm scale, the higher tunability of the material properties and the lower process temperatures (typically below 500°C). Through their stoichiometry variations, these thin film materials offer the possibility to tune the bandgap value, which is of interest for top cells in tandem applications using the well-established Si as bottom cell [15,16]. Moreover, the combination of Si solar cell and thin film technologies has the potential to lead to solar cells that are more

efficient than single junction structures, pushing further the performances of PV as a cheap electricity production source [15,17]. In the recent years, a great interest has emerged concerning this combined technology as it allows to combine materials advantages and to break through the thermodynamic limit of single junction efficiency, with already record as high as 36.1% for IIIIV-Si tandem solar cell efficiencies [12].

Moreover to reach industrial production, the thin film technology must fulfil several criteria such as low-cost thin film synthesis, high solar cell efficiency, and high materials resource availability and accessibility [10]. In relation with the latter point, in 2017, the European Commission published a list of critical raw materials and identified Ga and In as two of them, consequently highlighting the scarcity of those elements used for the synthesis of inorganic chalcogenide $\text{CuInGa}(\text{S},\text{Se})_2$ (CIGS) alloys [18]. In addition to scarcity, the toxicity appears also as another key point to take into account as for instance, As in GaAs absorber layer does not appear suited for large scale production. Finally, the material and even the complete cell recyclability is also still overlooked. As a result, over the last decades, focusing on the thin film solar cell technology as a complement to Si technology and taking into account raw materials accessibility, the scientific community has strengthened its interest in earth-abundant materials used as solar cell absorber layers.

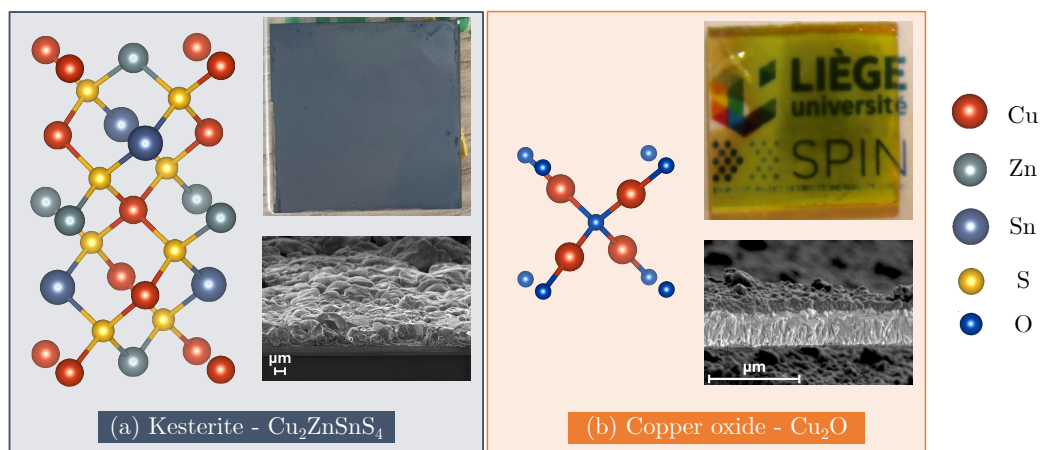


Figure 1.4: Introduction to (a) $\text{Cu}_2\text{ZnSnS}_4$ kesterite and (b) Cu_2O copper oxide materials. For each material, the crystalline structure is presented with the elemental legend on the right side of the figure. A photography of the deposited thin film highlighting the opaque and transparent nature of respectively kesterite and copper oxide. And, a cross section SEM image is provided.

Among earth-abundant materials, concerning PV applications, copper oxide Cu_2O and kesterite $\text{Cu}_2\text{ZnSnS}_4$ appear as compelling candidates. In **Fig.1.4**, an introduction to these two compounds is presented by illustrating some of their most salient features. First, through the depictions of the tetragonal and cubic crystal structures

corresponding, respectively, to the kesterite and to the copper oxide compound, we highlight the simpler atomistic nature of the binary Cu_2O with respect to quaternary $\text{Cu}_2\text{ZnSnS}_4$. In addition, the two Cu-based materials present both interesting physical behaviour with respect to crystalline defects that particularly impact their resulting PV performances. However, as underlined, the complex structure of kesterite drastically expands the number of possible deviations from the pristine crystal in the form of secondary phases or point defects. In addition, in **Fig.1.4**, a first glimpse on the physical appearance of both materials is also provided, as optical photographs and scanning electron microscopy (SEM) images of the materials, revealing the transparent look of copper oxide while the kesterite material is opaque. This feature highlights the distinct applications of these materials: copper oxide is more suited for transparent PV while kesterite for traditional PV that operates within the visible spectrum.

In the following, we venture through the history of these thin film materials as absorber layers. The objective is to identify the contributions that have improved the understanding of the scientific community concerning kesterites and copper oxides. Knowledge that is key to push further the cell efficiency over the years.

1.2.1 Cu_2O copper oxide, a transparent conducting material

By adding O to Cu, three oxides can be formed: CuO (direct, $E_G = 1.5$ eV), Cu_4O_3 (direct, $E_G = 1.6$ eV) and Cu_2O (direct, $E_G = 2.1$ eV) as a result of the two oxidation state of Cu: +1 and +2, Cu_4O_3 being a mixed phase of Cu in the two states [19–21]. Focusing on Cu_2O , as presented in **Fig.1.4(b)**, this compound possesses a cubic crystalline structure (Pn-3m space group) with a lattice constant of 4.27 Å [22]. Within this structure, each Cu atom ([Ar] $4s^1 3d^9$ - oxidation state +1) is bonded to two O atoms ([He] $2s^2 2p^4$) while each O atom is fourfold coordinated with Cu atoms. Its valence band states are dominantly Cu-3d states while the conduction band states are provided by a dominant Cu-3d and O-2p character [23]. Furthermore, the crystal structure can be viewed as the result of 2 interpenetrating Cu,O networks [22].

Copper oxides belong to a wide class of semiconductors referred to as transparent conducting oxides (TCOs) [24]. The vast majority of them are n-type crystals exhibiting commercial grade electrical and optical performances. However, their p-type counterparts, essential for transparent electronic devices, struggle to achieve efficient optoelectrical properties. These limitations are partially caused by the low charge carrier mobility between, 1 and $100 \text{ cm}^2\text{V}^{-1}\text{s}^{-1}$, related to the localised nature of the 2p oxygen orbital in most oxides [24, 25]. Cu_2O also appears as an interesting candidate for PV application with a large absorption coefficient of the order of 10^4 cm^{-1} and a p-type conductivity of the order of 10^{14} to 10^{17} cm^{-3} . In addition, thin films can be grown at room temperature using various chemical and physical routes such as sol-gel coating, thermal oxidation, magnetron sputtering or pulsed laser deposition [26, 27].

In **Fig.1.5**, we present the historic evolution of copper oxide based solar cell parameters as well as the theoretical limit of those as established by Shockley and Queisser in 1961 based on thermodynamic considerations [28, 29]. The solar cell indicators considered are the efficiency η , the short circuit current density J_{SC} , the open circuit voltage V_{OC} and the fill factor FF .

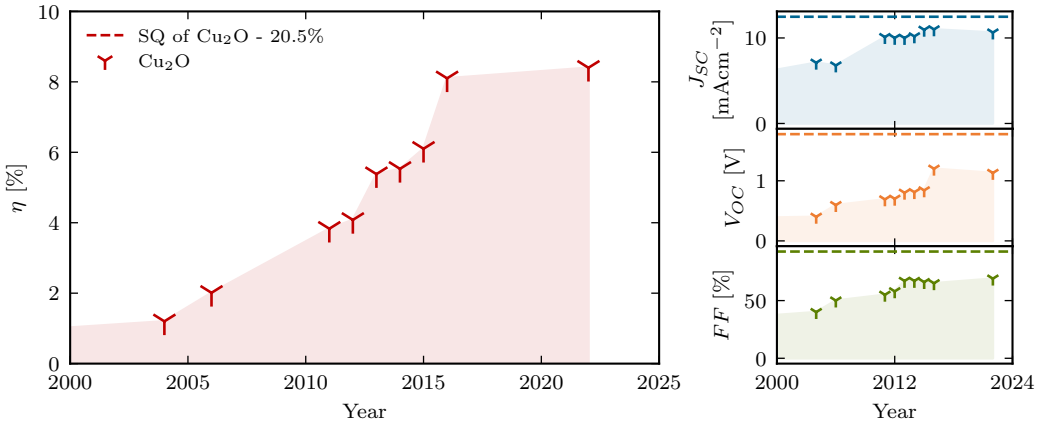


Figure 1.5: Evolution of the copper oxide based solar cell efficiency, along with related photovoltaic indicators: the short circuit current density J_{SC} , the open circuit voltage V_{OC} and the fill factor FF being related as $\eta = V_{OC}J_{SC}FF/\mathcal{P}_{in}$ with \mathcal{P}_{in} , the input solar power (usually the AMG1.5 spectrum). In addition, the Shockley-Queisser theoretical maximal parameters (20.5%, 12.48 mAcm^{-2} , 1.776 V and 92.5%) are provided in dashed lines based on a material bandgap of 2.1 eV for Cu_2O [28, 29]. The markers correspond to Refs. [30–39].

In 1979, the first solar cell was reported when research projects were conducted with the aim at fabricating Schottky rectifying junctions on copper oxide : an US patent did indeed report copper oxide based devices from early 1925 [26, 40]. One year later, a first PN junction made of ZnO deposited on Cu_2O was realised even though the weak efficiency that was then reported came from a Schottky-like behaviour of the contact between a reduced Cu layer and Cu_2O [30]. Then, since 2004, the efficiency of Cu_2O -based solar cells increased from close to 1% to 8.4% through various improvements, most of them related to the reduction of interface defects [19, 31, 32]: (i) first, suitable n-type materials such as ZnO and AZO were identified and the structure of the resulting solar cell was improved, smoothing the band alignment [33]. The introduction of buffer layers (including ZnO, Ga_2O_3 , $\text{Zn}_{1-x}\text{Ge}_x\text{O}$) or improved stacking structure were performed [34, 35, 38]. (ii) Second, the synthesis conditions were improved by enhancing the thermal oxidation of Cu (improved properties with respect to thin films) and also by improving the deposition of the n-type layer with optimal thickness on top of the copper oxide limiting the amount of electronic defects at the junction and optimising the charge extraction [37]. So far the highest efficiencies reported were obtained respectively in 2016 by Minami *et al.* (8.1%) [38]

and in 2021 by Shibasaki *et al.* (8.4%) [39]. In addition, Shibasaki *et al.* reported a high dependence of the thin film transmittance with respect to the amount of impurities. Using a finer control on the O₂ flow during the thin film growth, the authors managed to reduce the defect concentration, highlighting the close relation between transmittance, impurities and oxygen control.

In an article dated from 2022 [27], Lakshmanan *et al.* also reported on the efficiency enhancement in PV devices based on copper oxide over recent years. The authors addressed the improvement brought to the band alignment in the solar cell structure via the introduction of suitable buffer layers allowing to reduce the V_{OC} deficit by decreasing the amount of interface recombination, a problem that was also pointed out as the main issue for further efficiency improvement by Wong *et al.* in 2016 [19]. This V_{OC} improvement is especially prominent between the efficiencies reported in 2015 and 2016, of respectively 6.1 and 8.1% with increased V_{OC} values from 840 to 1200 mV for similar J_{SC} and FF both obtained by Minami *et al.* [37,38]. Wong *et al.* also highlighted the plausible application of Cu₂O in tandem solar cells with Si.

Concerning the low fill factor issue and the corresponding copper oxide poor electrical properties, the reduction of the material resistivity has been performed through the fine tuning of deposition parameters (*e.g.* O₂ flow) as well as doping such as Na [36,37]. Several doping strategies have already been investigated using alkali metals: Li, Na, alkaline earth metals: Mg, Ca, Sr, transition metals: Ni, Zn, Mn and Ag, non-metal: N or Halogen: F [41–44]. In addition, both magnesium and nitrogen strategies led to improved optoelectrical properties of the Cu₂O layers [45–49].

However as previously highlighted, there is still room for improvement with respect to the theoretical limits. As presented in **Fig.1.5** (right panels), even for the highest reported efficiencies, a large deviation with respect to the maximal theoretical limits are observed for the V_{OC} and FF values. The low open circuit voltage value indicates the presence of recombination either within the bulk or at the interfaces while the low FF value can be attributed to poor electrical properties and parasitic resistance of the junction. As a result, to further improve the cell efficiency, the material optoelectrical properties have to be enhanced and the impurity concentration leading to non-radiative recombination has to be reduced in addition to the improvement of the interface with the n-type layer. According to Lakshmanan *et al.*: “the major reason for low efficiency is the presence of secondary Cu and CuO phases in the absorber layer.” It is worth noting that these values of efficiency are more than two times lower than the theoretical efficiency of 20.5 %. Moreover, Wong *et al.* reported that: “a more fundamental understanding of these defects should explain why the efficiency of state-of-the-art Cu₂O devices are still well short of the theoretical maximum efficiency of 20%” [19].

In summary, several culprits have been identified as limiting factors to PV per-

performances of copper oxide based solar cells. Most of these are related to defect-like behaviour either through Cu, CuO phase formation, interface and bulk defects or poor material properties [19, 27].

1.2.2 $\text{Cu}_2\text{ZnSnS}_4$ kesterite, a close relative of CIGS material

Kesterite can be identified via their tetragonal crystal structure exhibiting a point group symmetry $I-4$, commonly formed of either S or Se as the chalcogen combined to three metallic elements: Cu, Zn and Sn and resulting in $\text{Cu}_2\text{ZnSnS}_4$ (direct, $E_G = 1.5$ eV) or $\text{Cu}_2\text{ZnSnSe}_4$ (direct, $E_G = 1$ eV). Similarly to copper oxide, but within the visible optical spectrum range, kesterites present high absorption coefficients of the order of 10^4 cm^{-1} , a p-type conductivity with a charge carrier concentration between 10^{16} and 10^{19} cm^{-3} and mobility values between 1 and $100 \text{ cm}^2\text{V}^{-1}\text{s}^{-1}$ depending on the material stoichiometry [50]. The physical properties of these materials, combined to the fair accessibility of their elementary constituents, make them promising as absorber layers in PV cells [10]. However, in the literature, short minority carrier lifetimes of the order of 100 ps are reported, pointing to the high concentrations of recombination centres within these materials [50, 51]. Moreover, kesterites offer industrially interesting vacuum and solution processes concerning the solar cell production. As detailed in appendix B, the growth of the kesterite layer can be performed using physical or chemical routes involving *low* temperatures around 500°C [52, 53]. These synthesis methods were mostly inherited from its older cousins, the chalcogenide $\text{CuGaIn}(\text{S},\text{Se})_2$ compounds. However, despite the high efficiencies reported for CIGS solar cells (with a record value of 23.3% [54, 55]), the incorporation of this material in a large-scale energy production technology might be compromised due to its elemental scarcity. At the time, this justifies the search for alternative compositions with comparable or better efficiencies than CIGS. As a consequence, as illustrated in **Fig.1.6(a)**, over the past 20 years, the scientific community has been investigating kesterite $\text{Cu}_2\text{ZnSn}(\text{S},\text{Se})_4$ materials [56].

Focusing first on the raw evolution of the PV parameters, as presented in **Fig.1.6**, over the past 25 years, the kesterite-based solar cell efficiencies increased steeply between 2010 and 2014. In addition, as the depicted in the panels on the right, this efficiency improvement is attributed to an enhancement of both the FF and the J_{SC} while the V_{OC} shows only a slight increase. Then, a 7-years stagnation period occurred until 2021 where a new breakthrough was achieved leading to further upgrades of the resulting performances. In 2023, J. Zhou *et al.* reported the highest kesterite-based cell efficiency, reaching 14.9 % [57]. In addition, one can observe that the theoretical FF for both CZTS and CZTSe kesterites are quite close to the reported value and have already quite well been approached. In quite a similar way, the J_{SC} values obtained for CZTSSe kesterite (with material bandgap between 1 and 1.5 eV and consequently, a theoretical limit between CZTS and CZTSe) are also quite close to the theoretical values. Thus, the open circuit voltage value has definitely been identified as the remaining PV parameter that currently limits the cell efficiency.

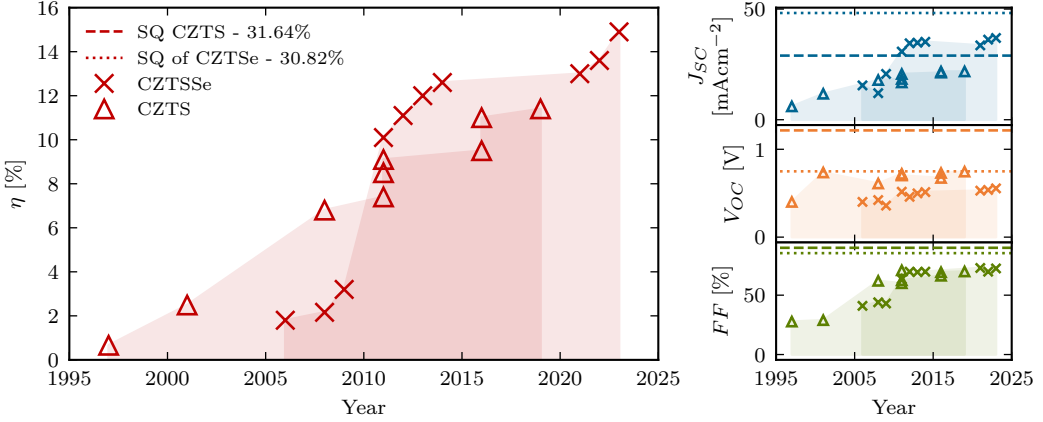


Figure 1.6: Evolution of the S-based and S,Se-based kesterite solar cell efficiencies and related photovoltaic indicators: the short circuit current density J_{SC} , the open circuit voltage V_{OC} and the fill factor FF being related as $\eta = V_{OC}J_{SC}FF/\mathcal{P}_{in}$ with \mathcal{P}_{in} , the input solar power (usually the AMG1.5 spectrum). S,Se-kesterite corresponds to compounds with either pure Se kesterite or mixed S,Se kesterite with a material bandgap between 1 and 1.5 eV. In addition, the Shockley-Queisser theoretical maximal parameters are provided in dashed lines based on a material bandgap of 1 eV and 1.5 eV for CZTSe (30.82%, 48.22 mAcm⁻², 0.749 V and 85.4%) and CZTS (31.64%, 28.97 mAcm⁻², 1.215 V and 89.9%) [28,29]. The markers correspond to Refs. [58–61] for CZTS and Refs. [62–67] for CZTSSe.

As presented by Giraldo *et al.* in 2019, the so-called "V_{OC} deficit", with respect to the theoretical limit, is more likely to be attributed to defects acting as recombination centres (therefore reducing the minority carrier lifetime), secondary phases (3D defects) and bandgap fluctuations due to cationic disorder [56]. As a result, gaining knowledge and control over the different types of defects in kesterite appears as a key ingredient to push further the material performances and to reach a first milestone of 15% allowing for tandem integration as top cell [16,68] and a second would be to equal the CIGS solar cell efficiency with a perspective of single cell operation [52].

Moreover, in order to achieve high efficiency, the kesterite composition has to be off stoichiometric with Cu-poor, Sn-stoichiometric and Zn-rich conditions. The reason why Cu-poor and Zn-rich compounds offer the highest efficiency can be linked to the chemical route that is followed during the material synthesis as well as to the control of the doping level through the formation of intrinsic point defects [69,70]. The first reason is commented in appendix B through the observation of the various secondary phases encountered during the kesterite synthesis while the second will be at the centre of the research presented in this thesis. As commented, the various secondary phases encountered are inherent to the complex nature of kesterite as quaternary compound. In addition, another reported issue is the Sn multi-valency. Sn can be in a +2 or a +4 oxidation state as a result of its electronic structure

[Kr]5s²4d¹⁰5p². In 2018, Kim *et al.* reported that deep defects can be introduced either via the reduction of Sn through S or Se vacancy or through the presence of Sn_{Zn} defects. As further emphasised by Wang *et al.* in 2023, the regulation of defects in kesterite absorber layers is critical in order to reach high performance devices [71]. They stressed that Sn-related defects (Sn_{Zn} or [Cu_{Zn}+Sn_{Zn}] cluster) are pointed out as recombination centres that can further degrade the performances through their possible activation by the formation of the 5s² "lone-pair" corresponding to the Sn in valence state +2 [72,73]. In addition, Sn²⁺ with respect to Sn⁴⁺ may lead to different lattice distortions and enlarged carrier capture cross-sections. As highlighted with much details in appendix B, the growth of CZTSSe using Sn⁴⁺ solution precursors results in a different chemical route with respect to Sn²⁺ which does not imply transition species but on the contrary forms directly the kesterite crystals, impacting significantly the PV performances. Such a direct kesterite growth mechanism reduces the risk of remaining secondary phases and defects.

To prevent or circumvent the formation of detrimental defects and secondary phases within the bulk absorber layer and to enhance the solar cell device performances, several strategies have been considered over the years. Most of them aim at the reduction on defects acting as recombination centres either within the bulk material or at the interfaces. Some of those strategies are inherited from the knowledge of CIGS materials, whose efficiency improvement to 23.35% was performed through Na doping, Ga bandgap grading and KF, RbF or CsF surface treatment for passivation [56]. Among the kesterite strategies, one can cite:

1. **Doping:** a wide range of extrinsic dopants were investigated in studies related to kesterites: Bi, Sb, Fe, In (exotic), Ag, Cd and Ge (isoelectronic) or Li, Na, K, Rb and Cs (alkaline from processes historically used for CIGS) [74–76]. Among them, positive results were reported regarding the incorporation of a small amount of Ge which resulted in an improvement of the V_{OC} and the FF [77,78]. This improvement could be attributed to the larger grain size and to a variation of the growth chemical pathway, leading to fewer defects and secondary phases formation [79].
2. **Alloying:** elemental substitution by a range of chemical elements including Ag (on Cu sites), Cd (on Zn sites) or Ge and Si (on Sn sites), seem ideal options for kesterite alloying [80]. Both substitutions of Ag on Cu and Cd on Zn aim at reducing the Cu/Zn disorder [81,82]. Then, it was demonstrated that alloying with Ge is associated to very good performances, corresponding to the reduction of the V_{OC} deficit [83].
3. **Bandgap grading:** used in order to improve the band bending with respect to the back and front interfaces (respectively, Mo and the n-type layer). This strategy, implemented using Ge/Sn cationic and S/Se anionic substitutions, was successfully demonstrated to improve the V_{OC} by reducing interface recombination [84].

4. **Post-treatment annealing:** in their 2021 review, He *et al.* reported on the annealing post-treatment of the bare absorber layer, the junction or the complete solar cell as an effective way to reduce non-radiative recombinations in the bulk or at the interface. Indeed, this process allows the relaxation of metastable defects formed due to an incomplete quenching process [84]. Post-deposition annealing (PDA) also allows to improve the interface quality via elemental interdiffusion such as Cd and Zn ions [66]. However, this treatment fails to prevent the inclusion of low formation energy detrimental defects.
5. **Interface passivation and alkali treatment:** finally, in view of reducing defect concentrations, surface passivation (particularly in the case of the front interface) appears as an interesting route, through post-doping via alkali elements or the application of a physical passivation layer such as Al_2O_3 [84, 85].

As a result, from kesterite reviews, in 2019, Giraldo *et al.* observed that: "*Very little is known regarding deep defects in these materials*" [56] and in 2021, He *et al.* mentioned that "*To move forward, the formation mechanisms of the detrimental defects and defect clusters need to be further investigated*". One can thus conclude that, in order to boost further kesterite-based cell efficiencies, it is essential to enhance our knowledge concerning the behaviour of defects and their impact on the PV performances.

1.3 OUTLINE AND OBJECTIVES

In this work, we investigate the physical behaviour of point defects in two earth-abundant semiconducting materials used as absorber layer for photovoltaic applications.

1. **Kesterite:** Using *ab initio* calculations, the Sn cationic substitution by Ge and Si is **theoretically investigated**, extracting the absorber optoelectrical properties and modelling the PV performances. The possible efficiency enhancement for both $\text{Cu}_2\text{ZnSnS}_4$ and $\text{Cu}_2\text{ZnGeS}_4$ upon reduction of the non-radiative recombination rate was consequently quantified. Then, via the computation of point defects in pure Sn and Ge kesterites, possible recombination centres that participate to the recombination rate presented in the first study were identified and/or confirmed.
2. **Copper oxide:** Focusing on the optimisation of thin film properties, the incorporation of Mg and N_2 were **experimentally reported** using RF magnetron sputtering at room temperature. Throughout this study, the dependence of the copper oxide crystal structure on the synthesis conditions was first reported. Second, the variations of the absorber optoelectrical properties were correlated to the material point defects as a result to the doping performed.

As mentioned above, the focal point of this thesis is set on the physics of point defects in two specific semiconducting materials, namely Cu_2O copper oxide and $\text{Cu}_2\text{ZnSnS}_4$ kesterite. Furthermore, for these two materials, our attention is fixed on photovoltaic applications in which they are meant to be used as absorber layers. Then, owing to their respective chemical compositions, kesterite and copper oxide can both be qualified as earth-abundant materials. **This research is therefore committed to extend our knowledge concerning the role of point defects on the physical properties of Cu_2O and $\text{Cu}_2\text{ZnSnS}_4$ absorber layers and consequently, on the resulting photovoltaic performances.** Here below, the thesis structure is outlined, along with a gradual clarification of the objectives to be achieved in each chapter.

First, in **chapter 2**, starting from an atomistic point of view and focusing on a pristine crystalline material, we detail the microscopic origin of the semiconductor properties. Then, we present the relevant material physical quantities as well as the energy band structure. This first description allows us to introduce and define the concept of defect and to theoretically highlight the role of these imperfections on

the described optoelectrical properties of the pristine semiconductor. This role is then further emphasised as we discuss the notion of defect-assisted recombination thanks to the presentation of both the Shockley-Read-Hall statistics and the microscopic origin of the capture coefficients. From the semiconductor physics and the relevant impact of defect incorporation, we describe the physics of the photovoltaic effect along with its limitations that include charge carrier recombinations. Finally, we provide a thorough description of an electrical conversion efficiency model that enables the computation of the photovoltaic performance indicators using as data input, the absorber layer optical parameters and, as parameter, a specific coefficient tuning the non-radiative recombination rate.

Then, in [chapter 3](#), we provide a description of the supercell approach that uses first-principles calculations to predict the physical properties of point defects in $\text{Cu}_2\text{ZnSnS}_4$ based on the computation of their formation energies. The first section of this chapter provides a description of the density functional theory, as well as the numerical implementation for cost- and time-effective calculations. From there, the supercell approach is then developed with a pedagogical description taking the case of a kesterite material as teaching example. The purpose of this chapter is to equip the reader with the theoretical notions required for the study of point defects using first-principles calculations.

In [chapter 2](#) and [chapter 3](#), using a pedagogical approach, we provide the reader the theoretical concepts concerning solid-state physics and density functional theory. Those already acquainted with these fundamentals and interested in the developments specific to the results presented in this thesis should focus their reading on [section 2.3.3](#) (defect-mediated recombination), [section 2.4.2](#) (modelling of the electrical conversion efficiency) and [section 3.3](#) (defect formation energy).

Following the layout of the theoretical aspects of the thesis, we present in [chapter 4](#), the investigation of the cationic substitution of Sn by isovalent atomic species: Ge and Si as published in Ref. [86]. Through this study, the material optoelectrical properties are first calculated using an *ab initio* approach. They are subsequently used as input data for the determination of the photovoltaic parameters based on a model presented by Blank *et al.* [87] (see section 2.4.2). This model allows us to tune the non-radiative recombination rate using a parameter Q_i . The objective of this investigation is to reveal the impact of cationic substitution on the absorber layer properties and consequently on the PV efficiency. In addition, we also discuss the possible efficiency improvement (through the reduction of the V_{OC} deficit) for both $\text{Cu}_2\text{ZnSnS}_4$ and $\text{Cu}_2\text{ZnGeS}_4$ following the reduction of the non-radiative recombination rate.

Building from the results gathered in the previous chapter, we extend in [chapter 5](#), the study of both $\text{Cu}_2\text{ZnSnS}_4$ and $\text{Cu}_2\text{ZnGeS}_4$ by investigating the physical behaviour of point defects in those matrices, as published in Ref. [88] (see section

3.3). First, as a point of comparison with respect to the literature [70], point defects in pure Sn-kesterite are predicted. Then, based on the established comparison, we study point defects in pure Ge-kesterite as well as the introduction of extrinsic Ge-related point defects in the pure Sn-kesterite matrix. Doing so, the origin of the material conductivity is presented based on the defect formation energies and the defect ionisation levels. These quantities allow us to qualitatively assess the trends in defect concentrations as well as to describe the nature of specific defects as acceptor, donor or possible recombination centre. Finally, using the theoretical notions regarding defect-assisted recombination established in section 2.3.3, the lattice distortion associated to defect incorporation is discussed. We finally establish a relation between specific defects acting as recombination centre and possible culprits for the low open circuit voltage reported in the literature. With the results presented in chapters 4 and 5, we hope to deepen the understanding of the role of defects in these materials, in the perspective of helping the wider community towards the fabrication of kesterite-based solar cells with higher efficiencies.

In [chapter 6](#), using an experimental approach and keeping our focus on earth-abundant PV absorber material, we report on the investigation of p-type doping mechanisms in copper oxide, focusing on the optoelectrical properties of Cu_2O upon N_2 and Mg doping as provided in Ref. [89]. Room-temperature deposition of copper oxide thin films by radio frequency magnetron sputtering were performed using various Mg-containing targets, while controlling the Ar/ N_2 gas flow ratio through the growth process. The morphological, structural, electrical and optical characterisations of the grown materials are subsequently discussed, with a focus on the effect of dopants and impurities on the material properties. Finally, in order to understand the role of defects on the material characteristics, Raman spectroscopy measurements are presented and discussed with respect to the experimental observations and the predictions, based on *ab initio* calculations, found in the literature [90]. With this study, we have the objective of unveiling possible correlations between the phase composition of copper oxide films, their physical properties and the nature of existing point defects, whether they are related or not to the incorporated doping species N_2 and Mg. This study specifically aims at boosting the optoelectrical properties of copper oxide in order to reduce the V_{OC} deficit and increase the FF value of solar cells fabricated with these p-type absorbers.

We conclude the thesis in [chapter 7](#) with a summary of the results obtained in the defect investigations that were conducted for both materials used in PV applications. In addition, some perspectives for future works are presented.

PHYSICS OF PHOTOVOLTAIC ABSORBER MATERIALS

2

2.1	Fundamentals of solid-state physics	22
2.1.1	Crystalline structure	22
2.1.2	Energy band structure	25
2.2	Perfect semiconducting materials	34
2.2.1	Light absorption	34
2.2.2	Charge carriers	37
2.3	Defects in crystalline semiconductors	39
2.3.1	Point defects: definitions and notations	41
2.3.2	Recombination processes	45
2.3.3	Defect-mediated recombination	48
2.4	The photovoltaic effect	61
2.4.1	Physics of the photovoltaic effect	63
2.4.2	Modelling of the electrical power conversion efficiency	71

In this chapter, the theoretical notions addressed in the study of absorber layers for PV applications are developed with a specific focus on point defects. An introduction to **solid-state physics** is provided, highlighting the origin of the material bandgap followed by a second section developing the **origin of the semiconductor properties** from a perfect crystal point of view. Then, in a third section, **point defects** and defect-mediated recombination processes are introduced. The last section is dedicated to the physics of the **photovoltaic effect**, highlighting its limitations and the impact of defects on the resulting efficiency. The reader acquainted with solid-state physics should focus on [section 2.3.3](#) and [section 2.4.2](#).

2.1 FUNDAMENTALS OF SOLID-STATE PHYSICS

To appropriately introduce the physics of photovoltaic absorber materials, we initiate the discussion through the description of the crystalline structure and the formalism used to represent the behaviour of the electrons in the system:

1. First, a brief description of crystalline materials is presented via the representation of a repeated atomic organisation known as the primitive cell or the first Brillouin zone respectively in the real or reciprocal space.
2. Then, a description of the energy band structure is provided. This structure represents the energetic landscape of the electrons and the accessible energy levels resulting from the electron-electron and electron-ion interactions.
3. Finally, the origin of the material bandgap and the distinction between insulating, semiconducting, and metallic materials are discussed.

To understand the different behaviours of solid-state materials, it is good-practice to classify them into different categories based on one *simple* idea: the way chemical species arrange themselves to create bonds between each other. Indeed, depending on the chemical nature of the constituents, the interactions that take place and the way the elements are assorted (stoichiometry), *nature* tends to arrange the atoms in an organised (crystal) or unorganised (amorphous) manner. Additionally, it is precisely the obtained atomic structure (*i.e.* the distances between the atoms and the various electronic configurations) that will set the macroscopic properties of the material. Among these properties, one can cite the following two examples: (i) optical properties, that tell us the way the material look to our eyes, how it interacts with an electromagnetic wave, (ii) electrical properties, that provide us information on how charge carriers are generated, recombined and carried through the material. These simple examples are presented among a multitude of other physical behaviours such thermal, mechanical or magnetic properties. All of these characteristics arise from the specific atomic structure and the interactions between the chemical elements within it.

2.1.1 Crystalline structure

Condensed matter physics includes both the study of crystalline solids, in which the atoms are arranged given a repeated 3-dimensional pattern (*e.g.* diamond) and amorphous solids where the atomic positions are more erratic (*e.g.* glass) and no spatial long range order can be identified. In addition, the atoms join each other by

establishing chemical bonds as a result of a balance between attractive and repulsive electrostatic interactions between the ion cores and the electronic clouds as presented in **Fig.2.1** for the case of a perfect crystal [91].

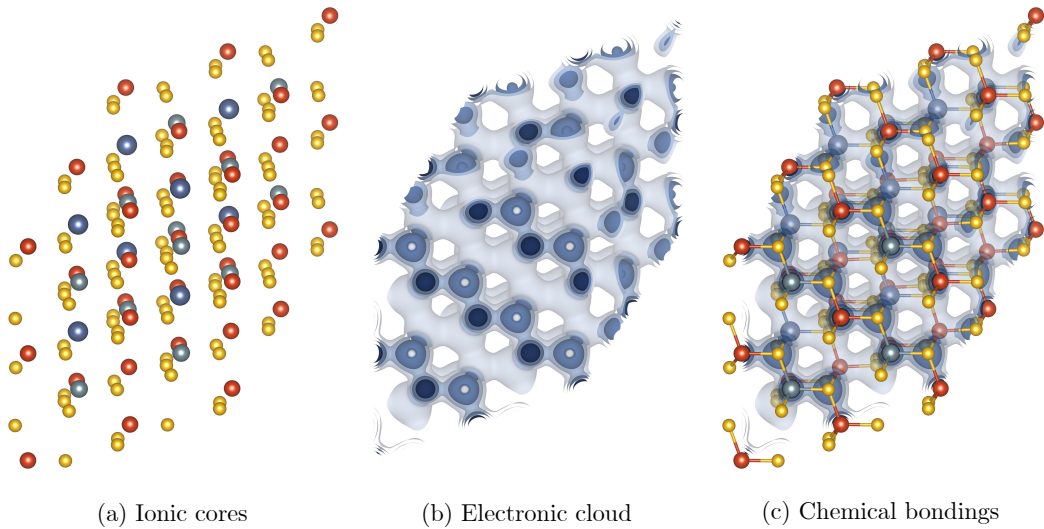


Figure 2.1: Representation of a perfect crystal material with (a) the ionic cores, each colour corresponding to a different chemical species and (b) the electronic clouds depicted by a blue gradient representing the electronic density. The interaction between these two components results in the various chemical bondings between the atoms composing the crystal lattice as presented in (c).

The attractive force originates from an electrostatic interaction between electrons (ionic and metallic bondings) and/or a sharing of valence electrons between atoms (covalent bonding). First, the ionic bonding is induced by a large electronegativity¹ difference between the involved atoms while metallic bondings result of the attraction between positively charged ions and negatively charged delocalised electrons shared by the lattice. In contrast, a covalent bond corresponds to a new organisation of the electronic cloud with respect to the isolated elements where electrons are shared between the atoms. On the other hand, the repulsive forces find their origin in the opposition of the atomic respective electronic clouds to penetrate each other as well as in the repulsion between the positively charged ion cores. Through these different types of interactions, a system energy minimum can be found, resulting of different bond types combination and ionic equilibrium distances.

In this thesis, we initially focus our attention on crystalline materials where atoms bonded together form a perfect crystalline structure represented by a given pattern that repeats itself by translation in the three lattice directions as highlighted in **Figs.2.2(a)** and (b). This pattern, known as the unit cell, is defined as the smallest atomic organisation that has all the crystal symmetries and from which the entire

¹The tendency of a chemical species to attract electrons.

lattice can be built by repetition. A particular unit cell is the primitive cell whose edges are the primitive vectors \mathbf{a}_1 , \mathbf{a}_2 and \mathbf{a}_3 (see **Fig.2.2(c)**). These ones have units of space and any position \mathbf{r} can be expressed as a linear combination of those. Furthermore, the whole material can be represented as a repetition of the primitive cell experiencing a translation vector \mathbf{R} :

$$\mathbf{R} = n_1\mathbf{a}_1 + n_2\mathbf{a}_2 + n_3\mathbf{a}_3, \quad (2.1)$$

with n_1, n_2, n_3 being integers.

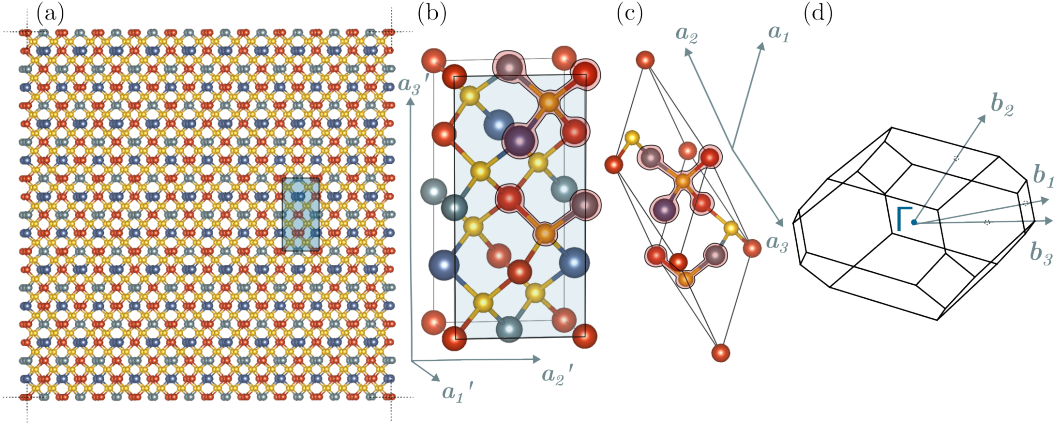


Figure 2.2: (a) Perfect crystal representation as the repetition in the 3 space directions of the conventional cell presented in (b). This one is defined by the space vectors \mathbf{a}'_1 , \mathbf{a}'_2 and \mathbf{a}'_3 . In (c), the lattice primitive cell defined as the smallest unit cell is represented along with the space vectors \mathbf{a}_1 , \mathbf{a}_2 and \mathbf{a}_3 . In (d), the associated reciprocal lattice is presented in the reciprocal space defined by the vectors \mathbf{b}_1 , \mathbf{b}_2 and \mathbf{b}_3 . This one is known as the first Brillouin zone (BZ). As it will be presented in the following, the reciprocal representation contains the same information as the real space representation but offers useful mathematical considerations.

Then, another representation of the crystal structure can be realised in the reciprocal space obtained thanks to a Fourier transformation [92–94]. This one includes the same information as the real space representation but, as presented in the next section, offers a more convenient approach for the mathematical description of the electrons. The counterpart of the primitive cell in the reciprocal space is the region represented by the reciprocal lattice vectors \mathbf{b}_1 , \mathbf{b}_2 and \mathbf{b}_3 having inverse space units and defined as

$$\mathbf{b}_{1,2,3} = 2\pi \frac{\mathbf{a}_{2,3,1} \times \mathbf{a}_{3,1,2}}{\mathbf{a}_1 \cdot \mathbf{a}_2 \times \mathbf{a}_3} = 2\pi \frac{\mathbf{a}_{2,3,1} \times \mathbf{a}_{3,1,2}}{\Omega}, \quad (2.2)$$

with $\Omega = |\mathbf{a}_1 \cdot (\mathbf{a}_2 \times \mathbf{a}_3)|$ the volume of the primitive cell. This region of the reciprocal space is known as the Brillouin zone (BZ) and has a volume $\Omega_{\text{BZ}} = |\mathbf{b}_1 \cdot (\mathbf{b}_2 \times \mathbf{b}_3)| = \frac{(2\pi)^3}{\Omega}$. Any point of the reciprocal space \mathbf{k} can be written as a linear combination of the reciprocal lattice wave vector and this physical quantity is linked to the electron

momentum $\mathbf{p} = \hbar\mathbf{k}$. Furthermore, any translation of the Brillouin zone by a vector \mathbf{G} into the reciprocal lattice² allows to reconstruct the entire crystal if

$$\mathbf{G} = m_1\mathbf{b}_1 + m_2\mathbf{b}_2 + m_3\mathbf{b}_3, \quad (2.3)$$

with m_1, m_2, m_3 integer numbers.

In the following, the established mathematical representation of the crystal will be used to depict the energetic landscape of electrons experiencing the coulombic potential generated by the ions of the lattice. The behaviour of the electrons within the reciprocal space, as a function of \mathbf{k} , will be described through the solutions of the Schrödinger equation considering first, a free electron gas and, second, interacting electrons. From this description, the first BZ will emerge as a specific region of the reciprocal space encompassing a finite number of specific \mathbf{k} points that are sufficient to describe the behaviour of the electrons in a perfect crystal. We will then focus on the physical origin of the bandgap energy E_G , quantity being a relevant parameter for characterising the physical properties of semiconductors.

2.1.2 Energy band structure

To describe the electron behaviour and obtain the optoelectrical properties of the material, the Schrödinger equation associated with the electronic system described by a wavefunction $\Psi(\mathbf{r})$ has to be solved for a given Hamiltonian $\mathcal{H}(\mathbf{r})$. The latter corresponds to a space function whose application onto the wavefunction provides the total energy of the system E_{tot} (see Eq.(2.4)).

$$\mathcal{H}(\mathbf{r})\Psi(\mathbf{r}) = E_{\text{tot}}\Psi(\mathbf{r}) \quad (2.4)$$

A usual representation of the electron energy levels within the reciprocal space is the **band structure**. As it will be presented in the following, various theories have been developed to describe the behaviour of electrons evolving within the repeating landscape of ions. Furthermore, these solid-state theories can be classified as a function of the degree of interaction between the electrons (e-e) and between the electrons and the ions (e-i) starting without interaction, proceeding to "weak" interactions³ and reaching "strong" interactions (tight binding) [92]:

First, in the **free electron model** we do not consider any interaction between electrons nor between electrons and ions of the lattice. Only the electron kinetic energy is considered as well as the electron particle nature through the Pauli exclusion principle. As electrons are fermions, these ones

²By the definition of the reciprocal lattice parameters $\mathbf{a}_i\mathbf{b}_j = \delta_{ij}$ and an interesting result emerges for plane waves calculation: $e^{i\mathbf{G}\mathbf{R}} = 1$.

³"Weak" interactions between valence electrons and the ions could be considered due to the large distance between these electrons and the nuclei as core electrons already occupy inner shells. These core electrons screen the coulombic potential of the nuclei.

cannot occupy the same state in a given quantum system. A brief description of this free electron model is provided in **box I**.

Secondly, in the **near-free-electron model**, electrons interact weakly with the potential of the lattice, but electron-electron interactions are still ignored. Within this model, bandgaps within the band structure arise from the additional potential.

Then in the **density functional theory (DFT)**, an electron-ion interaction is considered and electron interactions are approximated through a Hartree potential (coulombic interaction) and an exchange-correlation potential. This model will be developed in depth in chapter 3.

Finally, in the **tight binding theory**, the wavefunction describing the electrons is assumed to be a linear combination of atomic orbitals, which implies a high degree of interaction between the valence electrons and the ion cores.

In the **near-free electron model**, the interaction between electrons and ions results in the formation of energy bands composed of electron states separated by given energy gaps. This notion is however not represented in the simple free electron theory. It is induced by the additional perturbation brought to these "free electrons" by the lattice periodic potential. In the following, we develop the wavefunction of the electrons in such formalism and discuss the origin and implications of the material bandgaps [91, 92, 94].

First, we determine the wavefunction of an electron in a periodic potential generated by the ions of the crystal lattice. The potential energy of an electron $U(\mathbf{r})$ in such a lattice is invariant under translation by a vector \mathbf{R} (see Eq.(2.1)):

$$U(\mathbf{r} + \mathbf{R}) = U(\mathbf{r}), \quad (2.8)$$

and any function being invariant under translation (periodic) can be expanded as a Fourier series expressed as follows:

$$U(\mathbf{r}) = \sum_{\mathbf{G}} U_{\mathbf{G}} e^{i\mathbf{G}\cdot\mathbf{r}}, \quad (2.9)$$

where $U_{\mathbf{G}}$ are the Fourier coefficients of this development and \mathbf{G} , one of the specific translation vector in the reciprocal space defined in Eq.(2.3). Then, the Schrödinger equation associated with an electron evolving in this lattice potential is

I. Free electron model

Free, non-interacting electrons obeying only to the Pauli exclusion principle can be described using the following Schrödinger equation.

$$\frac{-\hbar^2}{2m_e} \frac{d^2\Psi(\mathbf{r})}{d\mathbf{r}^2} = \epsilon_n \Psi(\mathbf{r}), \quad (2.5)$$

with m_e the electron mass and \hbar the reduced Planck constant. In Eq.(2.5), the contribution to the Hamiltonian operator consists only of the electron kinetic energy. Meaning, no coulombic interactions between electrons nor with the lattice ions. The wavefunction associated with the electron system has to respect the Pauli exclusion principle and consequently be anti-symmetric in its construction ($\Psi(\mathbf{r}_1, \mathbf{r}_2) = -\Psi(\mathbf{r}_2, \mathbf{r}_1)$) [92]. As plane waves satisfy this requirement, the electron wavefunction can be written as such:

$$\Psi(\mathbf{r}) = A e^{i\mathbf{k}\cdot\mathbf{r}}, \quad (2.6)$$

with E^0 , the free electron energies:

$$E^0(\mathbf{k}) = \frac{\hbar^2 \mathbf{k}^2}{2m_e} \quad (2.7)$$

In this model, a conduction electron is not deflected by the ions of the lattice and

is *scattered* infrequently by other conduction electrons following the Pauli exclusion principle as two fermions cannot be in the same quantum state within the same system.

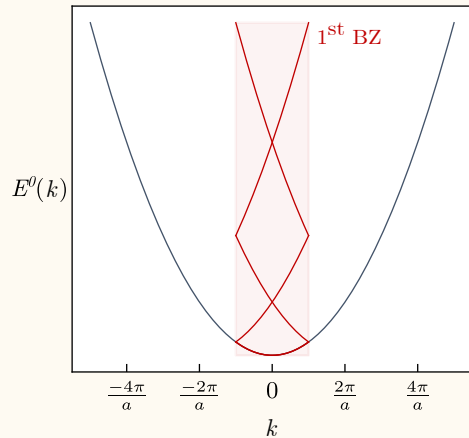


Figure 2.3: In blue, representation of the free electron energy evolution in the reciprocal space. In red, the reduced band structure scheme is presented in the first Brillouin zone as highlighted [92].

$$\left(\frac{-\hbar^2}{2m_e} \frac{d^2}{d\mathbf{r}^2} + \sum_{\mathbf{G}} U_{\mathbf{G}} e^{i\mathbf{G}\cdot\mathbf{r}} \right) \Psi(\mathbf{r}) = \epsilon \Psi(\mathbf{r}), \quad (2.10)$$

with ϵ the associated electron energy. In addition, if one assumes that the wavefunction can be developed into a Fourier series with an arbitrary periodicity \mathbf{L} which, for the moment, may be different from a lattice translation vector \mathbf{R} . Then, the electron wavefunction can be written as

$$\Psi_{\mathbf{k}'}(\mathbf{r}) = \sum_{\mathbf{k}'} C_{\mathbf{k}'} e^{i\mathbf{k}'\cdot\mathbf{r}}, \quad (2.11)$$

with $k' = n \frac{2\pi}{L}$, n an integer value. In the following, we will demonstrate that the

wavefunction periodicity corresponds to the periodicity of the lattice and that the values of \mathbf{k}' (any wave vector in the reciprocal space) contributing to the development of this one are restricted to $\mathbf{k} + \mathbf{G}$ with \mathbf{k} , the wave vectors encompassed in the first BZ. By injecting the development of the wavefunction (Eq.(2.11)) into the Schrödinger equation (Eq.(2.10)), the following expression is achieved:

$$\sum_{\mathbf{k}'} \frac{\hbar^2}{2m_e} \mathbf{k}'^2 C_{\mathbf{k}'} e^{i\mathbf{k}' \cdot \mathbf{r}} + \sum_{\mathbf{k}'} \sum_{\mathbf{G}} U_{\mathbf{G}} C_{\mathbf{k}'} e^{i(\mathbf{k}'+\mathbf{G}) \cdot \mathbf{r}} = \epsilon \sum_{\mathbf{k}'} C_{\mathbf{k}'} e^{i\mathbf{k}' \cdot \mathbf{r}}, \quad (2.12)$$

Then, Eq.(2.13) can be obtained via the multiplication of Eq.(2.12) by $e^{-i\mathbf{k}'' \cdot \mathbf{r}}$ ($k'' = \frac{2\pi m}{L}$) followed by its integration in the real space⁴ ($d\mathbf{r}$). Due to the orthogonality property of the Fourier coefficients, the only non zero value of the summation over \mathbf{k}' is obtained for $\mathbf{k}' = \mathbf{k}''$ and the double summation over \mathbf{k}' and \mathbf{G} is such that $\mathbf{k}' + \mathbf{G} = \mathbf{k}''$. As a result, the Fourier coefficients of the wavefunction expansion must satisfied Eq.(2.13).

$$\left(\frac{\hbar^2 \mathbf{k}''^2}{2m_e} - \epsilon \right) C_{\mathbf{k}''} + \sum_{\mathbf{G}} U_{\mathbf{G}} C_{\mathbf{k}'' - \mathbf{G}} = 0 \quad (2.13)$$

It is relevant to note that any Fourier coefficient $C_{\mathbf{k}''}$ (including the wave vector \mathbf{k}'') involved in the wavefunction is connected to every other Fourier coefficient including a wave vector translated by a vector \mathbf{G} from \mathbf{k}'' . As a result, the electron orbitals can be written including only the \mathbf{k} points contained in one Brillouin zone as each BZ is connected by a translation vector \mathbf{G} . Equation (2.13) can be reformulated into Eq.(2.14).

$$C_{\mathbf{k}} = \frac{\sum_{\mathbf{G}} U_{\mathbf{G}} C_{\mathbf{k}-\mathbf{G}}}{\frac{\hbar^2 \mathbf{k}^2}{2m} - \epsilon} \quad (2.14)$$

Finally, the electron wavefunction expressed in Eq.(2.11) using arbitrary wave vectors \mathbf{k}' are now be expressed using the specific vectors \mathbf{k} from the first BZ (see Eq.(2.15)). Indeed, as presented from Eq.(2.14), knowing the Fourier coefficients $C_{\mathbf{k}}$, all other $C_{\mathbf{k}-\mathbf{G}}$ coefficients included in the expansion of the wavefunction can be found. Furthermore, using the expression obtained in Eq.(2.15), the electron wavefunction can now be expressed as a Bloch function.

$$\Psi_{\mathbf{k}}(\mathbf{r}) = \sum_{\mathbf{G}} C_{\mathbf{k}-\mathbf{G}} e^{i(\mathbf{k}-\mathbf{G}) \cdot \mathbf{r}} \quad (2.15)$$

⁴ $\int_0^L e^{-ik''x} e^{ik'x} dx = 0$ if $k' \neq k''$ and equals L if $k' = k''$ such that $k' = \frac{2\pi n}{L}$ and $k'' = m \frac{2\pi}{L}$ with n and m two integers.

Bloch theorem

Bloch's theorem states that the expression of the wavefunction, solution of the Schrödinger equation for a periodic potential, can be expressed as a plane wave modulated by a function $u_{n,\mathbf{k}}(\mathbf{r})$ having the same periodicity as the corresponding potential (*i.e.* the lattice). Using the expression obtained for the wavefunction in Eq.(2.15), this one can be reorganised into

$$\Psi_{n,\mathbf{k}}(\mathbf{r}) = \underbrace{\left[\sum_{\mathbf{G}} C_{n,\mathbf{k}-\mathbf{G}} e^{-i\mathbf{G}\cdot\mathbf{r}} \right]}_{u_{n,\mathbf{k}}(\mathbf{r})} e^{i\mathbf{k}\cdot\mathbf{r}}, \quad (2.16)$$

where $u_{n,\mathbf{k}}(\mathbf{r})$ is a space function developed as Fourier series over the reciprocal lattice wave vector \mathbf{G} . As a result, this coefficient is invariant under lattice translation \mathbf{R} : $u_{n,\mathbf{k}}(\mathbf{r}) = u_{n,\mathbf{k}}(\mathbf{r} + \mathbf{R})$ and has the same periodicity as the crystal lattice. This new expression in Eq.(2.16) is a direct observation of the Bloch theorem as the wavefunction is expressed as a plane wave $e^{i\mathbf{k}\cdot\mathbf{r}}$ modulated by a function having the periodicity of the crystal ions $u_{n,\mathbf{k}}(\mathbf{r})$. The final form of the wavefunction can consequently be presented as

$$\Psi_{n,\mathbf{k}}(\mathbf{r}) = u_{n,\mathbf{k}}(\mathbf{r}) e^{i\mathbf{k}\cdot\mathbf{r}}. \quad (2.17)$$

In the development realised here above, we expressed the wavefunction of the electrons via a plane wave modulated by a Fourier development whose coefficients depends on \mathbf{k} values (related to specific electron momentum) within the first BZ. As a result, to depict the electron energy as a function of any reciprocal vector \mathbf{k}' , one can consider \mathbf{k} values only in the first BZ as well as every other $\mathbf{k} + \mathbf{G}$ values and reduce the representation to this first BZ. Furthermore, this result is induced by the form of the Hamiltonian in Eq.(2.10) and most importantly by the periodicity of the potential experienced by the electrons (linked to the perfect crystal lattice considered). In **Fig.2.4(a)**, the arrows represent the fold of the band structure within the first BZ highlighted in red and the associated n values correspond to the band index as for a given \mathbf{k} vector, multiple energy values ϵ_n can be found corresponding to different wavefunction $\Psi_{n,\mathbf{k}}$. This representation is known as the reduced scheme. Then, one can fill the available energy levels with the finite number of electrons of in system leading to filled (**valence**) and empty (**conduction**) bands respectively presented in blue and orange. In the following, using the periodicity approach, the emergence of forbidden energy bands is presented.

Nearly free electron model - Periodicity approach

As presented in **Fig.2.4(a)**, the representation of electron band structure considering an interaction between electrons and ions can be obtained by solving Eq.(2.10) using

a Bloch function as the electron wavefunction. A simple model using this approach is the Kronig-Penney model, which approaches the ionic periodic potential as a one-dimensional succession of energetic wells of a given width and height periodically separated in space [95].

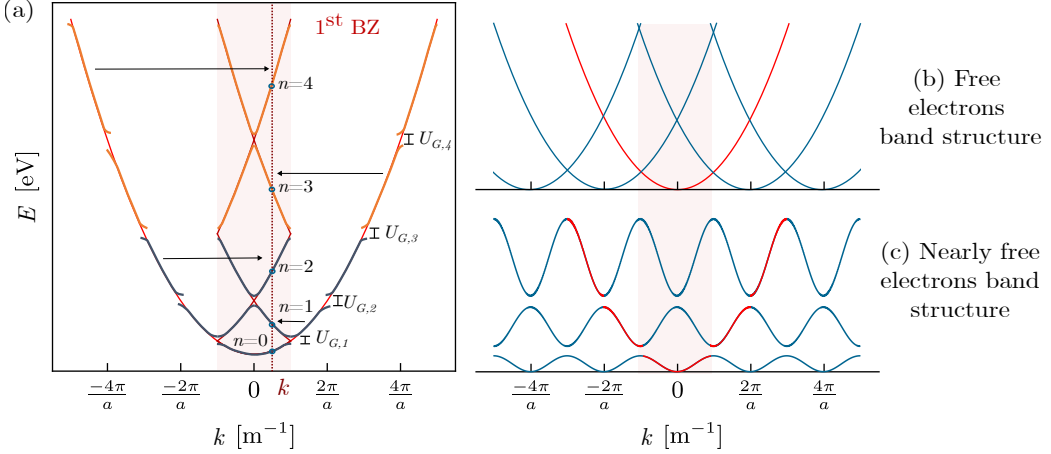


Figure 2.4: (a) Representation of the electron band structure in the nearly free electron model using the periodicity approach. The reduced scheme is highlighted in the first Brillouin zone with the respective energy level notation n associated to each band and corresponding to the fold of the energy level from the n^{th} BZ located at a given \mathbf{G} value from the first BZ. In the nearly free electron model, the interaction with the coulombic potential generated by the ions leads to forbidden energy bands whose magnitudes are function of the Fourier component $U_{\mathbf{G}}$ of the potential. Then, one can fill the available energy levels with the finite number of electrons of the system leading to filled (valence) and empty (conduction) bands. The valence and conduction band are respectively represented in blue and orange. In (b) and (c) the free electron and the nearly free electron band structures are respectively presented in red and blue, a periodic representation is depicted in the reciprocal space to highlight the resulting reduced scheme in the first BZ.

In addition, in **Figs.2.4(b)** and (c), the energetic landscape of free electrons is depicted periodically and a red highlight is set on the resulting band structure obtained in the free and nearly-free electron models. As presented in **Fig.2.4(b)**, in each Brillouin zone and consequently, in the first BZ represented in red, the electron energy as a function of \mathbf{k} is a parabola (see Eq.(2.7)) [93]. Then, if one switches on a small periodic potential (nearly free electron model), the energetic landscape is modified, leading to the emergence of forbidden bands whose magnitudes are function of the potential Fourier component $U_{\mathbf{G}}$, such as

$$E(\mathbf{k}_b)^{\pm} = \frac{1}{2}(E_{\mathbf{k}_b-\mathbf{G}}^0 + E_{\mathbf{k}_b}^0) \pm \sqrt{\frac{1}{4}(E_{\mathbf{k}_b-\mathbf{G}}^0 + E_{\mathbf{k}_b}^0)^2 + |U_{\mathbf{G}}|^2}, \quad (2.18)$$

with \mathbf{k}_b , the wave vector at the first BZ boundary. And, as presented in **Fig.2.4(a)**, if one defines the bandgap energy E_G as the energy separating the last filled band

(valence band) and the first empty band (conduction band) at the third Brillouin zone boundary, then in this example, the bandgap value is given by

$$E_G = 2|U_{\mathbf{G},\mathbf{3}}|, \quad (2.19)$$

with $U_{\mathbf{G},\mathbf{3}}$ the third Fourier component of the potential.

For a given value of \mathbf{k} , there will be an infinite set of energies corresponding to the infinite number of \mathbf{G} vectors. Finally, each primitive cell contributes for one \mathbf{k} -value per band, and taking into account the electron spins (up and down), one can find $2N$ orbital states in each energy band (N is the number of primitive cells) [92]. However, for an infinite number of bands, there is a finite number of electrons that can fill the band states. Depending on their number, the bands can consequently be filled, partially filled, or empty. At 0K, the energy of the highest filled state is known as the **Fermi energy** E_F . In addition, as the potential generated by the ions in the primitive cell becomes more complex with different chemical species and different atomic organisations, the resulting band structure also becomes more complex, leading to the diversity of materials.

Next, in addition to the discussed **periodicity approach**, the bandgap origin in solid-state physics can also be presented using a second approach: the **proximity approach** which percolates from the tight binding approximation.

Tight binding approximation - Proximity approach

As presented in **Fig.2.5**, the proximity approach considers the splitting of energy states associated with individual atoms when they are brought together in the same system (*i.e.* condensed matter). This splitting of atomic energy levels, shown as a function of the number of atoms in the system, results in the formation of bonding and antibonding states. The linear combination of atomic orbitals provided by the overlapping of the electron wavefunction of the individual atoms brought together in a material leads to the formation of energy bands consisting of multiple energy levels. As in the periodicity approach, the energetic distance between these levels becomes so small that Heisenber's uncertainty principle does not allow for their energetic distinction [91].

As a result of the emergence of forbidden bands provided by the interaction between electrons and the periodic potential of the lattice, materials can be classified into three categories which depend on the value of **bandgap energy** E_G . The bandgap energy is a function of the magnitude of the interaction between the electrons and the ions as this quantity is defined function of the Fourier coefficients of the lattice potential (see Eq.(2.19)).

Finally, as presented in **Fig.2.6(a)**, materials whose Fermi energy E_F lies within the middle of an energy band behave as metallic. The last filled band is called the

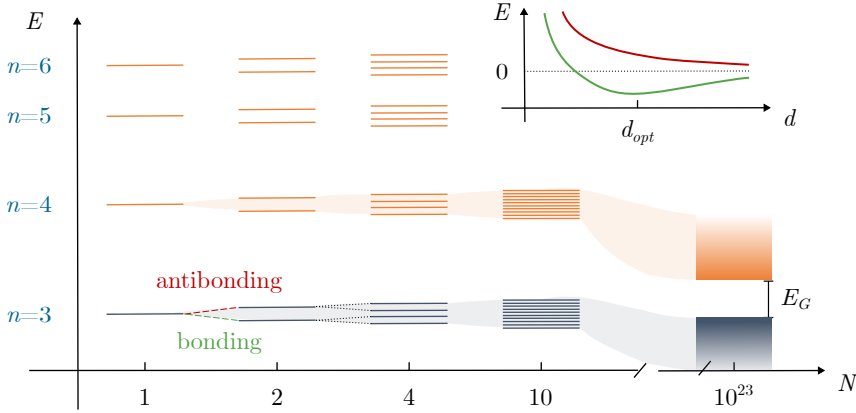


Figure 2.5: Representation of the electron band structure using the proximity approach and considering increasing number of atoms N . Starting from one isolated atom providing discrete energy levels, the addition of an extra atom leads to a new distribution of the electronic density forming bonding and antibonding orbitals. In the inset, the system energy according to the distance d between the two species is highlighted respectively for both types of bonding. The bonding orbital, in contrast to antibonding one leads to a decrease of the system total energy with respect to the two isolated atoms. Then, the energy levels are filled according to the number of electrons provided by the interacting atoms. Filled levels are highlighted in blue while empty energy levels are represented in orange. The increase number of atoms in the system lead to an increase number of energy states (provided by each atom interacting). In the case of a crystal, for a high number of atoms, the distinction between the individual energy level is not possible (the energetic distance between them falls below the Heisenberg principle) and it results available energy bands separated by forbidden band. The valence band and conduction band are highlighted, separated by a energy of E_G corresponding to the material bandgap.

valence band, referring to the valence electrons, and the highest energy level is called the valence band energy E_V . In contrast, the first empty band or partially filled band is known as the conduction band, whose electrons contribute to the conductivity of the material and for which the lowest energy level is the conduction band energy E_C . For metallic materials, a small amount of energy is sufficient to promote an electron from a filled state to an empty state as these states belong to the same band. The promoted electron will act as a free charge carrier participating to the material electrical conductivity. On the other hand, in **Figs.2.6(b)** and (c), the material bandgap is the energetic value required to promote an electron from the valence band to the conduction band (*i.e.* from the highest filled energy state to the lowest empty energy state). Depending on the value of E_G , the materials will be classified as semiconductors (moderate value less than 2.5 eV) or insulators for high bandgap values.

Using the atomic-scale description of the materials realised previously, in the next section, we will focus our interest on semiconducting materials and their optoelectrical properties. We specifically focus on the microscopic origin of the properties

through the study of the material band structure.

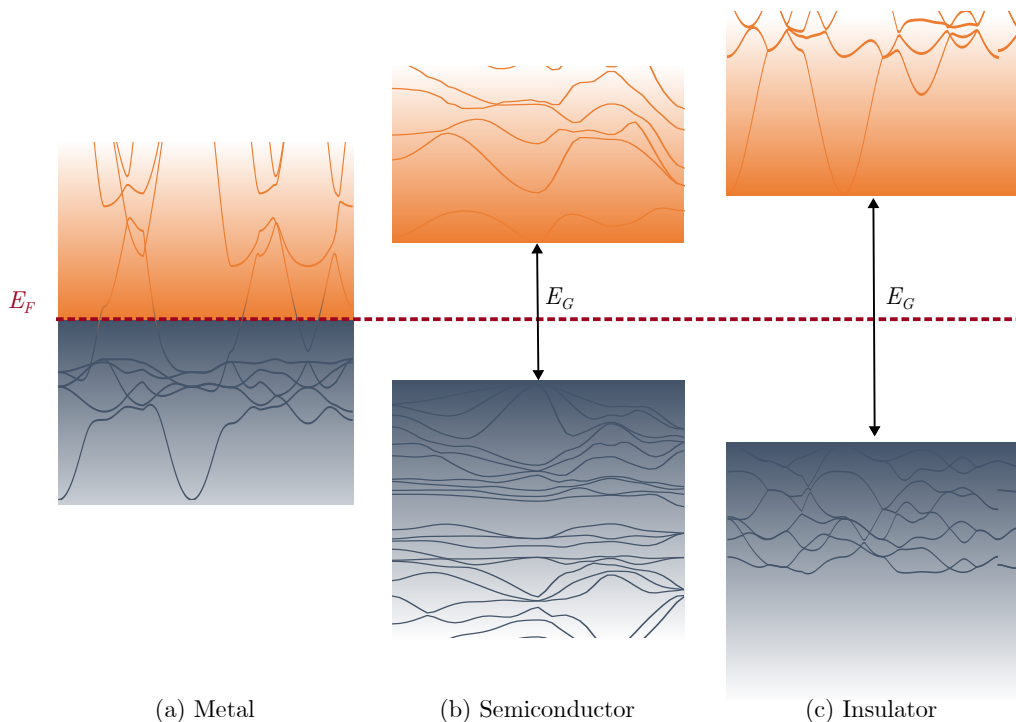


Figure 2.6: Schematic representation of the band structure at non-zero temperature respectively for: (a) a metallic material where the Fermi level is within the conduction band allowing any thermal excitations of charge carriers to participate to the whole lattice electrical conductivity. The blue and orange transparency highlights are provided as a link to the band diagram which represents the space variation of the valence (blue) and the conduction (orange) bands formed by the energy states described in this section as the band structure in the reciprocal space. (b) A semiconducting material with a bandgap energy of the order of 1 eV. (c) An insulator with a large bandgap prohibiting electron excitations.

2.2 PERFECT SEMICONDUCTING MATERIALS

This section aims at establishing a link between the solid-state theory presented previously and the material optical properties such as the absorption coefficient, a relevant physical quantity impacting the photovoltaic performances.

1. First, light absorption is approached through the calculation of the material complex dielectric tensor. Physical quantity from which the material optical properties: absorption coefficient and refractive index are computed.
2. Secondly, the notion of charge carriers: electrons and holes is presented. The thermal and light-induced generations of charge carriers are described along with the aspect of charge carrier effective mass.

This established correlation between the electron energy levels, the optical properties and the PV parameters represents the methodology used to gather the theoretical results presented in Chapter 4.

As stated by Hans J. Queisser, co-author of the Shockley-Queisser limit in 1961, "Now, we live in the Age of Semiconductors" [28, 91]. This statement testifies to the relevance of semiconducting materials in our society and consequently to the value of their physical properties.

2.2.1 Light absorption

To start, we describe the interaction between light, an electromagnetic wave and solid-state matter represented as a perfect semiconducting crystal. If one considers an incident light beam of intensity Φ_0 impacting a given material, a fraction of the incident intensity will be reflected on the surface of the material $\frac{\Phi_R}{\Phi_0} = R$ (reflectivity), another portion will be absorbed within the material $\frac{\Phi_A}{\Phi_0} = A$ (absorptance), and finally, the remaining intensity will be transmitted $\frac{\Phi_T}{\Phi_0} = T$ (transmittance) [96]. From this reasoning, the total incident intensity can be divided into three components as expressed in Eq.(2.20). All these physical quantities being energy E dependent (function of the incident electromagnetic wave frequency ν as $E = h\nu$).

$$1 = T(E) + A(E) + R(E) \quad (2.20)$$

Then, the contribution of each term in Eq.(2.20) depends on the specific interaction of the light with the considered material. A first insight of this interaction can be understood using either the wave (electromagnetic) or the corpuscular (photon) nature of light. For instance, light absorption can be seen through the motion of the

electronic cloud induced by the electric field of the electromagnetic wave as well as by the promotion of an electron from the valence to the conduction band mediated by the absorption of a photon. In the next part of this section, the relations between the absorptance, transmittance, and reflectance with respect to intrinsic material quantities are presented.

By considering a perfect crystal material as positive ions bonded together thanks to a negatively charged electronic cloud, it appears intuitive to consider that the application of an external electric field \mathbf{E} would change the charge distribution within the material. This variation of the electronic configuration is described by the electric displacement \mathbf{D} expressed in a simple case as

$$\mathbf{D} = \mathcal{E}\mathbf{E}, \quad (2.21)$$

with \mathcal{E} the material dielectric tensor. From this consideration, the material response to an external electromagnetic field \mathbf{E} can be obtained through the calculation of the dielectric tensor $\mathcal{E} = \epsilon_1 + i\epsilon_2$ (scaled by the electrical permittivity of the vacuum ϵ_0) [94]. To do so, we use a two-step approach. First, the imaginary part of this complex tensor is obtained via a Fermi golden rule. And, secondly, the real part is calculated thanks to a Kramers-Kronig transformation. As presented in Eq.(2.22), the imaginary part of the dielectric tensor $\epsilon_2(E)$ corresponds to the sum of the possible electronic transitions between filled valence states and empty conduction band states for various \mathbf{k} -points [94].

$$\epsilon_2(E) = \left(\frac{4\pi}{|\mathbf{E}(\omega)|} \right)^2 \sum_{C,V,\mathbf{k}} |\langle C_{\mathbf{k}} | \mathcal{H}_{\text{er}} | V_{\mathbf{k}} \rangle|^2 \delta(E_{C,\mathbf{k}} - E_{V,\mathbf{k}} - E) \quad (2.22)$$

As presented in **Fig.2.7(a)**, this summation is performed on the valence and conduction band energy levels V, C for each \mathbf{k} -point within the 1st BZ. E is the photon energy ($\hbar\omega$) and \mathcal{H}_{er} is the Hamiltonian of the electron-radiation interaction. The first term translates the probability of transition from a filled valence state $|V_{\mathbf{k}}\rangle$ to an empty conduction state $|C_{\mathbf{k}}\rangle$ at a given impulsion \mathbf{k} (the momentum is conserved during absorption). Then, the delta dirac distribution in the second term dictates that the photon energy E should be equal to the energy difference between the two considered states $E_{C,\mathbf{k}} - E_{V,\mathbf{k}}$. As a result, the absorption onset corresponds to the photon energy equals to the lowest possible transition energy between a filled state in the valence band and an empty state in the conduction band located at the same \mathbf{k} value. For a direct bandgap, this energy is therefore equals to the material bandgap⁵ E_G . Finally, $\mathbf{E}(\omega)$ is the applied external perturbation.

Then, the real part of the dielectric tensor $\epsilon_1(E)$ is obtained by a Kramers-Kronig transformation as presented in Eq.(2.23) [93, 94].

⁵For indirect bandgap materials a description of the dielectric response can be found in Ref. [94]: "Electron-hole interaction and phonon-assisted absorption"

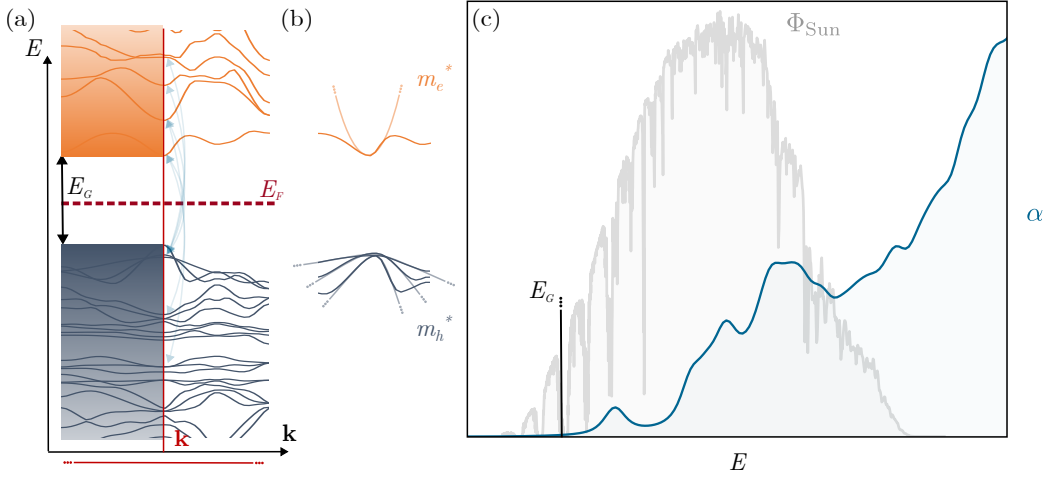


Figure 2.7: (a) Representation of a semiconductor band structure with a highlight of the valence (blue) and conduction (orange) energy levels. Conduction and valence bands highlights are also presented as usually depicted for a spatial representation of a band diagram. The material bandgap as well as the Fermi energy level is presented at a non-zero temperature. Using arrows representing the transition from energy levels in the valence band to levels in the conduction band, the Fermi golden rule used to compute the imaginary part of the dielectric tensor is illustrated for a given reciprocal vector \mathbf{k} (see Eq.(2.22)). Through this summation, the material absorption coefficient α can be computed as presented in (c) along with the AM1.5 solar spectrum Φ_{Sun} . In (b), a representation of the band curvature associated to the semiconductor effective masses for holes (valence band) and electrons (conduction band) is presented as described in Eq.(2.32).

$$\epsilon_1(E) = 1 + \frac{2}{\pi} P \int_0^{\infty} \frac{\epsilon_2(E')E'}{E'^2 - E^2} dE', \quad (2.23)$$

where P is a mathematical quantity which corresponds to the principal value of the integral. Based on the calculation of the dielectric tensor we are now able to access the material optical properties such as the absorption coefficient $\alpha(E)$ as presented in Eq.(2.25). This intrinsic physical quantity is calculated based on the extinction coefficient $\kappa(E)$ [97].

$$\kappa(E) = \frac{1}{\sqrt{2}} \sqrt{-\epsilon_1(E) + \sqrt{\epsilon_1^2(E) + \epsilon_2^2(E)}} \quad (2.24)$$

$$\alpha(E) = \frac{4\pi E \kappa(E)}{hc} \quad (2.25)$$

In addition, the refractive index $n(E)$ and the reflectivity $R(E)$ of the materials can be calculated using, respectively, Eqs.(2.26) and (2.27).

$$n(E) = \frac{1}{\sqrt{2}} \sqrt{\epsilon_1(E) + \sqrt{\epsilon_1^2(E) + \epsilon_2^2(E)}} \quad (2.26)$$

$$R(E) = \frac{(n-1)^2 + \kappa^2}{(n+1)^2 + \kappa^2} \quad (2.27)$$

From the resulting reflectivity $R(E)$ and absorption coefficient $\alpha(E)$, we now calculate the transmitted part of the incident intensity through the Beer-Lambert relation as expressed in Eq.(2.28) [98].

$$T(E, x) = (1 - R(E)) e^{-\alpha(E)x}, \quad (2.28)$$

with x the depth at which the transmittance is computed. Finally, the absorbance is obtained using Eq.(2.20) leading to $A(E) = 1 - T(E, d) - R(E)$ where d is the total thickness of the material. As a result, by measuring both the transmittance and reflectance of the thin film and by knowing its thickness, the absorption coefficient can be calculated using Eq.(2.28). For direct bandgap material, the usual representation of $\alpha^2(E)$ is known as the Tauc plot from which the material bandgap E_G can be extracted. This Tauc plot analysis will be used in chapter 6.

Finally, for terrestrial photovoltaic applications, the light spectrum considered is the AM1.5 spectrum⁶ (as presented in **Fig.2.7**). From this application point of view, one wants to maximise the light absorption while minimising the reflectance. Therefore, large absorption coefficient materials are appealing for such perspectives. In the following, a final comment is presented concerning the generation of charge carriers in perfect semiconducting crystals.

2.2.2 Charge carriers

Two types of charge carriers can be identified in a given material: either an electron, whose spatial concentration is noted n or the absence of an electron known as a hole whose concentration is labelled p . And, these charge carriers can be generated within a piece of semiconducting material at a given temperature T and/or under light illumination Φ_0 .

First, at a non-zero temperature, the atoms are not static; these ones vibrate, resulting in an overall lattice vibration that leads to a non-zero probability for the promotion of an electron from the valence band to the conduction band. This promotion to a higher energy state highlights the bond breaking of valence electrons, which are now free electrons that participate to the material conductivity. In addition, there exists a dynamic balance between charge carrier thermal generation and recombination. Under thermal equilibrium, the charge carrier concentration is given by:

⁶This solar spectrum is a reference spectral distribution defined by international standards and used to characterise solar cells in *standard* test conditions [98]. It corresponds to the solar irradiance received by a 37° tilted plate with respect to the sun light beam with a total irradiance of 1000 Wm^{-2} . This value is close to the irradiance received by the Earth surface on a cloudless day.

$$n_i^2 = np, \quad (2.29)$$

with n_i known as the intrinsic charge carrier concentration. Moreover, the rate of recombination R_T [$\text{m}^{-3}\text{s}^{-1}$] is equal to the rate of thermal generation G_T [$\text{m}^{-3}\text{s}^{-1}$] leading to a constant charge carrier concentration over time. Additionally, in this perfect semiconductor crystal description, the amount of holes is equal to the amount of electrons as each electron promoted and participating the material conductivity in the conduction band leaves behind a hole participating to the conductivity in the valence band. As a result, for a pristine semiconductor at a non-zero temperature T , $n = p$.

Furthermore, if one considers a light illumination, and photon energies $h\nu$ larger than the semiconductor bandgap energy E_G (as previously described for photon absorption), electrons on valence orbitals, bounded to their nuclei, will also be able to absorb the photon energy and break their bonds resulting into their promotion as free charge carriers. As presented in Eq.(2.28), light absorption by semiconductor materials can be calculated using Beer's Lambert law, where the light flux [$\text{Wm}^{-2}\text{s}^{-1}$] at a depth x in the material can be determined. Finally, as light is absorbed, electron-hole pairs (EHP) are generated with a generation rate $G_{L,E}$ expressed in $\text{m}^{-3}\text{s}^{-1}\text{eV}^{-1}$ such as

$$G_{L,E}(E, x) = \eta_g \alpha(E) \Phi_0 e^{-\alpha(E)x}, \quad (2.30)$$

where the generation quantum efficiency η_g is equal to 1 if for each absorbed photon, an EHP is generated. This light absorption leads to an excess of charge carriers within the semiconductor:

$$np > n_i^2. \quad (2.31)$$

In addition, a charge carrier evolving in a lattice potential does not evolve as freely as in a non-interacting system. Therefore, as presented in Eq.(2.32) and depicted in **Fig.2.7(b)**, to take into account this potential, the charge carrier mass is described using an effective mass defined as proportional to the inverse of the band structure curvature (valence band for holes and conduction band for electrons).

$$m_{e,h}^* = \frac{1}{\hbar^2} \frac{\delta^2 E_{c,v}}{\delta \mathbf{k}^2}. \quad (2.32)$$

Using the notions established, in the next sections, we will add to this perfect semiconductor description the physics of defects within the crystalline lattice. As we will see, in reality, these defects are the cornerstones of the semiconductor material properties. Then, the physics of the photovoltaic effect will be presented along with a description of the charge carrier motion.

2.3 DEFECTS IN CRYSTALLINE SEMICONDUCTORS

From the developed semiconducting properties of a pristine crystal, we introduce the notion of defects within the material, describing their impacts on the optoelectrical properties.

1. First, the different types of defect dimensions are presented. From there, we focus our interest on point defects explaining the nomenclature used to describe these defects as well as their various definitions. We differentiate intrinsic and extrinsic point defects highlighting the doping strategy; the charge carrier density tuning provided by the presence of chemical species intentionally introduced within the crystal lattice. We also describe the possible energy levels brought by defects acting as dopants or as possible recombination centres.
2. To further develop the impact of defects on the electrical properties of the material, the Shockley-Read-Hall statistics is described. To do so, we first present the various recombination processes that can occur in a semiconductor and then, the attention is set on the defect-assisted recombination and its associated microscopic description.

As presented in the previous section, a piece of material is a long range ordered crystal structure in which a specific 3-dimensional pattern of atoms known as the unit cell can be identified and from which the whole material can be represented if repeated infinitely in the 3 space directions. However, if a material was a perfect crystal with perfectly placed atoms frozen at given positions, the crystal physical properties would not be as rich as they are. Lattice vibrations (phonons) would not exist, preventing acoustic transfer, thermal conductivity, *etc.* Atomic diffusion, doping, and the control over the semiconducting properties would also be prevented. In reality, matter is *disorganised* and deviates with a given degree from the perfect crystalline structure either in zero, one, two or three space dimensions as presented in **Fig.2.8**. In the following, using arbitrary chemical species A and B, some examples of these possible deviations are presented:

1. Zero-dimensional defects, also known as point defects are limited to atomic dimensions, and the associated lattice distortion extends only few atomic distances from the defects.
2. One-dimensional defects, also known as line defects represent deviations from the perfect crystal that extend infinitely in 1 dimension, such as dislocations.

3. Two-dimensional defects, also known as surface defects extend in two space dimensions (not necessarily flat) such as grain boundaries, free surfaces, *etc.*
4. Three-dimensional defects include the formation of another phase, the presence of porosity, cracks, *etc.* within the material.

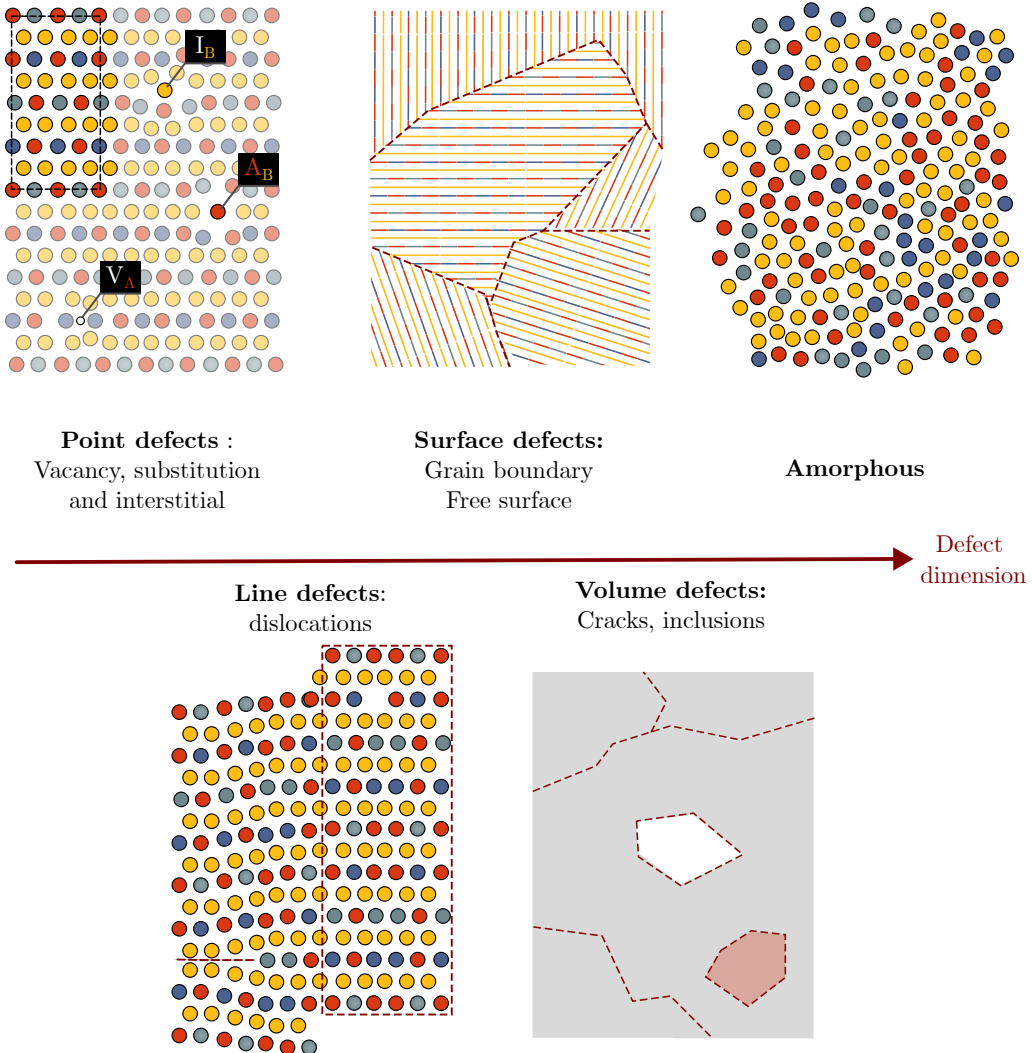


Figure 2.8: Schematic representation of the defect dimensions: point defects (0D), line defects (1D), surface defects (2D) and, volume defects (3D). In an extreme case, an amorphous material can be seen as a completely defected crystal where no spatial order can be identified concerning the atomic positions. Each colour illustrates a different chemical species.

Finally, amorphous materials could be approached as a completely defected crystal where no atomic spatial order or specific patterns can be identified.

As presented in chapter 1, in this thesis, we specifically focus on **the impact of point defects on the photovoltaic performances** of two earth-abundant absorber layers: Cu_2O and $\text{Cu}_2\text{ZnSnS}_4$. To properly lay the theoretical description of such defects, it appears necessary to also properly describe what is called a defect ? What is a dopant ? How intrinsic and extrinsic defects can be defined as well as the distinction between intentional or unintentional defects ? In the following part of this section, we aim at answering those questions concerning the defect nomenclature that will be used in this thesis as this one appears not settled in the scientific literature [92, 93, 98–102].

2.3.1 Point defects: definitions and notations

In this work, we define a defect as any deviation of the pristine crystal structure as expressed in Eq.(2.33) [101].

$$\text{Defect} = \text{Real material} - \text{Perfect crystal} \quad (2.33)$$

More specifically, concerning point defects, three types can be identified as presented in Fig.2.8 [102]:

1. The **substitution** of a chemical species B by a species A: A_B
2. The **vacancy** of an element A: V_A
3. The **interstitial** of an atom B: I_B

The presence of the point defects will change the microscopic arrangement of the lattice with respect to the perfect crystal. The resulting distortion can be associated to multiple origins such as different atomic radii, different electronic clouds around the nuclei resulting in a change in the chemical bonding, *etc.* In addition, the nomenclature around the point defect can be quite wide as different terms are used to describe this defect in more detail. In the following, we provide a clear explanation of the different defect definitions used in this work.

First, a point defect can be described as **intrinsic** or **extrinsic**. Intrinsic point defects describe deviations from the lattice that include only chemical species that are present in the perfect crystal lattice. In other words, point defects which do not include foreign chemical species with respect to chemical elements of the pristine material. Intrinsic point defects consequently include vacancies, substitutions, and interstitials. For example, defects including exclusively Cu, Zn, Sn or S can be described as intrinsic defects in $\text{Cu}_2\text{ZnSnS}_4$ kesterite material. In contrast, a point defect that includes Ge, a foreign atomic species of $\text{Cu}_2\text{ZnSnS}_4$, can be defined as an extrinsic point defect in kesterite. As a result, extrinsic point defects only include interstitials and substitutions.

II. Effect of dopants on the charge carrier concentration

As presented in **Fig.2.9**, the density of states in the valence and conduction band $\mathcal{N}_{C,V}(E)$ are given by the following relation [98]:

$$\mathcal{N}_{C,V}(E) = \frac{(2m_{e,h}^*)^{\frac{3}{2}}}{(\hbar^2)^{\frac{3}{2}} 2\pi^2} (E - E_{C,V})^{\frac{1}{2}} \quad (2.34)$$

In addition, electrons being fermions, they obey the Fermi-Dirac distribution:

$$f(E) = \frac{1}{e^{\frac{E-E_F}{k_B T}} + 1}, \quad (2.35)$$

with k_B the Boltzmann constant and T the system temperature. In **Fig.2.9**, the Fermi-Dirac distribution for various temperatures is depicted. Finally, the electron concentration in the conduction band is obtained by integration of the product between the density of state $\mathcal{N}_C(E)$ and the Fermi-Dirac distribution $f(E)$ giving the probability of finding an electron at an energy E .

$$n = \int_{E_C}^{\infty} \mathcal{N}_C(E) f(E) dE \quad (2.36)$$

$$n = 2 \underbrace{\left(\frac{m_e^* k_B T}{2\pi \hbar^2} \right)^{\frac{3}{2}}}_{N_C} e^{-\frac{E_C - E_F}{k_B T}} \quad (2.37)$$

A similar reasoning can be applied to the valence band considering holes for which the concentration is given by

$$p = 2 \underbrace{\left(\frac{m_h^* k_B T}{2\pi \hbar^2} \right)^{\frac{3}{2}}}_{N_V} e^{-\frac{E_F - E_V}{k_B T}}, \quad (2.38)$$

with $N_{C,V}$ the effective densities of states in the conduction and valence bands. As highlighted in **Fig.2.9(b)**, in the case of an intrinsic pristine semiconductor material, the Fermi energy E_F is located in the middle of the bandgap. As a result, the

electron and hole concentrations are equal ($n = p$) and the law of action mass, being the product of the two concentrations, is:

$$n_i^2 = np = N_C N_V e^{\frac{-E_G}{k_B T}} \quad (2.39)$$

As it can be observed, the intrinsic carrier concentration is proportional to the material bandgap energy E_G . Indeed as previously presented, this quantity represents the amount of energy required to promote an electron in the conduction band leaving behind a hole in the valence band.

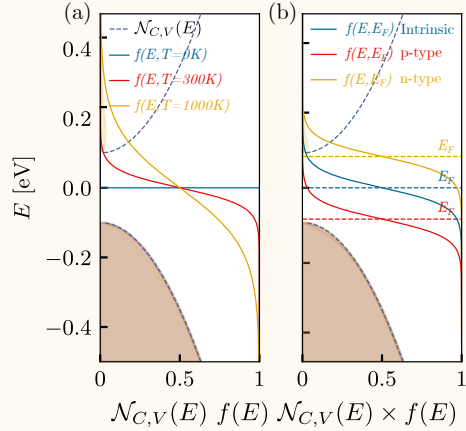


Figure 2.9: Representation of the density of states in the valence and conduction band $\mathcal{N}_{C,V}(E)$, the Fermi-Dirac distribution $f(E)$ and the product of the two for (a) different temperatures and (b) different doping types.

Upon doping, *i.e.* introduction of impurities providing an excess or lack of electrons, the type of conductivity of the semiconductor can be tuned, shifting the Fermi energy level closer to the conduction (n-type) or the valence band (p-type). This disparity between hole and electron concentrations lead to the distinction between majority (*e.g.* electron in n-type) and minority (*e.g.* hole in n-type) charge carriers.

In addition, one can add a distinction between **intentionally** and **unintentionally** introduced defect. As presented in **Fig.2.10(a)**, an intentional defect, purposefully added in the crystal can improve its properties either electrically or optically by adding an interesting energy level within the material bandgap. This intentionally introduced defect can be defined as a **dopant**. An **acceptor** (resp. **donor**) is a dopant introducing an additional energy level close to the valence band (resp. conduction band) providing extra hole(s) (resp. electron(s)) that can be easily promoted as free charge carriers participating to the material conductivity. This strategy is defined as **doping**. As a result, these chemical species (usually extrinsic), deliberately introduced into the lattice, deform the crystal with respect to the pristine one and lead to a change in the material properties. Within this description and following the definition given previously, a **doping** strategy can be described as an **extrinsic** (chemical species different from original crystal species) **defect** (disturbing the perfect crystal structure) placed **intentionally**. It is also relevant to note that intrinsic point defects can act as acceptors (resp. donors) leading to an intrinsic charge carrier concentrations which can also be described as p or n-type. As it will be described in section 3.3, intrinsic point defects are generated depending on thermodynamic considerations although experimental conditions can, within some extent, control these defects. In contrast, extrinsic point defects are incorporated via various experimental mechanisms. The description of the charge carrier concentration provided by extrinsic doping is provided in **box II**: "effect of dopants on the charge carrier concentration".

Then, as depicted in **Fig.2.10(a)**, the energy level(s) E_T brought upon defect incorporation could also be quite far from the bands, preventing thermal excitation to promote charge carriers to any of the bands. These extra energy levels could be detrimental to the material properties if they provide a recombination path for excited charge carriers in the conduction or the valence band. As a result, such defects would act as efficient recombination centres. Furthermore, the ingredient that determine the *efficiency* of a recombination centre will be central to the discussion conducted in the upcoming section 2.3.3.

Finally, as illustrated in **Figs.2.10(b)** and (c), a last element that is of importance when dealing with point defects is the **charge notation** used to describe the charge state of the defect. Indeed, a change in the defect charge state will impact the behaviour of defects and as a result of the material itself [101]. A choice would be to use the real charge notation to describe the defect charge state as presented in **Fig.2.10(b)**. For instance, taking Zn in $\text{Cu}_2\text{ZnSnS}_4$, by respect of the octet rule, each Zn atom brings four electrons within its chemical bonds. If we remove Zn, creating a vacancy V_{Zn} , then the charge state of this vacancy can be expressed using two different notations: the real charge or the relative charge. The real electronic charge of the Zn atoms within the crystal is -4 and, by removing this atom, the remaining charge is 0: V_{Zn}^0 and this vacancy can be charged, for example, with two electrons becoming V_{Zn}^{-2} . In contrast, as depicted in **Fig.2.10(c)**, if we are interested in the

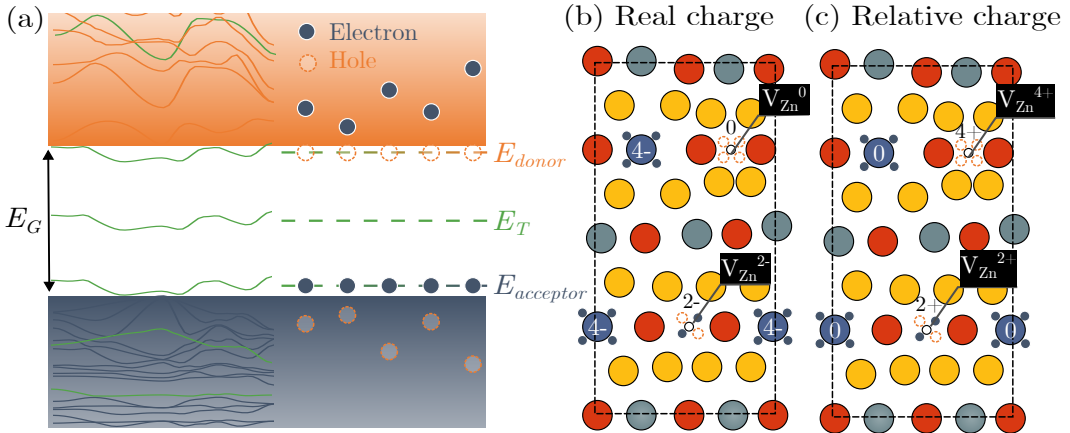


Figure 2.10: (a) Representation of the possible additional energy levels induced upon defect incorporation within the pristine lattice. These defects energy levels are highlighted in green in contrast to the pristine material conduction and valence states represented respectively in orange and blue. An additional energy level close to the conduction (resp. valence) band acts as a donor (resp. an acceptor) level bringing extra electrons (resp. holes) participating to the material conductivity. As described in section 2.3.3, defects can also add extra energy levels laying in the middle of the bandgap that could act as a possible recombination centre. Then, the defect charge state can be described using (b) the real or (c) the relative charge notation. As example, the Zn vacancy in the kesterite conventional cell is presented using the two different charge state representations.

relative charge with respect to the charge on the atom in the pristine material. Then the Zn atom charge in the pristine state is 0. Furthermore, the creation of a vacancy will lead to a relative charge state of +4 as we remove 4 electrons with respect to the pristine crystal: V_{Zn}^{+4} . Then again, this vacancy could be occupied by two electrons, becoming V_{Zn}^{+2} . In this thesis, we chose to express the defect charge state using the real charge state.

To summarise, in the usual language defects can be interpreted at first as a rather unwelcome and unwanted feature. They represent undesired elements that we would like to avoid [101]. In contrast, within solid-state physics, the rich physics brought by defects can be beneficial or detrimental to the materials properties and the performances within the desired application. The results presented in this thesis highlight this ambivalent feature of point defects in absorber materials for PV applications. In chapters 4 and 5, we aim establishing some predictions concerning the defect behaviours and more specifically to assess qualitatively the *efficiency* of possible recombination centres, limiting the photovoltaic performances. While, in chapter 6, we purposely introduce extrinsic defects in the absorber material, a doping strategy aiming at an enhancement of the optoelectrical properties through the introduction of interesting energy levels within the bandgap. In the following, defect-mediated recombinations are presented among the possible recombination processes that occur

in a semiconductor.

2.3.2 Recombination processes

A recombination corresponds to the suppression of a free charge carrier from the conduction band (an electron) and a free charge carrier from the valence band (a hole). If in a though experiment, one freezes the charge carrier generation and let the recombination processes occur for a infinite amount of time, all the electrons would end up in the valence band and, respectively, every hole would go back to an unexcited state in the conduction band. As a result, the free charge carrier value would be equal to zero. As a result a recombination reduces the overall material free charge carrier concentrations: n and p . In the following, we present the different recombination processes that can occur within the bulk or at interfaces of semiconductors as illustrated in **Fig.2.11(a)**.

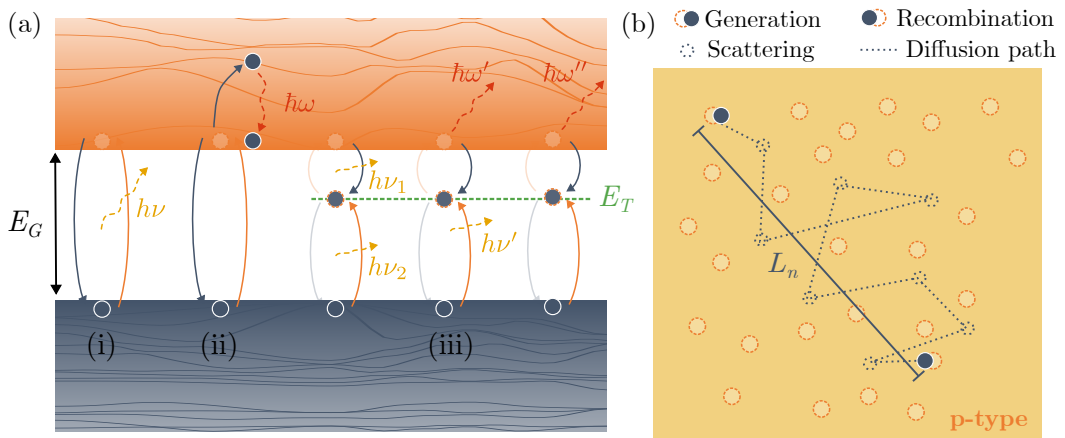


Figure 2.11: In (a) the representation of the various recombination processes that occur in bulk semiconductors is provided. (i) Band to band radiative recombination process (radiative process with a photon energy $h\nu$). (ii) Auger recombination process (non-radiative process with a phonon energy $\hbar\omega$). (iii) Defect-related recombination process described via the Shockley-Read-Hall statistics (radiative, phonon-mediated radiative and multi-phonon captures). In (b), the diffusion length of electrons as minority carriers in a p-type layer is depicted starting from the EHP generation, followed by the erratic diffusion of the electron and reaching the recombination.

In addition, the domination hierarchy between these processes depends on the semiconductor material under consideration [91, 93, 98, 99, 103, 104].

- (i) For a **direct bandgap** material behaving like a **perfect crystal** (absence of defects), the **band to band recombinations** are dominant. This process is a radiative recombination one. As presented in **Fig.2.11(a)(i)**, the extra energy resulting of the de-excitation of the free charge carriers is converted into a photon of energy $h\nu$.

- (ii) For an **indirect bandgap** material that behaves like a **perfect crystal** (absence of defects), the **Auger recombinations** are dominant. As presented in **Fig.2.11(a)(ii)**, the extra energy resulting of the desexcitation of the free charge carriers is converted into a phonon. This process is consequently non-radiative.
- (iii) For a semiconductor material whose crystalline structure presents some **defects** that introduce accessible energy levels E_T within the bandgap, the Shockley-Read-Hall processes, also known as the **defect-assisted recombinations** are dominant. In most operating conditions, using surface passivation, the limiting process for semiconductors in diverse applications is the SRH recombination. As presented in **Fig.2.11(a)(iii)** and as it will be described into details in the following, a defect-mediated recombination can be a radiative, a phonon-mediated radiative or a non-radiative capture process.
- (iv) Finally, in a very pure semiconductor (perfect crystal lattice without defects), **surface recombination** can also be the dominant process in addition to the Auger and band to band recombinations.

The total recombination rate being the sum of the respective recombination process rates:

$$R_{tot} = \sum_i R_i \quad (2.40)$$

From these recombinations, one can define a minority carrier lifetime as the mean lifetime of a minority charge carrier. This τ_{tot} for a free charge carrier is limited by the most limiting recombination process.

$$\frac{1}{\tau_{tot}} = \sum_i \frac{1}{\tau_i} \quad (2.41)$$

In addition to the lifetime of the minority carrier, the diffusion length of the minority carrier can also be associated as illustrated in **Fig.2.11(b)**. This diffusion length is the average distance covered by a charge carrier from its generation to its recombination. As expressed in Eq.(2.42), this physical quantity is a function of the lifetime of the minority charge carrier $\tau_{n,p}$ and the diffusion coefficient $D_{n,p}$:

$$L_{n,p} = \sqrt{\tau_{n,p} D_{n,p}} \quad (2.42)$$

In the following part of this section, the two first recombination processes will be discussed while the defect-assisted recombination will be treated specifically in section 2.3.3.

(i) Band to band recombination

Considering perfect crystal materials with a direct bandgap, the band to band recombination processes are the dominant ones [98]. As illustrated in **Fig.2.11(a)(i)**, concerning this process, the recombination rate is proportional to the amount of electrons in the conduction band n and the amount of free energy levels in the valence band: the hole concentration p such that

$$R = \beta np, \quad (2.43)$$

with β , a proportionality factor. In addition, assuming a steady-state equilibrium semiconductor, the charge carrier total generation rate G_{tot} is equal to the total recombination rate: $R_{tot} = G_{tot}$. Then, if on top of that, one we decide to add an source for the generation of charge carriers by considering a given light excitation for instance. Under the new equilibrium, the total recombination rate becomes the sum of the thermal contribution: $R_{th} = \beta n_0 p_0$ and the additional recombination processes due to the excess of charge carriers (Δn and Δp):

$$R_{tot} = \beta \underbrace{(n_0 + \Delta n)}_n \underbrace{(p_0 + \Delta p)}_p \quad (2.44)$$

As a result the recombination rate due to the excess of charges can be expressed as

$$R_{ex} = R_{tot} - R_{th} = \beta(np - n_0 p_0) \quad (2.45)$$

Then, assuming a p-type semiconductor, $p \gg n$ and a low-injection level $\Delta p \ll p$, this net recombination rate can be express as

$$R_{ex} \simeq \beta p_0 (n - n_0) = \frac{n - n_0}{\tau_n}, \quad (2.46)$$

where $\tau_n = 1/\beta p_0$ is defined as the lifetime of the electron, being in this case the minority carrier. And, finally, if one switches off the extra source of charge carrier (the light excitation), the evolution of the minority carrier concentration over time is such as expressed in Eq.(2.47).

$$\frac{dn}{dt} = -\frac{n(t) - n_0}{\tau_n} \quad (2.47)$$

considering that $n(t = 0) = \Delta n$. The excess of minority charge carriers created upon light illumination will decay towards zero, recovering the thermal equilibrium concentration n_0 .

(ii) Auger recombination

The Auger recombination, as presented in **Fig.2.11(a)(ii)**, is a three particles process involving either two electrons and a hole "eeh" or two holes and an electron "ehh".

Within the process, an electron from the conduction band recombines with a hole in the valence band by transferring the difference of energy and momentum to another electron in the conduction band (eeh). The second electron is excited to higher energy levels and relaxes by transferring its energy excess to the lattice as vibrational energy: a phonon. The same reasoning can be applied to a two holes, one electron Auger recombination process "ehh". As a result, the Auger recombination rate R_{Auger} is dependent two contributions:

$$R_{eeh} = C_n n^2 p, \quad (2.48)$$

$$R_{ehh} = C_p n p^2, \quad (2.49)$$

with C_n and C_p two proportionality constants dependent on the temperature [98]. Finally, a total Auger recombination rate is provided in Eq.(2.50).

$$R_{\text{Auger}} = C_p n p^2 + C_n n^2 p \quad (2.50)$$

2.3.3 Defect-mediated recombination

As highlighted before, non-radiative recombinations occur mainly via two mechanisms: Auger and defect-assisted recombinations. In 1952, defect-assisted recombination statistics were described by Shockley, Read, and Hall [103, 104], giving rise to the so-called Shockley-Read-Hall (SRH) statistics. In the following section, we address the behaviour of a defect as a recombination centre in a given material aiming at answering the following question: What are the characteristics a point defect that act as an *efficient* recombination centre ? [99, 105]

(iii) Shockley-Read-Hall recombination

The SRH statistics described here considers a single defect energy level which can be either negative (acceptor like), positive (donor like) or neutral.

For this model, we consider a given material (fixed bandgap value E_G equals to 1.5 eV) with a given doping level fixed by the Fermi level position E_F within the bandgap. The charge carrier concentration respectively in the conduction and valence bands are given by Eqs. (2.51) and (2.52):

$$n = N_C e^{\frac{-(E_C - E_{F,n})}{k_B T}}, \quad (2.51)$$

$$p = N_V e^{\frac{-(E_{F,p} - E_V)}{k_B T}}, \quad (2.52)$$

where $E_{F,n}$ and $E_{F,p}$ are the quasi-Fermi energy levels associated to, respectively, electrons and holes used to describe the charge carrier concentrations out of equilibrium. In addition, for an equilibrium situation, we have $E_F = E_{F,n} = E_{F,p}$. For

instance, under light illumination, a splitting of the quasi-Fermi levels occurs with $E_{F,n} = E_F + \frac{V_{app}}{2}$ and $E_{F,p} = E_F - \frac{V_{app}}{2}$. In this case, V_{app} represents the additional potential generated by the extra electron/hole generation in the material.

Then, in **Fig.2.12**, we describe the four different recombination/emission processes occurring between a defect at an energetic position E_T and either a valence band state for holes or a conduction band state for electrons. It is relevant to emphasise that the capture and emission of holes (resp. electrons) is realised with respect to the valence band (resp. conduction band). (1) As expressed in Eq.(2.53), the electron capture rate from the conduction band is proportional to the amount of electrons in the band as well as the amount of empty states provided by the defects equals to the defect concentration N_T multiplied by the probability for them to be empty: $(1 - f_T)$. (2) Then, the electron emission rate is proportional to the number of electron filling defect energy levels E_T : $f_T N_T$ multiplied by the probability of reaching an empty state located in the conduction band as expressed in Eq.(2.54). Then, equivalently for holes in (3) and (4) the hole capture rate is proportional to the number of holes in the valence band and the probability to reach a filled state on the defect energy level (see Eq.(2.55)) while the hole emission rate is proportional to the number of holes on the defects and the probability to reach a filled state in the valence band (see Eq.(2.56)).

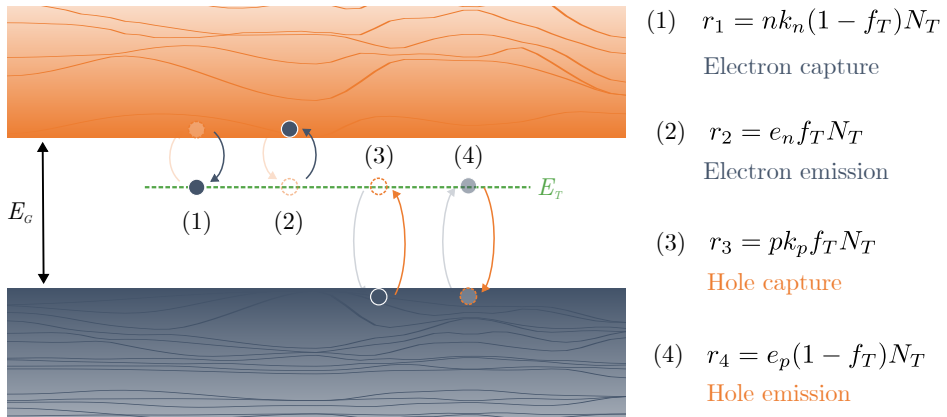


Figure 2.12: Capture and recombination processes on a defect located at an energy E_T : (1) electron capture with recombination rate $r_1(k_n)$, (2) electron emission with recombination rate $r_2(e_n)$, (3) hole capture with recombination rate $r_3(k_p)$ and (4) hole emission with recombination rate $r_4(e_p)$.

$$r_1 = \underbrace{N_C e^{-\frac{-(E_C - E_{F,n})}{k_B T}}}_n k_n (1 - f_T) N_T, \quad (2.53)$$

$$r_2 = \underbrace{k_n N_C e^{\frac{-(E_C - E_T)}{k_B T}}}_{e_n} f_T N_T, \quad (2.54)$$

$$r_3 = \underbrace{N_V e^{\frac{-(E_{F,p} - E_V)}{k_B T}}}_p k_p f_T N_T, \quad (2.55)$$

$$r_4 = \underbrace{k_p N_V e^{\frac{-(E_T - E_V)}{k_B T}}}_{e_p} (1 - f_T) N_T, \quad (2.56)$$

The emission coefficients $e_{n,p}$ are consequently defined by a given energetic distance between the defect energetic position E_T and the associated band state. Moreover, all these emission/capture rates are functions of the amount of electrons/holes in the initial state, the amount of free final states and, the electron/hole capture coefficients expressed in cm^3s^{-1} and given by

$$k_{n,p} = v_{th} \sigma_{n,p}, \quad (2.57)$$

with v_{th} the thermal velocity of the carriers⁷ and $\sigma_{n,p}$ the electron/hole capture cross sections. The capture coefficients $k_{n,p}$ represent the rate at which the charge carriers (electrons from the conduction band or holes from the valence band) are captured by the defect. From these coefficients, minority carrier lifetimes $\tau_{n,p}$ can be deduced as inversely proportional to the defect concentration N_T and to the capture coefficient $k_{n,p}$, namely

$$\tau_{n,p} = \frac{1}{N_T k_{n,p}} \quad (2.58)$$

As a starting point for the upcoming discussion, **we first assume constant electron/hole capture coefficients** $k_{n,p}$. For a constant thermal velocity, this assumption induces a constant electron/hole carrier capture cross section $\sigma_{n,p}$. In reality, as it will be discussed in the next section, the capture coefficients $k_{n,p}$ depend on various microscopic quantities resulting in a dependence on the defect energy position E_T . Based on the considerations developed here, the statistical defect occupancy $f_T(E_T)$ as well as the net recombination efficiency $R_{SRH}(E_T)$ can be computed using respectively Eq.(2.59) and Eq.(2.60), the latter being proportional to the defect density N_T .

$$f_T(E_T) = \frac{nk_n + e_p}{nk_n + pk_p + e_n + e_p} \quad (2.59)$$

$$R_{SRH}(E_T) = N_T \underbrace{\left[\frac{k_n k_p (np - n_0 p_0)}{nk_n + pk_p + e_n + e_p} \right]}_{\eta_R}, \quad (2.60)$$

⁷This velocity represents the average velocity of charge carriers in a crystal lattice at temperature T [91].

with n_0, p_0 the electron and hole charge carrier concentration under equilibrium conditions. A first observation is that without the generation of extra charge carriers, the net recombination rate $R_{SRH}(E_T)$ is equal to zero (for $E_F = E_{F,n} = E_{F,p}$). This charge concentration injection is represented by the quasi Fermi levels splitting: $E_{F,n} - E_{F,p}$. Then, as expressed respectively in Eq.(2.59), the defect occupancy is the ratio between the amount of electron captures either from the conduction band or through hole emissions in the valence band over all other capture and emission processes. Furthermore, in Eq.(2.60), one can find at the numerator, the extra charge concentration as well as the product of both electron and hole capture coefficients.

In **Fig.2.13**, the defect occupancy probability $f_T(E_T)$ as well as the net recombination rate $R_{SRH}(E_T)$ have been computed for constant capture coefficients $k_{n,p}$. In the following, this figure will be discussed column by column. As highlighted by the bottom legend, the first column corresponds to the investigation of different capture coefficient values $k_{n,p}$. The second column corresponds to the study of different charge carrier injections represented by various Fermi levels splitting values $E_{F,n} - E_{F,p}$ (*e.g.* light illumination). And, finally, the third column corresponds to the investigation of three doping configurations (p-type, intrinsic, n-type) fixed by the Fermi energy E_F . For each column, a triplet of values are presented for the investigated parameter ($k_{n,p}$, $E_{F,n} - E_{F,p}$ or E_F) and depicted in the insets the form of plain and dashed line styles.

First, in column one corresponding to the **Figs.2.13(a-c)**, focusing our attention on specific values of the capture coefficients $k_{n,p}$, for a series of fixed parameter: $E_F = E_G/2$ eV (setting an intrinsic conductivity, $n = p$), $E_{F,n} - E_{F,p} = 0.5$ eV, and $N_T = 10^{13}$ cm⁻³. Based on these parameters, we observe that for low defect energy ($E_T < E_{F,p}$), the defect occupancy f_T is equal to one, meaning a state filled with electrons. Then, it decreases for E_T with $E_{F,p} < E_T < E_{F,n}$ and goes to 0 for $E_T > E_{F,n}$. This observation can be explained using **Fig.2.13(b)** in which as the defect energy level increases, the hole emission rate e_p is first dominant over the other rates leading to a filled defect level, then for increased E_T values, the capture coefficients $k_{n,p}$ become dominant over the emission ones resulting in a partially filled state whose occupancy is limited by the smallest capture coefficient, either k_n or k_p . Finally, for higher energy levels, the electron emission rate e_n becomes dominant resulting in a state likely empty. One can also note that, in **Fig.2.13(c)**, the net recombination rate R_{SRH} is non-zero for a defect occupancy strictly between 0 and 1, corresponding to the defect energetic positions where it is likely to capture electrons and holes, the recombination rate is non negligible. We highlight here that **a net recombination rate requires both the capture of a hole and an electron**. Then, also as presented in **Figs.2.13(a-c)**, the values of the capture coefficients k_p and k_n are varied between, respectively, [2,1,0.5] and [0.5,1,2] 10^{-9} cm³ s⁻¹. As it can be observed in the inset (a), the variation of the capture coefficient fixes the defect occupancy between the quasi-Fermi energy levels. For $k_n = k_p$, the defect occupancy is 0.5, the defect level is as likely to be filled as empty. For $k_p > k_n$ (resp.

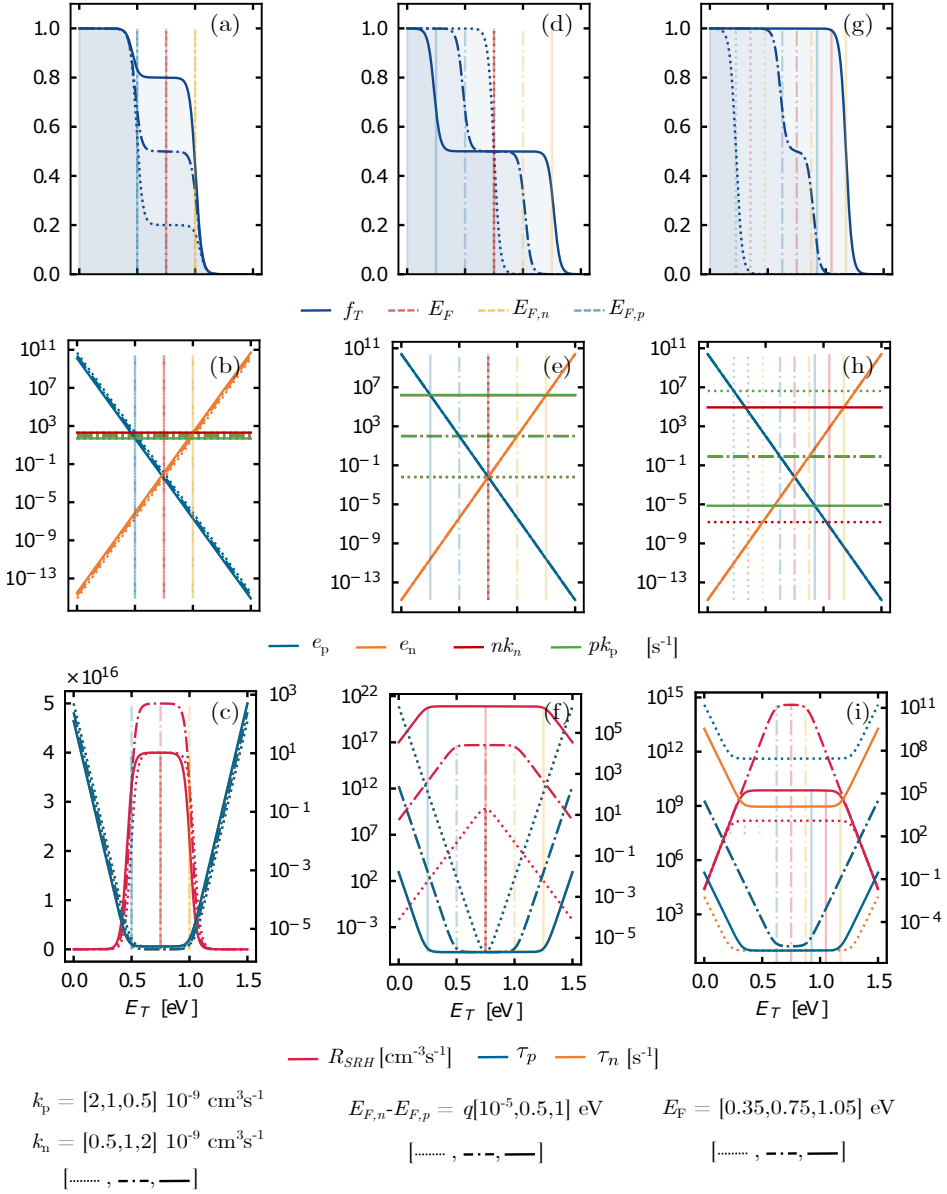


Figure 2.13: In the 1st line (a,d,g), the defect occupancy probability f_T is presented. The 2nd line (b,e,h) illustrates the emission and capture rates nk_n, pk_p, e_n, e_p [s^{-1}] both for electrons and holes with respect to respectively the conduction and valence band. Finally, in the 3rd line (c,f,i), we present the net recombination rate R_{SRH} [$cm^{-3}s^{-1}$] (left axis) and the electron/hole carrier lifetimes $\tau_{n,p}$ (right axis). Each quantity is represented as a function of the point defect energy level position E_T . Columns (a,b,c), (d,e,f) and (g,h,i) present respectively the study of the carrier capture coefficient $k_{n,p}$, the charge carrier injection represented by the quasi-Fermi level splitting $E_{F,n} - E_{F,p}$ and the material conductivity type E_F . [Python code provided to the reader here.](#)

$k_p < k_n$), the defect occupancy is more likely to be empty; fill with a hole (resp. electron). However, an interesting feature presented in **Fig.2.13(c)** is that the net recombination rate is limited by the smallest capture coefficient, either k_n or k_p . As we can see, for $k_{n,p} = \frac{k_{p,n}}{2}$, the defect occupancy is different (symmetrically distributed around half filled occupancy, this value corresponds to $k_n = k_p$ as $n = p$) but the net recombination rates are equal, highlighting the dependence of the recombination with respect to the slower capture rate. As an electron and a hole are both required to obtain a recombination, **the number of recombination will be limited by the charge carrier type whose rate of capture is the slowest.**

Then, in the second column, **Figs.2.13(d-f)**, the charge carrier injection is changed by varying the splitting of the quasi-Fermi energy levels for three specific values: $q[10^{-5}, 0.5, 1]$ expressed in eV. It results a different charge injection values ($np - n_0p_0$) (see Eq.(2.60)). This investigation is presented considering fixed carrier capture coefficient $k_{n,p} = 10^{-9} \text{ cm}^3 \text{ s}^{-1}$ and an intrinsic semiconductor doping fixed by $E_F = E_G/2$. The first observation presented in **Fig.2.13(f)**, is that the net recombination rate increases following the increase of extra charge carriers ($\nearrow E_{F,n} - E_{F,p}$). Furthermore, in the inset (e), as the charge injection increases, the nk_n and pk_p products also increase, leading to an expansion of the 0.5 plateau observed in defect occupancy f_T (see inset (d)). Then, for a low injection level, as presented in the inset (e), the E_T energy range for which the speed charge carrier captures is higher than the emission is quite narrow, while this range increases as a function of the quasi-Fermi energy levels spread around the Fermi energy under equilibrium conditions. For E_T below $E_{F,p}$ (resp. above $E_{F,n}$), the hole (resp. electron) emission rate becomes dominant, leading to a state filled with electrons (resp. holes) and a defect occupancy of 1 (resp. 0). One can also note that, in **Fig.2.13(f)**, due to the intrinsic doping considered, the charge carrier lifetime is equal for both electron and holes. And, as a result of the recombination rate spreading over E_T for higher injection levels, the lifetimes also spread over a large range of E_T . However, the values of the plateau are identical for each injection level corresponding to a half filled defect state. This is the result of the recombination rate balancing the higher level of injection and leading to an average time of life for the charge carrier being identical. As a result, **the larger the charge injection, the larger the recombination rate.**

Finally, if we consider either a p-type, intrinsic, or n-type semiconductor by changing the Fermi level energy as presented in **Figs.2.13(g-i)** for fixed carrier capture coefficient $k_{n,p} = 10^{-9} \text{ cm}^3 \text{ s}^{-1}$ and a fixed quasi Fermi levels splitting $E_{F,n} - E_{F,p} = 0.25 \text{ eV}$. We therefore establish a disparity between the charge carriers, these being as majority or minority charge carriers. As described above, for an intrinsic material, there is no disparity between electrons and holes resulting in a similar lifetime for both carriers. The recombination rate being a function of the charge injection, the speed of capture, and the distance with respect to the conduction or valence bands (speed of emission). However, in the case of a p-type material, $pk_p \gg nk_n$. The ob-

served net recombination rate features a plateau between $E_{F,p}$ and $E_C - (E_{F,p} - E_V)$, corresponding to the value of E_T where pk_p is higher than the emission rates. Within this range, the defect is most likely empty (filled with holes) and, as a result, the net recombination efficiency will be limited by the number of electrons that can be captured nk_n . **The net recombination rate will consequently be limited by the concentration of the minority charge carrier.** This can also be observed for the carriers lifetimes, for a p-type material, the electrons lifetime is several orders of magnitude lower than the holes lifetime. The same reasoning can be applied to a p-type material, where the holes lifetime will be smaller than the electron one. In addition, the higher the doping, the further the Fermi energy level is from the middle of the bandgap, the lower the net recombination rate will be as the minority charge carrier concentration will be small.

To summarise, the net recombination rate is a function of the number of holes and electrons that can be captured simultaneously on a given defect state level. For constant capture coefficients, it appears that the recombination rate presents a plateau in the middle of the bandgap that spreads towards the conduction and valence bands depending on the speed of capture of the majority carriers with respect to its emission rate. This range of E_T corresponds to defect energy levels far from the valence and conduction bands, leading to a low probability for charges to be emitted towards conduction or valence states, as presented in the underbrace of Eqs.(2.54) and (2.56). For example, for a p-type material, recombination occurs for defect levels E_T where pk_p is higher than e_p . However, the minority carrier concentrations as well as the value of the carrier capture coefficients are what fix the value of the plateau. The lower the excess concentration of the minority carrier, the lower the recombination rate. This value being controlled by the conductivity type, creating an initial distinction between majority and minority charge carriers, or by the injection levels, the rate at which electrons and holes are generated. As a result, the higher recombination rate is obtained when fulfilling the three following conditions:

$$nk_n \gg e_n \text{ and } pk_p \gg e_p \quad (2.61)$$

and

$$nk_n = pk_p \quad (2.62)$$

Then, in **Fig.2.14**, we highlight the impact of non-constant carrier capture coefficients $k_{n,p}$. As presented, the defect occupancy can be quite changed as a function of these coefficients. However, in order to correlate the carrier capture coefficients the defect level energetic position, some microscopic considerations have to be taken into account. The next section is dedicated to this purpose.

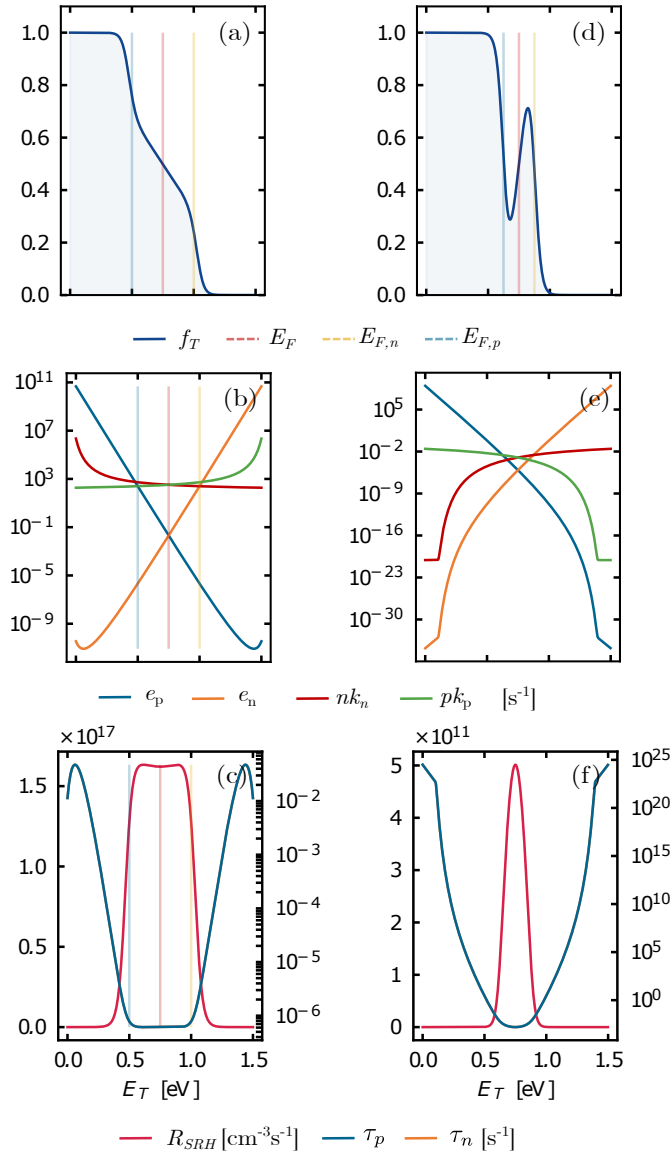


Figure 2.14: In the 1st line (a,d), the defect occupancy probability f_T is presented. The 2nd line (b,e) illustrates the emission and capture rates nk_n, pk_p, e_n, e_p [s^{-1}] both for electrons and holes with respect to respectively the conduction and valence band. Finally, in the 3rd line (c,f), we present the net recombination rate R_{SRH} [$\text{cm}^{-3} \text{s}^{-1}$] (left axis) and the electron/hole carrier lifetimes $\tau_{n,p}$ (right axis). Each quantity is represented as a function of the point defect energy level position E_T . Columns (a,b,c) and (d,e,f) present respectively the study of the carrier capture coefficient $k_{n,p}$, the charge carrier injection represented by the quasi-Fermi level splitting $E_{F,n} - E_{F,p}$ and the material conductivity type E_F . [Python code provided to the reader here.](#)

Microscopic origin of the capture coefficients $k_{n,p}$

Now that we perceive more clearly the SRH statistics describing the defect-assisted recombination for constant capture coefficients $k_{n,p}$, we proceed to understand the microscopic origin of these coefficients. As initially stated, the purpose of this discussion is to highlight the characteristics of point defects that act as *efficient* recombination centres.

As illustrated in **Fig.2.15**, the process of **carrier capture by a defect level** can happen radiatively (emission of a photon, see **Fig.2.15(a)**) or non-radiatively, the latter being accompanied by the emission of one or multiple phonon(s) (see **Fig.2.15(b,c)**). In this illustration, the possible electron-lattice system energy levels are represented in a configuration coordinate diagram where the total energy, function of the configuration coordinate \mathcal{Q} , is proportional to the lattice displacement X :

$$\mathcal{Q} = \sqrt{\frac{M_U \omega}{\hbar}} X, \quad (2.63)$$

where M_U is the unit cell mass and ω the angular frequency associated to the vibration of the lattice. Furthermore, the configuration coordinate \mathcal{Q} is a dimensionless quantity. In addition, in this development, the total energy of the system E_i is the sum of the electronic energy ϵ_i and the vibrational energy associated to the lattice $\mathcal{E}_{i,n}$ such as:

$$E_i = \epsilon_i + \mathcal{E}_i = \epsilon_i + \underbrace{\frac{1}{2} \hbar \omega_i (\mathcal{Q}_{\text{defect},i} - \mathcal{Q}_{\text{pristine}})^2}_{\text{classical approach}} \quad (2.64)$$

Using a classical approach⁸, the vibrational energy of the lattice followed a parabolic behaviour with respect to the distortion $\mathcal{E}_i \propto (\mathcal{Q}_{\text{defect},i} - \mathcal{Q}_{\text{pristine}})^2$. However, beyond the classical approach, the quantum mechanics tells us that a vibrating system can only occupy specific vibrational eigenstates of energy: $\mathcal{E}_{i,n} = \hbar \omega_i (n + 0.5)$ (with n an integer value). As presented in **Fig.2.15** through the respective density of the different excited vibrational states $|\chi_{i,n}|^2$.

Focusing the discussion on **Fig.2.15**, in the absence of defects, the lattice is at its equilibrium position $\mathcal{Q}_{\text{pristine}}$ and for a band to band transition (see inset 2.15(a)), the transition occurs between two electronic states $\epsilon_{1,2}$ in their respective vibrational ground states. However, the introduction of a defect will lead to a distortion of the lattice in the vicinity of the defect. The shift of the lattice equilibrium position is represented by the difference between $\mathcal{Q}_{\text{defect}}$ and $\mathcal{Q}_{\text{pristine}}$. Within this configuration, an electron (resp. hole) in a conduction (resp. valence) band state can be captured by a defect state within the material bandgap either through the emission of a photon and one/multiple phonon(s), the process being both radiative and phonon-mediated as

⁸This harmonic approximation for the lattice vibration fails to treat anharmonicities and to represent correctly the situation for large lattice displacement and strong lattice vibrations [99].

depicted in the inset 2.15(b) or purely non-radiative through the emission of phonons by tunnelling from the band state to a defect excited state (see inset 2.15(c)).

The vibrational state $|2\rangle$ (defect state) onto which the charge is transferred is determined by the Franck-Condon principle which declares that the higher the overlap between the band vibrational ground state of $|1\rangle$ (represented in orange) and the defect excited vibrational state $|2\rangle$ (represented in blue), the higher the probability of transition [106]. To illustrate this principle, in **Fig.2.15**, the insets (d) and (e) provide the normalised overlap between the probability density of the band ground state and the probability density of the defect states. As it can be observed, this overlap is a function of the distortion induced by the defect. The higher $\Delta Q = Q_{\text{defect}} - Q_{\text{pristine}}$, the larger the overlap between the initial band state $|1\rangle$ and an excited defect state $|2\rangle$ of higher energy. For a given distortion, the overlap with the first excited state becomes slightly larger. In addition, as the distortion increases, the higher transition probability occurs for higher n values.

Concerning the charge carrier capture coefficients, the probability of the transition from an initial state $|1\rangle$ (a band state) to a final state $|2\rangle$ (a defect state) is given by the Fermi's golden rule expressed in Eq.(2.65) [107].

$$W_{1,2} = \frac{2\pi}{\hbar} \underbrace{|\langle \Phi_1 | \mathbf{H}_{\text{int}} | \Phi_2 \rangle|^2}_{\mathcal{P}_{1,2}} V N(E_2), \quad (2.65)$$

where V is the volume of the system, $N(E_2)$ is the defect density of states, \mathbf{H}_{int} is the interaction Hamiltonian and Φ_i is the total system wavefunction (containing both the electronic and the vibrational information of the system) of the band state Φ_1 or the defect state Φ_2 .

Based on Eq.(2.65), the capture coefficient $k_{n,p}$ can be linked to this transition probability containing the electron-lattice interaction and the lattice displacement. First, using the Born-Oppenheimer approximation, one can assume that during the electronic transition the ions positions are unchanged. Therefore, the system wavefunction Φ_i can be expressed as the product of the electronic wavefunction Ψ_i and the vibrational wavefunction $\chi_{i,n}$. The latter corresponds to the information regarding the nuclei of the lattice:

$$\Phi_i(r, \mathcal{Q}) = \Psi_i(r, \mathcal{Q}) \chi_{i,n}(\mathcal{Q}) \quad (2.66)$$

The transition probability $\mathcal{P}_{1,2}$ can consequently be expressed as:

$$\mathcal{P}_{1,2} = \underbrace{\langle \Psi_1 | \mathbf{H}_{\text{int}} | \Psi_2 \rangle}_{\text{Electronic int. (i)}} \underbrace{\langle \chi_{1,n} | \chi_{2,n} \rangle}_{\text{Vibrational overlap (ii)}}, \quad (2.67)$$

where the overlap factor is, as explained previously, dependent on the strain introduced by the defect ΔQ . In Eq.(2.67), the transition probability from state $|1\rangle$ to $|2\rangle$

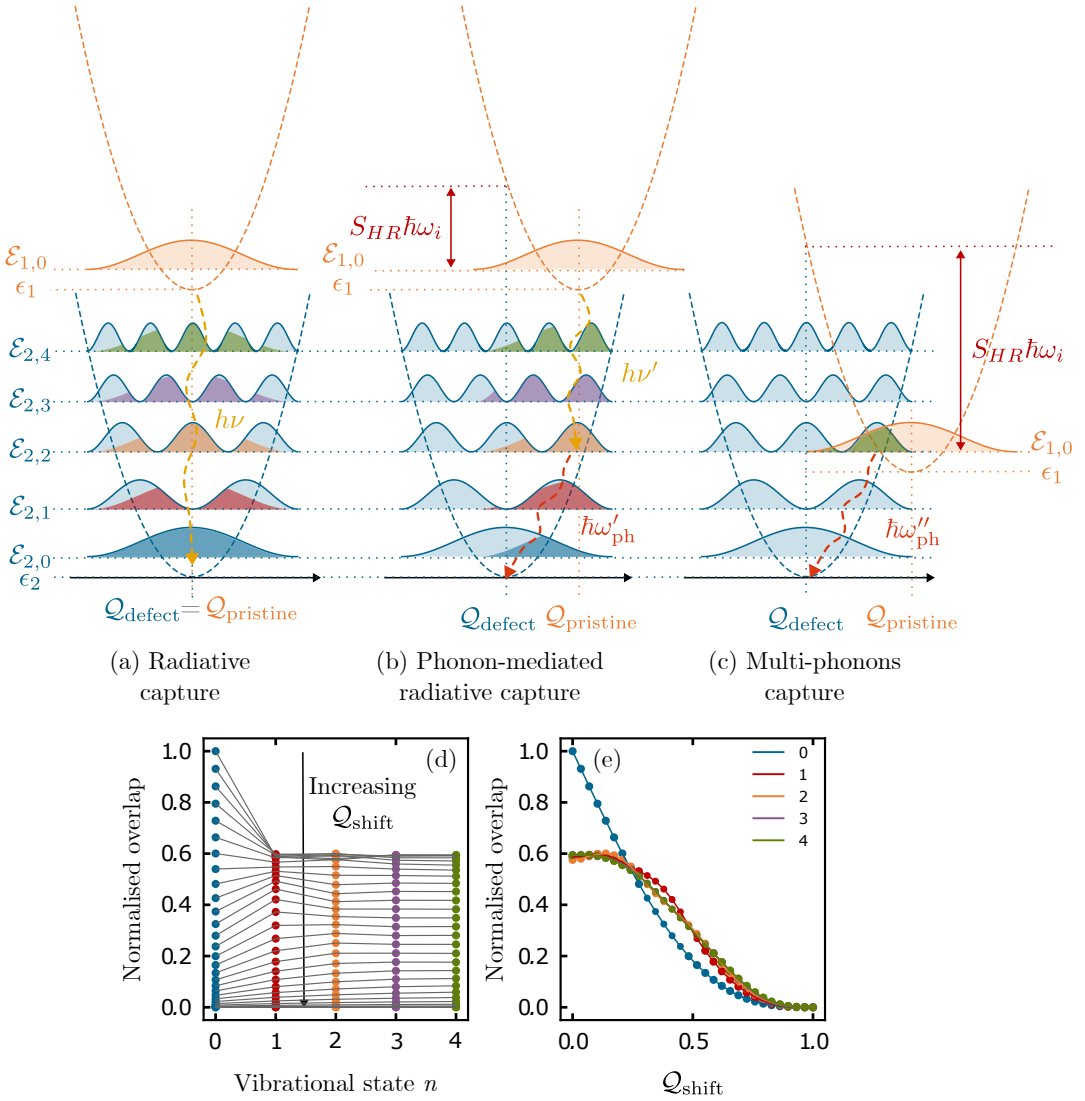


Figure 2.15: Representation of the different capture processes between a band state and a defect state. In insets (a), (b) and (c) the radiative, phonon-mediated and multi-phonon mediated captures are respectively represented. In those representations, ϵ_i is the electronic energy of respectively the band state (ϵ_1) and the defect state (ϵ_2). Then, the vibrational energy is represented in the form of a parabola (classical harmonic oscillator) with respect to the configuration coordinate $\propto (Q - Q_i)^2$. And, within the parabola, specific vibrational eigenstates are presented: $\mathcal{E}_i = \hbar\omega_i(n + 0.5)$. The recombination process is then highlighted by the emission of a photon $h\nu$ or a phonon $\hbar\omega'_{ph}$ along with the Huang-Rhys factor S_{HR} . In the insets (d) and (e) the normalised overlap between the band state density (orange) and the defect state densities are represented respectively as a function of the vibrational state n and then for various deformations $Q_{shift} = Q_{defect} - Q_{pristine}$ induced by the point defect. The figure is inspired of the work realised in Ref. [99].

depends on (i) the strength of the electronic interaction between the defect and the band state and (ii) on the overlap between the vibrational states being a function of the deformation in the vicinity of the defect with respect to the pristine lattice. The more localised the defect, the weaker the interaction between the band and the electronic states of the defect (\searrow (i)). This electronic contribution can be visualised through a quantum defect parameter \mathcal{R}_d which ensures that the deeper the defect, the more localised the wavefunction (small associated radius). \mathcal{R}_d being a dimensionless quantity which relates the change of the defect binding energy with the band state to the associated defect wavefunction radius:

$$\mathcal{R}_d = \frac{1}{\epsilon_\infty} \sqrt{\frac{m^* q^4}{32\pi^2 \hbar^2 \Delta E_{\min}}}, \quad (2.68)$$

with ΔE_{\min} being the energy difference to the closest band.

Furthermore, the vibrational contribution can be represented through the Franck-Condon energy $E_{FC} = S_{HR} \hbar \omega_n$ (assuming that the vibrational frequency of all electronic states are equal). The Huang-Rhys S_{HR} factor being defined in the classical approach as:

$$S_{HR} = \frac{(Q_{\text{pristine}} - Q_{\text{defect}})^2}{2} \quad (2.69)$$

This factor provides the number of phonon involved in the recombination process [91]. As a result, the larger the lattice distortion upon defect incorporation, the larger the Huang-Rhys factor and consequently the Franck-Codon energy resulting in a strong electron-lattice interaction.

Finally, the capture coefficients, the speed at which charge carriers are captured by the defect level, $k_{n,p}$ are related to this transition:

$$k_{n,p} = \frac{2\pi}{\hbar} |\langle \Psi_1 | \mathbf{H}_{\text{int}} | \Psi_2 \rangle \langle \chi_{1,n} | \chi_{2,n} \rangle|^2 V^2 N(E_2) \quad (2.70)$$

Finally, a *simple* rule to determine if the recombination process is more likely to be radiative or phonon-mediated is known as the Dexter-Klick-Russell rule [91, 108]. This one expresses that the larger the lattice distortion, implied by a strong electron-lattice coupling, the lower the luminescence efficiency. In other words, strong lattice distortion results in a capture process more likely to be purely non-radiative and mediated through multi-phonons emission [91, 99, 109].

Summary: What's an efficient recombination centre ?

To summarise, a point defect described as a recombination centre leads to the loss of the free charge carrier energy in the form of thermal processes through the emission of one or multiple phonons [91,108]. For a recombination centre to be qualified as *efficient*, such defect would be associated to large carrier capture coefficients $k_{n,p}$ (see Eq.(2.70)). One would therefore desire a strong electronic interaction with the band state, so a defect that is not too localised and a large overlap between the vibrational states. The latter would as a result require a small distortion of the lattice in the vicinity of the point defect following its incorporation. With these criteria, we would obtain large capture coefficients $k_{n,p}$. Then, to obtain a low minority carrier lifetime and a high rate of recombination, we would like the capture processes to be dominant over the emission ones in order for the defect state to be as likely empty as filled (occupancy probability 1/2) and also to capture as many electrons as holes ($nk_n = pk_p$). Of course, this last element leads to efficient recombination far from the bands, where the emission of electrons or holes is low and thus the captures are dominant, and this distance from the band will lead to a defect state which will be more localised. In addition, if we do want to capture as many electrons as holes, the range of energies for which it is verified is quite limited (tens of meV [99]). Outside this range, we would create a disparity between the amount of carriers of each type captured, which would reduce the recombination efficiency. Finally, another to obtain a pure non-radiative recombination, the distortion has to be quite large implying a strong electron-phonon coupling.

As a result, an *efficient* recombination centre requires the balance between two criteria: (i) large lattice distortion leading to pure non-radiative processes but also lower vibrational states overlap reducing the $k_{n,p}$ in contrast to values related to radiative processes. And, (ii) the defect has to capture both electrons and holes therefore compelling a defect provided energy level located in the middle of the bandgap, reducing the electronic interaction between the initial and final states.

The section developed here will be of great interest for the discussion realised in chapter 5.

2.4 THE PHOTOVOLTAIC EFFECT

From the developed theoretical notions concerning semiconductors and, the physical behaviour of point defects along with their related recombination, we now move to the application field of this thesis: the use of semiconductors as absorber layers for photovoltaic applications. In this section, we review the basics of the photo-electrical conversion of solar energy. The objective is to provide the reader the conceptual tools that are necessary to contextualise the upcoming discussions.

1. First, the physics of the PV effect is developed, highlighting the generation of electrical power through light-induced charge carrier generation, collection and dissipation through an external load. The PV effect is presented thanks to the description of the band diagram in short circuit and open-voltage conditions. Finally, the electrical conversion limitations are presented with a specific focus on the impact of charge carrier recombination on the PV performances.
2. Second, the approach used to model the electrical power conversion efficiency based on the physical properties of the absorber layer is presented by taking into account the amount of recombination through an external parameters Q_i . This approach is used to compute the results obtained in chapter 4.

The photovoltaic effect was discovered in 1839 by a French physicist, Edmond Becquerel, who wrote his observations in a report entitled "*Mémoire sur les effets électriques produits sous l'influence des rayons solaires*". M. Becquerel experimentally observed, upon illumination, the generation of a current between two metallic electrodes immersed in a liquid and separated by a thin membrane [110]. Furthermore, a few decades later, in 1883, the first solar cell was realised by Charles Fritts, an American inventor who used molten selenium pressed between two metallic plates [111,112]. Then, in 1940, Russel Ohl, a Bell Labs scientist observed the electrical redressing behaviour of a Si PN-junction [113]. This discovery was patented by Ohl in 1941 [13]. At the time, the efficiency of solar cells was around 1%. Years later, in 1954, the first Si solar cell with 5% efficiency was reached by three researchers at Bells Lab [114]. Solar cells made of As and B-doped Si reached an efficiency of 6% and were used to power radio transmitters. This point marked the beginning of the Si era in photovoltaic application. After years of research by Hoffman Electronics, the efficiency then reached 15.2% in 1961 before a long 10-year plateau was eventually breached by a new breakthrough coming from the antireflection processes in 1973 (15.4%) and

III. Primer on the physics of PN junctions

When a p-type and a n-type semiconductors are brought into contact, diffusion current densities at the junction occur due to the charge concentration gradients:

$$J_{\text{diff},n,p}(x) = -q_{n,p} D_{n,p} \frac{dn, p(x)}{dx}, \quad (2.71)$$

$q_{n,p}$ being the electron or hole charge. The diffusion of majority carriers induces a space charge region at the interface: positive on the n-type: N_D^+ and negative on the p-type: N_A^- (assuming that all dopants have been ionised) generating a local electric field E . This electric field is related to the energy band bending over a width W_D as a result of the built-in potential barrier V_{bi} . Charge carriers experiencing the electric field enter into motion, leading to drift current densities in opposition to the diffusion ones:

$$J_{\text{drift},n,p}(x) = q_{n,p} n, p \mu_{n,p} E(x) \quad (2.72)$$

As illustrated under thermodynamic equilibrium, without any applied voltage across the junction, the net current density is zero, and the Fermi levels of the two semiconductors are aligned.

$$J_{\text{drift},n,p}(x) + J_{\text{diff},n,p}(x) = 0 \quad (2.73)$$

Under **forward bias** (positive bias of type p with respect to type n), the applied voltage V_a reduces the potential barrier at the interface and increases the diffusion current densities by a factor $e^{qV_a/k_B T}$. Under **reverse bias**, the applied voltage increases the potential barrier at the interface, preventing the diffusion of charges via increased electric field and extension of the depletion width W_D . However, in both semiconductors, minority carriers are thermally generated, and some thermally diffuse towards the interface. When reaching the depletion region, they are swept across the junction by the electric field, leading to the so-called saturation current density J_0 . This quantity depends on how often minority carriers reach the depletion region and how often these carriers are thermally generated. The net current density is

$$J(V_a) = J_0 \left(e^{\frac{qV_a}{k_B T}} - 1 \right) \quad (2.74)$$

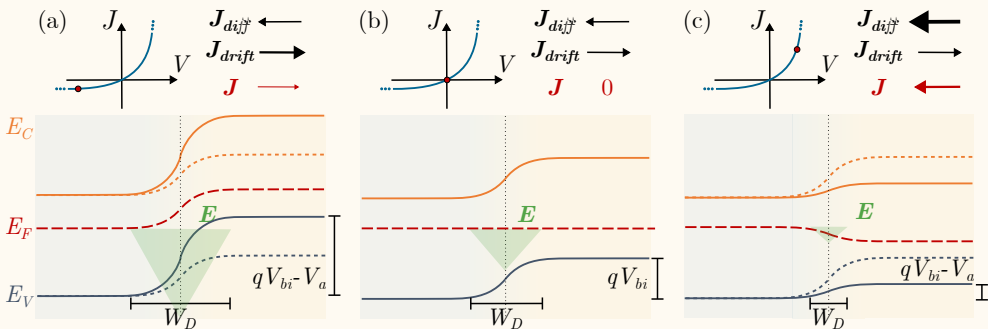


Figure 2.16: Band diagram of a PN homojunction under (a) reverse bias, (b) equilibrium and, (c) forward bias condition.

then texturing in 1974 (17.2%). Through new technologies, new breakthroughs via doping strategies, new cell architectures and contacts realisation, a record efficiency of 25% was achieved in 1985 with PERL (Passivated Emitter Rear Locally Diffused) cells [13]. Nowadays, the Si crystalline cell reached an efficiency of 26.8 % getting closer and closer to the theoretical limit of 32.23% for a bandgap of 1.1 eV established by Shockley-Queisser using thermodynamic conditions [28, 29]. As briefly described here, the breakthroughs brought to the solar technology come from material and architectural improvements. In order to achieved these ones, it is essential to understand both the physics of the materials and the physics (and limitations) behind the photovoltaic effect.

2.4.1 Physics of the photovoltaic effect

The photovoltaic effect is a physical phenomenon in which an initial electromagnetic radiation (*'photo'*) is converted into an electrical power (*'volt'*). This effect occurs notably in a PN junction under illumination, where energy is extracted from the generation of both a voltage and a current in the junction. As presented in **box III** dedicated to the physics of the PN junction, the resulting current density through the PN junction interface is a dynamic balance between, first, a diffusion of charge carriers from the semiconductor where they reside as majority carriers to the one where they become minority carriers (*i.e.* holes diffusing from the p-type to the n-type material) and, second, a drift current density of minority carriers as a result of the electric field within the depletion region. The origin of the drift and diffusion current densities is described in the "Charge carriers transport in solids" **box IV**. In the following, the physics of the photovoltaic effect is discussed taking as notation the current density \mathbf{J} and the related vectorial quantities under a one-dimensional consideration x . First, the total current density across the junction J can be expressed as a function of the derivatives of the quasi-Fermi levels⁹

$$J = J_n + J_p = \mu_n n \frac{dE_{F,n}}{dx} + \mu_p p \frac{dE_{F,p}}{dx} \quad (2.75)$$

In addition, under thermodynamic equilibrium conditions, the net current density through the junction is $J(V_A = 0) = 0$. Then, as presented in Eq.(2.74), in the dark and upon the application of an external voltage V_A , the diffusion current density increases by an exponential factor as a result of the reduction of the energetic barrier at the junction, giving a total current density flowing through the interface.

First, under reverse bias ($V_A < 0$) and in the dark ($J_{ph} = 0$), one can identify the saturation current density J_0 corresponding to the amount of minority charge carriers

⁹Expression of the total current density across the junction obtained as the sum of the drift (Eq.(2.72)) and diffusion (Eq.(2.71)) current densities for both electrons and holes and by injecting in these equations the charge carrier concentrations (Eqs.(2.36) and (2.38)). The final relation is obtained using the Einstein relations: $\frac{k_B T}{q} = \frac{D_{n,p}}{\mu_{n,p}}$.

IV. Charge carriers transport in solids.

Electrons can be described using a Bloch wavefunction (see Eq.(2.17)). This representation corresponds to electrons that are **delocalised**, which spread over the entire lattice. If we want to represent a **localised** electron, we have to consider wave packets resulting from the superposition of several wavefunctions whose description includes various wave vector \mathbf{k} [91]. Then, using this wave packet, a group velocity \mathbf{v}_g can be extracted (the speed of the envelope of the wave packet) as described in

$$\mathbf{v}_g(\mathbf{k}) = \frac{1}{\hbar} \frac{\delta E(\mathbf{k})}{\delta \mathbf{k}}. \quad (2.76)$$

Moreover, using the second Newton law: $\mathbf{F} = m \frac{\delta \mathbf{v}_g(\mathbf{k})}{\delta t}$ and the relation between the applied force and the electron momentum: $\mathbf{F} = \frac{\delta \mathbf{p}}{\delta t} = \frac{\delta \hbar \mathbf{k}}{\delta t}$, the electron mass within the crystal lattice can be expressed in the form of an effective mass $m_{n,h}^*(\mathbf{k})$ (see Eq.(2.32)). This specific mass represents the effect of the potential experienced by the charge carriers for a given \mathbf{k} point in the band structure on its motion [91, 93]. Then, as presented in Ref. [93], one can study how electrons move in a band, how electrons with different wave vector \mathbf{k} (effective mass) contribute to the current and how these ones experienced some scattering effects leading to the existence of a resistance to the charge carrier motion (current). However, in order to describe this motion, one must include a time-dependent Schrödinger equation and spe-

cific distribution statistics related to the electron nature (Fermi-Dirac distribution).

The **Boltzmann equation** presents a formalism for the carrier transport in a solid by taking into account the variation of the charge carrier population density in space \mathbf{r} and in momentum \mathbf{k} (energy) when exposed to some driving forces and dissipative effects [91, 93]. This relation is presented in Eq.(2.77) under local equilibrium conditions by the time evolution of the charge carrier distribution $f(\mathbf{r}, \mathbf{k}, t)$.

$$\underbrace{\frac{\delta f}{\delta \mathbf{k}} \frac{\delta \mathbf{k}}{\delta t}}_{\text{(i)Drift}} + \underbrace{\frac{\delta f}{\delta \mathbf{r}} \frac{\delta \mathbf{r}}{\delta t}}_{\text{(ii)Diffusion}} = \underbrace{\left(\frac{\delta f}{\delta t} \right)}_{\text{(iii)Scattering}} \text{coll} \quad (2.77)$$

where, the first term corresponds to the **drift** contribution determined by the force applied on the electrons (for instance due to an external electric field \mathbf{E})

$$\frac{\delta \mathbf{k}}{\delta t} = \frac{1}{\hbar} \frac{\delta \mathbf{p}}{\delta t} = \frac{\mathbf{F}}{\hbar} = \frac{-q\mathbf{E}}{\hbar}, \quad (2.78)$$

and, the second term corresponds to the spatial variation of the charge carrier concentration known as the **diffusion** component and related to the group velocity expressed in Eq.(2.76). Finally, the third term relates to the scattering that creates resistance to the charge carrier transport [91].

reaching or generated within the depletion region swept by the in-place electric field through the interface leading to a non-zero current density (see Eq.(2.81)). The saturation current density depends on the number of minority carriers thermally generated in the depletion region or at a distance smaller than the minority carrier diffusion length from the depletion region. In addition, since the net current density is 0 as the drift of minority carriers is cancelled by the diffusion of majority carriers,

the total current density can be expressed as

$$J(V_A = 0) = \underbrace{J_{\text{diff}}}_{\text{Majority carrier}} + \underbrace{J_{\text{drift}}}_{\text{Minority carriers}} = 0 \quad (2.79)$$

As a result, the saturation current density J_0 can be interpreted in terms of recombination at the PN junction, ensuring the cancellation of the drift current density composed of the minority carrier. As a result, if the number of recombinations increases, so does the saturation current density. This saturation current density can also be expressed as presented in Eq.(2.80) where for a larger minority carrier concentration, a lower minority carrier lifetime, and a larger minority carrier diffusion coefficient, a larger saturation current density is observed. Depending on the recombination process, the saturation current density can be expressed differently as described in Ref. [115].

$$J_0(T) = q\sqrt{\frac{D_p}{\tau_p} \frac{n_i(T)^2}{N_D}} + q\sqrt{\frac{D_n}{\tau_n} \frac{n_i(T)^2}{N_A}} \quad (2.80)$$

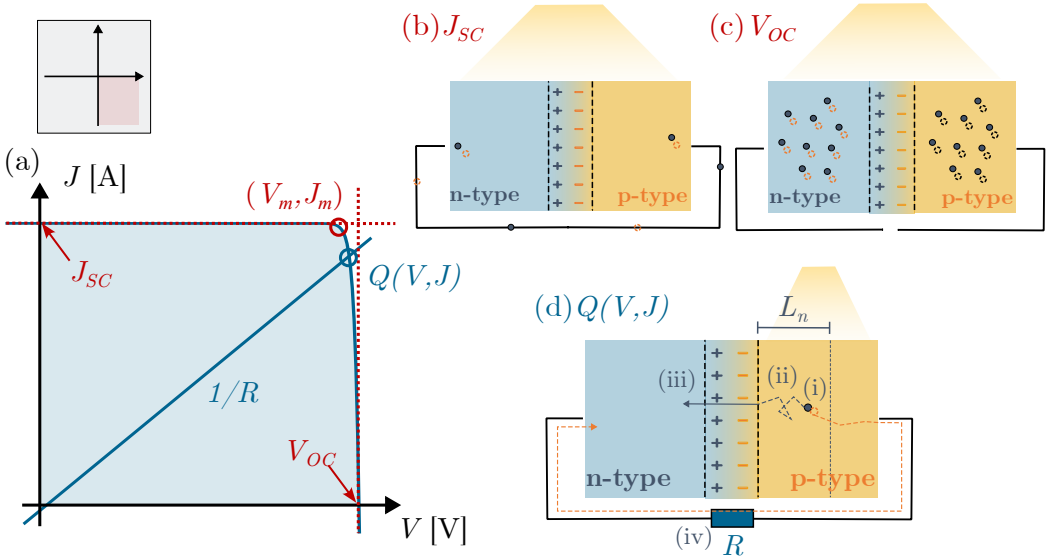


Figure 2.17: (a) The JV curve of a PN junction under illumination is presented and points of interest are highlighted. On the right panel, a representation of the PN junction is provided for three cases: (b) under open circuit condition, (c) under short circuit condition and, (d) at an operating point $Q(V, J)$ defined by the value of the external load R connected to the junction. For this third case, the photovoltaic effect is described from (i) the EHP generation, (ii) the thermal diffusion of the minority charge carrier towards the depletion region, (iii) the drift of the minority carrier swept into the n-type layer where it becomes a majority carrier and (iv) the energy loss of the majority charge within the external circuit landing into the n-type layer.

Then, as illustrated in **Fig.2.18** and as described in section 2.2.2, upon light illumination, electron-hole pairs are generated within the semiconducting materials. This charge generation results in the first term of Eq.(2.81) in the photogenerated current density representing the charge carriers **generated** by illumination and **extracted** out of the junction. In **Fig.2.17(a)**, we illustrate a practical way to represent this JV curve of a solar cell is to focus on the fourth quadrant taking the convention J_{ph} as positive.

$$J(V) = J_{ph} - \underbrace{J_0 \left(e^{\frac{qV_A}{k_B T}} - 1 \right)}_{\text{dark}} \quad (2.81)$$

This term leads to a shift on the y-axis of the JV curve. The thermally generated minority carriers J_0 and the current density of the photocarriers J_{ph} contribute to the total reverse current density. Indeed, the minority charge carriers generated at a distance lower than the diffusion length $L_{n,p}$ from the depletion region have a non-zero probability to thermally diffuse towards the interface where they will be swept by the in-place electric field towards semiconductors where they become majority carriers. As will be described further, depending on the conditions of the solar cell circuit (from open circuit to short circuit), the total current density can vary from 0 to J_{SC} . In addition to the current density, the generation of charges also leads to the generation of an electrical voltage across the junction. Similarly, depending on the condition of the solar cell circuit (from short circuit to open circuit), the photogenerated voltage can vary from 0 to V_{OC} . In Eq.(2.81), one can already observe that the generated voltage and current density are functions of each other, if one does extract a higher voltage, the extracted current density will decrease.

In order to understand the behaviour of a PN junction under illumination, let us first describe two extreme cases: open circuit (OC) and short circuit (SC) conditions. For both cases, the band diagram as well as a schematic of the PN junction are presented in **Figs.2.17** and 2.18.

First, under **open circuit condition**, no external connection is established between the p-type and the n-type materials of the junction. Under such conditions, the charge generation results in a voltage across the junction whose related electric field is opposite to the electric field at the junction without illumination. This voltage, as presented in **Fig.2.17(a)** and is labelled open circuit voltage V_{OC} . In addition, in **Fig.2.18(c)**, an electrical voltage difference of V_{OC} can be measured between the n-type and p-type semiconductors that corresponds to the energy difference between the electron and hole quasi-Fermi levels. Under such conditions, the zero current density across the junction is ensured by reducing the energetic barrier: $q(V_{bi} - V_{OC})$ resulting in an exponential increase in the diffusion current density counterbalancing

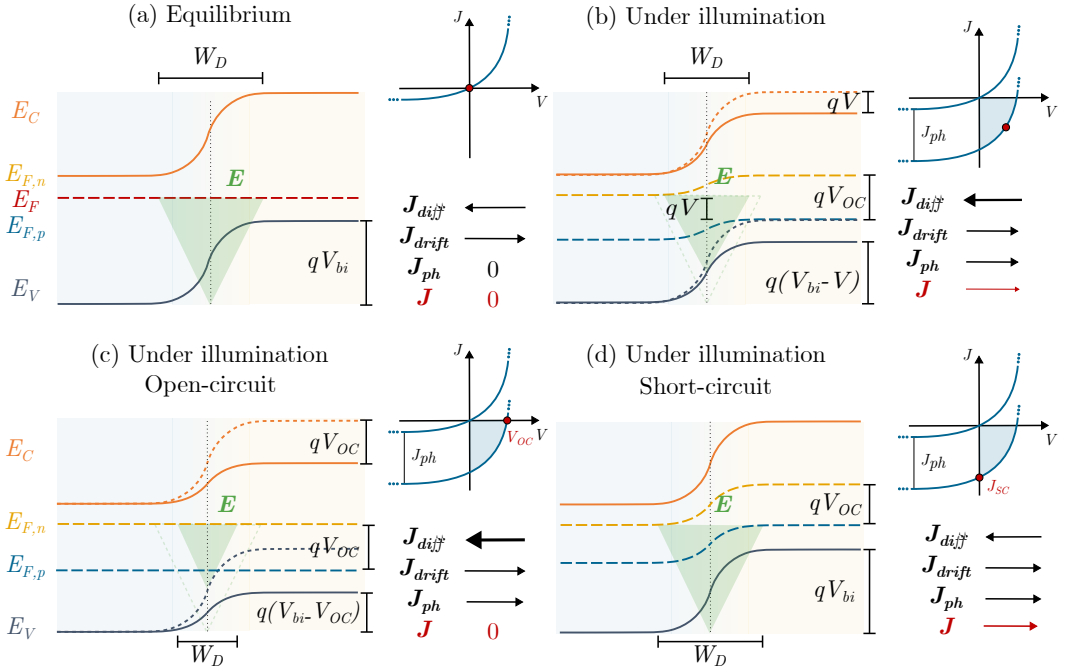


Figure 2.18: Band diagrams of a PN junction in four distinct cases: (a) under thermodynamic equilibrium conditions, there is a common flat Fermi level for electrons and holes resulting in a zero voltage and current across the junction. The diffusion current density is balanced by the drift current density. (b) Under illumination (assuming uniform illumination of the entire PN-junction) and open circuit condition, the illumination generates EHPs, resulting in a voltage drop across the junction represented by the energy split between the electron and hole quasi-Fermi levels. However, no net current flows through the junction. (c) Under illumination and short circuit condition, the voltage generated through the junction is consumed by the charge motion, leading to a bending of the quasi-Fermi energy levels and a resulting net current density across the junction. The diffusion current density does not compensate for the additional photocurrent (minority charge carriers swept by the in-place electric field at the interface). And, (d) under illumination and between short/open circuit conditions (load resistance), a net voltage and current can be measured across the junction.

the additional component of the drift current density that occurs because the generated minority carriers are swept by the electric field at the junction. As a result, the net current density is 0 and the voltage drop across the junction is V_{OC} . Moreover, as presented in **Fig.2.18(c)**, one can see that under open circuit conditions no Fermi level bending is observed, confirming the zero net current density. From Eq.(2.81) the open circuit voltage can be expressed as such:

$$V_{OC} = \frac{k_B T}{q} \ln \left(\frac{J_{ph}}{J_0} + 1 \right) \quad (2.82)$$

This relation highlights that this quantity is a function of the photogenerated current density, but also of the saturation current density J_0 and of the temperature

T . Note that the saturation current density is also a function of the temperature through the minority carrier charge generation as described earlier. From this relation, we highlight the link between the open circuit voltage and the number of recombination represented by the saturation current density: the larger the number of recombination, the larger the saturation current density and finally, the smaller the open circuit voltage. In addition, in the case of a homojunction, qV_{OC} is smaller than the material bandgap E_G as a higher potential value would lead to forward biasing of the PN junction and to the shift of the JV curve from the fourth quadrant where $JV < 0$ acts as a power source to the first quadrant where $JV > 0$ in which the diode requires some energy input.

Second, under **short circuit condition**, corresponding to an external connection between the p-type and the n-type materials of the junction (see **Fig.2.17(b)**), the voltage across the junction is zero, meaning that the Fermi energy levels of the majority charge carriers in both semiconductors are aligned (see **Fig.2.18(d)**). A large bending with a variation of qV_{OC} between the electrons (resp. holes) quasi-Fermi energy levels in the n-type and the p-type materials is observed. The voltage difference generated upon illumination is under short circuit conditions fully consumed by the charge carrier motion across the junction, resulting in a net current density called the short circuit current density J_{SC} .

As a result, to induce a net current density and a non-zero voltage across the junction turning the PN junction under illumination into a power source, one must also have a non-zero voltage difference between the p-side and the n-side of the junction and this one must be smaller than V_{OC} to obtain a non zero current density. This configuration corresponds to the case presented in **Fig.2.18(b)**. The quasi-Fermi energy levels bending is a direct observation of this current density. Then, as presented in **Fig.2.17(d)**, the voltage and current density collected from the solar cell are fixed by the external circuit defining an operating point $Q(V, J)$ as a result of the external load R . As a result, to obtain a voltage, the current density has to be smaller than J_{SC} and considering a realistic material, only a fraction of the photogenerated carriers will be collected (see Eq.(2.83))¹⁰.

¹⁰Let us now make a parenthesis in order to describe the distinction between the PV effect taking place in a **heterojunction** with respect to a **homojunction** as described in this section. First, the use of two different materials for the p-type and n-type semiconductors implies different bandgaps E_G and electronic affinity ξ values, producing different band alignment, resulting in three possible types of junctions [116]. In addition, usually one of the material bandgap will be fit to match the solar spectrum in order to absorb photons (*i.e.* the absorber layer), while the second material will not purposely be designed to absorb and generate charge carrier but only to generate the electric field at the interface in order to collect the charge carriers produced. As a result, in **Fig.2.18**, charge carriers will only be generated on one side of the PN junction (for instance, in the p-type layer). These generated carriers will be represented by the quasi-Fermi level splitting only in the p-type layer, and due to the electric field in place at the junction, the minority charge carriers will be swept in the n-type layer resulting in an additional component of the drift current density: J_{ph} . However, this charge generation will still be compensated by a reduction of the potential barrier at the interface and an increase of the diffusion current density whose magnitude will depend on

$$J_{\text{real}}(V) \underbrace{\leq}_{\text{Collection prob.}} J_{\text{ideal}}(V) \underbrace{\leq}_{\text{Circuit cond.}} J_{SC} = J(V=0) \quad (2.83)$$

Finally, the output power of the solar cell is the product between the voltage building up as the charge carriers are generated following the light absorption and the current density induced. As an indicator of the quality of the solar cell, the fill factor FF is defined as the ratio between the maximum output power (maximal power point corresponding to the current density and voltage J_m and V_m on the JV curve) and the product of J_{SC} and V_{OC} :

$$FF = \frac{J_m V_m}{J_{SC} V_{OC}} \quad (2.84)$$

The maximal efficiency of the photovoltaic conversion is calculated based on the ratio between the output power \mathcal{P}_{out} being the product between the number of charges extracted by unit of time J_{mpp} and the built-in voltage induced by the generation of electron-hole pairs V_{mpp} and the input power \mathcal{P}_{in} corresponding to the photon energy absorbed by unit of time by the solar cell.

$$\eta_m = \frac{FF V_{OC} J_{SC}}{\mathcal{P}_{in}} \quad (2.85)$$

As presented in Eq.(2.85), in order to maximise the solar cell efficiency, one must maximise the open circuit voltage, the short circuit current density, and the fill factor values. So what are the limitations of these physical quantities ?

First, we present in **Fig.2.19(a)**, some limitations to the solar energy conversion using a single junction solar cell that can be qualified as intrinsic losses [28, 117]. Among them, thermodynamic limits such as the Carnot losses (heat losses) and the Boltzmann losses (entropy generation), as well as emission-related losses, lead to the first reductions of the efficiency. However, the largest intrinsic losses come from both sub-bandgap losses and thermalisation. The first element describes the losses of photons whose energies are below the absorber layer value, leading to the impossibility of charge carrier generation. Then, thermalisation describes thermal losses concerning part of the absorbed incident radiation; part of the photon energy $E_G - h\nu$ that is lost through phonon emission as the charge carrier is promoted to an excited state in the conduction band. These limitations to solar energy conversion result in either a decrease of the photogenerated voltage or current. Both emission and sub-bandgap losses lead to a reduction of possible number of electron hole pair generated resulting in a reduction of the current density while Carnot, Boltzmann, and the thermalisation losses lead to a reduction of the possible voltage generated [117].

the circuit condition (from open circuit: reduction of V_{OC} to short circuit: no reduction of the potential barrier). Eventually, the band mismatch ΔE_C and ΔE_V at the interface could also lead to additional recombination.

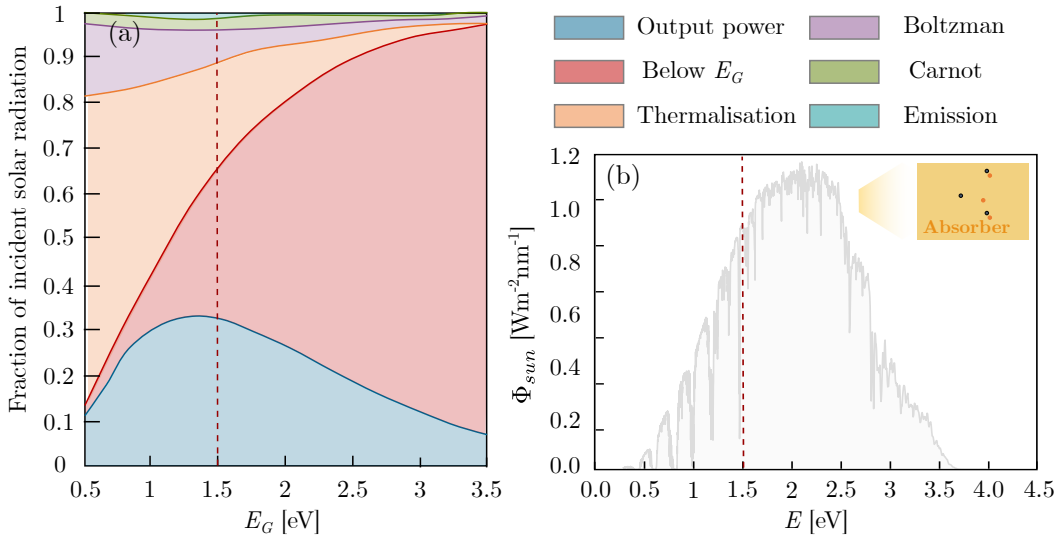


Figure 2.19: (a) The fraction of the incident solar radiation converted into an electrical output is presented as a function of the material . (inspired from Ref. [117]). The figure highlights the intrinsic losses occurring in a single solar cell. Besides these intrinsic losses, extrinsic losses such as recombination, light absorption, *etc.* are additional limitations that reduce the output power presented here. In parallel, the solar radiation spectrum is presented in (b) with a schematic representation of charge carrier generation in a p-type absorber layer.

Then, in addition to the intrinsic losses previously presented, extrinsic losses can again reduce the electrical output power and consequently the solar cell efficiency. To start, good **light absorption** is the first key parameter. Light absorption is usually performed by one material of the PN junction: the absorber layer which possess the adequate value with respect to the solar spectrum as illustrated in **Fig.2.19(b)**. As described in section 2.2, this absorption depends on the value of the semiconductor and on the absorption coefficient of the material. In addition, both of these physical quantities could be altered by any deviations from the pristine materials (*i.e.* defects). Ideally, each photon of the incident light should generated one EHP and consequently contribute to both the V_{OC} and the J_{SC} value. The absorber layer has to be thick enough to collect the incident light. Light absorption also depends on the fraction of the light which is reflected, the incident angle, *etc.*

Following the generation of an extra electron hole pair in the absorber layer, this one has to be **collected** in order to contribute to an external current density. First, in order to avoid recombination within the absorber layer, the charge generation has to happen not too far from the depletion region meaning at a distance lower than the minority carrier diffusion length away from that area (see **Fig.2.17(d)**). More generally, all types of recombination have to be avoided either within the absorber layer material or at the material interfaces. As a result, the conversion efficiency does

not only rely on a good light absorption but also on the prevention of the energy transformation into thermal losses through non-radiative recombination and phonons emission facilitated by the presence of detrimental defects. A practical way to assess both light collection is via a measure of the external quantum efficiency (EQE). The EQE is a measure of the ratio between amount of charges collected by unit of time and the amount of photon incident on the solar cell by unit of time. This measure is performed for different wavelength.

$$EQE(\lambda) = \frac{J}{q} \frac{h\nu}{\mathcal{P}_{in,\lambda}} \quad (2.86)$$

Finally, resistive losses modelled through series and shunt resistances are last key ingredients that can alter the efficiency of a solar cell through a reduction of the fill factor.

In the next section, based on Ref. [87], we present the modelling of the electrical power conversion efficiency providing *ab initio* inputs concerning the materials properties and using a parameter to tune the number of recombination limiting the resulting efficiency.

2.4.2 Modelling of the electrical power conversion efficiency

In 1960 work dedicated to the "detailed balance limit of efficiency", Shockley and Queisser (SQ) assessed the theoretical upper limit of a PN-junction solar cell [28]. This model assumes only radiative transitions as recombination mechanisms for electron-hole pairs (EHPs) and considers the solar cell as a black body (BB) at a given temperature T . In this case, the theoretical upper efficiency can be expressed as the maximal value of the ratio between the electrical power delivered by a solar cell and the incident solar power as described in Eq.(2.87), with V the voltage induced by the generation of EHPs, d the absorber layer thickness, q the electron charge and Φ_{Sun} the solar spectrum expressed in $\text{eV}^{-1}\text{m}^{-2}\text{s}^{-1}$. The SQ model assumes a solar cell with an ideality factor of 1 and an internal quantum efficiency $Q_i = 1$, which assumes that every absorbed incident photon generates an EHP which is either collected or re-emitted as a photon contributing to the solar cell black body spectrum (*i.e.* no non-radiative recombination).

$$\eta_m = \max \left(\frac{J(V, d)V}{\int_0^\infty E\Phi_{\text{sun}}(E)dE} \right), \quad (2.87)$$

$$J(V, d) = J_{\text{SC}}(d) + \underbrace{J_{\text{rad},0}(d)(1 - e^{qV/k_B T})}_{J_{\text{rad}}(d,V)} \quad (2.88)$$

with the total current density $J(V, d)$ (Eq.(2.88)) the sum of the short circuit current density J_{SC} (Eq.(2.89)) and the radiative saturation current density J_{rad} . The latter is presented in Eq.(2.90) with q the electron charge and k_B the Boltzmann constant.

The current density under short circuit condition can be expressed as the number of photons absorbed per unit of time. First SQ took as incident photon flux, the BB spectrum at $T = 6000\text{K}$ [28]. Then, the product of Φ_{sun} by the absorptance $A(E)$ results in the number of EHPs generated in the absorber layer and contributing to the short circuit current density. Assuming a Heaviside step function for the absorptance, every photon with an energy $\hbar\omega > E_G$ is absorbed.

$$J_{\text{SC}}(d) = q \int_{E_G}^{\infty} A(E, d) \Phi_{\text{sun}}(E) dE \quad (2.89)$$

Secondly, the radiative recombination current density term which describes the number of EHP recombinations in a solar cell at temperature T can be expressed as described in Eq.(2.90). In this equation, the radiative recombination rate under equilibrium condition, $R_{\text{rad},0}(d)$ is described as the integration over the energy of the product between the BB radiation spectrum at a temperature T and the materials absorptance spectrum (Eq.(2.91)).

$$J_{\text{rad},0}(d) = qR_{\text{rad},0}(d) \quad (2.90)$$

$$R_{\text{rad},0}(d) = \frac{2\pi}{c^2 h^3} \int_{E_G}^{\infty} A(E, d) \left[e^{E/k_B T} - 1 \right]^{-1} E^2 dE \quad (2.91)$$

As a result, the SQ model parameters are the solar cell temperature T (usually 300 K), the absorber layer thickness d and the materials E_G used to compute the material absorptance. In a certain way, the solar cell is thus assumed to be infinitely thin and infinitely thick. First, it is considered infinitely thin because it is assumed that every EHP generated is either recovered at the electrodes boundaries (*i.e.* no non-radiative recombination or $Q_i = 1$). And, secondly, it also has infinite thickness, because it is assumed that every photon for which the energy $\hbar\nu$ is greater than the bandgap energy E_G will be absorbed (Heaviside step function for the absorptance). A first straightforward improvement of this model can be obtained by taking the Air Mass 1.5 (AM1.5) photon flux as the emission spectrum of the sun which is commonly used to characterise solar cells under standard conditions. Secondly, using the *ab initio* optical results (*i.e.* the absorption coefficient $\alpha(E)$ and the materials reflectivity $R(E)$), the absorptance $A(E)$ of the absorber layer materials is computed. Assuming a flat solar cell surface and a layer thickness d , the Beer-Lambert law is used to calculate the absorptance as expressed in Eq.(2.92) [87]. A perfect reflection at the rear interface of the solar cell absorber layer is assumed while at the front interface, the material reflectivity $R(E)$ obtained via first principle calculation is taking into account. In addition, interference effects are neglected.

$$A(E, d) = [1 - R(E)] - e^{-2\alpha(E)d} \quad (2.92)$$

In addition to these improvements, in 2017, Blank *et al.* proposed an extended detailed balance model via: (i) the use of the internal quantum efficiency Q_i as model

parameter to take into account non-radiative recombinations and (ii) the incorporation of light trapping by taking into account the materials refractive index $n(E)$ in the calculation of the radiative current density $J_{\text{rad},0}(n, d)$ [87].

(i) First, the internal quantum efficiency is used as a parameter to take into account non-radiative recombinations. As those non-radiative recombinations depend on the presence of defects in the materials acting as recombination centres (intrinsic point defects, grain boundaries, *etc*), it is more convenient in this work, to use this physical quantity as a model parameter. This one is expressed as the ratio between the radiative recombination rate $R_{\text{rad},0}$ and the total recombination rate: $R_{\text{rad},0} + R_{\text{nrad},0}$, leading to a non-radiative recombination rate under equilibrium conditions expressed as described in Eq.(2.93). This model assumes an identical voltage dependency for the radiative and non-radiative recombination rates [87].

$$R_{\text{nrad},0} = \frac{R_{\text{rad},0}(1 - Q_i)}{Q_i} \quad (2.93)$$

(ii) In addition, to take into account the internal reflections and therefore re-absorption in the absorber layer, the Roosbroeck-Shockley equation is used to calculate the radiative recombination current density as described in Eq.(2.94). In this one, the absorber layer refractive index $n(E)$ is injected [87].

$$J_{\text{rad},0}(d, n) = qp_e(d, E) \int R_{\text{rad},0}(x, E) dx, \quad (2.94)$$

with

$$p_e(d, E) = \frac{\int_{E_G}^{\infty} A(E) \Phi_{\text{BB}}(E) dE}{4d \int_{E_G}^{\infty} n^2(E) \alpha(E) \Phi_{\text{BB}}(E) dE}, \quad (2.95)$$

with the BB radiation spectrum described in Eq.(2.96).

$$\Phi_{\text{BB}}(E, T) = \frac{2E^2}{h^3 c^2 [e^{E/k_B T} - 1]} \quad (2.96)$$

By implementing these two improvements, the total saturation current density under equilibrium conditions $J_0(d)$ can be expressed as the sum of the radiative saturation current density $J_{\text{rad},0}(d)$ and the non-radiative saturation current density $J_{\text{nrad},0}(d)$ obtained via the internal quantum Q_i efficiency parameter as presented in Eq.(2.97).

$$J_0(d) = \frac{J_{\text{rad},0}(1 + (p_e - 1)Q_i)}{p_e Q_i} \quad (2.97)$$

Finally, the total current density is obtained using Eq.(2.88). In addition, by injecting the voltage dependent current density $J(V, d)$ in Eq.(2.87), the maximal efficiency is calculated for a given layer thickness d , at a temperature T and for an internal quantum efficiency value Q_i . This one is a function of the absorber materials

refractive index $n(E)$, absorption coefficient $\alpha(E)$ and reflectivity $R(E)$. As realised in chapter 4, these materials properties can be obtained through *ab initio* calculations as described in appendix A.

Through this chapter, we focused on the theoretical description of first perfect crystalline materials, emphasising the origin of the materials bandgap E_G as well as the semiconducting properties arising from this succession of allowed and forbidden energy states. Then, the focus was set on the relevance of defects on the materials properties and their applications. A specific description of the photovoltaic effect and on performances using a PN junction was performed. In the next chapter, we describe the density functional theory (DFT) as a tool to predict materials properties as well as defect formation energies. The latter is a key ingredient to understand the physical behaviour of material point defects and consequently how these ones will impact the performances of these materials in PV applications.

DEFECT FORMATION ENERGY USING *AB INITIO* CALCULATIONS

3

3.1 Density functional theory	76
3.1.1 Many-body Schrödinger equation	76
3.1.2 One-electron Hartree-Fock equations	81
3.1.3 One-electron theory: Density Functional Theory (DFT)	86
3.2 Numerical implementation	92
3.2.1 Electron wavefunction	92
3.2.2 Brillouin zone meshing	95
3.3 Defect formation energy	98
3.3.1 Supercell approach	98
3.3.2 Material phase diagram	101
3.3.3 Corrections terms	103

Within the framework of this thesis, we use the density functional theory to predict the optoelectrical properties as well as the defect formation energies in kesterite materials. The latter quantity provides key information concerning the physical behaviour of defects and, as a result, their impact on the material application efficiency. In order to present the formalism used to compute these energies, in this chapter, we first present a pedagogical approach to the density functional theory as well as to the numerical implementation and the associated assumptions made to allow achievable computational costs (memory and time). Finally, in the last section, we highlight the approach used to compute the defect formation energy, as well as the physical information that can be extracted from it. The reader acquainted with the density functional theory should focus on [section 3.3](#).

3.1 DENSITY FUNCTIONAL THEORY

In this section, we focus on the presentation of the Density Functional Theory (DFT) used to solve the solid-state matter system and characteristic quantities such as the ground state energy levels, the wavefunction, the electronic density of states, *etc.*. Starting from the many-body Schrödinger equation, we present the exponential amount of parameters involved when dealing with real materials and known as the exponential wall. This problematic induced by the complex electrons-ions system to be solved is gradually transform into a solvable problem as proposed by the density functional theory [94, 118].

1. First, the many-body Schrödinger equation describing the interaction between electrons and ions in condensed matter is built and the various contributions of the particle kinetic energies and the coulomb interactions are presented.
2. Secondly, the assumptions used to circumvent the exponential wall problem are presented: the clamped nuclei approximation, the independent electron approximation and, the mean field approximation. Then, the one-electron Hartree-Fock equations are described using the variational principle and the electron wavefunction is adjusted to represent the quantum nature of the electrons and their respect concerning the Pauli's principle.
3. Finally, the density functional theory is presented via the Hohenberg-Kohn theory and eventually, the Kohn-Sham equations.

Across this section, through the implementation of the described assumptions and considerations, we gradually present in boxes, the computational cost related to the resolution of the Schrödinger equation describing the solid-state system. The objective is to highlight the reduction of the problem complexity attributed to the decrease parameters number. Starting from a large value leading to, from the point of view of computation time and memory, an unsolvable system of equations. And, gradually overcoming the so-called exponential wall by reducing the system complexity and eventually reaching a numerically solvable problem.

3.1.1 Many-body Schrödinger equation

On the basis of the solution related to the specific many-body quantum system composed of electrons and ions, the physical properties of the material can be extracted and exploited. Theoretically, this problem can be solved using the Schrödinger equation (see Eq.(3.1)) which allows, based on a given wavefunction associated with a

specific quantum system and a given Hamiltonian operator \mathcal{H} describing the interactions acting on the particles forming the system, to compute the total energy of this system E_{tot} :

$$\mathcal{H} \Psi_{el-i}(\mathbf{r}_1, \dots, \mathbf{r}_N, \mathbf{R}_1, \dots, \mathbf{R}_M) = E_{\text{tot}} \Psi_{el-i}(\mathbf{r}_1, \dots, \mathbf{r}_N, \mathbf{R}_1, \dots, \mathbf{R}_M) \quad (3.1)$$

The system wavefunction $\Psi_{el-i}(\mathbf{r}_1, \dots, \mathbf{r}_N, \mathbf{R}_1, \dots, \mathbf{R}_M)$ contains all the information regarding the quantum system consisting of an arrangement of electrons and ions with respective positions \mathbf{r}_i and \mathbf{R}_I . To solve this equation and obtain the system energy, one must determine the Hamiltonian operator \mathcal{H} , which will be applied onto the wavefunction. On top of that, on the basis of the nature of the particles under study, some requirements have to be fulfilled concerning the expression of the wavefunction.

First, we determine the form of the Hamiltonian \mathcal{H} . In solid-state matter, the contributions to the total energy are of two kinds:

1. Electrostatic coulomb interactions between charged particles.
2. Kinetic contributions related to the motion of the particles.

Consequently, through the action of the Hamiltonian on the wavefunction, five elements contribute to the total energy E_{tot} [92, 118].

$$\begin{aligned} \mathcal{H} = & - \sum_{i=1}^N \frac{\hbar^2}{2m_e} \nabla_i^2 \\ & - \sum_{I=1}^M \frac{\hbar^2}{2M_I} \nabla_I^2 \\ & + \frac{1}{2} \sum_{I \neq J}^M \frac{Z_I Z_J e^2}{4\pi\epsilon_0} \frac{1}{|\mathbf{R}_I - \mathbf{R}_J|} \\ & - \sum_{i,I}^{N,M} \frac{Z_I e^2}{4\pi\epsilon_0} \frac{1}{|\mathbf{r}_i - \mathbf{R}_I|} \\ & + \frac{1}{2} \sum_{i \neq j}^N \frac{e^2}{4\pi\epsilon_0} \frac{1}{|\mathbf{r}_i - \mathbf{r}_j|} \end{aligned} \quad (3.2)$$

In Eq.(3.2) the first two terms correspond respectively to the kinetic energy of the electrons and the kinetic energy of the ions with respectively, a number N of electrons (with index i) and a number M of ions (with index I). The derivatives in the Laplace operator ∇^2 are applied on the coordinates of each particle in the system: $\mathbf{r}_1, \dots, \mathbf{r}_N, \mathbf{R}_1, \dots, \mathbf{R}_M$. The three last contributions to the Hamiltonian operator correspond to coulomb interactions between ions, between electrons and ions, and between electrons. The former models the coulombic repulsions between positively

charged ions with a charge $Z_I e$ and $Z_J e$, respectively, at positions \mathbf{R}_I and \mathbf{R}_J . Z represents the atomic number. By taking into account all of these contributions to the Hamiltonian of the quantum system, the **many-body Schrödinger equation** (*cf.* Eq.(3.1)) can be written as such:

$$\left[-\sum_{i=1}^N \frac{\hbar^2}{2m_e} \nabla_i^2 - \sum_{I=1}^M \frac{\hbar^2}{2M_I} \nabla_I^2 + \frac{1}{2} \sum_{I \neq J}^M \frac{Z_I Z_J e^2}{4\pi\epsilon_0} \frac{1}{|\mathbf{R}_I - \mathbf{R}_J|} - \sum_{i,I}^{N,M} \frac{Z_I e^2}{4\pi\epsilon_0} \frac{1}{|\mathbf{r}_i - \mathbf{R}_I|} + \frac{1}{2} \sum_{i \neq j}^N \frac{e^2}{4\pi\epsilon_0} \frac{1}{|\mathbf{r}_i - \mathbf{r}_j|} \right] \Psi_{el-i}(\mathbf{r}_1, \dots, \mathbf{r}_N, \mathbf{R}_1, \dots, \mathbf{R}_M) = E_{tot} \Psi_{el-i}(\mathbf{r}_1, \dots, \mathbf{r}_N, \mathbf{R}_1, \dots, \mathbf{R}_M) \quad (3.3)$$

All the information describing the physical behaviour of the condensed matter system under equilibrium are contained in this relation. The physical quantities involved are:

- \hbar , the reduced Planck constant.
- m_e , the electron mass.
- M_I , the nucleus mass expressed in atomic mass units (a.m.u.).
- Z_I , the elemental atomic number.
- ϵ_0 , the electrical permittivity of vacuum.
- e , the elementary charge.

All of these are physical constants and besides these ones, no empirical measurements are required to solve the problem. As a consequence, the resolution of this equation is referred to as a **first-principles approach**. Equation (3.3) can also be expressed using a more convenient system unit, which is the Hartree energy¹ Ha (the development of this energy unit is presented in appendix A) as presented in Eq.(3.4). In this expression, the only external parameters needed are the atomic numbers Z and the atomic masses M .

¹One Hartree is equal to the potential energy of an immobile hydrogen atom $E_{\text{Ha}} = \frac{e^2}{4\pi\epsilon_0 a_0} = 27.21$ eV, with a_0 the Bohr radius (the characteristic distance between the electron and the proton in the classic hydrogen model).

$$\left[-\sum_{i=1}^N \frac{\nabla_i^2}{2} - \sum_{I=1}^M \frac{\nabla_I^2}{2M_I} + \frac{1}{2} \sum_{I \neq J}^M \frac{Z_I Z_J}{|\mathbf{R}_I - \mathbf{R}_J|} - \sum_{i,I}^{N,M} \frac{Z_I}{|\mathbf{r}_i - \mathbf{R}_I|} + \frac{1}{2} \sum_{i \neq j}^N \frac{1}{|\mathbf{r}_i - \mathbf{r}_j|} \right] \Psi_{el-i}(\mathbf{r}_1, \dots, \mathbf{r}_N, \mathbf{R}_1, \dots, \mathbf{R}_M) = E_{tot} \Psi_{el-i}(\mathbf{r}_1, \dots, \mathbf{r}_N, \mathbf{R}_1, \dots, \mathbf{R}_M) \quad (3.4)$$

I. Computational cost and approximations at this stage

Considering 2 Si atoms ($M = 2$) with 4 valence electrons each ($N = 8$):

- Number of parameters $30 = (2 + 8) \times 3$ (3 space-coordinates per electron and ion).
- One $3(N + M)$ -dimension Schrödinger equation coupling electron and ion positions.
- $\#_{grid}^{N+M} \sim 10^{30}$ complex numbers required to describe a quantum state $\Psi_{el-i}(\mathbf{r}_1, \dots, \mathbf{r}_8, \mathbf{R}_1, \mathbf{R}_2)$ for a number of points in the grid $\#_{grid} = 10^3$ [94].

Considerations and assumptions : None.

In the following, we will use the terms **action of the Hamiltonian** to express the term-by-term application of the Hamiltonian \mathcal{H} on the many-body wavefunction. As can be observed in Eq.(3.4), the last three terms correspond to sums over the ionic positions, the ionic and the electron positions, and finally over the electron positions between themselves. These last terms are consequently the limiting factors of the problem. **Considering solid-state materials**, an approximation that could be applied to simplify our problem is to consider the ions fixed to their positions \mathbf{R}_I and to focus on the resolution of a many-body quantum system consisting only of the electrons. This approximation is known as the **clamped nuclei approximation**². This approximation is reasonable considering the large ratio between the electron mass and the mass of the nucleus [91]. One can therefore consider the nuclei as immobile while investigating the electron behaviour. By applying this approximation, the ionic positions \mathbf{R}_I are now equal to constant values with several consequences.

1. By taking into account nuclei as clamped, the kinetic contributions of ions to the total energy can be removed. This approximation can be interpreted as the study of electrons in materials with ions so heavy that they cannot move and

²The clamped nuclei approximation is at the basis of the Born-Oppenheimer (BO) approximation that allows to separate the electron-ion wavefunction into an electronic and a nuclei component [91]. This BO approximation was used to describe the electron-phonon wavefunction associated to the study of recombination centre in Eq.(2.66).

thus with masses $M_I \rightarrow \infty$. The clamped nuclei approximation consequently deletes the second term of Eq.(3.4), meaning that

$$-\sum_{I=1}^M \frac{\nabla_I^2}{2M_I} \rightarrow 0 \quad (3.5)$$

2. Then, as a direct consequence of $\mathbf{R}_I = \text{cst}$, the ion-ion coulomb interactions are now equal to a constant. In addition, the energy is a relative quantity defined with respect to a given reference. As a consequence, we are free to withdraw this constant from this energy reference.

$$E_{el} = E_{tot} - \frac{1}{2} \sum_{I \neq J}^M \frac{Z_I Z_J}{|\mathbf{R}_I - \mathbf{R}_J|} \quad (3.6)$$

3. Furthermore, the fourth term of Eq.(3.4) related to the coulomb interactions between ions and electrons and expressed as a sum over both electron and ion positions can be expressed as a coulomb potential $V_n(\mathbf{r})$ induced by the fixed nuclei distribution and experienced by the electrons:

$$V_n(\mathbf{r}) = - \sum_I^M \frac{Z_I}{|\mathbf{r} - \mathbf{R}_I|} \quad (3.7)$$

4. Finally, the many-body wavefunction is now the representation of a many-body quantum system composed of N electrons experiencing a coulomb potential V_n generated by the fixed position lattice ions.

$$\Psi_{el-i}(\mathbf{r}_1, \dots, \mathbf{r}_N, \mathbf{R}_1, \dots, \mathbf{R}_M) \xrightarrow[\text{nuclei}]{\text{Clamped}} \Psi(\mathbf{r}_1, \dots, \mathbf{r}_N) \quad (3.8)$$

Focusing on solid-state materials and using this approximation, the Schrödinger equations expressed in Eq.(3.4) can be simplified as presented in Eq.(3.9). In the following sections, we deal with a problem of **electronic relaxation** corresponding to investigation of electrons evolving in a fixed crystal lattice of nuclei.

$$\underbrace{\left[- \sum_{i=1}^N \frac{\nabla_i^2}{2} + \sum_{i=1}^N V_n(\mathbf{r}_i) + \frac{1}{2} \sum_{i \neq j}^N \frac{1}{|\mathbf{r}_i - \mathbf{r}_j|} \right]}_{\mathcal{H}_{el}(\mathbf{r}_i)} \Psi(\mathbf{r}_1, \dots, \mathbf{r}_N) = E_{el} \Psi(\mathbf{r}_1, \dots, \mathbf{r}_N) \quad (3.9)$$

Using Eq.(3.9), one must admit that the problem we are dealing with is still unsolvable. Indeed, to solve Eq.(3.9), for each point of the grid, we would have to look at all the other points for the presence or not of an electron. The complexity of the problem increases exponentially with the number of electrons; this situation is known as an exponential wall.

II. Computational cost and approximations at this stage

Considering 2 Si atoms ($M = 2$) with 4 valence electrons each ($N = 8$):

- Number of parameters $24 = 3 \times 8$ (3 space-coordinates per electron).
- One $3N$ -dimension Schrödinger equation coupling electron positions.
- $\#_{grid}^N \sim 10^{24}$ complex numbers required to describe a quantum state $\Psi_{el-i}(\mathbf{r}_1, \dots, \mathbf{r}_8)$ for a number of points in the grid $\#_{grid} = 10^3$ [94].

Considerations and assumptions :

- Clamped nuclei approximation.

In order to again reduce the problem complexity, several approximations and methods are still required to solve this one. Part of the solution will be described in the two next sections, focusing on the transfer to the **one-electron theory**.

3.1.2 One-electron Hartree-Fock equations

As expressed in the previous section, the limiting factor is posed by the electron-electron interactions which leads to the power law concerning the problem complexity. One drastic simplification would be to assume that electrons do not interact with each other. Of course, this assumption of **independent electrons** is not correct. Still, we start willingly in an mistaken manner, and then we will improve our reasoning to obtain a simplified but correct version of the problem. By considering independent electrons, Eq.(3.9) can be reformulated by suppressing the electron-electron coulomb interaction:

$$\frac{1}{2} \sum_{i \neq j}^N \frac{1}{|\mathbf{r}_i - \mathbf{r}_j|} = 0 \quad (3.10)$$

Consequently, the many-body Schrödinger equation becomes:

$$\underbrace{\left[- \sum_{i=1}^N \frac{\nabla_i^2}{2} + \sum_i V_n(\mathbf{r}_i) \right]}_{\mathcal{H}_{el-indpt}(\mathbf{r}_i)} \Psi(\mathbf{r}_1, \dots, \mathbf{r}_N) = E_{el-indpt} \Psi(\mathbf{r}_1, \dots, \mathbf{r}_N) \quad (3.11)$$

This leads to an interesting result concerning the expression of the wavefunction that describes the quantum system. As the electrons are now independent, it means that the probability of finding electron 1 at position \mathbf{r}_1 , electron 2 at position \mathbf{r}_2 , and so on to electron N at position \mathbf{r}_N given by $|\Psi_{el}(\mathbf{r}_1, \dots, \mathbf{r}_N)|^2$ is equal to the product of the individual probabilities $|\phi_i(\mathbf{r}_i)|^2$ of finding electron i at position \mathbf{r}_i . As for two independent events, the probability of both events is the product of the individual probabilities. With $\phi_i(\mathbf{r}_i)$ the wavefunction associated with one electron. Consequently, the many-body electron wavefunction can be expressed the product of individual electron wavefunctions:

$$\Psi(\mathbf{r}_1, \dots, \mathbf{r}_N) = \phi_1(\mathbf{r}_1)\dots\phi_N(\mathbf{r}_N), \quad (3.12)$$

and, the many-body quantum system could be solved as a sum over single-electron Schrödinger equations:

$$\underbrace{\left[\sum_i^N \left[-\frac{\nabla_i^2}{2} + V_n(\mathbf{r}_i) \right] \right]}_{\mathcal{H}_{el-indpt}(\mathbf{r}_i)} \underbrace{\phi_1(\mathbf{r}_1)\dots\phi_N(\mathbf{r}_N)}_{\Psi(\mathbf{r}_1, \dots, \mathbf{r}_N)} = \underbrace{\left[\sum_i^N \epsilon'_i \right]}_{E_{el-indpt}} \underbrace{\phi_1(\mathbf{r}_1)\dots\phi_N(\mathbf{r}_N)}_{\Psi(\mathbf{r}_1, \dots, \mathbf{r}_N)}, \quad (3.13)$$

with ϵ'_i the solutions of the single electron Schrödinger equations for the wavefunctions associated with the N electrons of the quantum system. If we choose the label from 1 to N , from the lowest to the highest energy state, the wavefunction leads to the following eigenvalues: $\epsilon'_1 < \epsilon'_2 < \dots < \epsilon'_N$, the lowest energy configuration would be obtained by first filling in the lowest energy eigenstates of the system:

$$E_{el-indpt} = \epsilon'_1 + \dots + \epsilon'_N \quad (3.14)$$

However, considering the study of the system under this **independent electrons approximation**, two crucial ingredients are still missing to accurately represent the electron behaviour:

1. The electron interactions between themselves cannot be ignored. This error will be partially corrected by the **mean field approximation** and completely by the **Hartree-Fock theory**.
2. Electrons are **fermions**. Consequently, due to their natural behaviour, they obey the Pauli's principle, which states that two electrons in a same system cannot be in the same state. Taking this into account, the many-body wavefunction that describes these electrons cannot simply be written as a product of the wavefunction associated with each electron as expressed in Eq.(3.12). This must fulfil the requirement that if one exchanges two electrons, the many-body wavefunction changes in sign. This will be done respecting the **exclusion principle** and by expressing the wavefunction as a **Slater determinant**.

First, as expressed earlier in this section, coulomb interactions between electrons cannot be ignored. However, their suppression allows us to delete the computationally expensive double sum over all electron positions and the notion of independent electrons is practical for expressing the electron wavefunction. One step to improve the actual model is to consider an average electrostatic potential, **the Hartree potential** $V_H(\mathbf{r})$, experienced by each electron and generated by all other electrons. This classical approach removes all features linked to quantum mechanics and focus on the description of the electron interactions through electrostatic considerations as expressed in Eq.(3.15).

$$V_H(\mathbf{r}) = \int \frac{n(\mathbf{r}')}{|\mathbf{r} - \mathbf{r}'|} d\mathbf{r}' \quad (3.15)$$

This approximation is known as the **mean field approximation** and this term can now be added to the Schrödinger equation expressed in Eq.(3.13).

$$\sum_{i=1}^N \left[-\frac{\nabla_i^2}{2} + V_n(\mathbf{r}_i) + V_H(\mathbf{r}_i) \right] \underbrace{\phi_1(\mathbf{r}_1) \dots \phi_N(\mathbf{r}_N)}_{\Psi(\mathbf{r}_1, \dots, \mathbf{r}_N)} \simeq E_{el} \underbrace{\phi_1(\mathbf{r}_1) \dots \phi_N(\mathbf{r}_N)}_{\Psi(\mathbf{r}_1, \dots, \mathbf{r}_N)} \quad (3.16)$$

Moreover considering only single-electron wavefunction, the single-electron Schrödinger equation can be expressed as presented in Eq.(3.17). Using this independent electron approximations allow to move from one $3N$ -dimension Schrödinger equation (see Eq.(3.9)) to N 3-dimension Schrödinger equations (see Eq.(3.17)).

$$\left[-\frac{\nabla_i^2}{2} + V_n(\mathbf{r}_i) + V_H(\mathbf{r}_i) \right] \phi_i(\mathbf{r}_i) \simeq \epsilon_i \phi_i(\mathbf{r}_i) \quad (3.17)$$

Note that Eqs.(3.16) and (3.17) do not show a rigorous equality between the sides of the equation. In these relations, we reintroduce the total energy of the quantum system E_{el} (and $E_{el} = \epsilon_1 + \dots + \epsilon_N$). However, the Hamiltonian \mathcal{H} on the left side of Eqs. (3.16) and (3.17) does not yet contain a complete description of the electron-electron interaction term (only the mean field interaction term is considered here). To be accurate enough, we also need to take into account the nature of the particles we are dealing with and the resulting interaction. As expressed earlier, electrons are fermions and consequently obey the exclusion principle which states that two electrons cannot occupy the same quantum state. In the following part of this section we will express the many-body wavefunction associated with the system to fulfil the requirements of the exclusion principle. And, finally, we will complete the Hamiltonian to obtain a correct description of the system by taking into account this quantum behaviour of the electrons³.

³In a intuitive way, one can see this interaction as a repulsion between particle that would want to be in the same state.

First, in order to respect Pauli's principle stating that two fermions (particles with half-integer spin, in this case electrons with $S = \pm 1/2$) cannot be in the same quantum state. The wavefunction has to change in sign if two particles are exchanged (in position or in spin). For example, in this case of a 2 electron system ($N = 2$), one can write:

$$\Psi(\mathbf{r}_1, \mathbf{r}_2) = \frac{1}{\sqrt{2}}[\phi_1(\mathbf{r}_1)\phi_2(\mathbf{r}_2) - \phi_1(\mathbf{r}_2)\phi_2(\mathbf{r}_1)] = -\Psi(\mathbf{r}_2, \mathbf{r}_1) \quad (3.18)$$

For N electrons, this formulation of the many-body wavefunction can be expressed as a determinant known as the **Slater determinant**:

$$\Psi(\mathbf{r}_1, \dots, \mathbf{r}_N) = \frac{1}{\sqrt{N!}} \begin{vmatrix} \phi_1(\mathbf{r}_1) & \cdots & \phi_1(\mathbf{r}_N) \\ \vdots & \ddots & \vdots \\ \phi_N(\mathbf{r}_1) & \cdots & \phi_N(\mathbf{r}_N) \end{vmatrix} \quad (3.19)$$

Let us now consider this many-body wavefunction written as a Slater determinant and respecting Pauli's principle as the wavefunction associated to the system in its lowest energy state. This last point will be of importance for the variational principle to come as the wavefunction $\Psi(\mathbf{r}_1, \dots, \mathbf{r}_N)$ considered is now the **wavefunction associated to the ground state** of the system under study.

Finally, in order to take into account the quantum nature of the particles under consideration in the electron-electron interaction an additional term has to complete the Hamiltonian $\mathcal{H}_{\uparrow\downarrow}$ in complement to the Hartree potential $V_H(\mathbf{r})$. Assuming $\Psi(\mathbf{r}_1, \dots, \mathbf{r}_N)$ as the ground state wavefunction, if one minimises the energy E_{el} with respect to variations of the single-electron wavefunctions $\phi_i(\mathbf{r}_i)$ in Eq.(3.19) and by requiring that these functions are orthogonal (electron cannot occupy multiple state at once), the following relations can be expressed:

$$\frac{\delta E_{el}}{\delta \phi_i^*} = 0 \quad (3.20)$$

$$\langle \phi_i | \phi_j \rangle = \delta_{i,j} \quad (3.21)$$

From the variational principle expressed in Eq.(3.20), an additional potential $V_X(\mathbf{r}, \mathbf{r}')$ is expressed as:

$$V_X(\mathbf{r}, \mathbf{r}') = - \sum_j^N \frac{\phi_j^*(\mathbf{r}')\phi_j(\mathbf{r})}{|\mathbf{r} - \mathbf{r}'|} \quad (3.22)$$

This expression is a result of the energy minimisation with respect to the single-electron wavefunction in the Slater determinant (*cfr.* Eq.(3.20)). We obtain from the many-body Schrödinger equation (*cfr.* Eq.(3.9)), the **Hartree-Fock equations**:

$$\left[\frac{-\nabla^2}{2} + V_n(\mathbf{r}) + V_H(\mathbf{r}) \right] \phi_i(\mathbf{r}) + \int V_X(\mathbf{r}, \mathbf{r}') \phi_i(\mathbf{r}') d\mathbf{r}' = \epsilon_{i,0} \phi_i(\mathbf{r}) \quad (3.23)$$

with:

$$\begin{aligned} n(\mathbf{r}) &= \sum_i^N |\phi_i(\mathbf{r})|^2 \\ V_n(\mathbf{r}) &= - \sum_I^M \frac{Z_I}{|\mathbf{r} - \mathbf{R}_I|} \\ V_H(\mathbf{r}) &= \int \frac{n(\mathbf{r}')}{|\mathbf{r} - \mathbf{r}'|} d\mathbf{r}' \\ \nabla^2 V_H(\mathbf{r}) &= -4\pi n(\mathbf{r}) \\ V_X(\mathbf{r}, \mathbf{r}') &= - \sum_j^N \frac{\phi_j^*(\mathbf{r}') \phi_j(\mathbf{r})}{|\mathbf{r} - \mathbf{r}'|} \end{aligned}$$

Equations 3.23 now give the ground state energy $\epsilon_{i,0}$ of the single-electron wavefunction $\phi_i(\mathbf{r})$ by combining the contribution of the kinetic energy of the electron, the ions-electron electrostatic interaction, the classical electron-electron electrostatic interaction, and finally, the "quantum interactions of electrons" through the expression of total wavefunction via the Slater determinant and the potential $V_X(\mathbf{r}, \mathbf{r}')$ known as **the Fock exchange potential** which can be seen as first approximation as Pauli's repulsion between electrons forbids two electrons to be in the same quantum state.

Using the Slater determinant and the additional potential $V_X(\mathbf{r}, \mathbf{r}')$, the quantum nature of the electrons is now taking into account. To summarise, in the first term of Eq.(3.23), one can find the application of the Laplace operator onto the single-electron wavefunction. Then, in the second term, we calculate the electrostatic energy generated by the interaction of the clamped ions and the electron under consideration. In the third term, the electrostatic energy generated by the interaction of the electron under consideration and all other electrons is calculated on the basis of an average electrostatic potential generated by every other electrons at given positions. Finally, in opposition to the Hartree energy, the last term V_X corresponds to the integration of a function that combines several single-electron wavefunctions at all coordinates. It is therefore not easy to compute. This final problem will be solved within the **density functional theory** which is, similarly as the Hartree-Fock equations, a one-electron theory but that allows, in contrast to the Hartree-Fock equations, to reduce the numerical cost in order to reach a solvable problem from a numerical point of view.

III. Computational cost and approximations at this stage

Considering 2 Si atoms ($M = 2$) with 4 valence electrons each ($N = 8$):

- Number of parameters 3 (3 space-coordinates per electron).
- N 3-dimension Schrödinger equations including the integration over an additional variable \mathbf{r}' .
- $\#_{grid}$ complex numbers required to describe a quantum state $\phi_i(\mathbf{r}_i)$ for a number of points in the grid $\#_{grid}$ equals to 10^3 [94].

Considerations and assumptions :

- Clamped nuclei approximation.
- "Independent" electron approximation and mean-field approximation resulting in N independent Schrödinger equations.
- Quantum nature of electrons (fermions) with respect to the exclusion principle added through the Fock-exchange potential $V_X(\mathbf{r}, \mathbf{r}')$.

3.1.3 One-electron theory: Density Functional Theory (DFT)

In this section, and on the basis of the Hartree-Fock theory established, we move to the construction of the Kohn-Sham equations. These equations, in the form of numerical implementations, provide a feasible and powerful way to study the properties of materials using classical and quantum considerations. Let us restart from Eq.(3.9). This equation describes a quantum system consisting of several electrons that interact with each other and experience an electrostatic potential generated by the ions.

The calculated total energy refers to the energy of the system consisting of the electrons in the materials. This energy can be expressed as:

$$E_{el} = \langle \Psi(\mathbf{r}_1, \dots, \mathbf{r}_N) | \mathcal{H}_{el} | \Psi(\mathbf{r}_1, \dots, \mathbf{r}_N) \rangle \quad (3.24)$$

Also, as previously stated, the electronic Hamiltonian \mathcal{H}_{el} does not depend on the materials under consideration. Of course, depending on the positions of the ions and on the chemical species in presence, $V_n(\mathbf{r}_i)$ will be different, but the Hamiltonian structure is the same for any studied material. Consequently, from Eq.(3.24), the energy of the quantum system is associated to the many-body wavefunction $\Psi(\mathbf{r}_1, \dots, \mathbf{r}_N)$, which describes the electrons of the material. The energy of the system is therefore a functional⁴ of the many-body wavefunction.

⁴Similarly to a function which takes a number (scalar) to give a number (scalar) as $f(x) = x^2$, a functional takes a function in argument and give a number as a result. An simple example of a

$$E_{el} = \mathcal{F}[\Psi(\mathbf{r}_1, \dots, \mathbf{r}_N)] \quad (3.25)$$

This is true for any quantum system, in excited states or in the ground state. However, **the heart of the density functional theory is that in opposition to any excited state, the ground state energy of the quantum system under study is a functional of the electronic density only.**

$$E_{el,0} = \mathcal{F}[n(\mathbf{r})] \quad (3.26)$$

This observation was realised by Hohenberg and Kohn in 1964 [119]. As a result, all that is needed to calculate the ground state energy is its electronic density $n(\mathbf{r}) = \sum_i |\phi_i(\mathbf{r})|^2$. This result reduces also a lot the computational cost as the electronic density is a scalar function depending only on three space parameters. Let us start by describing why the ground state energy of the quantum system is a functional of the electronic density only. The proof is based on three arguments, which can be represented as follows:

$$n(\mathbf{r}) \xrightarrow{(1)} V_n(\mathbf{r}) \xrightarrow{(2)} \Psi(\mathbf{r}_1, \dots, \mathbf{r}_N) \xrightarrow{(3)} E_{el,0}, \quad (3.27)$$

(1) **in the ground state**, the electronic density uniquely determines the external potential of the nuclei $V_n(\mathbf{r})$. (2) **in any quantum state**, the external potential $V_n(\mathbf{r})$ uniquely determines the many-body wavefunction $\Psi(\mathbf{r}_1, \dots, \mathbf{r}_N)$. And, (3) in any quantum system, the total wavefunction uniquely determines the total energy of the system E_{el} . This theorem gives as a result that the total energy of the system in the ground state $E_{el,0}$ is functional of the electronic density.

In the previous section, we saw that it was possible to use single-electron wavefunctions to form a Slater determinant that describes the many-body wavefunction of the quantum system. Then, we establish a set of equations known as the Hartree-Fock equations, which are single-electron Schrödinger equations where the Hamiltonian is written as the sum of an Hamiltonian describing independent electrons in condensed matter and an additional term known as the Fock-exchange potential $V_X(\mathbf{r}, \mathbf{r}')$ describing the quantum interactions between electrons. The Kohn-Sham equations are built with a similar approach. We will express the ground state energy $E_{el,0}$ as the contribution of the independent electron energy within the mean-field approximation $E_{el-mf,0}$ plus an extra term accounting for all remaining interactions between electrons (similarly to $V_X(\mathbf{r}, \mathbf{r}')$). This extra term will be known as the **exchange and correlation energy** $E_{xc,0}$, energy that has to be determined.

$$\mathcal{F}[n(\mathbf{r})] = E_{el,0} = E_{el-mf,0} + E_{xc,0} \quad (3.28)$$

functional could be: $\mathcal{F}[g] = \int_0^8 g(x)dx$.

From Eq.(3.16) and including this extra term, we find the following eigenvalue equation:

$$\sum_i^N \left[-\frac{\nabla_i^2}{2} + V_n(\mathbf{r}_i) + V_H(\mathbf{r}_i) \right] \Psi(\mathbf{r}_1, \dots, \mathbf{r}_N) = [E_{el,0} - E_{xc,0}] \Psi(\mathbf{r}_1, \dots, \mathbf{r}_N) \quad (3.29)$$

$$\Leftrightarrow \int \Psi^*(\mathbf{r}_1, \dots, \mathbf{r}_N) \left[\sum_i^N \left[-\frac{\nabla_i^2}{2} + V_n(\mathbf{r}_i) + V_H(\mathbf{r}_i) \right] \right] \Psi(\mathbf{r}_1, \dots, \mathbf{r}_N) d\mathbf{r}_1 \dots d\mathbf{r}_N = \int \Psi^*(\mathbf{r}_1, \dots, \mathbf{r}_N) [E_{el,0} - E_{xc,0}] \Psi(\mathbf{r}_1, \dots, \mathbf{r}_N) d\mathbf{r}_1 \dots d\mathbf{r}_N \quad (3.30)$$

And, Eq.(3.30) can be rewritten using the electronic density:

$$n(\mathbf{r}) = N \int \Psi^*(\mathbf{r}_1, \dots, \mathbf{r}_N) \Psi(\mathbf{r}_1, \dots, \mathbf{r}_N) d\mathbf{r}_2 \dots d\mathbf{r}_N, \quad (3.31)$$

Then, in the independent electron approximation, this many-body wavefunction $\Psi(\mathbf{r}_1, \dots, \mathbf{r}_N)$ can be written as a product of single-electron wavefunctions. Furthermore, by using single-electron wavefunctions from which the electronic density is expressed as $n(\mathbf{r}) = \sum_i^N |\phi_i(\mathbf{r})|^2$, Eq.(3.30) becomes:

$$\underbrace{-\sum_i^N \int d\mathbf{r} \phi_i^*(\mathbf{r}) \frac{\nabla^2}{2} \phi_i(\mathbf{r}) + \int d\mathbf{r} n(\mathbf{r}) V_n(\mathbf{r}) + \int \int d\mathbf{r} d\mathbf{r}' \frac{n(\mathbf{r})n(\mathbf{r}')}{|\mathbf{r} - \mathbf{r}'|} + E_{xc,0}[n]}_{\text{Total energy in the mean-field approximation of independent electrons } (E_{el-mf,0})} = E_{el,0} \quad (3.32)$$

Based on Eq.(3.32), we aim at obtaining the ground state total energy knowing the electronic density $n(\mathbf{r})$. We do not know how to calculate the terms of the independent electrons energy contribution but we do not know the form of the extra term which is the exchange-correlation energy. We find ourselves in the same configuration as with the construction of the Hartree-Fock equations in the previous section. We can therefore use the same solution offered by the variational principle. Using the **Hohenberg-Kohn properties** which states that the electronic density in the ground state n_0 is the electronic density that minimises the total energy $E_{el,0} = \mathcal{F}[n_0]$:

$$\left. \frac{\delta \mathcal{F}[n]}{\delta n} \right|_{n_0} = 0 \quad (3.33)$$

, one can determine the exchange correlation potential using the variational principle. The question is now: "What is the expression of this functional?" Well, we still do not know. But we know some approximations of it. A first approximation of the expression of this functional was provided by Kohn and Sham in 1965 resulting

in the **Kohn-Sham equations** [120]. Finally, the combination of the Hohenberg-Kohn variational principle and the Kohn and Sham approximation of the exchange-correlation functional results in the **Kohn-Sham equations**:

$$\left[\frac{-\nabla^2}{2} + V_n(\mathbf{r}) + V_H(\mathbf{r}) + V_{xc}(\mathbf{r}) \right] \phi_i(\mathbf{r}) = \epsilon_i \phi_i(\mathbf{r}) \quad (3.34)$$

$$V_{xc}(\mathbf{r}) = \left. \frac{\delta E_{xc}[n]}{\delta n} \right|_{n_0(\mathbf{r})} \quad (3.35)$$

IV. Computational cost and approximations at this stage

Considering 2 Si atoms ($M = 2$) with 4 valence electrons each ($N = 8$):

- Number of parameters 3 (3 space-coordinates per electron).
- N 3-dimension Schrödinger equations.
- $\#_{grid}$ complex numbers required to describe a quantum state $\phi_i(\mathbf{r}_i)$ for a number of points in the grid $\#_{grid}$ equals to 10^3 [94].

Considerations and assumptions :

- Clamped nuclei approximation.
- "Independent" electron approximation and mean-field approximation resulting in N independent Schrödinger equations.
- Quantum nature of electrons (fermions) with respect to the exclusion principle added through the exchange correlation potential obtained for the energy of the ground state through the Hohenberg-Kohn variational principle : $V_{xc}(\mathbf{r}) = \left. \frac{\delta E_{xc}[n]}{\delta n} \right|_{n(\mathbf{r})}$

Using Eq.(3.34) for each independent electron wavefunction, the ground state energy of the system under consideration can be computed. However, to obtain the exact ground state energy, we have to know the exact form of the exchange-correlation energy functional $E_{xc}[n(\mathbf{r})]$. The practical implementation of DFT relies on obtaining an approximation of this functional that is not too far from the exact solution for limited time and computer costs [120]. Several approximations of this exchange-correlation term were "designed" such as the local density approximation (LDA), the generalised gradient approximation (GGA), the META-GGA: SCAN, MBJ or the hybrid exchange-correlation functional: HSE03, HSE06. For a given functional, the objective will consequently to minimise the electron system total energy E_{el} with

respect to the computed electronic density $n(\mathbf{r}) = \sum_i^N |\phi_i(\mathbf{r})|^2$. Furthermore, when reaching a given minimisation criterion, we assume that the wavefunction and the total energy obtained corresponds to the system ground state.

Using the N 3-dimensional Kohn-Sham equations, to solve our N electron problem, one can express the self-consistent energy minimisation whose starting point is the atomic positions. Indeed, to know the total potential V_{tot} one must know the electronic density n that is computed based on the electronic wavefunctions ϕ_i , which are the solutions of our problem. As a result and as presented in **Fig.3.1**, the self-consistent calculation starts with the atomic positions \mathbf{R}_I and an initial electronic density $n_{\text{init}}(\mathbf{r})$ (for example, the electronic density of the isolated atom). From the atomic positions, the electric potential V_n can be deduced, while the Hartree and exchange correlation potentials are determined based on the initial guess of the electronic density and using a given exchange correlation functional. From there, solutions of the Kohn-Sham equations can be computed, giving a new electronic density. Finally, based on a minimisation criterion, one decides to reiterate the calculation or to accept a sufficient convergence of it, meaning that the obtained electron density corresponds to the ground state one and the resulting energy through the Kohn-Sham equations is the ground state energy.

A last remark regarding the DFT which is of particular relevance to study the absorber layer for PV applications is related to the bandgap problem [94]. The material bandgap energy is defined as the energy difference between the bottom of the conduction band E_C and the top of the valence band E_V :

$$E_G = E_C - E_V \simeq \underbrace{E_{N+1} - E_N}_{\text{Electron affinity} \simeq E_C} - \underbrace{E_N - E_{N-1}}_{\text{Work function} \simeq E_V} \quad (3.36)$$

As highlighted in Eq.(3.36), this bandgap energy can also be expressed in terms of system total energy $E_{N,N-1,N+1}$ with respectively $N, N+1$ or $N-1$ electrons. And, the \simeq between the two sides of the equations comes from the fact that upon the addition or the removal an electron, the electronic density will be modified n and as a result the Kohn-Sham equations Hamiltonian will change. However, in a solid-state material, the induced electronic density modification is very small $\Delta n \sim 10^{-20}n$ [94]. It is possible to show that, the difference between the DFT predicted bandgap and the experimental bandgap energy is a function of the exchange correlation functional. However, this functional is not exactly known and therefore the resulting bandgap energy does not match with the exact experimental bandgap value. The choice of the exchange-correlation functional is therefore of particular importance for material calculation. Different strategies has been employed to approach the right bandgap value.

In the next section, we discuss some numerical implementations used to reduce the size of the wavefunction as well as the number of \mathbf{k} -points values for which the Kohn-Sham equations has to be solved to obtain the system ground state energy.

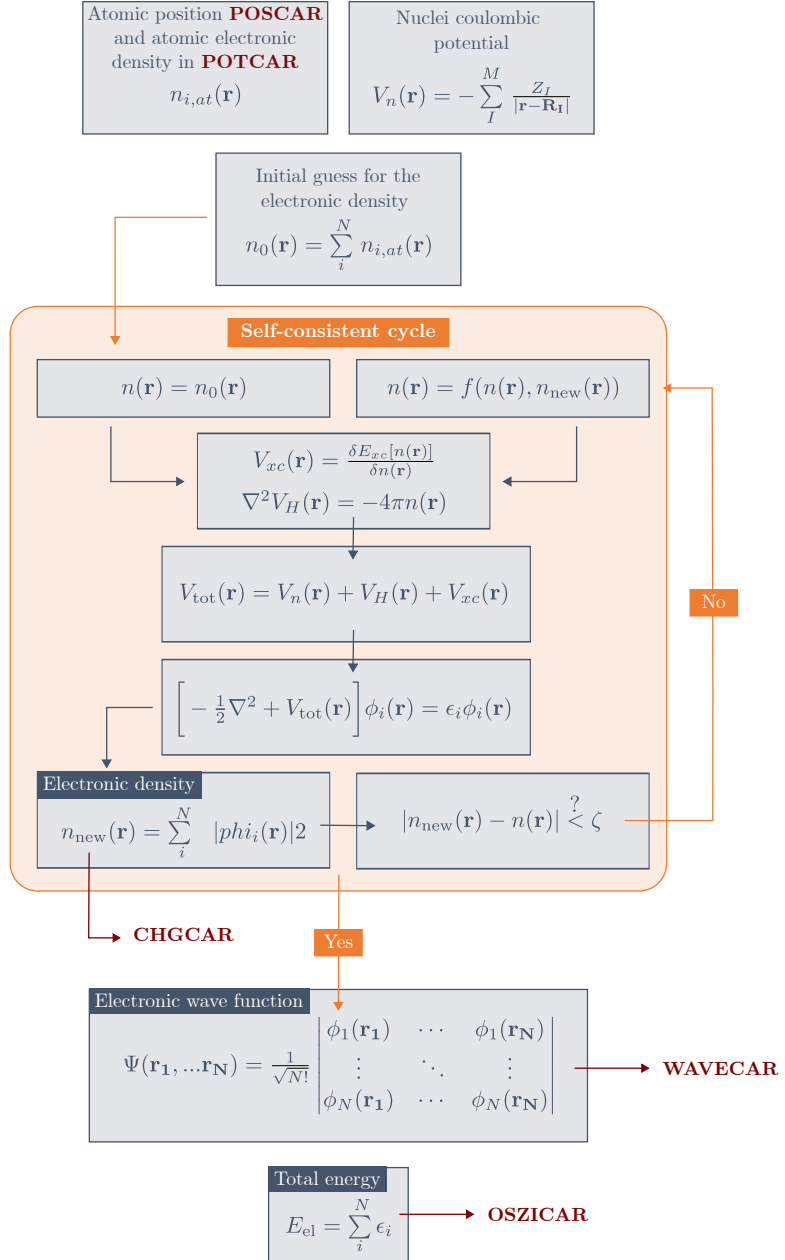


Figure 3.1: Self-consistent energy minimisation method use to solve the Kohn-Sham equations (see Eqs.(3.34) and (3.35)). The results presented in this thesis are obtained based on these equations implemented in the VASP software. To provide a complete description, in maroon, we highlight the name of the initial VASP files containing the respective elements (wavefunction, density of states, *etc.*) presented in this self-consistent cycle illustration. A description of these files can be found in appendix A.

3.2 NUMERICAL IMPLEMENTATION

The concepts presented in this section are related to the discretisation and the reduction of the wavefunction size that allows the resolution of the Kohn-Sham equations for a given discrete number of \mathbf{k} -point restricted to the first Brillouin zone (BZ).

1. Bloch's theorem and the representation of the one-electron wavefunction as a plane wave are again introduced and the basis set of the Fourier series is fixed by the cutoff energy. **This step implies the convergence of the cutoff energy E_{cutoff} .**
2. The projector-augmented wave method (PAW) used to compute only the electronic density involved in the chemical bonding between the atoms in the crystal is described. This approximation, in addition to the frozen core approximation, allows the reduction of the calculation size by differentiating valence electrons (included in the calculations) and core electrons (frozen during the calculations) and additionally, the simplification of the valence electron wavefunction via the use of **pseudopotentials**.
3. Finally, the first BZ meshing is realised using the symmetry operations of the crystal under consideration to obtain the irreducible \mathbf{k} -points. For each irreducible \mathbf{k} -point, the electron wavefunction has to be computed by solving the Kohn-Sham equations. **This step implies the convergence over the number of \mathbf{k} -point meshing.**

3.2.1 Electron wavefunction

Now that we have expressed the Kohn-Sham equations (Eqs.(3.34) and (3.35)) allowing us to compute the energy of interacting electrons evolving in an energetic landscape generated by the ions of the material, we develop the one-electron wavefunctions associated to this system. Injecting these one-electron wavefunctions in the Kohn-Sham equations, one can compute the ground state energy of the material.

As it was presented in a chapter 2 (see section 2.1.2), the wavefunction, solution of the Kohn-Sham equation, can be expressed as plane waves known as Bloch states being the results of the Bloch theorem (the solution of the Schrödinger equation including a periodic potential (*i.e.* the lattice) can be expressed as a plane wave modulated by a periodic function $u_{n,\mathbf{k}}(\mathbf{r})$ with the same periodicity as the potential):

$$\Psi_{n,\mathbf{k}}(\mathbf{r}) = u_{n,\mathbf{k}}(\mathbf{r})e^{i\mathbf{k}\mathbf{r}}, \quad (3.37)$$

that is obtained as a result of the periodicity of the coulomb potential generated by the ions of the lattice. The Fourier expansion is done for a given wave vector \mathbf{k} within the first BZ then the other Fourier components run over $\mathbf{k} + \mathbf{G}$ wave vectors (see Eq.(3.38)).

$$\Psi_{n,\mathbf{k}}(\mathbf{r}) = \sum_{\mathbf{G}} C_{\mathbf{G},n,\mathbf{k}} e^{i(\mathbf{G}+\mathbf{k})\mathbf{r}} \quad (3.38)$$

And, as a result, there is an infinite number of terms in this expansion. Using plane waves as the basis set, it is convenient for DFT calculations to limit the number of Fourier coefficients used to describe the wavefunction to a given momentum value $\mathbf{k} + \mathbf{G}$ corresponding to an energy called the cutoff energy E_{cutoff} as expressed in Eq.(3.39). Doing so, we restrict the size of the Fourier expansion to a finite value, enabling its numerical treatment.

$$\frac{\hbar^2}{2m_e} |\mathbf{G} + \mathbf{k}|^2 < E_{\text{cutoff}} \quad (3.39)$$

In order to preserve the desired accuracy, a **convergence over the cutoff energy** has to be performed with respect to the system ground state energy. Of course, as illustrated in **Fig.3.2**, the larger the cutoff energy, the higher the frequency contribution to the description of the wavefunction and the more accurate the final wave form.

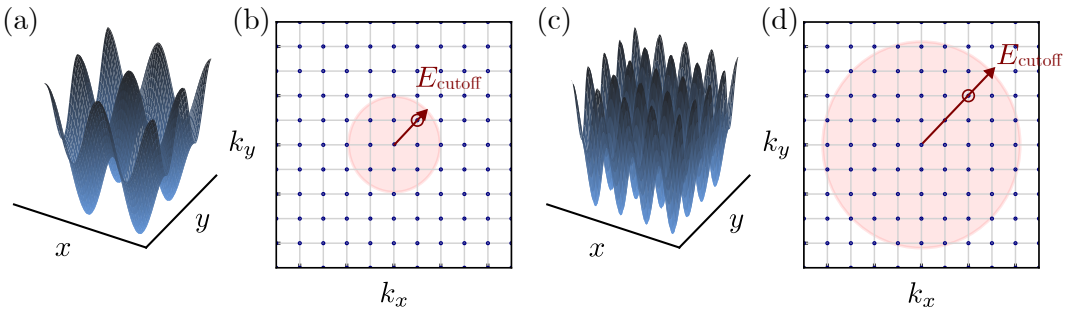


Figure 3.2: Schematic representation of the possible complexity of the electron wavefunction development in Fourier series as a function of the selected cutoff energy. As represented, the increase of the cutoff energy from panels (a,b) to panels (c,d) allows for a more refine representation of the electron wavefunction.

Then, it is still possible to go further to reduce the size of the calculation without losing too much accuracy. Except for simple atomic structures such as H and Li, the rapid fluctuations of the orbitals near the nucleus leading to the strongly spatially localised states required a large number of plane waves (large E_{cutoff}) to be correctly represented, which is above the usual computational limit [94]. To make the problem

solvable for crystal structure between 10 to 100 of atoms with heavier electronic structures, a common solution is to use two additional approximations:

1. **The frozen core approximation.** This approximation relies on the fact that core electrons are not strongly involved in the chemical bonding between atoms. These electrons are not relevant for bonding mechanisms within the crystal. As a result, only a given number of valence electrons will be considered [94].
2. **The projector-augmented-wave (PAW) method** presents the use of a pseudopotential instead of the exact potential. As illustrated by $\Psi(r)$ in **Fig.3.3(a)**, the valence electron wavefunctions present some rapid oscillations (mostly near the nucleus) that are numerically expensive if represented correctly in the electron wavefunction expansion (see Eq.(3.38)). Using the PAW method, we will efficiently circumvent this limitation.

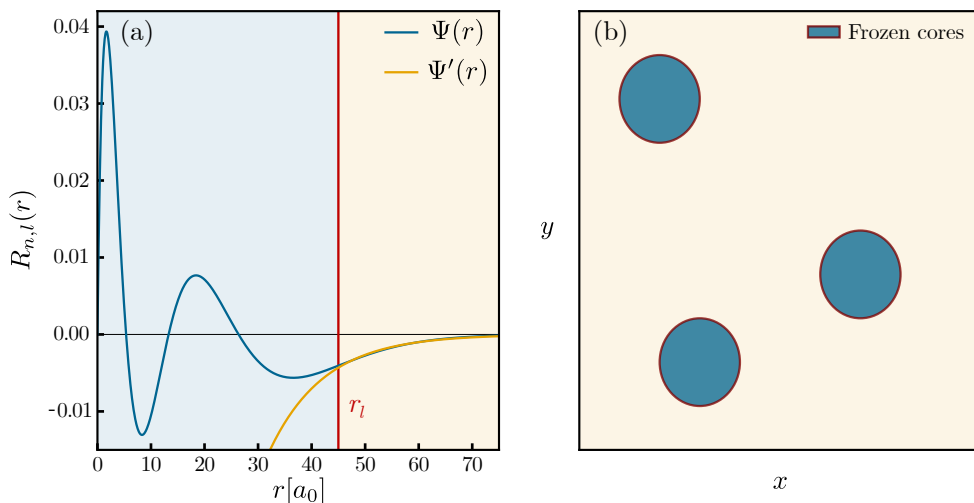


Figure 3.3: Illustration of the projector augmented wave method presented in (a) a radial view and (b) a top view. The electron wavefunction $\Psi(r)$ is presented along with the pseudo-wavefunction $\Psi'(r)$. In addition, the radius criterion r_l is highlighted.

The idea behind the PAW method is to use for valence electrons a pseudopotential that lead to a pseudo-wavefunction $\Psi'(r)$ that exactly matches the true wavefunction $\Psi(r)$ until a given radius r_l from the nucleus as presented in **Fig.3.3**. The true electron orbital is therefore represented in two different basis:

- the pseudo-orbital represented in plane waves. This pseudo-part $\Psi'(r)$ is computed for each element with the same exchange-correlation functional as the one used in the calculation. This is the part shown in orange in **Figs.3.3(a)** and (b).
- within a sphere around nucleus, the remaining part is represented in a radial way allowing to maintain the nodal features close to the nucleus but without

representing this one using plane waves. This is the part represented in blue in **Figs.3.3(a)** and **(b)**.

Doing so, we reduce (i) the number of electrons involved in the calculation and (ii), for valence electrons, we reduce the size of the previously discretised wavefunction via a pseudopotential and the PAW method. In the next section, as a last ease for the calculation, we will limit the number of \mathbf{k} -points on which the calculation is performed.

3.2.2 Brillouin zone meshing

From the Kohn-sham equation expressed in Eqs.(3.34) and (3.35) and the development of the valence electron wavefunction converged using a given cutoff energy E_{cutoff} , the solid-state system can now be solved for different \mathbf{k} -points. As presented in the previous chapter, there exist as many wave vectors in the first BZ as there are primitive cells within the considered crystal. As a result, if one considers a macroscopic material, there exists a huge number of independent wave vectors \mathbf{k} . For the sake of computational cost, it is therefore required to restrict the calculation to irreducible lattice wave vectors \mathbf{k}_{ir} obtained using a mesh of the first BZ and the lattice symmetry of the crystal considered.

To compute the iterative resolution of the Kohn-Sham equation using the Bloch wavefunctions $\Psi_{n,\mathbf{k}}(\mathbf{r})$ one needs to obtain the charge density:

$$n(\mathbf{r}) = \frac{1}{\Omega_{\text{BZ}}} \sum_n \int_{\text{BZ}} |\Psi_{n,\mathbf{k}}(\mathbf{r})|^2 d\mathbf{k} \quad (3.40)$$

Numerically, this charge density is reduced to a discrete summation over a few reciprocal lattice wave vectors $\mathbf{k}_{\text{ir},i}$:

$$n(\mathbf{r}) = \frac{1}{\Omega_{\text{BZ}}} \sum_n \sum_i |\Psi_{n,\mathbf{k}_{\text{ir},i}}(\mathbf{r})|^2 d\mathbf{k}_{\text{ir}} \quad (3.41)$$

Moreover, to obtain a discrete number of \mathbf{k} for the calculation of the wavefunctions, a meshing of the first Brillouin zone is carried out. For example, regular sampling can be performed, such as

$$\{\mathbf{k}_i\} = \sum_{j=i}^3 \frac{n_j + s_j}{N_j} \mathbf{b}_j, \quad (3.42)$$

for $n_j \in [0, N_j]$ with N_j being the sampling number in each reciprocal space direction and s_j representing the possible mesh shift.

Then, following this sampling, an additional reduction of the number of reciprocal vectors \mathbf{k} can be made using the symmetries of the crystal under study, leading

to $\mathbf{k}_{i,j}$. Doing so if, for example, by symmetry, an equivalent lattice vector is represented multiple times, the calculations will therefore be performed only once and a weight will be attributed to this specific point according to its multiplicity. The wave vectors of the sampled reciprocal lattice obtained are called irreducible wave vectors. Furthermore, a convergence of the 1st BZ meshing (see Eq.(3.42)) has to be performed with respect to the system ground state energy. Indeed, in practice, the number of subdivisions N_i used to set the number \mathbf{k} -points included in the calculation and representing the reciprocal primitive cell has to be converged to ensure a correct balance between the calculation costs (time and memory) and the accuracy of the results. This step corresponds to the **convergence over the \mathbf{k} -points**. Conveniently, the convergence of the cutoff energy and, the convergence over the 1st BZ \mathbf{k} -point meshing has to be realised iteratively to ensure the proper accuracy of the calculation.

Following these numerical implementations, we present in the next page a *summary* that encompassed the notions, approximations and principles described in the present chapter to (i) express the Kohn-Sham equations starting from the electrons many body Schrödinger equation, (ii) reduce the size of the one-electron wavefunctions as required by the numerical constraints along with respecting the electron quantum nature and (iii) reduce the number of \mathbf{k} -points onto which the calculation is realised based on the self-consistent cycle presented in **Fig.3.1**. In chapter 5, the presented kesterite material optoelectrical properties are computed on the basis of the developed density functional theory.

Then, in the next section, we present the supercell approach, methodology used to compute defect formation energies ΔH_F . As it will be described, ΔH_F is a key physical quantity for the understanding of the behaviour of point defects in crystalline materials. It is computed based on ground state energies as provided by the Kohn-Sham equations.

Summary

(i) From Schrödinger to Kohn-Sham

1. Many-body Schrödinger equation $\Psi_{el-i}(\mathbf{r}_1, \dots, \mathbf{r}_N, \mathbf{R}_1, \dots, \mathbf{R}_M)$
2. Clamped nuclei approximation $\Psi(\mathbf{r}_1, \dots, \mathbf{r}_N)$ and electronic hamiltonian \mathcal{H}_{el}
3. One-electron Hartree-Fock equations: mean field approximation $V_H(\mathbf{r})$ and single-electron wavefunction $\phi_i(\mathbf{r})$. Pauli exclusion principle through the construction of the Fock exchange potential $V_X(\mathbf{r}, \mathbf{r}')$ and the Slater determinant. Ground state wavefunction and variational principle.
4. Density functional theory (DFT) through the Hohenberg-Kohn theorem and the variational principle using the charge density: $E_{el,0} = \mathcal{F}[n(\mathbf{r})]$ and $V_{xc}(\mathbf{r}) = \left. \frac{\delta E_{xc}[n]}{\delta n} \right|_{n_0(\mathbf{r})}$ [119]. Finally, Kohn and Sham give a first approximation of the functional [120]. Need for the construction of a functional.
5. Self-consistent resolution of the Kohn-Sham equations.

(ii) Wavefunction Ψ

1. Expression of the electron wavefunction as a Slater determinant.
2. Discretisation and reduction of the wavefunction via a Fourier series development using a plane wave basis set following the Bloch theorem: **cutoff energy convergence**
3. Frozen core approximation considering only valence electrons in the calculation.
4. Projector-augmented-wave method (PAW) resulting in the use of pre-computed pseudopotential (with the same exchange-correlation functional) to describe the valence electron wavefunction close to the nuclei.

(iii) Numerical implementation: reciprocal space

1. Solution for specific \mathbf{k} -points in the 1st BZ: **k-point convergence**
2. Use of symmetry operation to reduce the problem in the first Brillouin zone.

3.3 DEFECT FORMATION ENERGY

In this final section, we develop the method used to compute the defect formation energy using the density functional theory. As the developed methodology is directly applied to the computation of kesterite defects presented in chapter 5, the description here below uses as example $\text{Cu}_2\text{ZnSnS}_4$. Of course, this one can be generalised for any material.

1. First, the physical meaning of the defect formation energy, including the description of its underlying components as well as the physical quantities that can be determined from ΔH_F are presented using the supercell approach. This first description leads to the necessity to quantify chemical potentials of the species involved in the crystal lattice or use as doping species.
2. Then, on the basis of the chemical potential requirements, the description of the material phase diagrams and their construction are presented
3. Finally, some correction terms are introduced and described.

3.3.1 Supercell approach

Beyond materials properties predictions, the first-principles approach is a powerful tool to understand the behaviour of defects in semiconductor compounds [121–125]. Within the density functional theory (DFT) formalism, in this work, the supercell approach is considered and the calculations are performed with a 64 atom supercell corresponding to an expansion of $2 \times 2 \times 2$ of the kesterite conventional cell as presented in **Fig.3.4** [121, 126]. The size of the computational box is assumed to be large enough to allow for full relaxation of the defect-induced elastic constraint over the supercell dimension. Consequently, we assume no mechanical stress as a result of the interaction between defects and their periodic repetitions produced by the applied periodic boundary conditions. In addition, the long-range coulomb interaction between charged defects is accounted for via a correction term added to the defect formation energy relation as described later on.

Using the supercell approach, the formation energy of a defect α in a charge state q can be calculated as

$$\Delta H_F(\alpha, q, E_F, \mu_i) = E(\alpha, q) - E_{\text{host}} - \sum_i n_i (E_i + \mu_i) + q[\epsilon_{\text{VBM,host}} + E_F], \quad (3.43)$$

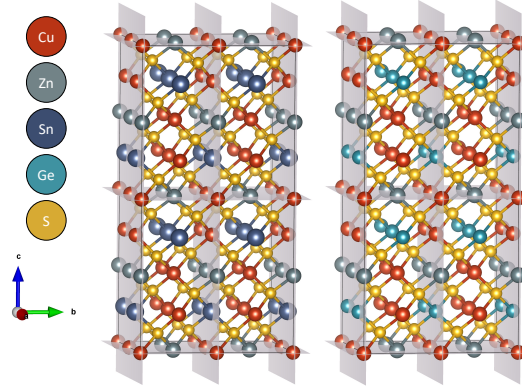


Figure 3.4: Undefected kesterites 64-atoms supercells used to compute the defects formation energies. The supercell corresponds to an expansion of $2 \times 2 \times 2$ of the kesterite conventional cell as represented by the grey shadings.

where $E(\alpha, q)$ is the total energy of the supercell with a defect α in the charge state q . E_{host} is the total energy of the 64-atom undefected supercell, while n_i is the number of atom(s) of the species i removed (< 0) from or added (> 0) to the host supercell with E_i , the energy per atom of the pure phase of the species i and μ_i , the chemical potential of the corresponding element. The third term accounts for an exchange of particles between the system under study and an external reservoir, implying an energy transfer according to the chemical potential of the species. Then, assuming a defect in charge state q , an extra term is added to this equation, which considers an exchange of charge(s) between an external electronic reservoir and the system under study. In this term, $\epsilon_{\text{VBM,host}}$ refers to the valence band maximum (VBM) of the host supercell and E_F is the Fermi level that acts as a parameter of the defect formation energy function and varies from VBM to the bandgap energy E_G of the kesterite material. By taking a closer look at this equation, one can observe that for each intrinsic point defect α in a charge state q , the formation energy depends on two variables:

1. The energy exchanged due to the exchange of particles between an external reservoir and the system μ_i : this chemical potential parameter is related to the experimental conditions under which the material is synthesised, such as the atmosphere, the pressure, the temperature, *etc.* The values of μ_i are set by the position in the phase diagram of the material.
2. For a charged defect, the energy was exchanged due to the transfer of charges related to the Fermi energy value $E_F \in [0; E_G]$.

As a first introduction, **Fig.3.5** shows a schematic representation of a defect formation energy as a function of the Fermi energy E_F considering three charge states: 0, -1, -2. Each charge state corresponds, according to Eq.(3.43), to a line with a slope given by the charge state q . The lowest formation energy (the plain line) represents

the minimal defect formation energy as a function of the Fermi level.

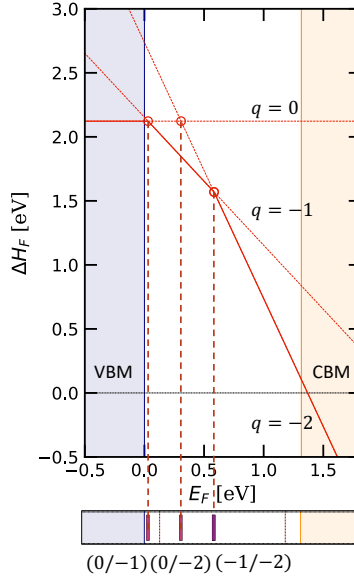


Figure 3.5: Schematic representation of the evolution of a defect formation energy in which three charge states are considered: 0, -1, -2 giving three possible transition levels: (0/-1), (0/-2) and (-1/-2). The different charge state lines are represented using a dashed style.

Furthermore, on the basis of the formation energy of a given defect, it is possible to extract its ionisation levels. This quantity allows to classify the behaviour of the defect via the determination of the energetic position of the ionisation levels. For a level located close to the edges of the bandgap (*i.e.* the conduction band minimum: $E_F \simeq E_G$ or the valence band maximum: $E_F \simeq 0$), the defect can be classified as a donor or an acceptor. In opposition, defects close to the middle of the bandgap could be classified as possible recombination centres, which could lead to a degradation of the solar cell performance depending on the defect concentration and carrier capture cross section. The defect ionisation energies are calculated using the following relation:

$$\mathcal{E}(\alpha, q, q') = \frac{\Delta H_F(\alpha, q) - \Delta H_F(\alpha, q')}{q' - q}, \quad (3.44)$$

where q and q' are the charge states of the defect α considered for the transition. As a consequence, this transition energy corresponds to the Fermi energy E_F for which the defect in a charge state q has the same formation energy as the defect in a charge state q' . Furthermore, as shown in **Fig.3.5**, the transition levels correspond to the intersection between each dashed line. These transitions are represented via a marker whose abscissa corresponds to the energetic position of the transition level in the material bandgap.

Then, to compute the Fermi energy level E_F under thermodynamic equilibrium conditions as described in solid-state physics, one can use the charge neutrality equation [121]:

$$\sum_{\alpha,q} qC(\alpha(q)) + p - n = 0, \quad (3.45)$$

where n, p are respectively the concentrations of electrons and holes, and $C(\alpha(q))$ is the concentration of the defect α in its charge state q . The defect concentration $C(\alpha(q))$ is directly related to its formation energy as follows:

$$C(\alpha(q), E_F) = N e^{-\Delta H_F(\alpha,q,E_F)/k_B T}, \quad (3.46)$$

with N the number of possible sites where the defect α could form. In addition, the number of charge carriers that participate in the conductivity of the materials (n- or p-type) can be expressed as

$$n - p = \sum_{\alpha,q} qC(\alpha(q), E_F), \quad (3.47)$$

Moreover, for a non-degenerate semiconductor, it is an excellent approximation, with respect to the Fermi-Dirac distribution, to express the electron (resp. hole) concentration using Maxwell-Boltzmann statistics as expressed in Eqs. (2.37) and (2.38). Finally, based on the electron (resp. hole) effective masses m_e^* (resp. m_h^*) of Ref. [86] (chapter 4), the Fermi energy E_F can be computed iteratively reaching the equality expressed in Eq.(3.47) for a given criterion.

3.3.2 Material phase diagram

A variation in the material synthesis conditions can induce changes to the thin film composition and, consequently, the lattice environment in which the defect will be formed. As a result, the formation energy of the point defect and its concentration will be impacted accordingly by the amount of energy required for the exchange of particles necessary to form the defect. This energetic cost is described by the chemical potential of the chemical species (μ_i), which is defined as the Gibbs free energy variation caused by the exchange of particles between the system and an external reservoir, namely: $\mu_i = \left(\frac{dG}{dN_i}\right)$ [121]. Thus, one has to determine the chemical potentials μ_i that lead to the formation of a stable kesterite phase without any secondary phase. In order to address this challenge, kesterite phase diagrams have to be computed by fulfilling the following thermodynamic conditions :

- (i) First, each chemical potential related to a species should favour the formation of the kesterite material instead of the species pure crystalline phase. A chemical potential value equal to 0 corresponding to the pure element crystalline phase (*e.g.* $\mu_{Cu} = 0$ implies a pure phase of Cu), the chemical potential values should be strictly negative to avoid the formation of pure compounds. This condition is expressed by the following inequalities:

$$\mu_{Cu} < 0, \mu_{Zn} < 0, \mu_X < 0, \mu_S < 0. \quad (3.48)$$

- (ii) Second, the sum of the chemical potentials must be equal to the formation energy of the desired compound: the kesterite material Cu_2ZnXS_4 ($X = \text{Sn, Ge}$). This condition means that under thermodynamic equilibrium conditions, the desired stable phase is the kesterite compound:

$$\Delta H_F(\text{CZXS}) = 2\mu_{Cu} + \mu_{Zn} + \mu_X + 4\mu_S. \quad (3.49)$$

Based on this equation and knowing the kesterite formation energy, one variable can be isolated as expressed in Eq.(3.50). Moreover, the formation energy of a compound is the difference between the total energy of the compound and the pure phase energy of each element within the compound: $\Delta H_F(A_i B_j) = E_{A_i, B_j} - n_i E_A - n_j E_B$. Ground state total energies as obtained from the solutions of the Kohn-Sham equations.

$$\mu_S = [\Delta H_F(\text{CZXS}) - \mu_{Zn} - \mu_X - 2\mu_{Cu}]/4. \quad (3.50)$$

As a result, the phase diagram of this quaternary compound can be represented as a 3-dimensional map. For the sake of clarity, in this work, we represent the kesterite phase diagrams using a 2D-plot (μ_X ($X = \text{Sn, Ge}$) VS μ_{Zn}) for a fixed value of μ_{Cu} .

- (iii) Third, based on the chemical species involved, several secondary phases could form. Kesterite compounds are known to be synthesised through a chemical pathway that includes binary or ternary compounds [56]. However, such secondary phases are detrimental to solar cell applications and are consequently undesirable [127]. The condition to be respected to avoid their formation can be expressed as follows: the sum of the involved chemical species potential values must be lower than the formation energy of the secondary phase under consideration.

$$\sum_i n_i \mu_i < \Delta H_F(X_i, n_i) \quad (3.51)$$

Finally, to compute the formation energy of Ge-related defects (dopants) in the Sn-kesterite compound, one has to calculate the chemical potential of Ge μ_{Ge} within the Sn matrix. To do so, additional secondary phases including the Ge element were calculated. Using Eq.(3.49) combined with the criterion expressed in Eq.(3.51), the chemical potential of Ge was obtained. And, as pointed out by Wexler *et al.* in Ref. [128], using the SCAN exchange-correlation functional, the formation energy in absolute value of every compound containing Ge is systematically underestimated with respect to the experimental values. To deal with this effect, a correction of -0.27 eV/Ge was applied to each secondary phase formation energy for Ge-containing

material.

From now on, using Eq.(3.43) and the chemical potential values obtained from the description above, the defects formation energies can be calculated for various charge states and thermodynamic environments.

3.3.3 Corrections terms

To accurately predict the energies of defect formation, two correction terms were added to Eq.(3.43). First, a potential alignment term, and second, a correction term dealing with the electrostatic interaction between charged defects located in the neighbouring supercell images as a result of the periodic conditions used in the *ab initio* approach [129, 130].

1. The first correction arises from the divergence of the electrostatic potential upon charging. In consequence, the net energy is ill-defined, and reference levels have to be aligned using Kohn-Sham energy levels of core orbitals of atoms located far from the defect.
2. The second correction comes from the need to suppress the interaction between the charged defect located in the supercell and the ones located in the image supercells produced by the periodic boundary conditions applied. To do so, we correct the image charge interactions by adding to Eq.(3.43), the following term :

$$\Delta E_i = [1 + c_{sh}(1 - \epsilon^{-1})] \frac{q^2 \alpha_M}{2\epsilon L}, \quad (3.52)$$

where c_{sh} is a value dependent on the crystal symmetry, ϵ is the dielectric constant, α_M is the crystal Madelung constant and L is the characteristic size of the supercell.

Using the supercell approach, the prediction of the defect formation energy is limited by two main factors: the DFT underestimation of the material bandgap and the size of the supercell considered [125]. In this work, the material bandgap underestimation is limited via the choice of an hybrid exchange-correlation functional (HSE06) leading to an unavoidable increase of the computational cost [131, 132]. On the other hand, the supercell size-dependent issue is corrected thanks to the previously presented corrections terms [133].

The results presented in chapter 5 are calculated on the basis of the developed supercell approach. Moreover, from the theoretical notions presented in chapters 2 and 3, in the upcoming chapters, we present and discuss the material properties of kesterite and copper oxide as well as the impact of specific point defects on the photovoltaic parameters of solar cell using these earth-abundant compounds as absorber layer.

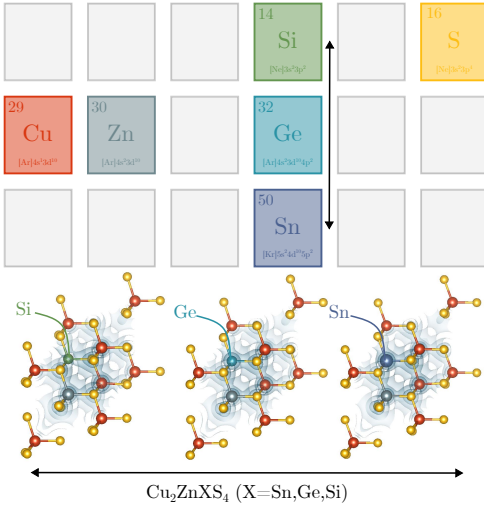
Sn CATIONIC SUBSTITUTION IN KESTERITE

4

4.1	Introduction	107
4.2	Computational method	108
4.3	Cationic substitution in kesterite	109
4.3.1	Crystalline structure	109
4.3.2	Electronic properties	110
4.3.3	Optical properties	113
4.4	Conversion efficiency modelling	115
4.5	Conclusion	121

This chapter is based on the following work:

Ratz, T., Raty, J. Y., Brammertz, G., Vermang, B., & Nguyen, N. D. (2021). *Opto-electronic properties and solar cell efficiency modelling of Cu_2ZnXS_4 ($X = Sn, Ge, Si$) kesterites*. Journal of Physics: Energy, **3(3)**, 035005.



Abstract In this work, first-principles calculations of $\text{Cu}_2\text{ZnSnS}_4$, $\text{Cu}_2\text{ZnGeS}_4$ and $\text{Cu}_2\text{ZnSiS}_4$ are performed to highlight the impact of the cationic substitution on the structural, electronic and optical properties of kesterite compounds. Direct bandgaps are reported with values of 1.32, 1.89 and 3.06 eV respectively for $\text{Cu}_2\text{ZnSnS}_4$, $\text{Cu}_2\text{ZnGeS}_4$ and $\text{Cu}_2\text{ZnSiS}_4$ and absorption coefficients of the order of 10^4 cm^{-1} are obtained, confirming the applicability of these materials as absorber layer for solar cell applications in different niches. In the second part of this study, *ab initio* results are used as input data to model the electrical

power conversion efficiency of kesterite-based solar cells. In that perspective, we used an improved version of the Shockley-Queisser model including non-radiative recombination via an external parameter Q_i defined as the internal quantum efficiency. Based on predicted optimal absorber layer thicknesses, the variation of the solar cell maximal efficiency is studied as a function of the non-radiative recombination rate. Maximal efficiencies of 25.71, 19.85 and 3.10% are reported respectively for $\text{Cu}_2\text{ZnSnS}_4$, $\text{Cu}_2\text{ZnGeS}_4$ and $\text{Cu}_2\text{ZnSiS}_4$ for vanishing non-radiative recombination rate. Using an internal quantum efficiency value providing experimentally comparable V_{OC} , cell efficiencies of 15.88, 14.98 and 2.66% are reported respectively for $\text{Cu}_2\text{ZnSnS}_4$, $\text{Cu}_2\text{ZnGeS}_4$ and $\text{Cu}_2\text{ZnSiS}_4$. We confirm the suitability of $\text{Cu}_2\text{ZnSnS}_4$ in single or tandem (top cell) solar cells, with a possible efficiency improvement of nearly 10% enabled through the reduction of the non-radiative recombination rate. In addition, $\text{Cu}_2\text{ZnGeS}_4$ appears to be an interesting candidate as top cell absorber layer for tandem approaches with an efficiency room for improvement of 5 points.

4.1 INTRODUCTION

As presented in the introduction chapter of this thesis, concerning kesterite-based solar cells, large open circuit voltage V_{OC} deficits have been reported as responsible for the efficiency limitation encountered [50, 56]. Several elements have been pointed out as possible culprits for the V_{OC} deficits, including interface recombination due to bands misalignment [85, 134], formation of secondary phases, and/or high concentration of intrinsic point defects leading to non-radiative recombinations in bulk kesterite materials [70, 72]. Recombination centres are therefore present both at the architectural level (band misalignments with the buffer layer) and at the compositional/morphological level (defects and/or secondary phases) within the absorber layer. Moreover, in order to deal with these recombination sites, substitution strategies were highlighted as a possible solution to consequently improve the V_{OC} .

Focusing on the isoelectronic substitution within the kesterite absorber layer, several paths have been considered such as Ag for Cu, Ge for Sn or Se for S [74, 76] or via the cationic substitution of Zn or Sn [80, 135]. In the past, alternative kesterite materials have been studied both theoretically and experimentally, leading to promising efficiencies for Ge-containing kesterite compounds [15, 77, 78, 83, 136, 137]. Using DFT calculations, a few works reported predictions over structural properties, electrical properties or optical properties of alternative kesterite materials such as $\text{Cu}_2\text{ZnSnS}_4$ [138–144], $\text{Cu}_2\text{ZnGeS}_4$ [138–140, 145, 146] and $\text{Cu}_2\text{ZnSiS}_4$ [138–140]. However, the variety of computational approaches do not facilitate the comparison of the materials physical properties. In addition, to the best of our knowledge, the DFT results are rarely compared to experimental measurements.

In this chapter, we first investigate theoretically the cationic substitution of Sn by Ge and Si, in $\text{Cu}_2\text{ZnSnS}_4$ kesterite. The structural and optoelectrical properties are calculated for $\text{Cu}_2\text{ZnSnS}_4$ as the reference material [52], $\text{Cu}_2\text{ZnGeS}_4$ as a promising material regarding the experimental efficiency achieved [15, 52] and $\text{Cu}_2\text{ZnSiS}_4$ as an interesting candidate regarding the elemental abundance [10]. Then, the obtained *ab initio* results are used as input data to feed an improved version of the Shockley-Queisser model [28], allowing us to connect the intrinsic material properties to the solar cell macroscopic properties. Via this cell efficiency modelling, physical quantities such as the open circuit voltage V_{OC} , the short circuit current density J_{SC} and the fill factor FF are computed.

First, the structural properties of the materials are presented. Then, in the following sections, the Heyd–Scuseria–Ernzerhof exchange-correlation functional (HSE06) [147] is used to compute the electronic and optical properties. Based on the band structures and the densities of states (DOS), the electrical properties of the materials are reported and compared. To complete the investigation, the optical properties are

presented and related to the electrical ones. This approach allows us to extract the general trends highlighting the impact of the cationic substitution of Sn by Ge and Si on the optoelectrical properties. In the second part of this work, using the *ab initio* results as input data, the upper limit of the kesterite-based solar cell efficiency is calculated using the theoretical model proposed by Blank *et al.* [87]. This model allows us to compute physical quantities that can be compared to experimental results such as the solar cell efficiency η using as parameters the solar cell temperature T , the absorber layer thickness d and the internal quantum efficiency Q_i . Then, based on experimentally reported V_{OC} values, the room for improvement for $\text{Cu}_2\text{ZnSnXS}_4$ (X=Sn,Ge,Si) based cell efficiencies is emphasised.

4.2 COMPUTATIONAL METHOD

First-principles calculations have been performed using Vienna *Ab initio* Simulation Package (VASP) code [148] with the Projector-Augmented Wave (PAW) potential method [149]. Perdew-Burke-Ernzerhof (PBE) GGA pseudo-potentials [150] were used with the following valence electrons considered for each element: Cu: $3d^{10}4s^1$, Zn: $3d^{10}4s^2$, Sn: $4d^{10}5s^25p^2$, Ge: $3d^{10}4s^24p^2$, Si: $3s^23p^2$ and S: $3s^23p^4$.

Ionic and electronic relaxation were achieved using a cut-off energy of 550 eV and a Γ -centered uniform \mathbf{k} -points mesh of $6 \times 6 \times 6$ \mathbf{k} -points. Applying the strongly constrained and appropriately normed semilocal density functional (SCAN) [151, 152], the structures were relaxed until the numerical convergence regarding the self-consistent cycles reaches forces between ions less than 10^{-3} eV/Å. The system total energy was converged down to 10^{-6} eV. During relaxation, the symmetry was kept constant to the kesterite point group symmetry ($I - 4$) and the atomic positions, cell volume and cell shape were allowed to relax. The SCAN meta-GGA functional was proven effective to predict improved geometries for a computational cost comparable to the GGA functional. Moreover, Fritsch *et al.* reported that the combination of SCAN functional calculations for ionic relaxations followed by a single HSE06 functional electronic calculation provides accurate results for kesterite materials [153]. Starting from the relaxed structure, the HSE06 exchange-correlation functional, known for its bandgap prediction accuracy [131], was used to compute the electronic and optical properties. To this regard, appendix A offers an overview of the VASP software practical features pertinent to these calculations.

Concerning the optical calculations, the imaginary part of the dielectric tensor was first obtained by applying the Fermi golden rule between valence band and conduction band states at a given \mathbf{k} -point (*cfr.* Eq.(2.22)) for which the convergence was properly ensured via a sufficiently high number of conduction band energy levels included in the calculation. Then, the real part of the dielectric tensor was obtained thanks to a Kramers-Kronig transformation (*cfr.* Eq.(2.23)).

4.3 CATIONIC SUBSTITUTION IN KESTERITE

4.3.1 Crystalline structure

Table 4.1 presents the lattice parameters a , b , c (*cf.* **Fig.4.1**), the conventional cell volume V and the atomic distances $d_{\text{Cu-S}}$ and $d_{\text{X-S}}$ ($\text{X}=\text{Sn,Ge,Si}$) obtained as a result of the ionic relaxation. These ones are compared to experimental or theoretical values reported in the literature.

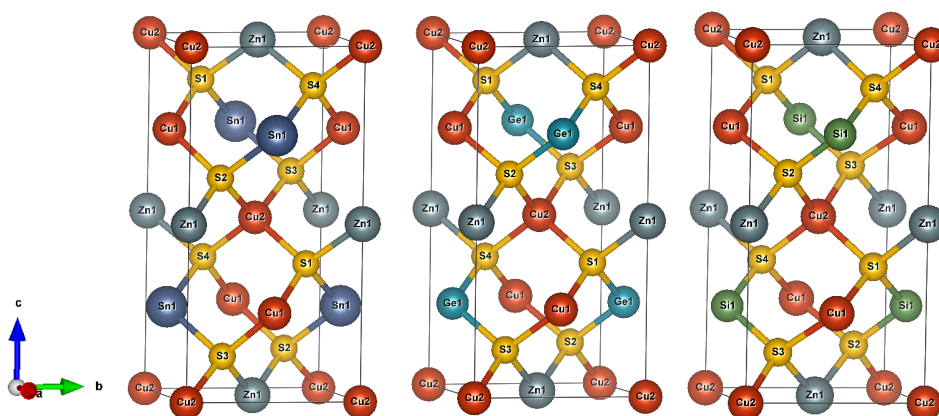


Figure 4.1: Representation of the conventional cells of the Cu_2ZnXS_4 ($\text{X}=\text{Sn,Ge,Si}$) kesterites.

The sequential substitution of Sn by Ge and Si induces a contraction of the kesterite lattice parameters. A reduction of a and b from 5.40 Å ($\text{Cu}_2\text{ZnSnS}_4$) to 5.25 Å ($\text{Cu}_2\text{ZnSiS}_4$) is observed while the c parameter is reduced from 10.79 Å to 10.32 Å. The results reported in **Tab.4.1** are in good agreement with experimental measurements for $\text{Cu}_2\text{ZnSnS}_4$ [154–159] and $\text{Cu}_2\text{ZnGeS}_4$ [157, 159–161]. To our knowledge, experimental characterisation of Si-pure kesterite crystal structures has not been reported yet. According to Refs. [162, 163], an orthorhombic crystalline structure is observed for high Si concentrations. Nevertheless, several theoretical works [139, 140] reported values close to $a, b = 5.25$ Å and $c = 10.32$ Å as obtained here. This lattice contraction can be interpreted by taking into account the successive reduction of the atomic radius of the substitutional cation from $r_{\text{Sn}} = 1.45$ Å, to $r_{\text{Ge}} = 1.25$ Å and to $r_{\text{Si}} = 1.10$ Å [164]. Consequently, the conventional cell volume decreases from 314.9 Å³ for the Sn-containing compound to 294.87 Å³ for $\text{Cu}_2\text{ZnGeS}_4$ and to 283.94 Å³ for $\text{Cu}_2\text{ZnSiS}_4$. One can also notice that the cation substitution does not impact the $d_{\text{Cu-S}}$ distances. In the following section, the results presented here will be put into perspective with the electronic properties.

Materials	Ref. (Type)	a,b [Å]	c [Å]	V [Å ³]	d_{X-S} [Å]	d_{Cu-S} [Å]
Cu ₂ ZnSnS ₄	This work.	5.40	10.79	314.90	2.44	2.29
	[154] (Exp.)	5.67	11.30			
	[155] (Exp.)	5.42	10.79		2.39	2.33
	[156] (Exp.)	5.42	10.79			
	[157] (Exp.)	5.43	10.86			
	[158] (Exp.)	5.43	10.86			
	[159] (Exp.)	5.42	10.86			
	[139] (Theo.)	5.44	10.76			
	[141] (Theo.)	5.33	10.66			
	[142] (Theo.)	5.47	10.92			
	[140] (Theo.)	5.45				
	[143] (Theo.)	5.43	10.86			
[144] (Theo.)	5.45	10.89				
Cu ₂ ZnGeS ₄	This work.	5.30	10.51	294.87	2.26	2.28
	[157] (Exp.)	5.34	10.57			
	[159] (Exp.)	5.28	10.71			
	[160] (Exp.)	5.33-5.34	10.52-10.59	299.54-301.95		
	[161] (Exp.)	5.30-5.37	10.49-10.69			
	[139] (Theo.)	5.28	10.49			
	[140] (Theo.)	5.35				
	[145] (Theo.)	5.35	10.49			
[146] (Theo.)	5.38	10.49				
Cu ₂ ZnSiS ₄	This work.	5.25	10.32	283.94	2.15	2.28
	[139] (Theo.)	5.22	10.30			
	[140] (Theo.)	5.31				

Table 4.1: Lattice parameters a, b and c (see **Fig.4.1**) and conventional cell volume V of Cu₂ZnXS₄ (X=Sn,Ge,Si) kesterites. Interatomic distances between the cation (X=Sn,Ge,Si) and the sulphur atom d_{X-S} are reported as well as the copper-sulphur distances d_{Cu-S} . Empty cells denote the absence of available data.

4.3.2 Electronic properties

As it can be observed in **Fig.4.2**, all calculated kesterite bands present a direct bandgap located at the Γ point. Using an approach similar to that reported in Refs. [138–140], the bandgap values reported in **Tab.4.2** were obtained from the energy differences between the conduction band minimum and the valence band maximum energy levels as extracted from the Kohn-Sham eigenvalues. As reported, the bandgap energy E_G increases from 1.32 eV for Cu₂ZnSnS₄ to 1.89 eV for Cu₂ZnGeS₄ and to 3.06 eV for Cu₂ZnSiS₄. These results are comparable to those reported by Zamulko *et al.* in their theoretical investigation [139]. In comparison to experimental values, the Sn-containing kesterite bandgap is underestimated by 0.18 eV as usual reported values are around 1.5 eV [52]. In contrast, the Cu₂ZnGeS₄ bandgap value of 1.89 eV fits with the reported experimental bandgaps with values between 1.88

and 2.25 eV [159–161, 165–167]. According to Ref. [168], a bandgap value of 2.71 eV was experimentally obtained for $\text{Cu}_2\text{ZnSiS}_4$. The DFT predicted bandgap underestimation was commented in chapter 3 (cfr. Eq.(3.36)).

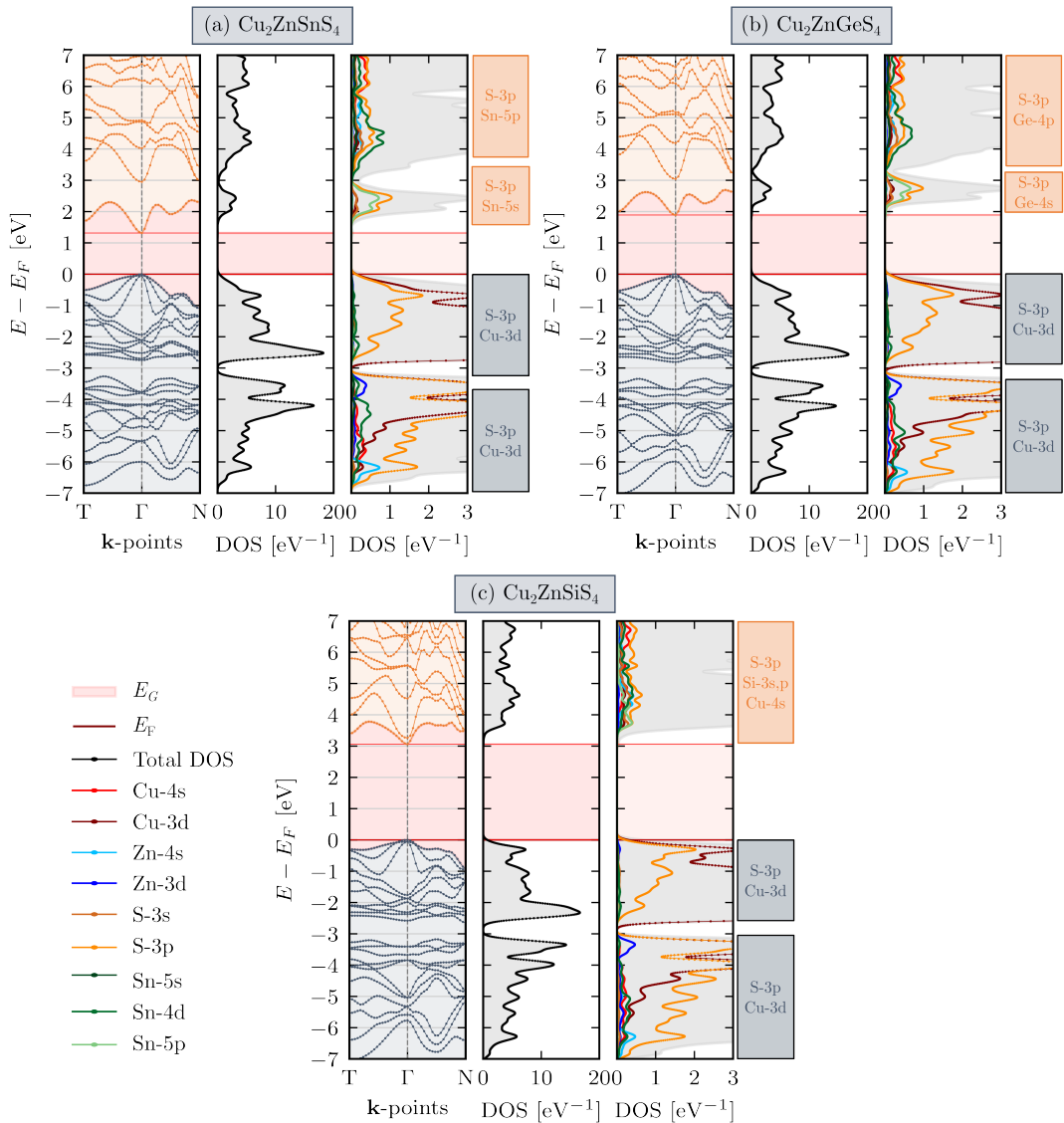


Figure 4.2: Band structures, densities of states and orbital projected densities of states of Cu_2ZnXS_4 ($X=\text{Sn,Ge,Si}$) kesterites. The densities of states are presented with an applied gaussian smearing of 0.08 eV. The band dispersion is calculated along $T: [0,0,1/2] - \Gamma: [0,0,0] - N: [1/2,1/2,1/2]$. Main atomic orbital contributions to the DOS are presented alongside the figures.

We provide here a focus on the orbitals projected DOS and their contributions to electronic states in the band structure, for the Sn-kesterite compound (**Fig.4.2(a)**).

The main contributions to the conduction band states come from S 3p and Sn 5s atomic orbitals close to the bottom of the band and S 3p and Sn 5p atomic orbitals for higher energy levels. Concerning the valence band, the hybridisation between Cu 3d and S 3p orbitals provides the main contributions to energy states at the top of the band. These results are corroborated by the work of Paier *et al.* in Ref. [144]. This tendency is also observed for the two other kesterite materials, *e.g.* the bottom of the conduction band is formed by either the s atomic orbital of the cation X (X=Sn, Ge) or the p orbital of the cation Si and the 3p orbital of the chalcogen S, while the contributions to the top of the valence band come from the 3d atomic orbital of Cu and the 3p atomic orbital of the sulphur element.

For $\text{Cu}_2\text{ZnGeS}_4$ and $\text{Cu}_2\text{ZnSiS}_4$, the substitution of Sn by Ge and Si (**Figs.4.2(b)** & 4.2(c)) seems to slightly flatten the energy level at the bottom of the conduction band. The bandgap increase from 1.32 to 3.06 eV is due to the variation of the chemical interaction between the cation and the sulphur, which leads to (i) a weak flattening of the energy level at the bottom of the conduction band and (ii) a shift of this energy level towards higher energies. To link those observations to the structural properties of the materials one can put into perspective the decrease of the cation-sulphur interatomic distance d_{X-S} with the increase of the kesterite bandgap. In contrast, the substitution of the cation atoms leaves the valence band unchanged as the orbitals contributing to these states are from Cu and S for which the interatomic distances d_{Cu-S} are reported constant from one kesterite material to another (*cf.* **Tab.4.1**).

In addition to the bandgaps, the effective masses are presented in **Tab.4.2**. These ones have been calculated around the Γ point, at the direct bandgap location, and along two directions in the reciprocal space: $[0,0,0]$ to $[0,0,1]$ for the first effective mass component m_{\perp} and along $[0,0,0]$ to $[0,1,0]$ for the second component $m_{//}$. As shown in **Fig.4.2**, one energy level is present at the bottom of the conduction band and three energy levels are located at the top of the valence band. Consequently, the effective masses have been calculated for the lowest energy level in the conduction band named Γ_c and for the three highest energy levels at the top of the valence band $\Gamma_{v,1}$, $\Gamma_{v,2}$, $\Gamma_{v,3}$, labeled from the highest energy level to the lowest one. For both the conduction and valence band, the general trend observed is a slight increase of the effective mass absolute value, with only two occasions of exceptions (for $\Gamma_{v,1}$ and $\Gamma_{v,2}$ of the m_{\perp}^* component), when Sn is sequentially substituted by Ge and Si. Then, as kesterite materials behave electrically as p-type semiconductor [50], we first discuss the hole effective mass values. As presented in **Tab.4.2**, concerning the $m_{//}^*$ component, $\Gamma_{v,2}$ effective masses are significantly higher than $\Gamma_{v,1}$ and $\Gamma_{v,3}$, highlighting the presence of light and heavy holes in this particular direction. In addition, similar values are reported regarding $\Gamma_{v,1}$ and $\Gamma_{v,3}$ for the perpendicular component while, in contrast, $\Gamma_{v,2}$ is five times lower than in the parallel direction. Concerning the electron effective masses, similar values are obtained for both components $m_{//}^*$ and m_{\perp}^* with a slight increase from a minimal value of $0.18 m_e$ to a maximal value of $0.26 m_e$ observed as

the Sn cation is substituted. These values are in good agreement with those obtained by Liu *et al.* with reported effective masses of 0.18, 0.21 and 0.26 m_e (resp. 0.19, 0.22, 0.24 m_e) in the parallel (resp. perpendicular) direction [140]. This suggests that the hole and electron effective masses would only slightly increase as Sn is substituted by Ge and then Si. In summary, the cationic substitution does not impact significantly the hole nor electron effective masses but leads to a significant increase of the kesterite bandgap.

Materials	E_G [eV]	$m_{//}^* [m_e]$				$m_{\perp}^* [m_e]$				$\epsilon_{\infty} [\epsilon_0]$
		$\Gamma_{v,1}$	$\Gamma_{v,2}$	$\Gamma_{v,3}$	Γ_c	$\Gamma_{v,1}$	$\Gamma_{v,2}$	$\Gamma_{v,3}$	Γ_c	
$\text{Cu}_2\text{ZnSnS}_4$	1.32 (This work)									
	1.50 (Exp.) [52]	-0.69	-3.32	-0.16	0.19	-0.77	-0.64	-0.19	0.18	6.77
	1.26-1.77 (Theo.)									
	[138, 139, 143, 144]									
$\text{Cu}_2\text{ZnGeS}_4$	1.89 (This work)									
	1.88-2.25 (Exp.)	-0.72	-3.49	-0.19	0.23	-0.72	-0.63	-0.24	0.22	6.44
	[159–161, 165–167]									
	2.10-2.38 (Theo.)									
[138, 139, 143, 145]										
$\text{Cu}_2\text{ZnSiS}_4$	3.06 (This work)									
	2.71 (Exp.) [168]	-1.44	-3.65	-0.25	0.26	-1.63	-0.68	-0.33	0.25	5.78
	3.05 (Theo.) [138, 139]									

Table 4.2: Bandgaps E_G and effective masses m^* scaled by the free electron mass m_0 of Cu_2ZnXS_4 (X=Sn,Ge,Si) kesterites. Effective masses have been calculated around the Γ high symmetry \mathbf{k} -point and along two directions in the reciprocal space: $[0,0,0]$ to $[0,0,1]$ (resp. $[0,0,0]$ to $[0,1,0]$) for the first effective mass component m_{\perp} (resp. for the second component $m_{//}$) comparable to values reported in Ref. [140]. High-frequency dielectric constants ϵ_{∞} of the materials are also presented and scaled with the vacuum electrical permittivity ϵ_0 comparable to values reported in Ref. [139].

4.3.3 Optical properties

Following the computation of the electronic properties, the optical properties of the kesterite materials have been determined via the calculation of the dielectric tensor $\mathcal{E}(E)$ whose real ϵ_1 and imaginary ϵ_2 parts are shown in **Fig.4.3(a)** (see section 2.2). In this figure, the components xx , yy and zz of $\epsilon_{1,2}(E)$ are presented for each compound. It appears that the sequential substitution of Sn with Ge and Si leads to a decrease of the high frequency dielectric response ϵ_{∞} from 6.77 ϵ_0 ($\text{Cu}_2\text{ZnSnS}_4$) to 6.44 ϵ_0 ($\text{Cu}_2\text{ZnGeS}_4$) and reaching 5.78 ϵ_0 for the Si-containing compound (*cfr.* **Tab.4.2**). These results are comparable to the values of 6.7 ($\text{Cu}_2\text{ZnSnS}_4$), 6.6 ($\text{Cu}_2\text{ZnGeS}_4$) and 5.7 ($\text{Cu}_2\text{ZnSiS}_4$) reported by Zamulko *et al.* in Ref. [139]. As expected, the decrease in ϵ_{∞} is in agreement with the increase of the materials bandgap. Concerning the imaginary part of the dielectric tensor $\epsilon_2(E)$, the onset of absorption is also shifted towards higher energies as the bandgap increases. In addition, in **Fig.4.3(a)**, one can

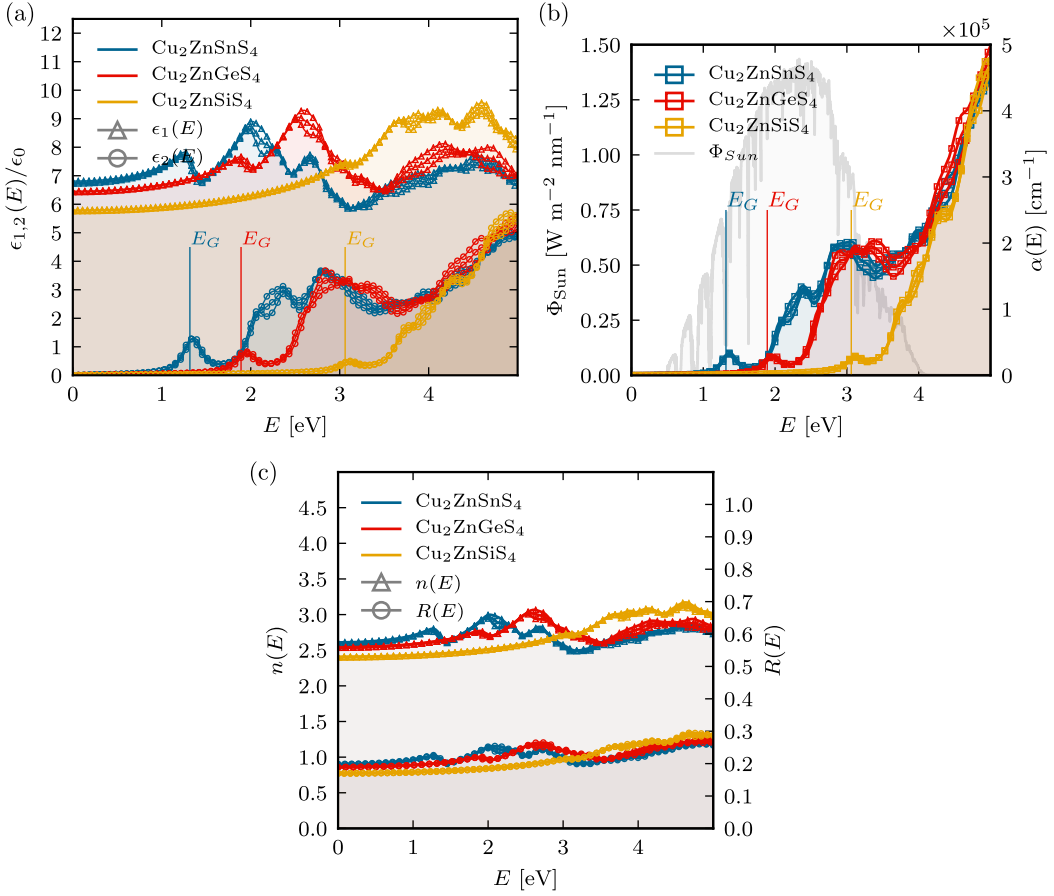


Figure 4.3: (a) Real ϵ_1 and imaginary ϵ_2 parts of the dielectric tensor $\mathcal{E}(E)$. For each compound, the xx , yy and zz components of the tensor are presented. (b) The absorption coefficients $\alpha(E)$ and the solar irradiance spectrum are presented. (c) Materials refractive indices $n(E)$ and reflectivity $R(E)$ spectra.

notice that the peaks positions correspond well to the bandgaps reported in **Tab.4.2**.

Then, the absorption coefficient $\alpha(E)$ as well as the reflectivity $R(E)$ and refractive index $n(E)$ are computed as described in section 2.2. In **Fig.4.3(b)** the absorption coefficient of the materials are presented alongside the AM1.5 solar irradiance spectrum. First, one can notice that the kesterite compounds exhibit absorption coefficient values between 0 and $2 \times 10^5 \text{ cm}^{-1}$ within the energy range of non-negligible solar irradiance (between 0.5 and 4 eV). This result highlights the applicability of these kesterite materials as absorber layer in solar cell applications. However, an energetic shift of the absorption curves is also observed from the Sn-containing kesterite to the Si-containing kesterite with a first absorption peak located at the respective bandgap energies of the materials. The $\text{Cu}_2\text{ZnSnS}_4$ and $\text{Cu}_2\text{ZnGeS}_4$ curves have a similar behaviour while for the Si-containing kesterite curve, the plateau observed for

the two other kesterites disappears as a consequence of the energy level shift at the bottom of the conduction (*cfr.* **Fig.4.2(c)**). Finally, in **Fig.4.3(c)**, the refractive index $n(E)$ and reflectivity $R(E)$ are presented. As reported, the refractive indices at 0 eV are 2.59, 2.53 and 2.40 respectively for $\text{Cu}_2\text{ZnSnS}_4$, $\text{Cu}_2\text{ZnGeS}_4$ and $\text{Cu}_2\text{ZnSiS}_4$ with variations of 0.6 in values between 0 and 5 eV. Concerning the reflectivity values, a variation from 20 to 30% within the 0 to 5 eV energy range is observed. Additionally, it is worth noticing some reflectivity differences of nearly 10% between $\text{Cu}_2\text{ZnSnS}_4$ and $\text{Cu}_2\text{ZnSiS}_4$ for some energy values.

4.4 CONVERSION EFFICIENCY MODELLING

In this section, we focus on the theoretical modelling of solar cell macroscopic physical quantities such as the short circuit current density J_{SC} , the open circuit voltage V_{OC} and the solar cell electrical power conversion efficiency η using Cu_2ZnXS_4 (X=Sn,Ge,Si) as absorber layer. The predictions are realised based on the theoretical model proposed by Blank *et al.* [87] and detailed in section 2.4.2. As explained, the improvements proposed by Blank *et al.* over the Shockley-Queisser model [28] are (i) the use of the internal quantum efficiency Q_i as a model parameter to take into account non-radiative recombinations and (ii) the incorporation of light trapping by taking into account the refractive index $n(E)$ in the calculation of the radiative current density $J_{\text{rad},0}(n, d)$ (see Eq.(2.94)).

Non-radiative recombinations occur via recombination centres: intrinsic point defects, defect clusters and grain boundaries in the bulk material or also through recombination centres at the interfaces of the various layers composing the solar cell. As a consequence, these recombination centres have an impact on the solar cell properties. Therefore, in this theoretical work, we chose to use the non-radiative recombination rate as a model parameter. In that perspective, the internal quantum efficiency is expressed as the ratio between the radiative recombination rate $R_{\text{rad},0}$ and the total recombination rate: $R_{\text{rad},0} + R_{\text{nr},0}$, leading to a non-radiative recombination rate under equilibrium conditions,

$$R_{\text{nr},0} = R_{\text{rad},0} \frac{(1 - Q_i)}{Q_i}. \quad (4.1)$$

Considering a perfectly crystalline material, all recombinations are radiative and the photons emitted (and not reabsorbed) contribute to the emission spectrum of the material which, in this model, is assumed as the black body spectrum at temperature $T = 300$ K. These radiative recombinations are therefore thermodynamically required and are proportional to the amount of electrons within the conduction band (proportional to the temperature). This first situation corresponds to an internal luminescence quantum efficiency Q_i value equals to unity for which the total recombination rate R_0 is equal to the radiative recombination rate $R_{\text{rad},0}$. In the case

of recombination centres within the bulk materials or at the interfaces, both radiative and non-radiative recombination are included. The thermodynamic condition of emission must still be fulfilled ($R_{\text{rad},0}$) and additionally, recombinations via recombination centres occur ($R_{\text{nr},0}$), leading to an increase of the total recombination rate R_0 . In this work, the Q_i value is related to the amount of non-radiative recombinations which is proportional to the number of radiative recombinations (Eq.(4.1)). To feed this theoretical model we use the previously calculated optical results ($\alpha(E)$, $n(E)$ and $R(E)$) as input data. It is worth noticing that the computed material properties obtained correspond to a perfect crystal situation ($Q_i = 1$). As the internal quantum efficiency tends to vanish, variations of the optical properties are expected as defects will introduce new electronic states. However, in this work the perfect crystal optical properties are considered for each value of Q_i . Accordingly, the absorptance $A(E)$ of the absorber layer is determined via Eq.(2.92), assuming a flat solar cell surface and a thin film thickness d .

The obtained results are presented for a solar cell temperature $T=300\text{K}$ as follow:

- First, we evaluate the optimal thicknesses (associated to a maximum for η) of the absorber layer as a function of Q_i . To this perspective, the efficiency of the solar cell is calculated for different values of the absorber layer thickness d and for various internal quantum efficiency values $Q_i \in [10^{-6}; 1]$ (see **Fig.4.4**). The efficiencies were calculated using the materials reflectivity $R(E)$ as obtained from the first-principles calculations.
- Using this optimal thickness, we compute the maximal efficiency for a range of internal quantum efficiency values $Q_i \in [10^{-6}; 1]$ (see **Fig.4.5**). In addition, to highlight the impact of the absorber layer reflectivity on the solar cell properties, the calculation is performed with and without taking into account the materials reflectivity $R(E)$ in the calculation of the absorptance $A(E)$ (*cfr.* Eq.(2.92)).
- Then, in **Fig.4.6**, the current density voltage curves for the respective kesterite-based solar cells are presented for different internal quantum efficiency values $Q_i \in [10^{-6}; 1]$ and for a usual absorber layer thickness of $1.5 \mu\text{m}$.
- In **Tab.4.3**, the main solar cell electrical characteristics are reported first by assuming no non-radiative recombination ($Q_i = 1$) and secondly by assuming a non-radiative recombination rate fixed by $Q_i = 10^{-4}$ in order to obtain results comparable to actual experimental device characteristics (*e. g.*, experimentally comparable V_{OC} values). Finally, the results obtained are compared to various experimental works.

In **Fig.4.4**, the maximal efficiency is calculated as a function of the absorber layer thickness. Each curve represents an internal quantum efficiency value ranging logarithmically from 1 (highest efficiency) to 10^{-6} (lowest efficiency). Here, we report a significant disparity between the Cu_2ZnSi_4 -based solar cell efficiencies with values

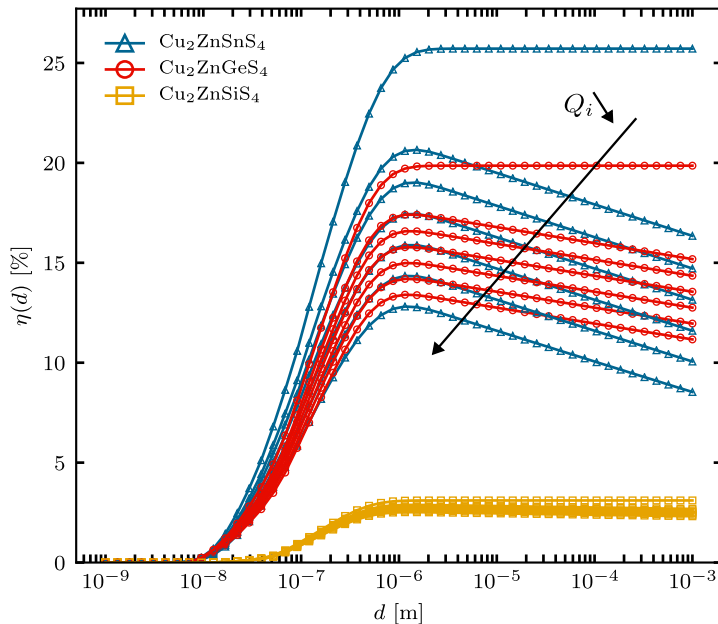


Figure 4.4: Solar cell efficiency modelling presented as a function of the absorber thin film thickness d for various internal quantum efficiency $Q_i \in [10^{-6}; 1]$. The efficiencies were calculated using the materials reflectivity $R(E)$ as obtained from the first-principles calculations.

below 5% for all Q_i , compared to the cells based on the two other kesterite materials. This observation is linked to the larger bandgap of $\text{Cu}_2\text{ZnSiS}_4$, which limits drastically the short circuit current density (see section 2.4.2 and Eq.(2.89)) as illustrated in **Fig.4.6** and **Tab.4.3**. The general trend observed for all materials is an increase of the efficiency as the absorber thickness increases over 10 nm. Then, for d just above $1 \mu\text{m}$, the efficiency reaches a plateau, for $Q_i = 1$, with maximal efficiency values of 25.71, 19.85 and 3.1 % respectively for the Sn-, Ge- and Si-kesterite compound. In contrast, for $Q_i < 1$, the efficiencies reach a maximal value for an optimal thickness before decaying linearly as d increases. The optimal thicknesses reported for the absorber layer thin films are between 1.15 and $2.68 \mu\text{m}$ (*cf.* **Tab.4.3**). The observed increase of η with d can be explained by the optimisation of the absorptance function $A(E)$ which gets closer to $1 - R(E)$ for $E > E_G$, thus maximising the short circuit current density. The optimisation of the absorptance also maximises $J_{\text{rad},0}$ which reduces V_{OC} and reduces η but this phenomenon is not dominant here. Then, for a unit value of Q_i , J_{SC} asymptotically reaches a maximum value and any further increase of the thickness (over the optimal thickness value) does not result in any notable increase of the efficiency value. In contrast, for internal quantum efficiency values $Q_i < 1$, as the absorber layer gets thicker, the non-radiative recombination rate increases, leading to a decrease of the open circuit voltage and, consequently, to the efficiency drop (see section 2.4.2).

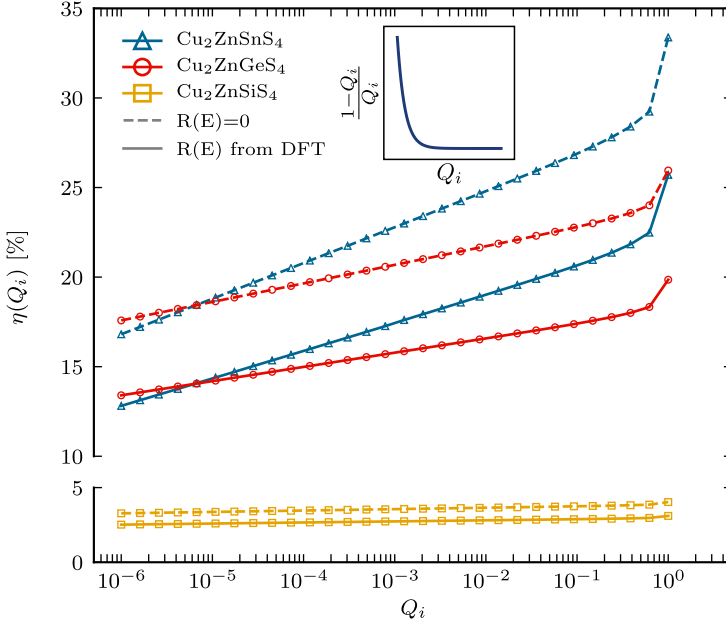


Figure 4.5: Solar cell efficiency modelling for an optimal absorber layer thickness extracted from **Fig.4.4** presented as a function of the internal quantum efficiency $Q_i \in [10^{-6}; 1]$. Results from simulations taking into account the materials reflectivity $R(E)$ are presented in full lines while dashed lines represent the maximal efficiencies obtained assuming $R(E) = 0$. In inset, evolution of the prefactor fixing the non-radiative recombination rate as described in Eq.(4.1) with respect of Q_i .

From the previous calculations, for each Q_i value, the absorber layer thickness giving the maximum efficiency is extracted as the optimal absorber thickness value d_{opt} . Then, in a second calculation (*cfr.* **Fig.4.5**), the evolution of the maximal efficiency as a function of the internal quantum efficiency for an optimal thickness is reported both without (dashed lines, $R(E) = 0$) and with (full lines, $R(E)$ from DFT results in section 4.3.3) taking into account the materials reflectivity in the absorbance calculation (see Eq.(2.92)). Concerning the impact of the materials reflectivity on the solar cell efficiency for the $\text{Cu}_2\text{ZnSnS}_4$ compound, depending on the Q_i value, a percentage point loss of 4 to 8 in efficiency is observed (decrease of 4 to 6 observed for $\text{Cu}_2\text{ZnGeS}_4$ and of 1 for $\text{Cu}_2\text{ZnSiS}_4$). Concerning the behaviour of η with respect to Q_i , the cell efficiency increases as Q_i tends to unity and as the non-radiative recombination rate decays towards 0 (see Eq.(4.1)). Then, as the internal quantum efficiency decreases, the efficiencies reported also decrease with absolute percentage point losses of 1.54, 0.79 and 0.07 per order of magnitude, respectively for $\text{Cu}_2\text{ZnSnS}_4$, $\text{Cu}_2\text{ZnGeS}_4$ and $\text{Cu}_2\text{ZnSiS}_4$. The variation of the slopes of the material curves observed in **Fig.4.5** from one kesterite to another is a direct consequence of the materials optical properties variations. Following the cationic substitution, the

variation of the material absorptance function leads to a decrease of the radiative recombination rate value. As a consequence, for lower value of $R_{\text{rad},0}$, a variation of Q_i implies a smaller variation of the non-radiative recombination rate and consequently of the total recombination rate. In addition, any increase of the saturation current density J_0 will lead to a decrease of the open circuit voltage and consequently of the efficiency. Combining these two explanations, as the material absorptance gets optimal with respect to the black body spectrum (from $\text{Cu}_2\text{ZnSiS}_4$ to $\text{Cu}_2\text{ZnSnS}_4$), the larger the radiative recombination rate is, the larger the efficiency variation per decade of Q_i will be. Then, following the variation of the slope observed, for a fixed efficiency value (for example 15%), $\text{Cu}_2\text{ZnSnS}_4$ appears more "robust" to larger non-radiative recombination rate as the Q_i value required to reach this efficiency is lower for $\text{Cu}_2\text{ZnSnS}_4$ than for $\text{Cu}_2\text{ZnGeS}_4$. This highlights the fact that even for a lower ratio of radiative over total recombination rates, a same efficiency is obtained. This tendency is reversed for Q_i value lower than 10^{-5} .

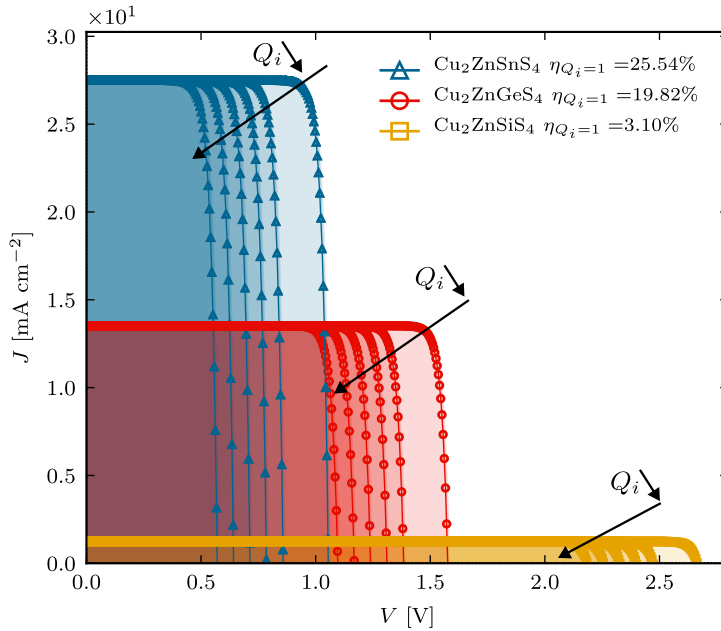


Figure 4.6: Current density-voltage curves of solar cell modelling for various internal quantum efficiency $Q_i \in [10^{-6}; 1]$. Results obtained for an absorber layer thickness of $1.5 \mu\text{m}$.

As shown in **Fig.4.6**, the short circuit current density J_{SC} is independent of Q_i as this one is related to the total number of electron-hole pair (EHP) generated by photons absorption (see section 2.4.2). This quantity depends only on the absorptance of the materials. Following the cationic substitution, the J_{SC} value decreases as the absorptance function worsen with respect to the solar spectrum. In opposition, an increase of the open circuit voltage is observed as the cation is substituted. Indeed, as the optical properties degrades, the radiative recombination rate decreases and consequently the V_{OC} value increases. In addition V_{OC} is Q_i dependent. For a given

material, as Q_i tends towards a null value, the total recombination rate will increase resulting in a decrease of the V_{OC} value, leading to the decrease of the cell efficiency as reported in **Fig.4.5**. Finally, the differences in η between the three kesterite materials are associated to the decreasing value of J_{SC} which is not fully compensated by the increase of the V_{OC} both attributed to the poorer absorptance as we move from the Sn-containing compound to the Si-containing compound.

Materials	E_G [eV]	$R(E)$	Q_i	d_{opt} [μm]	J_{SC} [mAcm^{-2}]	V_{OC} [V]	FF [%]	η [%]	Exp.	Theo.
$\text{Cu}_2\text{ZnSnS}_4$	1.32	0	1	2.68	35.69	1.06	88.62	33.38	[52]	[87, 169]
		0	10^{-4}	1.15	35.21	0.70	84.56	20.78		
		DFT	1	2.68	27.68	1.06	88.54	25.71		
		DFT	10^{-4}	1.15	27.19	0.70	84.39	15.88		
$\text{Cu}_2\text{ZnGeS}_4$	1.89	0	1	2.02	17.62	1.58	91.65	25.95	[15]	[15, 143, 161]
		0	10^{-4}	1.15	17.53	1.23	89.82	19.65		
		DFT	1	2.02	13.55	1.58	91.59	19.85		
		DFT	10^{-4}	1.15	13.45	1.22	89.73	14.98		
$\text{Cu}_2\text{ZnSiS}_4$	3.06	0	1	1.53	1.61	2.67	94.58	4.03	N.A.	N.A.
		0	10^{-4}	1.15	1.60	2.32	93.88	3.46		
		DFT	1	1.53	1.24	2.66	94.55	3.10		
		DFT	10^{-4}	1.15	1.23	2.31	93.85	2.66		

Table 4.3: Kesterite Cu_2ZnXS_4 (X=Sn,Ge,Si)-based solar cell efficiency modelling using the theoretical model proposed by Blank *et al.* [87]. Short circuit current density J_{SC} , open circuit voltage V_{OC} , fill factor FF and cell efficiency η values are presented. For each calculation, the optimal absorber layer thickness d_{opt} has been precalculated and then used as parameter. Results are presented for an internal quantum efficiency $Q_i = 1$ and $Q_i = 10^{-4}$ for experimentally comparable V_{OC} values. In order to highlight the impact of the materials reflectivity $R(E)$, the calculation have been performed both for $R(E) = 0$ and for $R(E)$ values as obtained using DFT calculations.

In **Tab.4.3**, we report the electrical solar cell characteristics for each kesterite material incorporated as the absorber layer with the optimal thickness d_{opt} and for an internal quantum efficiency Q_i . Focusing on the results obtained using DFT-calculated reflectivity $R(E)$ and using an internal quantum efficiency of $Q_i = 10^{-4}$ giving open circuit voltage value comparable to experimental ones [52], solar cell efficiencies of 15.88, 14.98 and 2.66 % are reported respectively for $\text{Cu}_2\text{ZnSnS}_4$, $\text{Cu}_2\text{ZnGeS}_4$ and $\text{Cu}_2\text{ZnSiS}_4$ (for an optimal thickness of 1.15 μm). In comparison to efficiency values obtained for vanishing radiative recombination rate (25.71, 19.85 and 3.1 % respectively for the Sn-, Ge- and Si-kesterite), one can observe a percentage point loss of nearly 10 for the Sn-compound (4.86 and 0.44 for the Ge- and Si-compound respectively). Then, experimentally, lower J_{SC} values around 21.5 mAcm^{-2} and smaller fill factors values between 60 and 65 % are reported [52]. This observation highlights

that the predictions realised with this model corresponds to upper limits. Indeed, nor the materials reflectivity or the absorption of the solar cell upper layers are taken into account, leading to an overestimation of J_{SC} . Concerning the fill factor, the electrical behaviour of the electrodes is assumed to be ideal. By repeating the calculation with a fixed short circuit current density matching the experimental value, a cell efficiency of 12.29 % is reported as well as a V_{OC} value of 685 mV. This result is in good agreement with the values reported experimentally [52].

Using this methodology, we confirmed the interest regarding $\text{Cu}_2\text{ZnSnS}_4$ for single-junction solar cell and we highlight a possible efficiency improvement of nearly 10 % which might be achieved by reducing the non-radiative recombination rate. Then, $\text{Cu}_2\text{ZnGeS}_4$ might be interesting as top cell for tandem approaches [15, 170] as this material provides higher bandgap value and interesting cell efficiencies. Finally, the low efficiency values reported for $\text{Cu}_2\text{ZnSiS}_4$, imputed to its high bandgap value, reduces the range of PV applications for this material.

4.5 CONCLUSION

In conclusion, we reported direct bandgap values of 1.32, 1.89 and 3.06 eV and absorption coefficients of the order of 10^4 cm^{-1} for, respectively, $\text{Cu}_2\text{ZnSnS}_4$, $\text{Cu}_2\text{ZnGeS}_4$ and $\text{Cu}_2\text{ZnSiS}_4$. Simultaneously a slight increase of the effective mass values is reported following the sequential substitution. Then, using as input data the optical properties of the materials, the solar cell electrical characteristics are predicted based on an improved version of the Shockley-Queisser model. Optimal absorber layer thicknesses between 1.15 and 2.68 μm are reported and efficiencies of 25.71, 19.85 and 3.10 % are obtained for the kesterite compounds following the cationic substitution and the induced variation of the materials properties. In addition, using optical results, we highlighted the negative impact of the materials reflectivity on the solar cell characteristics. Using a non-radiative recombination rate giving V_{OC} values comparable to actual experimental measurements, we reported a decrease of the solar cell efficiencies to 15.88, 14.98 and 2.66 % respectively for $\text{Cu}_2\text{ZnSnS}_4$, $\text{Cu}_2\text{ZnGeS}_4$ and $\text{Cu}_2\text{ZnSiS}_4$. Pointing out these results as upper limits, by reducing the non-radiative recombination current density, the efficiency of $\text{Cu}_2\text{ZnSnS}_4$ and $\text{Cu}_2\text{ZnGeS}_4$ could be improved respectively by 9.83 and 4.87 %, putting forward these kesterite compounds as promising absorber layer materials.

In this work, we consequently highlight the possible efficiency improvement concerning kesterite-based solar cell if one does reduce the non-radiative recombination rate. However, here, we do not point out any specific recombination centre that could effectively participate to these bulk recombinations. This investigation will be at the heart of the following chapter in which we decided to study the physical behaviour of point defects in $\text{Cu}_2\text{ZnSnS}_4$ and $\text{Cu}_2\text{ZnGeS}_4$ leaving aside the $\text{Cu}_2\text{ZnSiS}_4$ kesterite

material due to the limited efficiencies reported.

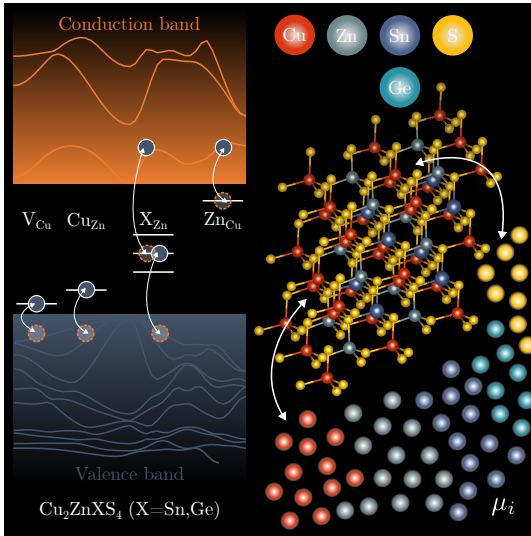
PHYSICS OF POINT DEFECTS IN KESTERITE

5

5.1	Introduction	125
5.2	Computational method	127
5.3	Point defect landscape	128
5.3.1	Kesterite growth: chemical environment	128
5.3.2	Intrinsic point defect formation energies	130
5.3.3	Defect identification: ionisation levels	135
5.4	Atomic distortions	137
5.5	Conclusion	140

This chapter is based on the following work:

Ratz, T., Nguyen, N. D., Brammertz, G., Vermang, B., & Raty, J. Y. (2022). *Relevance of Ge incorporation to control the physical behaviour of point defects in kesterite*. Journal of Materials Chemistry A, **10(8)**, 4355-4365.



Abstract To reduce the prominent V_{OC} -deficit that limits kesterite-based solar cell efficiencies, Ge has been proposed over the recent years with encouraging results as the reduction of the non-radiative recombination rate is considered as a way to improve the well-known Sn-kesterite world record efficiency. To gain further insight into this mechanism, we investigate the physical behaviour of intrinsic point defects both upon Ge doping and alloying of $\text{Cu}_2\text{ZnSnS}_4$ kesterite. Using a first-principles approach, we confirm the p-type conductivity of both $\text{Cu}_2\text{ZnSnS}_4$ and $\text{Cu}_2\text{ZnGeS}_4$, attributed to the low formation energies of the V_{Cu}

and Cu_{Zn} acceptor defects within the whole stable phase diagram range. Via doping of the Sn-kesterite matrix, we report the lowest formation energy for the substitutional defect Ge_{Sn} . We also confirm the detrimental role of the substitutional defects X_{Zn} ($X=\text{Sn,Ge}$) acting as recombination centres within the Sn-based, the Ge-doped and the Ge-based kesterite. Upon Ge incorporation, we highlight, along with the increase of the X_{Zn} ($X=\text{Sn,Ge}$) neutral defect formation energy, the reduction of the lattice distortion. Both of these elements leading to a decrease of the non-radiative recombination rate within the bulk material following the Sn substitution by Ge.

5.1 INTRODUCTION

In the previous chapter, we highlight the room for improvement for both $\text{Cu}_2\text{ZnSnS}_4$ and $\text{Cu}_2\text{ZnGeS}_4$ by reducing the non-radiative recombination rate. Moreover, as already pointed out, possible culprits for the actual efficiency limitation are electronic defects [50, 70, 72, 127, 171, 172] together with other obstacles such as band alignments [85, 134, 171], secondary phases [127, 172] and/or band tailing caused by electrostatic potential fluctuations due to the presence of charged impurities [50, 171, 173].

Focusing on defects, as a result of the complex structure of kesterite materials, a wide range of intrinsic and cluster defects can form within the crystal, leading to various impacts on the kesterite absorber layer optoelectrical properties. Using first-principles calculations, Chen *et al.* were able to predict the p-type conductivity of $\text{Cu}_2\text{ZnSn}(\text{S},\text{Se})_4$ via the high population of the Cu_{Zn} and V_{Cu} defects while identifying the $[2 \text{Cu}_{\text{Zn}} + \text{Sn}_{\text{Zn}}]$ cluster defect as recombination centre leading to charge carrier losses [70]. Experimentally, Dimitrievska *et al.* reported the possible tuning of the V_{OC} value according to the Cu concentration and consequently the amount of $[\text{V}_{\text{Cu}} + \text{Zn}_{\text{Cu}}]$ defect clusters [127]. More recently, Kim *et al.* identified the intrinsic defect Sn_{Zn} as the origin of the electron capture and emission in the $\text{Cu}_2\text{ZnSnS}_4$ compound resulting of the Sn multivalence [72, 174]. The same authors also highlighted the large lattice distortion imputed to the Sn in its oxidation state +2 with respect to its +4 state leading to a large carrier capture cross section associated to this so-called "lone-pair effect" [73]. Furthermore, Gong *et al.* established a link between the Sn oxidation states Sn^{+2} and Sn^{+4} and the kesterite growth conditions [175]. Consequently, gaining further knowledge into point defects and cluster defects in kesterite materials could allow the control of the absorber layer physical properties in view of increasing the kesterite-based cell efficiencies.

Over the recent years, attempts have been made to circumvent these actual limitations using alloying and doping of kesterite materials with other elements [56, 74–76, 79, 176, 177]. Both theoretical and experimental approaches have been used. A wide range of cationic substitutions have been investigated: Cu by Ag [82, 178], Zn by Cd [81, 178–180], Sn by Ge [15, 137, 180–182], S by Se [52] and doping of both $\text{Cu}_2\text{ZnSnS}_4$ and $\text{Cu}_2\text{ZnSnSe}_4$ by Na, Li, Ga [183] and Ge [74, 77, 78, 184] or even using more exotic elements as in Ref. [75]. Some of these substitutions resulted in cell efficiencies as large as 12.3 % as in the case of Ga or Ge doping [78, 183]. Double cation incorporation like Ge and Ag [185] or Ge and Cd [180, 186] were also realised simultaneously allying the benefits of both substitutional elements. Nevertheless, at the time, the reported efficiencies were still below the 2013-record of pure Sn-kesterite compounds [65]. More recently, in 2023, the world record efficiency of 14.9% now includes Ag-alloyed $\text{Cu}_2\text{ZnSn}(\text{S},\text{Se})_4$ [57].

From these investigations, Ge emerged as an interesting doping/alloying element as several studies reported high solar cell efficiencies through the improvement of the V_{OC} values following the incorporation of small amounts of Ge [77] or via the complete substitution of Sn by Ge [181]. In a recent study, Deng *et al.* demonstrated experimentally that Ge⁴⁺ can be introduced in $\text{Cu}_2\text{ZnSnS}_4$ to suppress the detrimental deep Sn_{Zn} defects [184]. In addition, compared to $\text{Cu}_2\text{ZnSnS}_4$, pure Ge-kesterite absorber layers present a larger bandgap value which limits the maximal single solar cell efficiency [86]. Nevertheless, Ge alloying could be used for the synthesis of wide bandgap kesterite which is of high interest in a tandem approach [15, 137] both for bottom and top cells with respectively perovskite and Si as presented in detailed by Jimenez *et al.* in Ref. [16]. Gaining further insight into the physical behaviour of intrinsic defects in Ge-kesterite and into the mechanisms of Ge doping within the Sn-kesterite is therefore strongly desirable.

Moreover, although several material modelling studies have focused on the physical behaviour of defects in kesterite compounds [70, 72, 75, 183], only a few works have been dedicated so far to Ge compounds [128, 180, 187]. To fill this void, in this work, we report the investigation of point defects in both $\text{Cu}_2\text{ZnSnS}_4$ and $\text{Cu}_2\text{ZnGeS}_4$. We first study the physical behaviour of intrinsic point defects in both kesterite materials to highlight the impact of Ge alloying and secondly, we investigate Ge-related point defects in the Sn-kesterite compound to illustrate the Ge doping mechanism. Focusing on the physical behaviour of point defects in these materials, our aim is to establish a link between the growth conditions of the kesterite thin films, the formation of point defects and the resulting kesterite solar cell performances by identifying the defect physical behaviour (dopant or recombination centre). In addition, based on the empirical rule proposed by Li *et al.* we derive meaningful trends concerning the defect carrier capture cross sections $\sigma_{n,p}$. Indeed, it was reported that this quantity can be related to the lattice distortion caused by the defect incorporation in its various charge states q [109]. This interpretation is then discussed based on the SRH statistics and the microscopic origin of the capture coefficients $k_{n,p}$ (functions of $\sigma_{n,p}$) presented in section 2.3.3.

The chapter is organised as follows. The phase diagrams of the two kesterites are first presented. Once proper chemical potential ranges are set, avoiding secondary phases and obtaining the desired kesterite phase, the defect formation energies are obtained according to the Fermi level position. Then, we present the defect charged states and their possible ionisation levels in order to evaluate their physical behaviour in their various electronic configurations. This approach allows us to identify their roles as dopant or as recombination centre. Finally, in the last part, we present a study of the lattice distortions around the different incorporated defects. This information allows us to provide a guide for the extraction of general trends concerning the charge capture of the various point defects at play. As a result, we are able to predict which point defects are the most abundant in the kesterite materials and eventually, to characterise the defect levels (acceptor, donor or recombination centre) and their

relative impact on the capture of charge carriers. Considering various locations in the phase diagram, we also consider different growth conditions of the kesterite materials. This study allows to highlight (i) the impact of Ge-alloying of kesterite on the intrinsic point defects physical behaviour and (ii) the physical behaviour of Ge dopants in $\text{Cu}_2\text{ZnSnS}_4$.

5.2 COMPUTATIONAL METHOD

Using the theoretical description of the supercell approach presented in section 3.3, the defect formation energies are computed according to Eq.(5.1), displayed a second time here to ease reading.

$$\Delta H_F(\alpha, q, E_F, \mu_i) = \underbrace{E(\alpha, q) - E_{\text{host}}}_{\text{Pristine/defected cells energy difference}} - \underbrace{\sum_i n_i(E_i + \mu_i)}_{\text{Cost of element exchange}} + \underbrace{q[\epsilon_{V_{BM,host}} + E_F]}_{\text{Cost of charge exchange}}, \quad (5.1)$$

with α the point defect under study (as defined in section 2.3.1), q the defect charge state (integer number), E_F the Fermi energy level and μ_i the elemental chemical potential. First, to obtain the total energies of the defected $E(\alpha, q)$ and host supercells E_{host} and of the secondary phases and pure elemental phases E_i , first-principles calculations have been performed using the Vienna *ab initio* Simulation Package (VASP) code [148] with the Projector-Augmented Wave (PAW) potential method [149]. Perdew-Burke-Ernzerhof (PBE) GGA pseudo-potentials [150] were used with the following valence electrons considered for each element: Cu: $3d^{10}4s^1$, Zn: $3d^{10}4s^2$, Sn: $4d^{10}5s^25p^2$, Ge: $3d^{10}4s^24p^2$ and S: $3s^23p^4$. To this regard, appendix A offers an overview of the VASP software practical features pertinent to these calculations.

Within a 64-atoms supercell, ionic and electronic relaxations were achieved using a cut-off energy of 520 eV and a Γ -centred uniform \mathbf{k} -points mesh of $2 \times 2 \times 2$ \mathbf{k} -points. Applying the strongly constrained and appropriately normed semilocal density functional (SCAN) [151, 152], the structures were relaxed until the numerical convergence regarding the self-consistent cycles reached forces between ions less than 10^{-3} eV/Å. Starting from the relaxed structures, a single-shot calculation using the Heyd–Scuse-ria–Ernzerhof exchange-correlation functional (HSE06) [147] is performed using an energy convergence criterion upon 10^{-3} eV. The combination of SCAN ionic relaxations followed by a single HSE06 electronic relaxation was reported as an efficient method to obtain accurate results by Fritsch *et al.* in Ref. [153]. Concerning Ge-containing compounds, a correction was applied to the Ge-chalcogenide formation energies to tackle the systematic underestimation reported by Wexler *et al.* [128]. This correction is further described in section 3.3.3.

First, from the presented methodology, $\text{Cu}_2\text{ZnSnS}_4$ and $\text{Cu}_2\text{ZnGeS}_4$ kesterite phase diagrams are computed in order to fix the growth conditions of the material under study by computing the element chemical potentials μ_i . Then, the defect formation energies are depicted using the format presented in section 3.3.1 (see **Fig.3.5**).

5.3 POINT DEFECT LANDSCAPE

5.3.1 Kesterite growth: chemical environment

Let us first determine the chemical environment in which the kesterite materials can be synthesised without secondary phases¹. In **Fig.5.1**, the phase diagrams of Sn-based and Ge-based kesterites are presented for three different Cu concentrations: $\mu_{\text{Cu}} = -0.27$ (Cu-rich) eV, $\mu_{\text{Cu}} = -0.55$ eV (Cu-moderate) and $\mu_{\text{Cu}} = -0.82$ eV (Cu-poor).

A first general observation is the narrow chemical potential range in which the kesterite phase can be found without any secondary phase (green shading) in comparison to the possible chemical potentials combinations that could lead to the formation of the kesterite (grey shading). For lower Cu concentrations, corresponding to a μ_{Cu} value lower than -0.82 eV (resp. -0.85 eV for $\text{Cu}_2\text{ZnGeS}_4$), no pure kesterite phase is available within stable combinations of chemical potentials values. This means that below such a critical μ_{Cu} value, the kesterite phase cannot be formed without the presence of secondary phases. In addition, as presented in **Fig.5.1(a)**, we observe a reduction of the stable kesterite phase area (grey shading) as we move towards lower Cu concentration. If one chemical potential absolute value increases for a constant kesterite formation energy, the available chemical potential combination range is reduced (the edge of the stable kesterite phase corresponding to $\mu_{\text{S}} = 0$ is shrunk). Physically, it means that for a lower chemical potential value corresponding to a lower concentration, another element concentration has to increase to keep obtaining a stable kesterite phase.

The reduction of the stable kesterite areas (grey shading) to the pure kesterite areas (green shading) is the result of the multiple secondary phases that can be formed using the 4 chemical elements composing the kesterite compounds. As shown in **Fig.5.1(a)**, around the green area, the dominant secondary phases are ZnS , Cu_7S_4 , Cu_2SnS_3 and SnS . The phases predicted by our calculations are in good agreement with those reported by Chen *et al.* in Ref. [70]. In addition, in the recent review of Schorr *et al.*, the authors reported the presence of ZnS in each thin film where the composition Zn/Sn exceeded the value of 1. It was also reported that the concentrations of both ZnS and SnS secondary phases increase upon deviation from the

¹In **Tab.4.3** of appendix A, the secondary phases formation energies values are presented as computed from $\Delta H_F(A_i B_j) = E_{A_i, B_j} - n_i E_A - n_j E_B$.

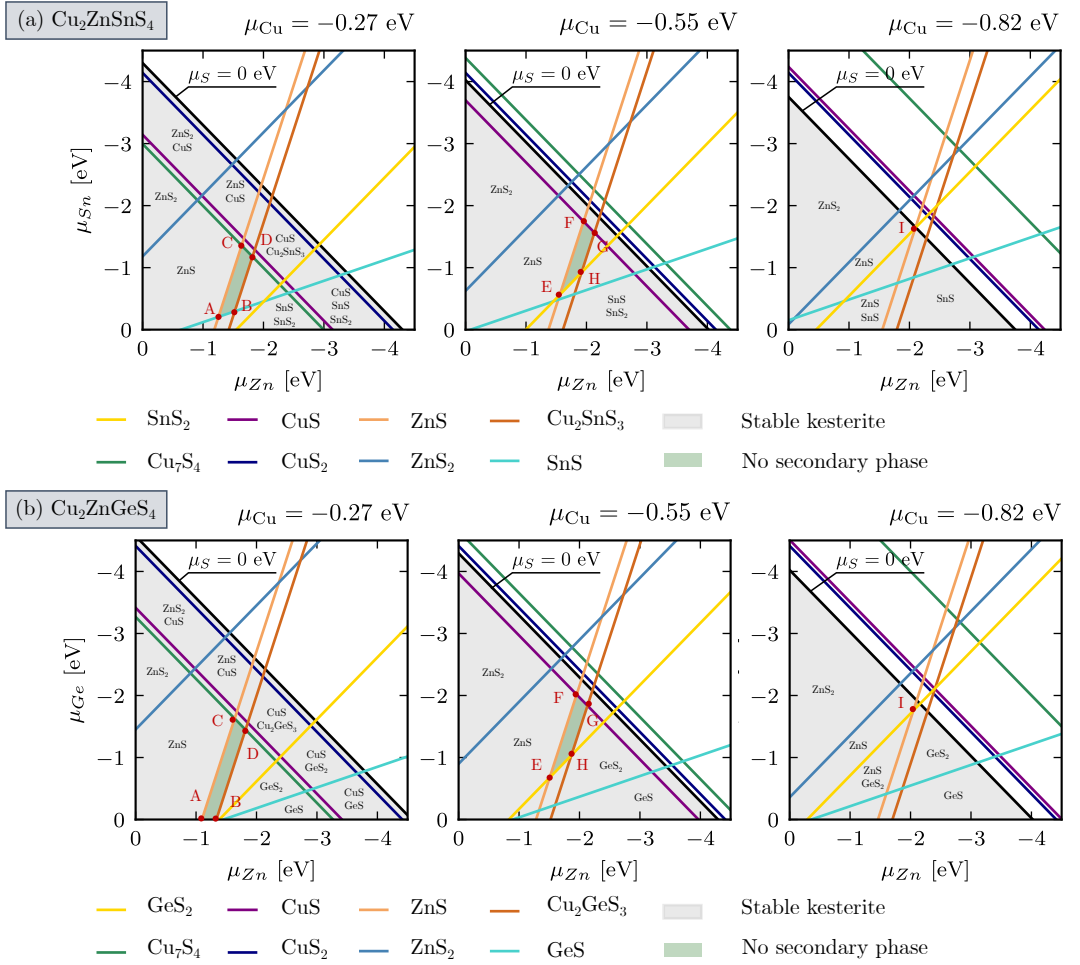


Figure 5.1: Phase diagrams of $\text{Cu}_2\text{ZnSnS}_4$ and $\text{Cu}_2\text{ZnGeS}_4$ for three different Cu concentrations. Each line corresponds to a secondary phase as listed in the legends (see section 3.3 for the secondary phase calculations). The grey-shaded areas correspond to chemical potential values for which the kesterite can be thermodynamically synthesised (stable phase). Upon taking into account the possible presence of the secondary phases, the green shading indicates the chemical potential ranges for which a kesterite stable phase is encountered without any secondary phase. [Python code provided to the reader here.](#)

stoichiometry [127, 172, 188]. Similarly, for the Ge-compound in **Fig.5.1(b)**, the secondary phases located next to the pure kesterite phase are ZnS, Cu₇S₄ and Cu₂GeS₃. Experimentally, using XRD and HAADF-STEM imaging, Khelifi *et al.* held the ZnSe secondary phase at the top of the absorber layer and a thick Cu₂GeSe₃ secondary phase (120-160 nm) at the bottom of the kesterite thin film accountable for the main efficiency loss [137]. In the case of the Ge-based compound and in comparison with the SnS phase in the Sn-kesterite, the GeS secondary phase appears to be shifted towards positive Ge chemical potential values. As a result, the Ge-kesterite pure phase

area (green shading) is slightly larger compared to the Sn-kesterite one. Following the phase diagram evolution from **Fig.5.1(a)**, we observe that, as the absolute value of the Cu chemical potential increases, the SnS₂ and SnS secondary phase limits shift towards lower Sn concentrations while the ZnS secondary edge shifts towards lower Zn concentrations until both SnS₂ and ZnS secondary phase edges cross each other for a Cu chemical potential value of $\mu_{Cu}=-0.82$ eV, leading to the vanishing of the pure kesterite area. The same behaviour can be observed for Cu₂ZnGeS₄ with an extreme copper chemical potential value of -0.85 eV involving the following secondary phases: GeS, GeS₂ and ZnS. Recently, Choubrac *et al.* reported for Cu₂ZnGeS₄ the effectiveness of a set of different surface treatments to get rid off all detrimental secondary phases [181].

Then, to compute Ge-doping point defects in the Sn-based kesterite, one has to obtain a chemical potential value for the Ge (μ_{Ge}). To do so, as presented **Tab.4.3** of appendix A, several additional secondary phases were computed. Moreover, in same appendix, in **Tab.A.2**, the specific chemical potential values labelled from A to I in **Fig.5.1** are detailed. In addition, using the following [link](#), an applet is provided to the reader where both Cu₂ZnSnS₄ and Cu₂ZnGeS₄ phases diagrams can be tuned using a slider setting the copper chemical potential value μ_{Cu} .

In the next section, we will focus on the formation energy of the point defects using chemical potential combinations providing a pure kesterite phase. As explained with additional details in section 3.3, using Eq.(5.1) to compute the defect formation energies, one has to ensure that the chemical reservoirs used (*e. g.*, chemical potentials) contribute only to the formation of the kesterite phase and not to the synthesis of secondary phases.

5.3.2 Intrinsic point defect formation energies

In **Fig.5.2**, we present the formation energies of kesterite point defects for the chemical potentials μ_i corresponding to point E in **Figs.5.1(a)** and (b) (see Eq.(5.1)). The choice for this particular composition point was motivated by the perspective of selecting a chemical potential combination corresponding to a pure kesterite phase and as close as possible to the Cu-poor and Zn-rich conditions usually used to synthesise kesterite thin films [65, 70, 172]. One has to keep in mind that **Fig.5.2** corresponds to a glimpse of the defect formation energy function for one material growth condition. In each frame (constant chemical potential values μ_i), each line corresponds to a specific defect α in a given charge state q . Using the following [link](#), a second applet is provided to the reader where the defect formation energies in both Cu₂ZnSnS₄ and Cu₂ZnGeS₄ can be tuned using sliders. According to Eq.(5.1), the defect formation energy $\Delta H_F(E_F)$ is represented as a function of the Fermi energy level within the kesterite bandgaps as predicted by the HOMO-LUMO Kohn-Sham eigenvalues extracted from the first-principles calculations which are equal to 1.32 eV and 1.89 eV respectively for Cu₂ZnSnS₄ and Cu₂ZnGeS₄ [86].

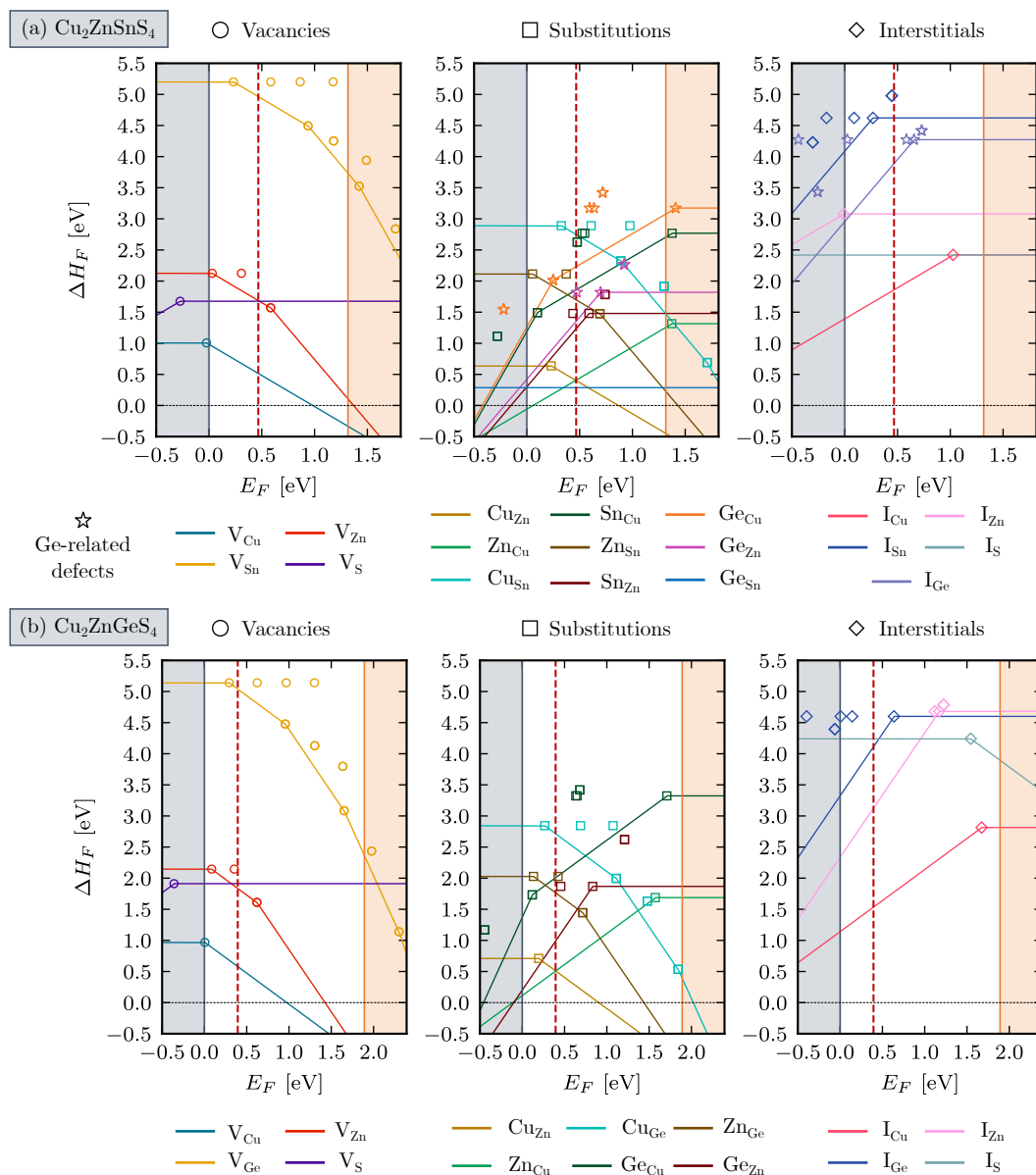


Figure 5.2: Formation energies of point defects in (a) $\text{Cu}_2\text{ZnSnS}_4$ and (b) $\text{Cu}_2\text{ZnGeS}_4$ for three different types of defects calculated at the chemical potential point E corresponding to $\mu_{\text{Cu}} = -0.55$ eV, $\mu_{\text{Zn}} = -1.56$ eV, $\mu_{\text{Sn}} = -0.56$ eV and $\mu_{\text{Ge}} = -0.79$ eV for the Sn-kesterite and $\mu_{\text{Cu}} = -0.55$ eV, $\mu_{\text{Zn}} = -1.506$ eV and $\mu_{\text{Ge}} = -0.675$ eV for the Ge-compound. The Fermi level under thermodynamic equilibrium conditions is represented by the maroon dashed lines. Each marker corresponds to a possible transition level between two different charge states of a same defect. [Python code provided to the reader here.](#)

Let us first focus on the intrinsic point defect formation energies in the Sn-compound as it is used as our reference material. As shown in **Fig.5.2(a)**, independently of the Fermi energy value, a first general trend is the lower formation energies of the vacancies (except V_{Zn}) and the substitutional defects in comparison to the interstitial ones. This observation can be explained by the lattice distortion cost induced by the interstitial incorporation. As it can be observed, the lowest formations energies (below 1.5 eV) are reported for the copper vacancy V_{Cu} , and for Cu_{Zn} , Sn_{Zn} and Zn_{Cu} substitutional defects. In **Fig.5.2(b)** we report the same trend concerning the behaviour of the intrinsic point defect formation energies in the Ge-based compound, highlighting the similarity of intrinsic defects in both kesterites.

In addition, as presented in **Fig.5.2** using the methodology described in the section 3.3.1 (see Eq.(3.47)), the Fermi level under thermodynamic equilibrium conditions can be extracted. As shown, in both kesterites, under equilibrium conditions the Fermi energy is pinned mainly by the charged defects V_{Cu} and Cu_{Zn} , both being in a charge state of -1 thus providing holes to the electrical conductivity while the substitutional defect Zn_{Cu} is in a charge state of +1, supplying electrons. Under equilibrium, the extracted Fermi energy level value is located 0.468 eV and 0.409 eV above the VBM, respectively for $\text{Cu}_2\text{ZnSnS}_4$ and $\text{Cu}_2\text{ZnGeS}_4$. Through this observation, we consequently highlight the p-type conductivity of $\text{Cu}_2\text{ZnSnS}_4$, a well-established experimental fact, also confirmed theoretically by Chen *et al.* [70]. More interestingly, we highlight the same behaviour for the Ge-based kesterite. To complete these observations, we also report the substitutional defect Sn_{Zn} (resp. Ge_{Zn}) which would be in a charge state +2. However as it will be described later on, Sn_{Zn} (resp. Ge_{Zn}) would more likely behave as a recombination centre.

Then, we present Ge-doping extrinsic point defects in the Sn-kesterite matrix such as Ge_{Cu} , Ge_{Zn} , Ge_{Sn} substitutional defects and I_{Ge} interstitial defect. As shown in **Fig.5.2(a)**, Ge_{Cu} and I_{Ge} have both high formation energies with values above 2 eV. This result highlights the low probability for the Ge element to be incorporated in the Sn-kesterite via Cu substitution or as interstitial. In contrast, the substitutional defect Ge_{Zn} presents a formation energy below 2 eV, whereas Ge_{Sn} has a formation energy below 0.5 eV, meaning that this defect could form quite spontaneously in presence of Ge. It is also interesting to note that in **Fig.5.2(a)**, if one compares Ge_{Cu} and Sn_{Cu} (resp. Ge_{Zn} and Sn_{Zn}), both extrinsic doping substitutional defects present higher formation energies than the intrinsic ones. It is also worth noticing that the Ge chemical potential μ_{Ge} used to compute the Ge-doping defects corresponds to the richest composition value leading consequently to the lowest formation energies. As a result, for a Ge chemical potential value lower than $\mu_{\text{Ge}} = -0.79$ eV (poorer composition), the Ge-related defect formation energies will increase (see section 3.3.1).

However, depending on the growth conditions of the materials, the defect formation energies will vary. Indeed, for a lower concentration of copper during the

materials growth, Cu vacancies will form with a greater ease and will consequently be present in a higher concentration. This behaviour is captured by the lowering of the formation energy following the change of the Cu chemical potential value in Eq.(5.1). To visualise these trends, as shown in **Fig.5.3**, the defect formation energies were represented for different hypothetical growth conditions. To do so, we represent the evolution of the formation energies following a specific path in the phase diagrams presented in **Fig.5.1** and for a Fermi energy value under thermodynamic equilibrium conditions. As presented in the phase diagrams of the Sn- and the Ge-kesterite, the chemical potential path study here is labelled as A-B-C-D-E-F-G-H-I. The chemical potentials coordinates A-B-C-D correspond to Cu-rich conditions, E-F-G-H to Cu-moderate conditions and finally the I label corresponds to a Cu-poor condition (see **Tab.A.2** for the specific chemical potential values). This path was selected to study the behaviour of the formation energies at the edges of the kesterite pure phases (as represented via the green shading in **Fig.5.1**) and following a Cu concentration from high values to lower ones. The relevant message here is consequently focused on the trends of the defect formation energies for different growth conditions and not specifically on the selected path.

In **Fig.5.3**, we identify $\text{Cu}_{\text{Zn}}^{-1}$, $\text{Zn}_{\text{Cu}}^{+1}$, $\text{Sn}_{\text{Zn}}^{+2}$ (resp. $\text{Ge}_{\text{Zn}}^{+2}$) and $\text{V}_{\text{Cu}}^{-1}$ as the intrinsic point defects showing the lowest formation energies over the different chemical potential combinations. Following these results, the usually observed Cu/Zn disorder in Sn-kesterite can also be expected in the Ge-kesterite as the two substitutional defects $\text{Cu}_{\text{Zn}}^{-1}$ and $\text{Zn}_{\text{Cu}}^{+1}$ present formation energies below 1 eV for any chemical potential combination. This result is in good agreement with those of Chen *et al.* where $\text{Cu}_{\text{Zn}}^{-1}$ is the dominant point defect [70]. In addition, we report a lower formation energy concerning the $\text{Zn}_{\text{Cu}}^{+1}$ antisite with a formation energy between 0.03 eV and 0.63 eV while this previous work predicted a formation energy between 0.6 and 0.9 eV. As a results, our calculations predict a substitutional defect $\text{Zn}_{\text{Cu}}^{+1}$ concentration within the same range as the $\text{Cu}_{\text{Zn}}^{-1}$ defect. This observation is in good agreement with the work of Du *et al.* reporting a similar $\text{Zn}_{\text{Cu}}^{+1}$ behaviour [183]. The facilitated formation of these defects could be explained by the similar atomic radii of Zn ($r_{\text{Zn}} = 1.35 \text{ \AA}$) and Cu ($r_{\text{Cu}} = 1.35 \text{ \AA}$) while their electronic configurations differ only by one electron [164]. Several studies hold the related Cu/Zn disorder defects accountable for potential fluctuations detrimental for solar cell performances [189, 190] which could however be suppressed via Ag incorporation [186].

As shown in **Fig.5.3(a)**, focusing on the Ge extrinsic doping defects, the substitutional defect Ge_{Sn} presents formation energy values below 0.5 eV for every chemical potential combination. The smaller atomic radius of Ge ($r_{\text{Ge}} = 1.25 \text{ \AA}$) in comparison to the Sn element ($r_{\text{Sn}} = 1.45 \text{ \AA}$) and their similar electronic behaviours could explain the high occurrence of this defect. Then, a general trend observed, moving from the Sn-based kesterite to the Ge-doped kesterite, is the increase of the formation energy from the intrinsic defect $\text{Sn}_{\text{Zn}}^{+2}$ with $\Delta H_F = 1.24 \text{ eV}$ to $\text{Ge}_{\text{Zn}}^{+2}$ with

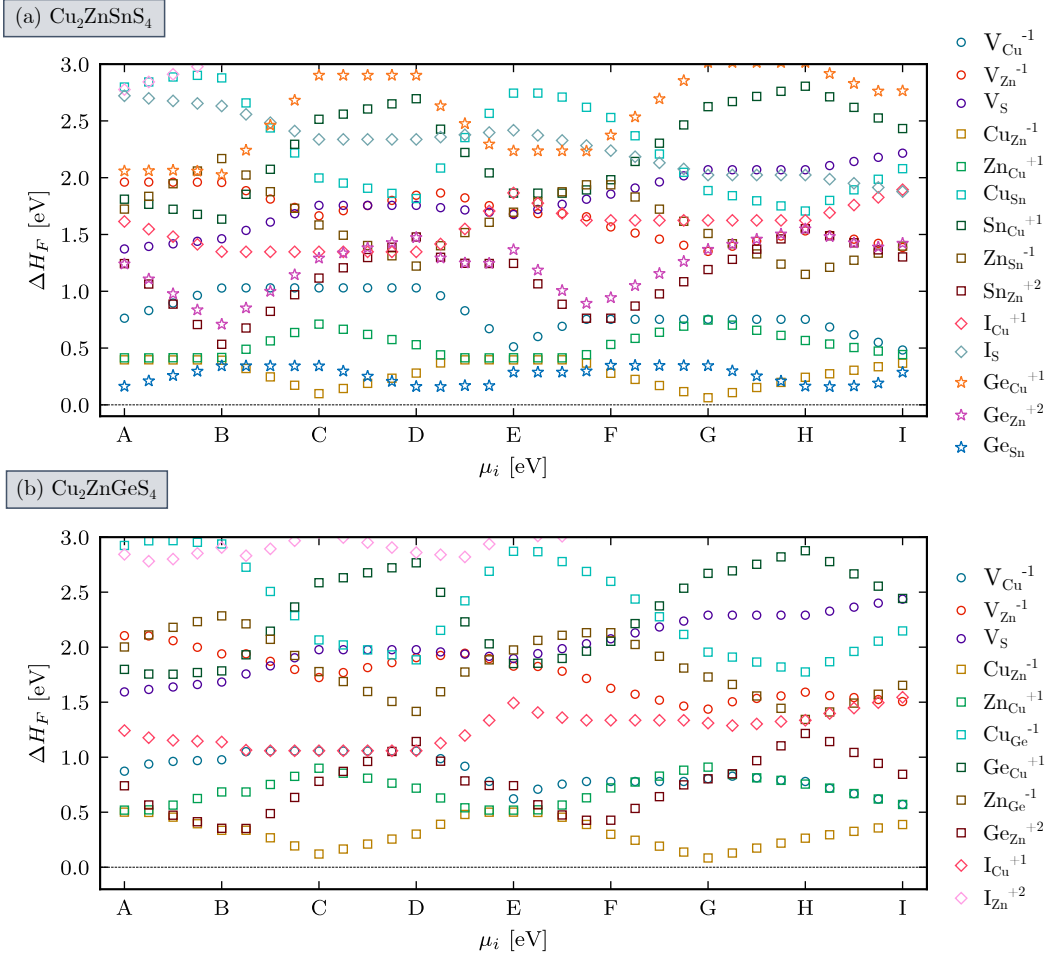


Figure 5.3: Evolution of the point defect formation energies in (a) $\text{Cu}_2\text{ZnSnS}_4$ and (b) $\text{Cu}_2\text{ZnGeS}_4$ for different hypothetical growth conditions. The calculations were performed at various chemical potential combinations corresponding to the label points presented in Figure 5.1 and for the Fermi energy levels under thermodynamic equilibrium conditions located at 0.468 eV and 0.409 eV above the VBM respectively for $\text{Cu}_2\text{ZnSnS}_4$ and $\text{Cu}_2\text{ZnGeS}_4$. Each defect is represented using a specific colour and using the following markers: circles for intrinsic vacancies, squares for intrinsic substitutional defects, diamonds for intrinsic interstitials and stars for Ge extrinsic doping defects in the Sn-based kesterite.

$\Delta H_F = 1.34$ eV (one should also note that for some chemical potentials, those quantities can be equal). As reported in **Fig.5.2**, an increase of the formation energy is also observed as we move from the neutral defect Sn_{Zn} in the Sn-based kesterite to the Ge-doped and then Ge-alloyed kesterite defect Ge_{Zn} with values of 1.45, 1.79 and 1.85 eV respectively. This implies that if Ge is available, the ease of formation of the Zn substitutional defect would be further reduced, first in the Sn-kesterite following Ge doping and then in the Ge-kesterite upon complete substitution of Sn. In their

study, Wexler *et al.* reported an increase of the $2\text{Cu}_{\text{Zn}} + \text{X}_{\text{Zn}}$ defect cluster formation energy following the complete Sn substitution [180]. This observation was attributed to the multivalence of Sn which can reduce from a 4+ to a 2+ oxidation state. This change of oxidation allows the Sn to exist in a +2 state on the Zn^{+2} site. In contrast, the Ge only exists in a 4+ state explaining the formation energy increase between the Ge_{Zn} and the Sn_{Zn} substitutional defects [73, 174, 180].

Here, we have reported $\text{Cu}_{\text{Zn}}^{-1}$, $\text{Zn}_{\text{Cu}}^{+1}$, $\text{Sn}_{\text{Zn}}^{+2}$ (resp. $\text{Ge}_{\text{Zn}}^{+2}$) and $\text{V}_{\text{Cu}}^{-1}$ as the most abundant point defects in $\text{Cu}_2\text{ZnSnS}_4$ (resp. $\text{Cu}_2\text{ZnGeS}_4$). In the next section, we focus on the physical behaviour of the following ones: acceptors, donors or recombination centres.

5.3.3 Defect identification: ionisation levels

In **Fig.5.4**, we show the ionisation levels for each defect according to Eq.(3.44). It is important to note that these levels within the kesterite bandgap are, in contrast to the formation energies, independent of the chemical potential values. The relevant information here are (i) the position of the ionisation level in the material bandgap, which determines the behaviour of the defect, and (ii) as a guide for the eye, the "formation energy value" of the ionisation energy level β for a Fermi level located at the transition level within the kesterite bandgap (see also markers in **Fig.5.2**).

For both $\text{Cu}_2\text{ZnSnS}_4$ and $\text{Cu}_2\text{ZnGeS}_4$, as shown **Fig.5.4**, we highlight the (0/-1) transition levels of Cu_{Zn} and V_{Cu} located a few $k_B T$ over the VBM. From the calculation of the Fermi energy under thermodynamic equilibrium conditions, these transition levels are ionised and consequently, these defects act as acceptors both providing holes to the kesterite conductivity. Combined with their low formation energies, these levels are particularly suited to account for the p-type intrinsic conductivity of these compounds. Then, as donor defects, we report the (+1/0) transition level of the substitutional defect Zn_{Cu} located close to the conduction band minimum (CBM). With its previously reported low formation energy, this defect is the most abundant donor in both kesterites. We can also note that in the case of the Ge-compound, in opposition to the Sn-kesterite, the (+1/0) transition level of Zn_{Cu} is below the CBM. This is a direct consequence of the bandgap increase associated to the Ge alloying. The pinning of the Fermi level under thermodynamic equilibrium condition is a result of these two observations, which explain the p-type conductivity of kesterite materials generally reported in the literature [70]. We also notice that the V_{Zn} defect provides energy levels close to the VBM, however, assuming a p-type material, the Fermi level would be close to the valence band leading to an unionised defect with a high formation energy as presented in **Fig.5.2(a)**. Concerning the substitutional defect Sn_{Cu} (resp. Ge_{Cu}), they present ionisation states not suited for intrinsic doping (*e. g.*, "donor states" close to the valence band). A similar behaviour is observed for the substitutional defect Cu_{Sn} . As a consequence, these defects should not contribute significantly to the conductivity in any of the two kesterites.

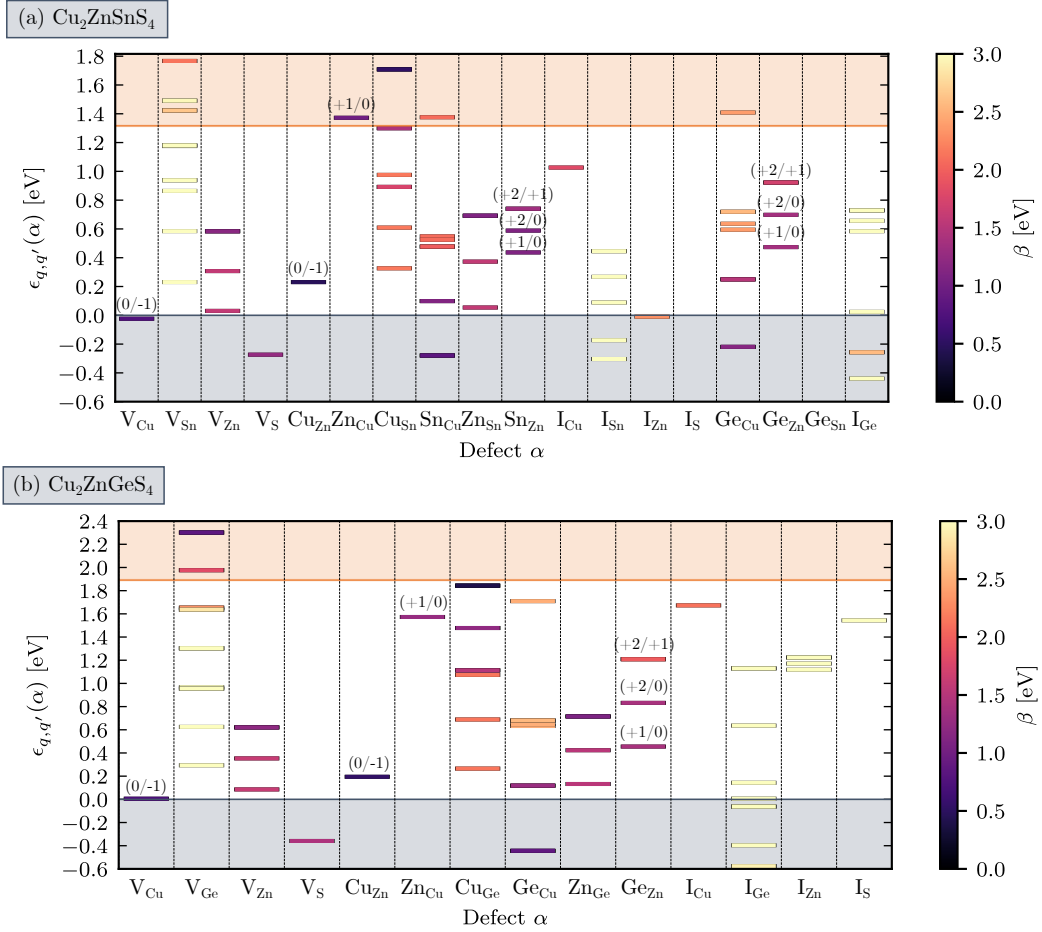


Figure 5.4: Ionisation energy levels of intrinsic point defects in (a) $\text{Cu}_2\text{ZnSnS}_4$ and (b) $\text{Cu}_2\text{ZnGeS}_4$ calculated for a chemical potential combination corresponding to point E in **Fig.5.1(a)** and **Fig.5.1(b)**. Their locations within the kesterite bandgaps are reported here on the y-axis while the β value corresponds to the formation energy value at which the transition occurs in **Fig.5.2**. This β value is provided as a guide for the eye to highlight the most dominant transition levels. In addition, the (q/q') charge state transitions are highlighted for the lowest formation energy point defects reported in **Fig.5.2**. [Python code provided to the reader here.](#)

One can identify Sn_{Zn} (resp. Ge_{Zn}), Zn_{Sn} (resp. Zn_{Ge}) and to a lesser extent Cu_{Sn} (resp. Cu_{Ge}) and Sn_{Cu} (resp. Ge_{Cu}) as deep defects. Indeed, all these substitutional defects offer transition levels located close to the middle of the kesterite bandgap. In addition, as presented in **Fig.5.3**, the substitution of Zn by Sn (resp. Ge) is the only defect presenting also a low formation energy. The latter has several transition levels within the kesterite bandgap corresponding to the various transitions between its various charge states: $(+2/0)$ at 0.584 eV (resp. 0.736 eV), $(+2/+1)$ at 0.735 eV

(resp. 0.585 eV) and (+1/0) at 0.43 eV (resp. 0.890 eV) above the VBM (below the CBM). These values are comparable to those reported by Li *et al.* with Sn_{Zn} (+1/0) at 0.86 eV and (+2/0) at 0.67 eV below the CBM [109]. Moreover, as a result of the p-type conductivity, the Sn_{Zn} (resp. Ge_{Zn}) defect should be ionised into a charge state +2 (see Fig.5.2). Using deep-level transient spectroscopy, Deng *et al.* reported a defect activation energy of 0.581 eV for the Sn-based kesterite, and identified this defect as a recombination centre [184]. As shown in Fig.5.4(a) and in agreement with this experimental observation, this defect could be reported as the substitutional defect Sn_{Zn} with its two-electron transition level (+2/0) at 0.584 eV above the VBM. Furthermore, the same authors reported a decrease of the transition level position to 0.542 eV following Ge incorporation, while in this work, upon Ge incorporation we report the spreading of the ionisation levels located between 0.42 eV and 0.73 eV for Sn_{Zn}, between 0.46 eV and 0.91 eV for Ge_{Zn} (in Sn-based kesterite) and between 0.44 eV and 1.9 eV for Ge_{Zn} (in Ge-based kesterite). It should also be noted that in all three situations, the transition level (+2/0) is the closest to the middle of the gap.

Beyond, formation energies, as presented in section 2.3.3, other physical parameter can also act as indicators for the evaluation of the impact of point defects on solar cell properties. In the following section, we consider capture coefficients $k_{n,p}$, that can be related to the kesterite lattice distortion upon introduction of the defect (see Eq.(2.70)).

5.4 ATOMIC DISTORTIONS

In Fig.5.5, we present the evolution of the interatomic distances between the defect position and the surrounding S atoms $d_{\alpha-S}$ with respect to the charge states q of the defect², both in the Sn-based (plain lines) and the Ge-based (dashed lines) compounds. A first general trend that can be observed for each defect is that as the charge state of the defect gets closer to the electronic configuration of the pristine system, the lattice distortion tends to get closer to the reference distance ($q = 0$). For example, in the case of a substitutional defect, if both elements have similar atomic radii and if their electronic configurations are close, one could expect a small distortion undergone by the lattice upon defect incorporation.

A similar behaviour is observed in both Cu₂ZnSnS₄ and Cu₂ZnGeS₄ concerning defects providing transition levels close to the bandgap edges and showing low formation energies (Cu_{Zn}, Zn_{Cu} and V_{Cu}). The introduction of the copper vacancy leads only to a small distortion of the lattice as the interatomic distance variation is less than 0.1 Å. In addition, assuming the capture of an electron by such a defect, the

²As presented in section 2.3.1, the charge state notation used in this work is the real charge state. For instance, concerning the Cu vacancy, V_{Cu} in a charge state -1 corresponds to the charge state of the Cu atom in the pristine kesterite.

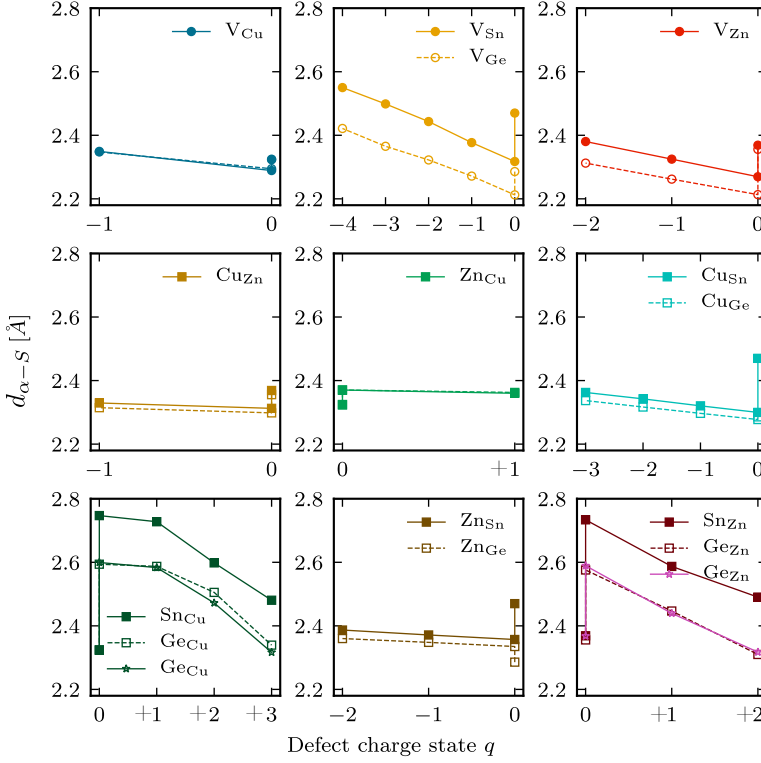


Figure 5.5: Representation of the interatomic distance between the defect position and the surrounding S atoms with respect to the defect charge state q . For a charge state $q = 0$, the evolution corresponds to the distortion undergone by the lattice following the defect incorporation while the evolution along the x-axis corresponds to the lattice distortion as a result of the capture/emission of electrons by the defect. The results corresponding to the $\text{Cu}_2\text{ZnSnS}_4$ (resp. $\text{Cu}_2\text{ZnGeS}_4$) compound are reported in plain (resp. dashed) lines. Ge-doping distortions in Sn-kesterite are reported in plain lines using a star symbol.

value of the interatomic distance remains quite constant in comparison to the one in the pristine lattice. This result supports the readiness of these defects to provide charge carriers in kesterite materials. We report the same behaviour for the substitutional defects Cu_{Zn} and Zn_{Cu} . The results also support that the Cu/Zn disorder commonly observed in Sn-based kesterite should be present as well in the Ge-based compound. In addition, for the Ge_{Sn} substitutional defect in the Ge-based kesterite, we report a reduction of the X-S ($X=\text{Sn,Ge}$) interatomic distance from 2.46 Å in the Sn-based compound to 2.30 Å in the Ge-based material. This can be interpreted as a direct consequence of the smaller atomic radius of Ge ($r_{\text{Ge}} = 1.25$ Å compare to the Sn element: $r_{\text{Sn}} = 1.45$ Å [164]).

Moreover, we observe the largest lattice distortions for both substitutional defects Sn_{Cu} (resp. Ge_{Cu}) and Sn_{Zn} (resp. Ge_{Zn}) which were identified as possible

recombination centres in the previous section. In good agreement with our calculations, Li *et al.* reported similar values concerning the Sn-S distances for various charged states of the Sn_{Zn} defect, *i.e.* 2.71 Å ($q = 0$), 2.57 Å ($q = +1$) and 2.43 Å ($q = +2$) while the values obtained in this work are 2.73 Å, 2.59 Å and 2.49 Å respectively for $q = 0, +1$ and $+2$ [109]. The authors also discussed on the computed Sn_{Zn} capture cross sections. They reported significantly higher values associated to the electron capture of $\text{Sn}_{\text{Zn}}^{+2}$ (ionisation level $(+2/+1)$) compared to $\text{Sn}_{\text{Zn}}^{+1}$ (ionisation level $(+1/0)$) exhibiting values that are several orders of magnitude lower [109]. However, these observations were contradicted by Kim *et al.* as they report that the electron capture cross section of $\text{Sn}_{\text{Zn}}^{+1}$ is one order of magnitude higher than that of $\text{Sn}_{\text{Zn}}^{+2}$ [73]. Despite this contradiction, both papers identify Sn_{Zn} substitutions as recombination centres that induce important structural relaxation upon charge capture, corroborating the results obtained in this work.

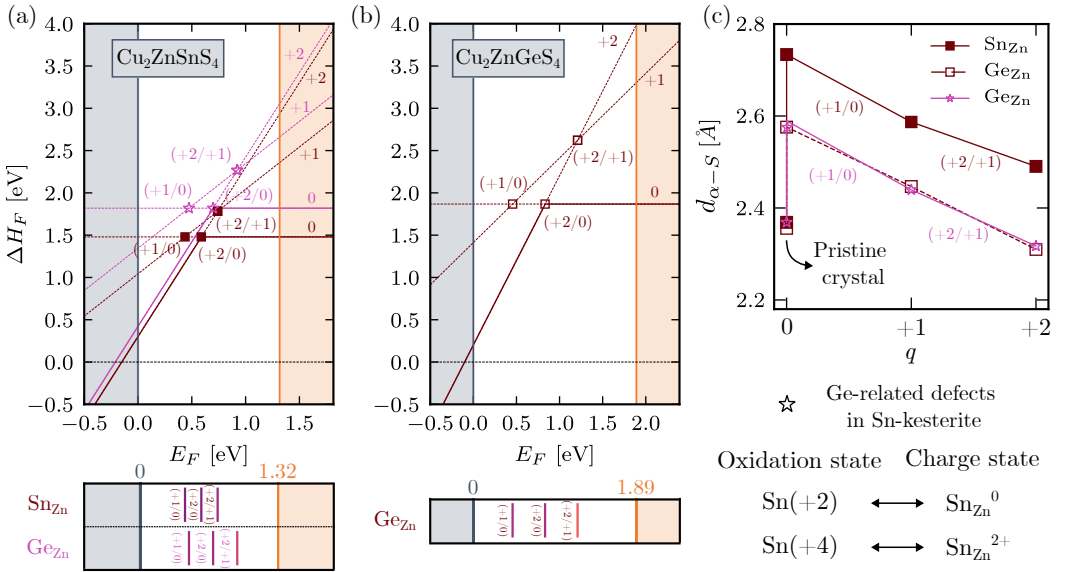


Figure 5.6: This figure provides the reader an exhaustive overview of the results concerning the X_{Zn} ($\text{X}=\text{Sn},\text{Ge}$) substitutional defects acquired in this work. (a) and (b) present respectively the defect formation energies in $\text{Cu}_2\text{ZnSnS}_4$ and $\text{Cu}_2\text{ZnGeS}_4$. The defect charge state q as well as the associated ionisation energy levels (q'/q) are illustrated. Finally, in (c), we present the structural distortion with respect to the charge state variation upon charge capture or emission. The lattice deformation is represented here by the evolution of the α -S distances. Eventually, correspondences between Sn oxidation states and defect charge states are provided.

Li *et al.* also proposed an empirical approach to evaluate defect carrier capture cross sections that consists in studying the local structural relaxation undergone by the lattice when the defect captures/emits electron(s) [109]. They suggested that strong bonds and large structural relaxations imply large defect capture cross sec-

tions. Such a qualitative approach can be more firmly grounded using a quantitative study of the defect carrier capture cross section via the computation of the phonon-electron Hamiltonian [73, 109, 191]. However, we would like to add some nuance to this statement. As detailed in section 2.3.3, for a defect to effectively capture free charge carriers, this one must provide an ionisation level close to the middle of the bandgap (see Eq.(2.61)) and be characterised by large charge carrier capture coefficients $k_{n,p}$ (see Eq.(2.62)). These coefficients depend on the lattice distortion induced by the introduction of the defect or a change in its charge state (see Eq.(2.70)). A larger distortion leads to a smaller vibrational overlap. However, for a recombination to be purely non-radiative (multi-phonon processes), large lattice distortions are required (see **Fig.2.15**).

Building on this knowledge, in **Fig.5.6**, we present an overview of the results obtained in this work regarding X_{Zn} ($X=Sn,Ge$) point defects. In **Figs.5.6(a)** and **(b)**, following the Ge incorporation in the Sn-kesterite, from Ge-doping to pure Ge-alloyed material, we report an increase of the neutral X_{Zn} ($X=Sn,Ge$) substitutional defect formation energies which consequently results in a decrease of the defect concentrations. Secondly, along with this observation, the ionisation levels associated to the X_{Zn} ($X=Sn,Ge$) defect tend to spread within the material bandgap as we move from Ge doping to Ge alloying with the (+2/0) transition level still located in the middle of the gap. Then, as shown in **Fig.5.6(c)**, the distortion induced by Sn_{Zn} in Cu_2ZnSnS_4 is stronger than that caused by Ge-related defects: Ge_{Zn} . Furthermore, in charge state +2, the Ge_{Zn} -S distance is similar to the Zn-S distance in the pristine kesterite. This suggests that, in contrast to Sn, the substitution of Zn by Ge results in a defect that is less likely to facilitate pure non-radiative recombinations. This would partially explain the smaller V_{OC} deficit reported in the Ge-based kesterite with respect to the Sn-based material.

In addition to these observations, in chapter 4, we previously reported an increase of the V_{OC} value as well as a decrease of the J_{SC} value as a result of the increase of the material bandgap from 1.32 eV (Cu_2ZnSnS_4) to 1.89 eV (Cu_2ZnGeS_4) [86]. Combining the results from both investigations, we thus conclude that the improvement of the solar cell efficiency associated to Ge doping of Sn-based kesterites is ascribed to the improvement of the V_{OC} value while maintaining the J_{SC} value of Sn-based kesterite cell. In comparison to the Sn counterpart, this enhancement is the result of both the increase of the Ge_{Zn} substitutional defect formation energy and the reduction of the associated lattice deformation.

5.5 CONCLUSION

This work was devoted to first-principles investigations of Ge-related defects in kesterite. First, we highlight the slightly wider pure phase range of chemical po-

tential values of the Ge-based kesterite compared to the Sn-based kesterite. In both cases, in terms of possible chemical potential ranges, the pure phase remains limited due to the numerous secondary phases, which are a direct consequence of all four elements present in these kesterites. Near the stable phase region, the secondary phases are ZnS, CuS and Cu_2SnS_3 (resp. Cu_2GeS_3) in the Sn-kesterite (resp. Ge-kesterite). This observation can be put into perspective with the multiple secondary phases observed during the kesterite synthesis commented in appendix B.

Moreover, we found a similar physical behaviour of intrinsic point defects for the Sn-kesterite and the Ge-kesterite. In both compounds, we identified V_{Cu}^{-1} , $\text{Cu}_{\text{Zn}}^{-1}$ and $\text{Zn}_{\text{Cu}}^{+1}$ as low formation energy defects acting as acceptors and as donor defect for the latter. By calculating the Fermi level under equilibrium conditions, we confirmed the p-type conductivity reported in the literature for both the Sn-based and the Ge-based compounds. We also shed a light on the commonly observed Cu/Zn disorder encountered in kesterite compounds. In addition, via the study of Ge doping in the Sn-kesterite compound, we identified the Ge_{Sn} neutral defect as a quite spontaneous defect, an indication that the Ge doping within the kesterite matrix occurs via a Sn substitution. Finally, we identified Sn_{Zn} and Ge_{Zn} as recombination centres. We reported an increase of the substitutional defect formation energy following the Ge-doping and alloying which would result in a decrease of the defect concentration.

In addition, it appeared that the lattice distortion induced by the formation of these defects or by variation of their charge states is reduced for the Ge_{Zn} substitutional defect in comparison to its Sn counterpart. This result hints at a less detrimental defect behaviour to be ascribed to Ge_{Zn} with respect to Sn_{Zn} . As a consequence, we point out the concentration decrease and the lattice distortion reduction of the detrimental defect X_{Zn} ($\text{X}=\text{Sn,Ge}$) as possible sources of the V_{OC} improvement reported in the literature upon Ge incorporation. Additional calculations of the electron-phonon matrix and the resulting carrier capture coefficients would give further information regarding the specific behaviour of these point defects [191].

The achieved objective of this work was to strengthen the understanding of the effects of Ge doping and Ge alloying in kesterite materials for photovoltaic applications. We believe that our results clarified the fundamental mechanisms that operate at the atomic scale via the formation of a wide range of point defects. Following the definitions of the different types of defects, we theoretically studied intrinsic point defects in two kesterite compounds as well as extrinsic Ge-related defects in the Sn-kesterite matrix. Some of these defects, like V_{Cu} and Cu_{Zn} , are beneficial to the material, providing charge carriers to the electrical conductivity. However, others, such as (X_{Zn} , $\text{X}=\text{Sn,Ge}$), act as recombination centre that degrade the PV performances. In the following chapter, we experimentally study doping (intentional incorporation of extrinsic defects) in another Cu-based material, Cu_2O copper oxide. The aim is to boost the material optoelectrical properties and to correlate these enhancements to specific point defects.

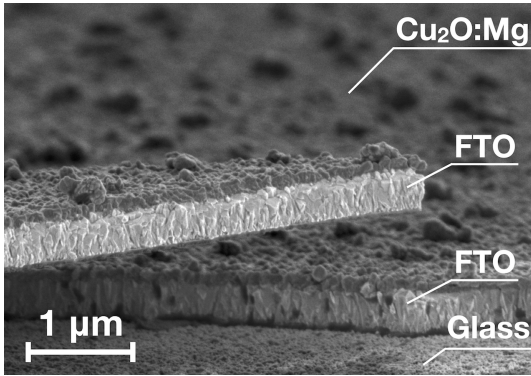
PHASES AND POINT DEFECTS IN N,Mg DOPED COPPER OXIDE

6

6.1	Introduction	145
6.2	Experimental methodology	148
6.2.1	Thin film synthesis and characterisation	148
6.2.2	Sputtering target crystallinity and composition	149
6.2.3	Plasma pressure optimisation	150
6.3	N,Mg doping of copper oxide	152
6.3.1	Crystallographic investigation	152
6.3.2	Thin film elemental composition	154
6.3.3	Electrical and optical properties	156
6.3.4	Phase and defects correlation through Raman spectroscopy	160
6.3.5	Point defect discussion	162
6.3.6	Experimental reproducibility	162
6.4	Conclusion	164

This chapter is based on the following work:

Ratz, T., Fourneau E., Sliti N., Baret A., Malherbe C., Vertruyen B., Silhanek A. & Nguyen, N. D., *Correlation between material properties, crystalline transitions, and point defects in RF sputtered (N,Mg)-doped copper oxide thin films*, under submission process, (2024)



Abstract In the present chapter, we investigate the effects of N and Mg doping on Cu_2O thin films deposited using RF magnetron sputtering at room temperature. First, electrical and optical properties of the materials are studied as function of the Mg and N concentrations. Subsequently, we interpret and discuss the sample optoelectrical behaviours using the correlation between the material defects and the associated Raman activity. Through complementary XRD and

EDX spectroscopic measurements, we study the structural phase transitions occurring during thin film deposition using a CuO target. Our analysis reveals the emergence of a Cu_4O_3 phase in undoped thin films and the formation of a Cu_2O phase upon in-situ nitrogen doping. Starting from a CuO crystalline phase, we therefore unravel a possible synthesis mechanism for a N-doped Cu_2O layers. Furthermore, the nitrogen incorporation enhances both the electrical and optical properties, with resistivity reaching value as low as $1.15 \Omega\text{cm}$ and an average visible transmittance of 31.74%, consistent with previous reports. Raman spectroscopy indicates an increase in $(\text{N}_2)_{\text{Cu}}$ shallow acceptor point defects with higher nitrogen flow rates, explaining the probed enhancement of p-type majority charge carriers observed via Hall measurements. With respect to the established literature, we also confirm the improvement of the sample optoelectrical properties as Mg is introduced. Conversely, we demonstrate that co-doping with Mg and N degrades the material crystallinity, leading to a reduction in thin film conductivity that could be attributed to high nitrogen incorporation, as indicated by EDX measurements.

6.1 INTRODUCTION

As described in chapter 1, the efficiency of copper oxide based solar cell are currently limited by low values for both the open-circuit voltage V_{OC} and the fill factor FF . The first one as a result of charge recombination processes in the bulk and at the interfaces, while the latter is partially associated to the poor electrical performances of the copper oxide absorber layer. In order to circumvent those limitations, a better understanding of the microscopic mechanisms underlying the material conductivity and related to the physics of point defects is required. In addition, material doping offers an interesting strategy both to inhibit the presence of defects acting as recombination centres and secondly to boost the material optoelectrical properties. And, as addressed in chapter 1, among the possible doping species, Mg and N appear both as compelling candidates in the case of copper oxide.

As reported in **Tab.6.1**, Cu_2O presents a variety of intrinsic point defects: vacancies (V_{Cu} , $V_{\text{Cu,split}}$ and V_{O}), substitutions (O_{Cu} and Cu_{O}) and interstitials (I_{Cu} , I_{O} and $\text{I}_{\text{O,oct}}$) with different impacts on the material properties [192–195]. In 2006, Nolan *et al.* identified two kinds of Cu vacancies, respectively V_{Cu} which leaves two oxygen atoms with three bondings instead of four, and $V_{\text{Cu,split}}$, resulting from the displacement of a neighbour copper atom towards the copper vacancy site allowing the four bounds state to be recovered [42]. Using first-principles calculations, they studied the p-type conductivity in copper oxide, reporting V_{Cu} as the origin of the delocalised hole states participating to the material conductivity [22]. Then, in 2009, the results obtained by Nolan were strengthened in a study by Scaloni *et al.* in which the authors reported acceptor levels in copper oxide [194]. They underlined that both copper vacancies behave as shallow defects participating to the material p-type conductivity with formation energies below 1.5 eV. It was measured later by Paul *et al.* using Deep Level Transient Spectroscopy (DLTS), providing transition energy levels at 0.22 and 0.45 eV above the valence band for respectively V_{Cu} and $V_{\text{Cu,split}}$ [192]. In contrast, both oxygen interstitials (I_{O} and $\text{I}_{\text{O,oct}}$) are associated with defect energy levels located at about the centre of the material bandgap but exhibiting high formation energies in the range from 1.5 to 2 eV. Concerning the copper interstitial, a high formation energy was reported by Raebiger *et al.*, who also confirmed V_{Cu} as an acceptor level. More specifically, they reported the anionic oxygen vacancy V_{O} as a potential "hole killer". However, its efficiency in this role is debated as Raebiger *et al.* present V_{O} as inefficient due to its lack of transition level inside the material bandgap [193] while Sekkat *et al.* point out V_{O} as responsible for the decreasing hole concentration [196]. Indeed, in 2022, Sekkat *et al.* reported on the deposition of low resistivity (0.4 Ωcm) copper oxide thin films by controlling the fraction of oxygen in an atomic layer deposition process. Using Raman, photoluminescence (PL) and positron annihilation spectroscopies (PAS), they ultimately managed to correlate the sample properties to the defect signatures [196, 197]. In

these works, large defect complexes ($2V_{\text{Cu}} + 2V_{\text{O}}$ or $2V_{\text{Cu}} + V_{\text{Cu,split}} - V_{\text{O}}$) were revealed and a reduction of the defect concentration was observed when increasing the oxygen ratio. The authors attributed the reduction of the resistivity following the increase in the oxygen ratio during the deposition to the decrease of the oxygen vacancy V_{O} that reduces the number of hole captures, consequently leading to an increase in charge carrier concentration in steady-state operation.

Defects	ΔH_F [eV]	Behaviour	E_T [eV]	Raman activity [cm^{-1}]	Exp.	Theo.
V_{Cu}	Low	Acceptor, delocalised hole	0.23	\searrow 515 (T_{2g}) and \nearrow 541,(318,510) (A_{1g},E_g)	[192]	[22, 90, 194]
$V_{\text{Cu,split}}$	Low	Deep acceptor, localised hole	0.47	All	[192]	[22, 194]
V_{O}	/	Possible hole killer	/	All except 90 (T_{2u})	[196]	[90, 193]
CuO	/	/	/	All except 90 (T_{2u})	/	[90]
O_{Cu}	/	/	/	\searrow 515 (T_{2g}) and \nearrow 541,(318,510) (A_{1g},E_g)	/	[90]
$\text{I}_{\text{O,oct}}$	High	Deep	1.08	\searrow 515 (T_{2g}) and \nearrow 541,(318,510) (A_{1g},E_g)	[192]	[194]
$\text{I}_{\text{O,tetr}}$	High	Deep	1.27	All	[192]	[194]
I_{Cu}	/	/	/	/	/	/
Mg on $V_{\text{Cu,split}}$	Spontaneous (< 0)	Indirect acceptor, V_{Cu} interaction	/	/	[45]	[42]
$(\text{N}_2)_{\text{Cu}}$	Low	Acceptor	0.2	2280		[198]
$(\text{N}_2)_{\text{O}}$	High	Deep donor	0.38	1309,1929		[198]
N_{O}	Low	Deep acceptor	0.53	/		[198, 199]

Table 6.1: Recent assessment of point defects in copper oxide films. The defect type and the chemical species involved are highlighted, as well as the corresponding formation energy. As this quantity is a function of the material stoichiometry, a qualitative value is provided as *low* (below 1.5eV) and *high* (above 1.5 eV). Finally, the behaviour or character of a given defect is qualified as either acceptor, donor or deep. The latter qualification underlines the possible behaviour of the defect as a recombination centre. The Raman bands of the reported defects are also provided with the corresponding phonon modes (90, 110, 145, 155, 320, 515, 620, 655 cm^{-1} as described in Refs. [90, 200]). Finally, the two last columns show the associated experimental or theoretical works reported in the literature.

Then, concerning Mg doping in copper oxide, Isseroff *et al.* used hybrid DFT to study the doping of Cu_2O via Li, Mg, Mn and Zn [42]. In their work, the authors reported on V_{Cu} and $V_{\text{Cu,split}}$, assessing that the simple copper vacancy produces a delocalised hole while the split vacancy generates a localised hole, in contrast to previously reported works. This localised hole plays a key role in the origin of the minority carrier trapping in copper oxide. This split vacancy could therefore inhibit the diffusion of minority carriers, acting as a trap state. In addition, corroborating the established state-of-the-art, the simple copper vacancy was reported as the lowest formation energy defect of the two. The authors finally reported that these specific trap states can be prevented by doping the material with Li, Mg, Mn or Zn resulting in single vacancies providing delocalised holes. These predictions were further confirm by experimental work using both physical and chemical routes for the synthesis of copper oxide thin films [45, 201, 202].

Finally, concerning nitrogen doping, in 2015, using hybrid density functional theory, Thienprasert *et al.* studied the nitrogen related defects in copper oxide. Among the studied defects, substitutions N_O and $(N_2)_{Cu}$ were identified as the most dominant ones with formation energies lower than 1.5 eV. One can therefore expect similar concentration values as for both copper vacancies V_{Cu} and $V_{Cu,split}$ [198]. Moreover, N_O and $(N_2)_{Cu}$ are identified as acceptor-type defects with transition energy levels respectively of 0.53 and 0.2 eV above the valence band. Zhao *et al.* also discussed that the substitution of oxygen by nitrogen N_O could create a new absorption peak near 0.9 eV [199]. In addition to a range of predictive studies, several works also successfully achieved N-doped Cu_2O thin films using various synthesis techniques: Ar, N_2 and O_2 reactive magnetron sputtering of Cu target at high deposition temperature [49, 203], magnetron sputtering of Cu_2O target with Ar, N_2 flows at RT [48, 204], post-oxidation using oxygen-nitrogen plasma [46]. Using the latter process, Li *et al.* reported a high concentration of nitrogen interstitials (I_N) as well as N_O and V_O . In opposition, in their work, Thienprasert *et al.* reported formation energies higher than 1.5 eV for each nitrogen interstitial type [198]. Moreover, in 2023, Mudhaffar *et al.* reported on the N-doping of Cu_2O using radio frequency (RF) sputtering from ceramic target at room temperature (RT) with 19:1 SCCM (Ar:N) flows followed by annealing at 200°C [204]. They measured a material bandgap close to 2.5 eV. In the N-doped thin film, they also report through PL measurement a lower V_O content and fewer Cu dangling bonds produced by ion bombardment via the sputtering. As a result, they proposed to interpret those results as the filling of oxygen vacancies with nitrogen N_O .

Building from enhancement of the copper oxide properties resulting of individual nitrogen and magnesium doping reported in the literature, in this chapter, we investigate the Mg,N co-doping of copper oxide thin films deposited using RF magnetron sputtering at room temperature. To the best of our knowledge, it is the first work reporting on this specific co-doping in Cu_2O layers. It is worth noticing that this co-doping was successfully implemented in another Cu-based material: $CuCrO_2$ as reported in Ref. [205].

In the following sections, we first present the experimental methodology that was applied to perform this study. In the description, the synthesis and characterisation protocols are first detailed. Then, we present the crystallographic characterisation of the sputtering targets themselves. Eventually, after a preliminary study of the optimal plasma pressure, the results obtained for the N,Mg doping process are presented and discussed. In the subsequent development, we correlate the optoelectrical properties, the crystalline structure as well as the material point defects through the wide range of characterisation techniques. By the end of the chapter, we propose a full microscopic and macroscopic description of the physics behind the doping strategy employed in this work.

6.2 EXPERIMENTAL METHODOLOGY

6.2.1 Thin film synthesis and characterisation

Copper oxide thin films were deposited by RF magnetron sputtering using a Nexdep physical vapour deposition (PVD) system from Angstrom Engineering Inc. The deposition was performed on $1.5 \times 1.5 \text{ cm}^2$ glass substrates previously cleaned in an ultrasonic bath using acetone followed by isopropyl alcohol (IPA) treatment (5 min each). Prior deposition, a pre-sputtering over a 30 nm thickness was performed under a nominal base pressure of the order of $1\text{E-}7$ Torr. The specific deposition parameters of each sample are listed in **Tab.C.1** of appendix C. The Mg content was tuned using two different 2-inch ceramic sputtering targets (99.99% purity): undoped and doped ($\sim 4\text{w/w\%:Mg}$), with the Mg content expressed via the $\text{Cu}/[\text{Cu}+\text{Mg}]$ mass ratio. Then, during the deposition a plasma pressure of 5 mTorr, a constant flow of 20 SCCM of Ar and a variable flow of N_2 between 0 and 20 SCCM were used along with a sputtering power of 69 W without substrate rotation. As a result, the synthesised samples are close to 200 nm in thickness as measured using a Veeco Multimode 8 atomic force microscope (AFM) in tapping mode.

Following the sample synthesis, two main types of characterisations were performed. First, the thin film optoelectrical properties were measured using a UV-VIS 3600 Shimadzu spectrophotometer equipped with an integrating sphere and a Phys-Tech RH 20351 Hall measurement system. First, transmittance measurements were performed between 200 nm and 1600 nm by ensuring a proper baseline realised in air. The resulting data were then processed and the material optical bandgaps were extracted via a Tauc plot analysis using a computed material reflectivity based on a copper oxide refractive index of 2.63 [206] and on the AFM measured layer thicknesses. In addition, the arithmetic mean transmittance value is computed in the visible wavelength range between 380 and 750 nm as the mean transparency value. Using the same thickness values, electrical measurements were performed on samples under Van der Pauw configuration at room temperature using a static magnetic field of 0.4 T. The measurements were repeated 4 times aiming at a measured voltage of 1, 2.5, 5 and 10 V with various applied currents. Acquisition times were respectively 20 and 200 ms for the sheet resistance measurements and for the Hall effect measurements.

Then, in a second part of the study, the same samples were analysed by X-ray diffraction (XRD), Raman and energy dispersive X-ray (EDX) spectroscopies. For the structural and crystallographic characterisations, a Twin-Twin Discovery XRD system from Bruker was used with 2θ angles between 25 and 70° in a $(\theta-2\theta)$ configuration (θ fixed at 1°) using a $\text{CuK}\alpha 1$ source ($\lambda = 0.154 \text{ nm}$). The XRD analysis volume on the sample corresponds to a spot of $\sim 1 \times 1 \text{ cm}^2$ \times a depth of $\sim 1 \text{ }\mu\text{m}$. To properly present the measured spectra, a baseline correction was

performed. Concerning the Raman characterisation, the focus was set on the Raman shifts between 90 and 2600 cm^{-1} using a 532 nm laser source and a power of 0.4 mW. The system used a high pass filter with a cutoff frequency of 85 cm^{-1} . The raw Raman data were also corrected using a baseline offset following by a spectrum normalisation. The latter was carried out based on the area of the Raman band located at 515 cm^{-1} corresponding to the only active phonon mode for a pristine copper oxide crystal [90]. The area was computed following a Voigt fit. In addition, systematic hot pixels located at 710, 1950 cm^{-1} were deleted. The volume scanned using the Raman measurements is of the order of 1 μm^3 . Finally, the EDX measurements were performed on a Tescan Vega 3 scanning electron microscope SEM-EDS system with an acceleration voltage of 5 kV and a beam intensity corresponding to a penetration of 590 nm. The measurements were repeated at three different locations for each sample with a magnification of 500 and an acquisition time of 30 seconds. The relative elemental composition were then extracted based on the deconvolution algorithm provided by the tool manufacturer. The overall accuracy concerning the relative stoichiometries obtained is of the order of $\pm 2\%$ [207].

6.2.2 Sputtering target crystallinity and composition

To realise the N,Mg-doping study, several sputtering targets were used and characterised as listed in **Tab.6.2**.

Label	Purchased	Date	XRD	$\frac{\text{Cu}}{\text{Cu+O}}$ [%]	$\frac{\text{O}}{\text{Cu+O}}$ [%]	$\frac{\text{Mg}}{\text{Cu+Mg}}$ [%]
S2018-0	Cu ₂ O	2018	Cu₂O - CuO	64	35	/
S2021-0	Cu ₂ O	2021	CuO	53	47	/
S2023-0	Cu ₂ O	2023	CuO	56	44	/
S2021-4	Cu ₂ O:Mg($\sim 4\%$)	2018	Cu₂O - Cu - MgO	67	33	10

Table 6.2: Listing of the sputtering targets used with their respective labels. The purchased composition from Angstrom Engineering Inc. and purchased date are shown in the second column. The third column presents the main phase (in bold) and secondary phases (in plain text) deduced from XRD measurements. The last column displays the material stoichiometries obtained by EDX characterisations with an overall accuracy of $\pm 2\%$ [207].

All purchased sputtering targets aimed at a Cu₂O material phase either Mg undoped or Mg-doped with a Cu/[Cu+Mg] weight ratio of $\sim 4\text{w}/\text{w}\%:\text{Mg}$ (corresponding to a 9% molar ratio). In contrast, as presented in **Fig.6.1**, for the S2021-0 and the S2023-0 targets, the crystallographic measurements indicate a main CuO material phase while the S2018-0 shows a Cu₂O main phase with few traces of CuO as secondary phase. Concerning the Mg-doped target, a correct Cu₂O material phase is reported with traces of Cu as secondary phase. Complementary to the crystallographic characterisation, EDX measurements were performed on the targets with stoichiometric values listed in **Tab.6.2**. We report a Mg concentration value of 10% close to the purchased molar ratio of 9%. Furthermore, the EDX results are in good agreement with the conclusions deduced from the XRD acquisitions: either a Cu₂O

or a CuO main material phase. As consequence, we believe that significant oxygen incorporation occurred during the manufacturing processes of the S2021-0 and S2023-0 sputtering targets, leading to the CuO material phase detected in both XRD and EDX data. Moreover, in 2019, Resende *et al.* highlighted the inhibiting role of Mg with respect to the nucleation of CuO sites in air annealed Cu₂O samples [201]. Therefore, based on the knowledge of a similar fabrication process for each sputtering target manufactured after 2021, we believe that the presence of Mg in the S2021-4 target has stabilised the Cu₂O material phase by preventing the formation of CuO secondary phases.

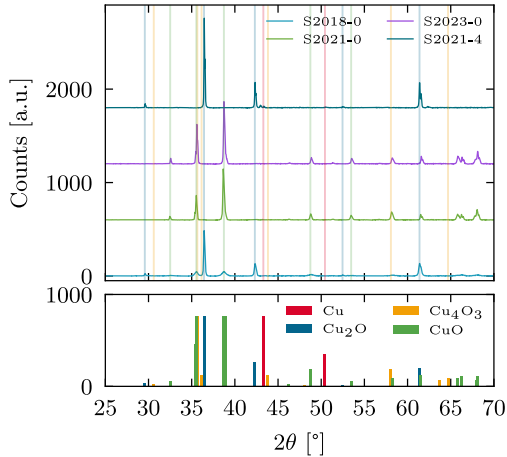


Figure 6.1: Crystallographic characterisation copper oxide sputtering targets listed in **Tab.6.2**. In the top panel, the crystallographic target measurements highlight the good correspondence between the peaks and the main copper oxide phases as reported in the bottom panel.

In the next section, the results of a preliminary search for the optimal sputtering pressure was carried out with the aim of properly selecting the plasma pressure value at which the N and/or Mg doping of Cu₂O thin films will be investigated.

6.2.3 Plasma pressure optimisation

Using the sputtering targets S2023-0 and S2021-4, thin film depositions at 5, 10, 15 and 20 mTorr were carried out. The purpose is to identify the deposition conditions providing good electrical and optical performances for the upcoming co-doping investigation. This plasma pressure optimisation was realised with a nitrogen flow of 0 SCCM.

As presented in **Fig.6.2(a)**, following the increase of the deposition pressure, we observe for both sputtering targets, a decrease of the measured thin film thickness attributed to a lower deposition rate value. As highlighted in a previous work, this

observation can be explained by the deposition pressure increase and the subsequent reduction of the particle mean free path [202].

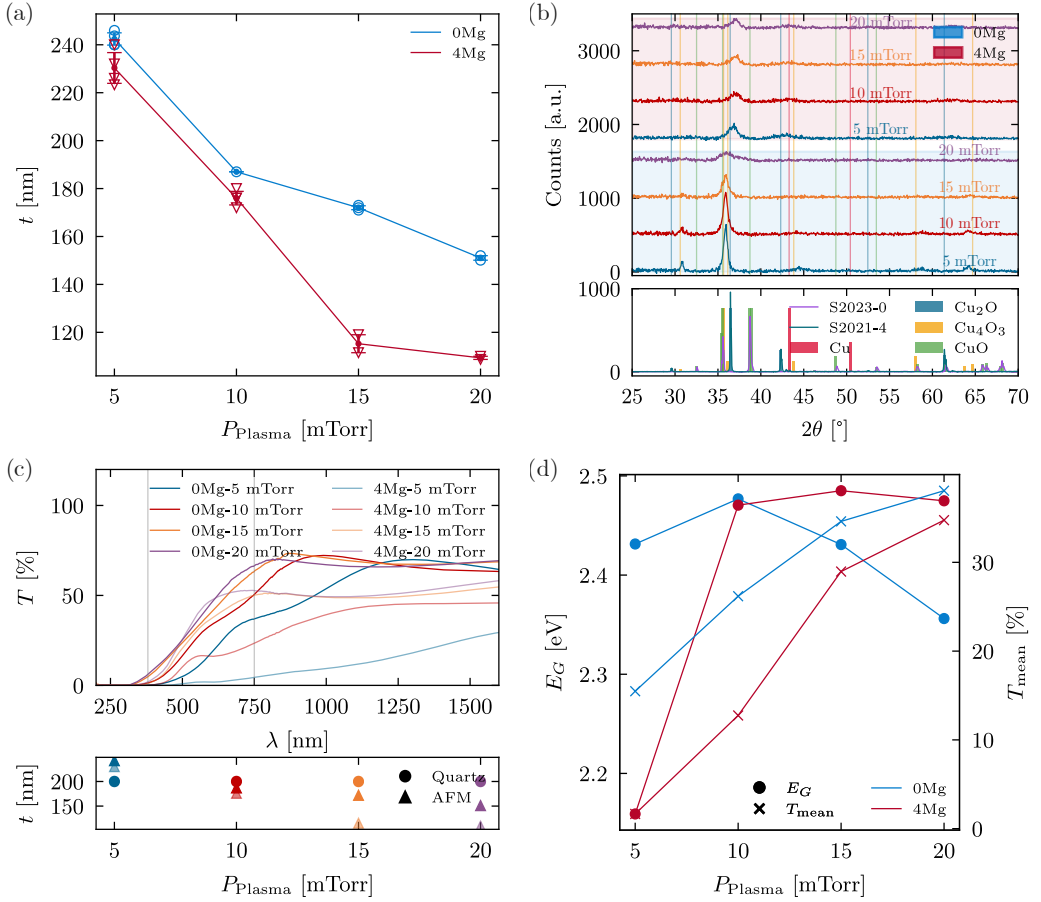


Figure 6.2: Crystallographic and optoelectrical results concerning the study of the sputtering plasma pressure P_{Plasma} with values of 5, 10, 15 and 20 mTorr using sputtering targets S2023-0 (blue highlight) and S2021-4 (red highlight). (a) We present the evolution of the thin film thickness as measured using AFM for a fixed aimed deposition thickness (quartz thickness). This characterisation allows us to calibrate the correct tooling factor for the upcoming depositions. (b) In the top panel, the thin films crystallographic characterisations are presented highlighting the main copper oxide phases presented in the bottom panel along with the sputtering target measurements. Then, in (c), the measured thin film transmittance curves, allowing the transparency and bandgap extractions detailed in (d), are presented.

Then, in **Fig.6.2(b)**, we report for the S2023-0 sputtered samples, a Cu_4O_3 main crystalline phase for each plasma pressure. This observation is in line with the results presented by Almazan *et al.* where using XRD and Raman characterisations, the authors reported on the non-reactive RF sputtering synthesis of Cu_4O_3 thin films from a CuO material target [208]. We believe that without oxygen control during the

material deposition, elemental losses drive the crystalline phase from CuO to Cu_4O_3 . As highlighted in different papers, the oxygen regulation impacts the crystallographic structure as well as the thin film impurity concentrations [39, 197, 209]. In addition, we observe a degradation of the sample crystallinity following the increase of the deposition pressure. As a result, a first attention point to take into account concerning the S2023-0 target would be the higher thin film crystallinity reported for lower plasma pressure values. In contrast, the plasma pressure does not significantly impact the S2021-4 sputtered samples since each of these presents a Cu_2O material phase with similar crystallinities.

Then, as presented in **Fig.6.2(c)** and (d), concerning the optoelectrical properties, we observe a clear increase of the sample mean transparency following the increase plasma pressure with consistently lower values for the Mg-doped layers. We also emphasize the significantly low transmittance value reported for the Mg-doped sample at 5 mTorr. In addition, this sample presents a bandgap value of 2.16 eV in contrast to the 2.43 eV value reported for the undoped sample. In the literature, the evolution of the copper oxide bandgap upon Mg doping does not seem settled as, based on *ab initio* calculations, Nolan *et al.* reported an increase of this value following the Mg incorporation [41] while, using nebuliser pyrolysis technique, Jacob *et al.* observed a decrease of the bandgap. Then, in **Fig.6.2(d)** at 10 mTorr, similar values are obtained followed by a decrease of the undoped sample bandgaps as the plasma pressure further increases. Finally, concerning the electrical properties, the film sheet resistances for plasma pressures higher than 5 mTorr were consistently above 40 M Ω . As a result, in order to preserve a better crystallinity of as-deposited layers while aiming at lower sheet resistances, the 5 mTorr value was selected as the sputtering pressure for the upcoming co-doping study.

6.3 N,Mg DOPING OF COPPER OXIDE

6.3.1 Crystallographic investigation

Figure 6.3 presents the XRD characterisation of the undoped (0Mg) and Mg-doped (4Mg) samples as nitrogen is introduced with a N_2 flow between 0 and 20 SCCM.

First, as depicted in **Fig.6.3(a)**, concerning the S2023-0 synthesised layers (0Mg), at 0 SCCM, we report a Cu_4O_3 crystallinity followed by a crystalline shift to Cu_2O as the nitrogen flow is increased from 0 to 4 SCCM. The dominant peak located around 36° is shifted to higher values while, XRD peaks located just above 30° and below 45° are respectively translated towards 29° and 43° as illustrated by the dashed arrows. Consequently, starting from the target CuO crystal phase, the desired sample crystallinity (Cu_2O) is achieved for nitrogen flow values higher than 4 SCCM. From this observation, we emphasize both the change of crystallinity that occurs first, (i) from

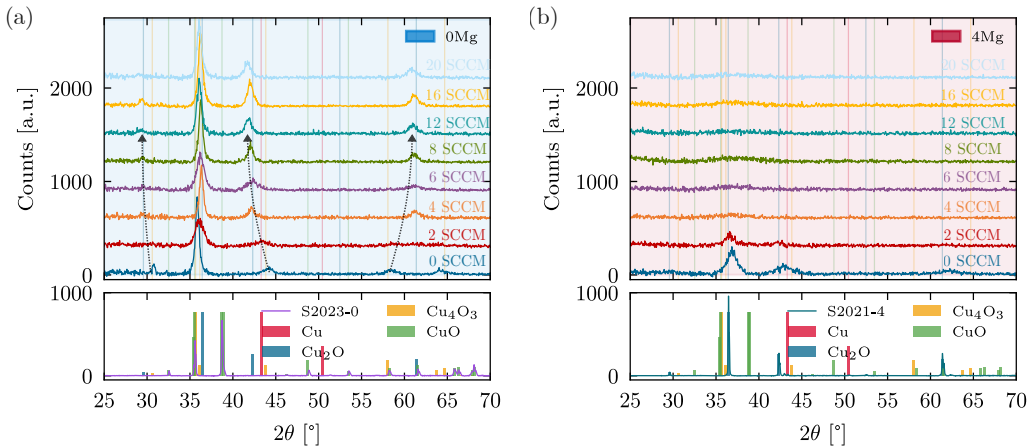


Figure 6.3: Crystallographic characterisation of (a) N-doped (S2023-0, blue highlight) and (b) (N,Mg)-doped (S2021-4, red highlight) thin films deposited using a N_2 flow varying between 0 and 20 SCCM. The top panels show the XRD measurements of the thin films while the bottom panel provides the XRD characterisation of the sputtering targets themselves as well as the main copper oxide phases also reported in the top panel to facilitate the phase identification. In (a), the dashed arrows present a guide for the eye concerning observed crystalline transition from Cu_4O_3 to Cu_2O .

the target to the 0 SCCM layer (following the sputtering deposition) and, secondly, (ii) as the nitrogen is introduced in the synthesised thin film. (i) As described in section 6.2.3, the reduction of the oxygen content inside the synthesised layer (Cu_4O_3) with respect to the S2023-0 sputtering target (CuO) could be attributed to the lack of control on the oxygen flow during the material deposition [39, 197, 208, 209]. And (ii), the second crystallinity transition from Cu_4O_3 to Cu_2O that could again be attributed to an oxygen reduction. In 2020, Patwary *et al.* reported on the nitrogen doping of Cu_4O_3 thin films without observing any material phase transition [210]. However, in their work, the authors described an additional oxygen regulation during the reactive sputtering deposition. As a result, the control of this parameter could explain the absence of the crystallinity change. Moreover, as this second crystalline transition is observed for an increased nitrogen flow between 0 and 4 SCCM, this one could also reveal a possible interaction between nitrogen and oxygen through the formation of N_O point defects as reported in different works [46]. Finally, the sample crystallinities seem to be equivalent as similar XRD peak intensities are observed for each N doping values.

In contrast, as presented in **Fig.6.3(b)**, concerning the Mg-doped samples, a Cu_2O material phase is reported for each nitrogen flow. Based on a first comparison between the 0 SCCM thin films presented in **Figs.6.3(a)** and (b), we observe a decrease of the material crystallinity as a result of the Mg doping. Then, in **Fig.6.3(b)**, upon both Mg and N doping, we report a degradation of the film crystallinity as the nitrogen

flow increases. Indeed, for nitrogen flow above 2 SCCM, the samples behaviour tends towards amorphous like layers with a peak around 36° spreading over a large 2θ range.

6.3.2 Thin film elemental composition

As presented in section 6.2.2, the relative elemental composition of the sputtering targets obtained by EDX confirms the crystalline phase reported following the XRD characterisation. In **Fig.6.4**, we present the evolution of the EDX deduced sample stoichiometries, starting from the sputtering target (red background highlight), proceeding to the nitrogen undoped thin films and, finally, reaching N-doped layers as the N is incorporated via the N_2 flow increase to 20 SCCM. In **Fig.6.4(a)**, the Cu and O relative stoichiometries are presented with dashed lines corresponding respectively to CuO (purple), Cu_4O_3 (green) and Cu_2O (cyan) and used as guides or the eyes. Then, **Fig.6.4(b)** displays the relative compositions of the nitrogen and magnesium doping species. It is relevant to note that the EDX technique is also known to be quite insensitive to low atomic number elements such as nitrogen. Moreover, unlike bulk sputtering target measurements, the characterisation of 200nm-thick thin films includes contributions from the glass substrate. This consideration supports the decision not to link the characterisation markers of the sputtering targets to those of the samples in **Fig.6.4(a)**. However, the measurements presented in this work are well supported by the time-of-flight secondary ion mass spectrometry measurements realised on the same layers.

In **Fig.6.4(a)**, upon nitrogen doping of the Mg free Cu_2O samples (blue curve - 0Mg), we observe an increase of the Cu content and a decrease of the O content before reaching a plateau for N_2 flows above 4 SCCM. The reported trend is in good agreement with the crystalline phase transitions reported based on the XRD results: first (i) from CuO to Cu_4O_3 (from the sputtering target to the 0 N_2 flow thin film) and, secondly, (ii) from Cu_4O_3 to Cu_2O . Furthermore, we can also carefully point out the resilience of the Cu_2O material phase to the off stoichiometry reported with a Cu-rich and an O-poor composition as a result of the oxygen flow lack of control during the deposition. The only oxygen source is the oxygen content within the sputtering target. Concerning the nitrogen incorporation, as shown in **Fig.6.4(b)** (blue curve - 0Mg), we report first a negligible amount inside the synthesised layer for N_2 flow values between 0 and 4 SCCM. In contrast, for values above 4 SCCM, an increased nitrogen inclusion is observed followed by a plateau for N_2 values above 12 SCCM.

Concerning the Mg-doped thin film without nitrogen inclusion, we observe, similarly to the 0Mg study, a deviation of the stoichiometry to a more Cu-rich and O-poor material phase with respect to the S2021-4 sputtering target. Following the nitrogen flow increases, a slight decrease (resp. increase) of the O content (resp. Cu content) is observed. However, as reported in the XRD measurements, the Cu_2O crystalline

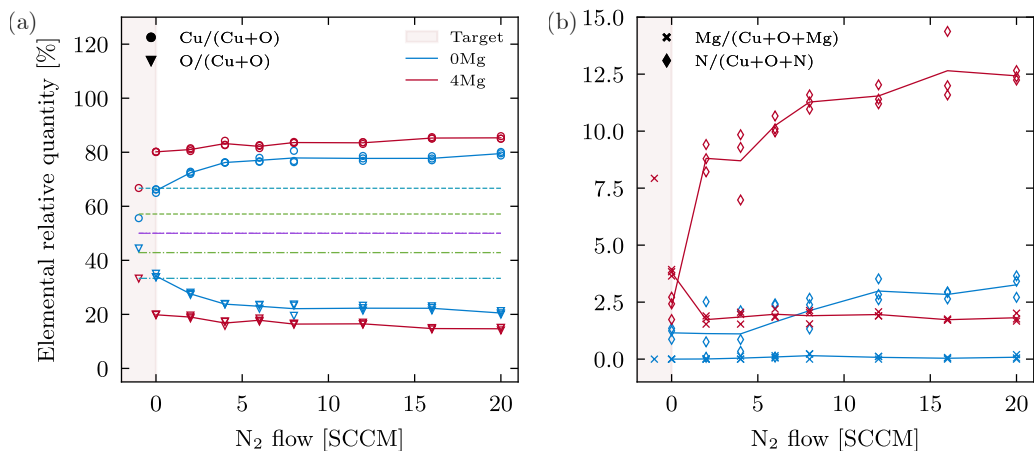


Figure 6.4: Relative elemental composition of N-doped (S2023-0, blue highlight) and (N,Mg)-doped (S2021-4, red highlight) thin films deposited using a N₂ flow varying between 0 and 20 SCCM. We present the Cu and O relative compositions (left panel) as well as the N and Mg relative compositions for both the sputtering targets (first point, transparent red highlight) and the deposited samples. In addition, using respectively purple, green and cyan dashed lines, the stoichiometric compositions of CuO, Cu₄O₃ and CuO are provided as a guide for the eye. The overall accuracy concerning the relative stoichiometries obtained is of the order of $\pm 2\%$ [207].

phase is conserved. Concerning the doping species, in **Fig.6.4(b)**, we highlight a 2-step reduction of the Mg content. First, following the material deposition, a decrease from 8 to 4% (from the S2021-4 sputtering target to the nitrogen free thin films) is reported and is further extended from 4 to 2%, upon nitrogen incorporation. Corroborating this observation, in 2016, Resende *et al.* also reported a reduction of the Mg content inside the synthesised thin film with value 2.3 times lower with respect to the Mg content in the prepared solution [45]. Moreover, each sample deposited with a non-zero N₂ flow, presents an equivalent Mg stoichiometry. As previously underlined based on the XRD characterisation, we further express, based on the Mg stoichiometry reduction upon nitrogen incorporation, a possible interaction between the N and Mg doping species. Finally, concerning the nitrogen content in the films, we report a drastic increase of the elemental composition first from 0 to 2 SCCM (reaching a value of 9%). This observation is to be placed into perspective with the 1% nitrogen incorporation reported for the Mg undoped sample for the same N₂ flow. Proceeding, as the N₂ flow increases, a constant nitrogen incorporation is observed until a maximum value of $\sim 12\%$.

By further focusing on a comparison between the 0Mg (blue curve) and 4Mg (red curve) investigations, one can notice that the Mg-doped sample stoichiometries deviate more largely from the Cu₂O stoichiometry in contrast to the undoped layers. For N₂ flows above 4 SCCM, they all present a Cu-rich and O-poor Cu₂O composition. Then, regarding the nitrogen incorporation, an increase of the N₂ flow leads for each

study to a higher nitrogen incorporation. However, the magnitude of this inclusion is nearly four times larger in the Mg doped layers. In fact, for the highest nitrogen flow, the nitrogen content in the 4Mg thin films reaches nearly the O content value. As a result, we could wonder if this large nitrogen incorporation is facilitated by the presence of Mg and, if this one is the responsible for the amorphisation of the (N,Mg)-doped samples.

6.3.3 Electrical and optical properties

From the knowledge acquired concerning the material crystal structure and elemental composition, we now present and discuss the results obtained for the electrical characterisations. In **Figs.6.5(a)** and **(b)**, the p-type charge carrier concentrations and mobilities are displayed to support the thin film resistivity variations presented in **Fig.6.5(c)**. Concerning Mg,N free sample, a p-type resistivity of 192 Ωcm corresponding to a mobility and charge carrier concentration of respectively $7.71\text{E}16\text{ cm}^{-3}$ and $0.48\text{ cm}^2\text{V}^{-1}\text{s}^{-1}$ is reported¹. The electrical behaviour reported here is in good agreement with state-of-the-art copper oxide resistivity values of the order of $1\text{E}2\text{ }\Omega\text{cm}$ obtained in several works [45, 48, 49, 202].

As shown in **Fig.6.5(c)**, without Mg and upon incorporation of N via an increasing flow from 0 to 4 SCCM, we identify a two order magnitude decrease in resistivity with a resulting value as low as 4.7 Ωcm . From **Fig.6.5(a)**, we attribute this decrease mainly to the nearly two order increase in charge carrier concentration² from $7.7\text{E}16\text{ cm}^{-3}$ to $2.3\text{E}18\text{ cm}^{-3}$. Then, coming back to the 0Mg study presented in **Fig.6.5(c)**, as the nitrogen flow is further increased above 4 SCCM, a slight improvement of the material conductivity to 1.15 Ωcm is identified for a N_2 flow of 12 SCCM. The resistivity behaviour for nitrogen flows above 4 SCCM is attributed to a constant increase of the charge carrier concentration to a maximal value of $4.4\text{E}20$ (20 SCCM) and to a decrease of the mobility to $\sim 0.1\text{ cm}^2\text{V}^{-1}\text{s}^{-1}$ (see **Fig.6.5(a)**). The 0Mg thin film resistivities tend to decrease asymptotically from a $1\text{E}2$ order of magnitude towards 1 Ωcm . Overall, the nitrogen incorporation results first, for low N_2 flow, to a large decrease of the material resistivity followed by a slight improvement ending up in a saturation value between 1 and 10 Ωcm . These observations are corroborated by similar electrical improvements reported in the literature as nitrogen is introduced in Cu_2O samples synthesised using various growth processes [46, 48, 49, 203].

¹A similar result (high resistivity, with a sheet resistance over 40 $\text{M}\Omega$) is obtained for a Cu_2O sample synthesised from the S2018-0 sputtering target presenting an initial Cu_2O material phase.

²The nitrogen flow range on which this behaviour is reported also corresponds to the Cu_4O_3 to Cu_2O crystalline transition reported in the XRD and EDX measurements. However, from additional samples grown using the S2018-0 sputtering target at 0 and 12 SCCM and presenting both a Cu_2O material phase, a decrease of the sheet resistance is observed from over 40 $\text{M}\Omega$ to 9 $\text{k}\Omega$ (0.2 Ωcm). It is associated to a p-type charge carrier concentration increase reaching $3.0\text{E}20\text{ cm}^{-3}$ for the 12 SCCM sample. Therefore, we point out that the crystalline transition reported in the XRD and EDX measurements is consequently not the dominant mechanism that explain such variation of the electrical properties in contrast to possible variations of shallow acceptor defect concentrations.

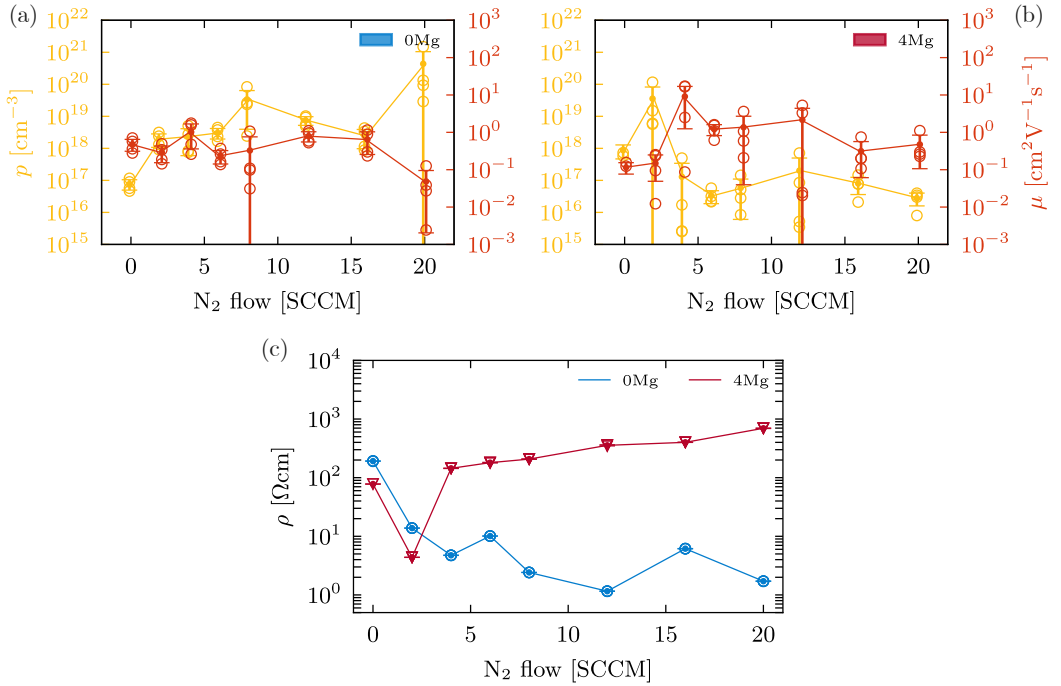
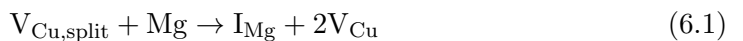


Figure 6.5: Electrical characterisation of N-doped (S2023-0, blue highlight) and (N,Mg)-doped (S2021-4, red highlight) thin films deposited using a N₂ flow varying between 0 and 20 SCCM. In (a) and (b) the thin film majority charge carrier concentration and mobility corresponding to the N-doped and (N,Mg)-doped thin films are presented as a function of the N₂ flow. In figure (c), the resulting thin film resistivity is provided for each study.

Focusing our attention on the two 0 SCCM data points corresponding to the evolution of the resistivity upon Mg doping, we report a decrease of resistivity from 191.7 Ωcm to 77.8 Ωcm. Comparing **Figs.6.5(a)** and (b), this evolution is induced by a dominant charge carrier concentration increase from 7.7E16 to 8.7E17 cm⁻³ and slightly counterbalanced by a mobility decrease from 0.5 to 0.1 cm²V⁻¹s⁻¹. In a previous study, we also reported that the Mg incorporation leads to a nearly two order increase of the charge carrier concentration while reducing the mobility value by a factor 3 [202]. Observations further corroborated in Ref. [45]. Then, as proposed by Iseroff and Carter in Ref. [42], such an electrical resistivity decrease can be explained by the interaction between Mg and the split copper vacancy point defect V_{Cu,split}. Indeed, Mg tends to fill V_{Cu,split} resulting in the cluster defect I_{Mg} + 2V_{Cu} as expressed in Eq.(6.1) [201]. And, as V_{Cu} acts as shallow acceptor, the increase copper vacancy concentration (\nearrow V_{Cu} due to the \searrow V_{Cu,split}) consequently explains the hole concentration improvement presented in **Figs.6.5(a)** and (b) (from 7.7E16 to 8.7E17 cm⁻³).



Finally, upon both N and Mg doping, in **Fig.6.5**, we observe a decrease of the resistivity for low nitrogen incorporations ($4.3 \text{ } \Omega\text{cm}$ for a N_2 flow of 2 SCCM) followed by a constant increase up to $695.25 \text{ } \Omega\text{cm}$. The first resistivity decrease is attributed to an increase of the charge carrier concentration from $8.7\text{E}17$ to $3.6\text{E}19 \text{ cm}^{-3}$ which then constantly decreases down to $2.8\text{E}16 \text{ cm}^{-3}$. Further refined investigations at low N_2 flows would be required to confirm the 2 SCCM data point reported here³. Therefore, while copper oxide doping using either nitrogen or magnesium enhances the material electrical properties, the co-doping strategy leads to a deterioration of the electrical conductivity due to the decrease of the charge carrier concentration. Additionally, in terms of nitrogen flow range, the conductivity degradation matches with the high nitrogen incorporation reported in the EDX measurements (see **Fig.6.4**).

Furthermore, concerning the optical characterisation of the 0Mg samples presented in **Fig.6.6**, we reveal a mean transparency improvement from 17.02% to 33.74% following the nitrogen flow increase. Similarly to the electrical trends reported, this transparency enhancement is characterised by a large improvement from 0 to 6 SCCM followed by a saturation for N_2 flows above 6 SCCM. We also report an increase of the material bandgap from 2.37 eV (0 SCCM) to 2.49 eV (6 SCCM) as displayed in **Fig.6.6(c)**. However, as presented in **Fig.6.6(b)**, the onsets of the absorption coefficient for the 0 and 2 SCCM curves are not as sharp as the ones for higher nitrogen doping values. Concerning the absorption behaviour, Zhao *et al.* predicted an additional subband absorption peak located between 0.9 and 2 eV and attributed to the N_O point defect [199]. This prediction was experimentally observed by Malerba *et al.* in Ref. [49] but seems to be absent or not detected from the Tauc plot analysis performed in this work. On the contrary, only variations associated to interference effects are observed within this energy range. As a result, the presence of N_O point defects could not be established.

In relation to the optical properties, upon Mg doping, the material bandgap decreases from 2.37 to 2.04 eV, observation corroborated Jacob *et al.* in Ref. [47]. In addition, contrasting the reported electrical improvement, the Mg incorporation leads to a drastic deterioration of the thin film optical properties with an average transparency decreasing from 17.02 to below $\sim 1\%$. Then, as a result of the nitrogen incorporation in the Mg-doped layers, the mean transparency improved to values between 7.32 and 13.87 % and bandgap values fluctuate around 2.1 eV (see **Fig.6.6(c)**). In addition, based on the Tauc analysis presented in **Fig.6.6(a)**, we report a sharper onset of the absorption coefficient for N,Mg co-doped samples in opposition to the Mg-doped sample.

To summarise, concerning the co-doped samples, the material properties reported were consistently poorer than the ones associated to N-doped samples. The com-

³A similar behaviour was also identified in the 15 mTorr study presented in appendix C.

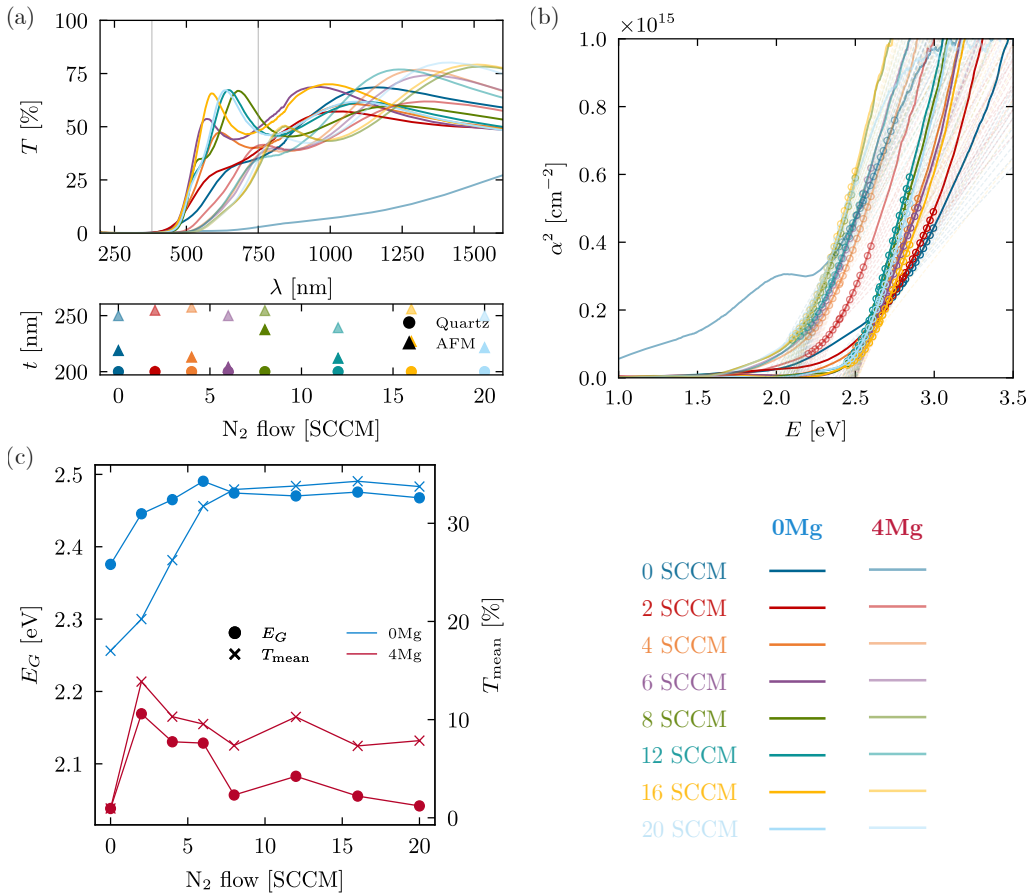


Figure 6.6: Optical characterisation of N-doped (S2023-0, blue highlight) and (N,Mg)-doped (S2021-4, red highlight) thin films deposited using a N_2 flow varying between 0 and 20 SCCM. In figure (a), we present the measured thin film transmittance curves as well as the measured thicknesses in the bottom panel. From the transmittance measurements, a tauc plot analysis is realised and presented in figure (b). The extracted bandgap values have an error margin of 0.05 eV. The legend for the two figures is presented alongside to avoid an overcrowding of the curves. Finally, from the Tauc plot analysis and the measured transmittance curves, the thin film bandgap and transparency values are presented in figure (c).

bined effect of Mg doping and high nitrogen flow conditions results in a constant degradation of the film conductivity while slightly improving the optical properties. Moreover, based respectively on the EDX and XRD characterisations, important nitrogen incorporation and thin film amorphisation were also reported within that N_2 flow range. In order to understand the physical mechanisms behind the evolution of the thin film properties, the analysis needs to focus on the effects of possible defects in the layers.

6.3.4 Phase and defects correlation through Raman spectroscopy

In this section, using Raman spectroscopy, possible copper oxide point defects are correlated to specific phonon activities. As described by Sander *et al.* and Debibichi *et al.*, the Raman activity of copper oxide material is quite interesting in the point of view of phases and point defects. Indeed, according to the group theory, pristine Cu_2O crystal only allows one phonon mode, T_{2g} , corresponding to an active Raman band located at 515 cm^{-1} [90,211]. In addition, as presented by Sander *et al.*, a typical Raman spectrum of copper oxide Cu_2O is much richer than only the T_{2g} phonon mode. Intrinsic point defects located at different crystallographic sites possess specific local symmetries which are usually lower than the one of the perfect crystal resulting in the activation of different Raman modes coupled to Raman bands in the measured spectrum as presented in **Tab.6.1** [90,200]. Among such intrinsic point defects, the most noteworthy, identified in the introduction are copper vacancies V_{Cu} and $V_{\text{Cu,split}}$ and oxygen vacancy V_{O} . Concerning their Raman activity, Sander *et al.* reported that the simple copper vacancy has a small impact on the Raman spectrum with only a splitting of the $T_{2g} - 515 \text{ cm}^{-1}$ mode into $A_{1g} - 541 \text{ cm}^{-1}$ and $E_g - 318, 510 \text{ cm}^{-1}$. Then, V_{O} results in the activation of all phonon modes excepts the $T_{2u} - 90 \text{ cm}^{-1}$. Finally, upon generation of split copper vacancies, Raman activity is introduced for all bands. Moreover, concerning extrinsic point defects related to Mg and N_2 , one can mention the following ones in particular: Mg on $V_{\text{Cu,split}}$ as well as $(\text{N}_2)_{\text{Cu}}$ and N_{O} as reported in Ref. [198].

As pointed out by Debibichi *et al.*, Raman spectroscopy is also an interesting analysis method to differentiate the distinct Raman response of the various copper oxide crystalline phases (CuO , Cu_4O_3 and Cu_2O) [26,211]. Concerning Cu_4O_3 , several Raman active modes are predicted by the group theory: $A_{1g} - 541 \text{ cm}^{-1}$, $B_{1g} - 651 \text{ cm}^{-1}$ and $E_g - 318, 510 \text{ cm}^{-1}$. These theoretical predictions were also corroborated by experimental results as Wang *et al.* reported upon various oxygen flow rates, Raman bands at 311, 505 and 531 cm^{-1} for the Cu_4O_3 material phase. Concerning Cu_2O , a large activity in the range between 90 and 216 cm^{-1} as well as a band located at 609 cm^{-1} were observed and can be associated to defects [212,213].

Based on the Raman characterisations presented in **Fig.6.7**, we provide the reader possible explanations concerning the microscopic origin of the charge carrier variations reported previously. Concerning the N-doped Cu_2O sample spectra shown in **Fig.6.7(a)**, a distinct variation is identified between the undoped thin film (N_2 flow of 0 SCCM) and the thin films synthesised with a N_2 flow parameter above 4 SCCM. This behaviour is further highlighted by the smooth transformation of the 0, 2, 4 and finally 6 SCCM Raman spectra observed. We distinguish an increase Raman activity for all bands between 90 and 250 cm^{-1} as well as for the bands located around 610 cm^{-1} . In contrast, the band at 515 cm^{-1} tends to decrease in intensity and to flatten due to the splitting into two adjacent bands at 510 and 540 cm^{-1} . This observation is clearly corroborated by the results reported in Refs. [211–213] corresponding to a

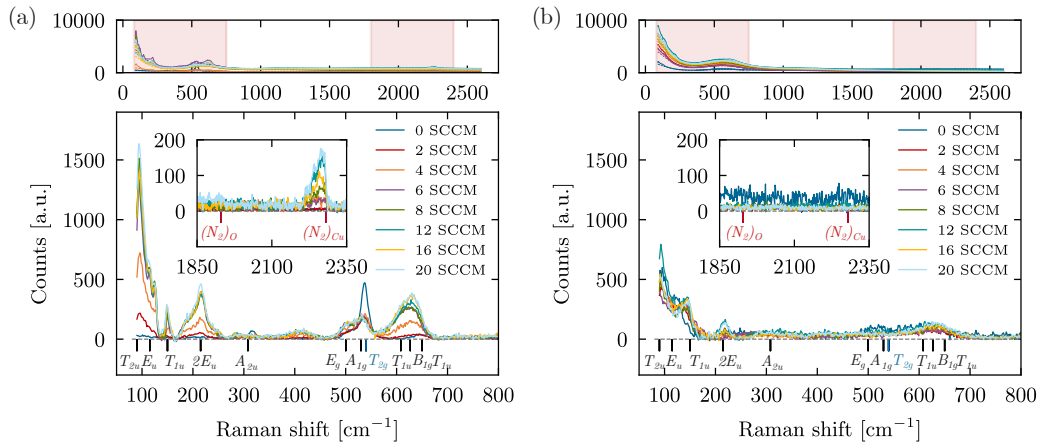


Figure 6.7: Raman spectra of (a) the N-doped (S2023-0, blue highlight) and (b) the (N,Mg)-doped (S2021-4, red highlight) thin films deposited using a N_2 flow varying between 0 and 20 SCCM. The top panel displays the acquired raw data while the red highlight corresponds to zones of interest. In the bottom panels, we present the treated measurements as well as the phonon mode associated to the different Raman bands (in black). In blue, the T_{2g} mode corresponds to the only active phonon mode for a perfect copper oxide crystal [90]. Finally, in the figure insets, the Raman bands associated to nitrogen-related defects are presented in red. This figure is interpreted based on **Tab.6.1**.

crystalline transition from Cu_4O_3 to Cu_2O .

Secondly, from a defect perspective, as the nitrogen flow increases, two phenomena can be observed and supported by Raman activities reported in **Tab.6.1**. First, concerning intrinsic defects, the splitting of the T_{2g} mode into the A_{1g} and E_g illustrates an increase of copper vacancy V_{Cu} . And, in addition, the increase of the Raman activity for each band below 250 cm^{-1} is attributed to an increase of $V_{Cu,split}$. Both of these leading to a possible explanation regarding the increase of free charge carriers previously reported. Then, secondly, in addition to the increase of intrinsic defects, in the inset of **Fig.6.7(a)**, we report a strong band activity close to 2280 cm^{-1} which corresponds according to Thienprasert *et al.* to the phonon mode of $(N_2)_{Cu}$ [198]. This point defect possesses a low formation energy as well as a shallow acceptor behaviour. Moreover, as the band intensity is a function of the nitrogen flow, we consequently believe that the charge carrier increase reported upon nitrogen doping is attributed to the increased concentration of $(N_2)_{Cu}$.

Concerning the (N,Mg)-doped thin films presented in **Fig.6.7(b)**, the Raman signatures indicate a Cu_2O material phase as already reported in the EDX and XRD measurements. Unfortunately, the relatively poor material crystallinity does not allow us to observe any fine features that could be related to the impact of Mg doping in contrast to the results presented by Jacob *et al.* [47]. In addition, no band activity is detected within the inset figure concerning the $(N_2)_{Cu}$ point defects.

6.3.5 Point defect discussion

Firstly, concerning the Mg doping, from the literature, it is accepted that the Mg incorporates in a split copper vacancy site forming the $I_{Mg} + 2V_{Cu}$ cluster defects [42]. In this work, this statement seems also quite reasonable as, with respect to the observations of Resende *et al.*, the same material phase stability and charge carrier concentration increase are reported here [45, 201] (see **Fig.6.5(a)**). Upon Mg doping, the observed hole concentration increase is therefore related to the increase of the simple copper vacancies acting as shallow acceptor defects.

Secondly, concerning the nitrogen doping, some publications reported that the most dominant defect would be the substitution of oxygen by nitrogen: N_O [46, 199]. Indeed, using *ab initio* calculations, Jiraroj T-Thienprasert *et al.* also predicted N_O as low formation energy defects along with $(N_2)_{Cu}$. However, the authors identify N_O as a deep acceptor that cannot be responsible for the charge carrier variation reported in opposition to the shallow acceptor $(N_2)_{Cu}$ (associated to a Raman band at 2280 cm^{-1}) [198]. Moreover, using Raman measurements, in this work, $(N_2)_{Cu}$ point defects were clearly identified in the case of N-doped Cu_2O samples (see **Fig.6.7(a)**). The band activity is also reported to be proportional to the nitrogen flow. In opposition, within the absorption spectra no subband absorption corresponding to N_O was reported (see **Fig.6.6(b)**).

Finally, concerning the (N,Mg)-doped sample, unfortunately, the deterioration of the crystallinity does not allow us to extract much information concerning point defects. However, in the scope of EDX measurements, we report a strong increase of the nitrogen incorporation in contrast to the Mg undoped samples. As a result, it seems that the presence of Mg drastically facilitates the incorporation of nitrogen. A possible explanation could be that as the Mg replaces the split copper vacancy, the number of simple copper vacancies V_{Cu} , possible sites for nitrogen incorporation also increases. The co-doping would then enhance the nitrogen incorporation. In addition, it is also possible that an excessive amount of nitrogen leads to the film amorphisation resulting in the subsequent degradation of the optoelectrical properties.

6.3.6 Experimental reproducibility

In addition to the nitrogen doping using the S2023-0 sputtering target, the experimental reproducibility of the process was investigated using the corresponding S2021-0 target on a full range of nitrogen flow values from 0 to 21 SCCM (see **Tab.C.1** for specific values).

Figures 6.8(a) and **(b)** present respectively the crystallographic and Raman measurements of the deposited thin films by purposely superimposing the similar nitrogen flow of the samples from the S2021-0 and S2023-0 targets. We observe a very similar

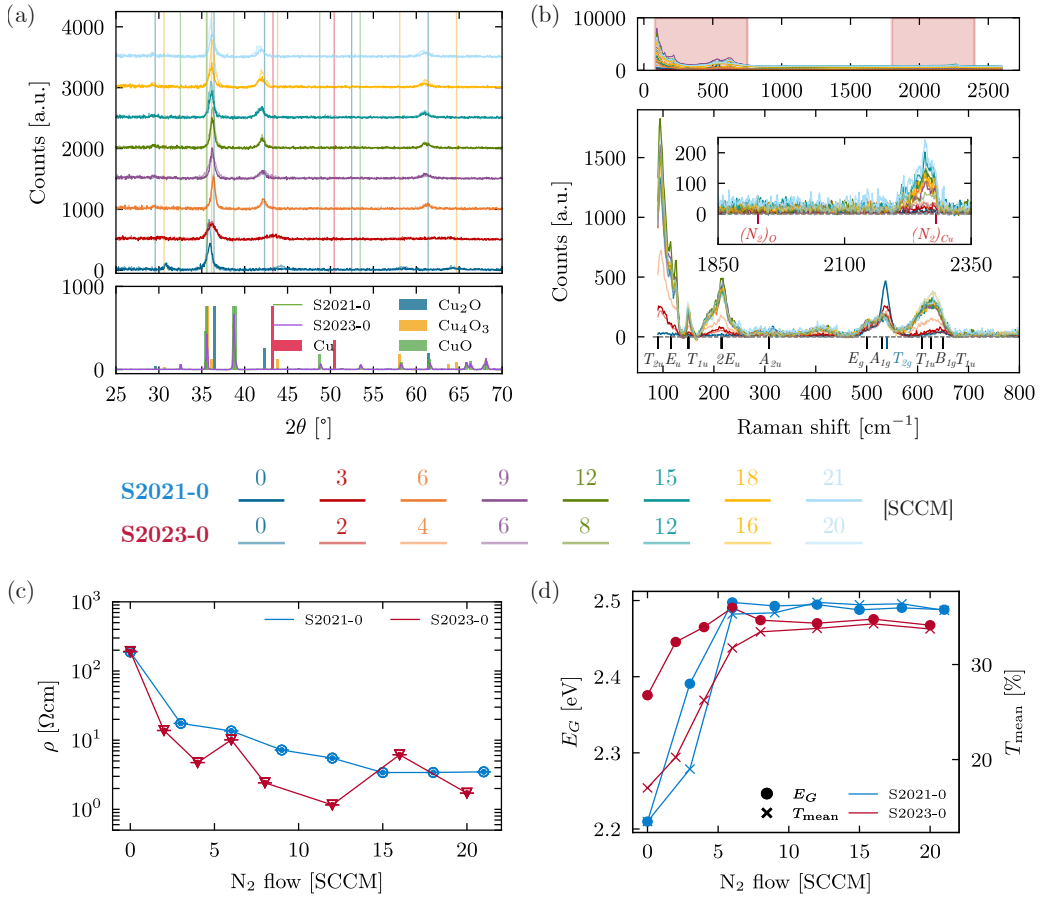


Figure 6.8: Investigation of the nitrogen doping reproducibility using different sputtering targets: S2021-0 and S-2023-0 with respectively (a) the crystallography investigation using XRD by purposely superimposed the corresponding nitrogen flow XRD spectra. (b) The Raman spectra, (c) the thin film resistivity and (d) the thin film bandgap and average transparency values. The extracted bandgap values have an error margin of 0.05 eV.

trend with the 0 SCCM samples presenting a main Cu₄O₃ crystalline phase before experiencing a crystallographic transition to a Cu₂O crystal between 0 and 4 SCCM. In addition, concerning the Raman measurement, in the figure inset, the 2280 cm⁻¹ band increase associated to the (N₂)_{Cu} point defects is clearly observed for both studies. Regarding the samples optoelectrical properties, we present in **Fig.6.8(c)** the VdP measurements realised on each N-doped thin film. A good reproducibility is also observed here with a nearly two order of magnitude reduction of the resistivity. Finally, a similar observation is realised in **Fig.6.8(d)** concerning the extracted bandgap and average transparency values. A good reproducibility is therefore established concerning the nitrogen doping of copper oxide thin films deposited using RF magnetron sputtering at room temperature.

6.4 CONCLUSION

Throughout the investigation of the nitrogen and magnesium doping of copper oxide thin films, several main results were obtained. First, we highlight the possible synthesis of Cu_2O crystalline phase from a CuO sputtering target. Elemental losses lead to a crystalline transition from an oxygen rich copper oxide phase (CuO) to a poorer O phase: Cu_4O_3 . Then, as the nitrogen is introduced following the nitrogen flow increase, a second crystalline transition is reported from Cu_4O_3 to Cu_2O . We believe that this crystalline transition is attributed to a reduction of the oxygen inside the synthesised layers due to the lack of control of the O flow during the RF sputtering depositions. Assumption further supported by the EDX results presented.

Then, by implementing the nitrogen doping strategy of the S2023-0 (and S2021-0 as presented in the reproducibility section), a possible interaction between nitrogen and oxygen via the formation of N_O point defects could be considered. However, from optical characterisation results, no absorption subband between 1 and 2 eV were reported for any of the samples. Absorption subband predicted as associated to the N_O substitution. In addition, the nitrogen doping lead to a drastic improvement of both the electrical and optical properties with resistivity and transparency enhancements from 192 to $1.15 \Omega\text{cm}$ and from 17.02 to 33.74%, respectively. This electrical improvement is mainly attributed to a charge carrier concentration increase from $7.7\text{E}16 \text{ cm}^{-3}$ to a maximal value of $4.4\text{E}20 \text{ cm}^{-3}$. Additionally, predictive studies on defects using DFT reported that N_O could not be the source of this charge carrier concentration increase as the associated acceptor level is too deep in the material bandgap. In contrast, the literature also reports $(\text{N}_2)_{\text{Cu}}$ as a low formation energy defect acting as a shallow acceptor. The latter provides an ionisation energy level closer to the valence band maximum. In this work, using Raman spectroscopy, we confirm the prediction realised. For each N-doped Cu_2O thin film, we report an active Raman band located around 2280 cm^{-1} , associated to the $(\text{N}_2)_{\text{Cu}}$ point defect, whose intensity is proportional to the deposition nitrogen flow. This observation consequently suggests that the thin film electrical improvement is attributed to the increase concentration of N_2 on Cu sites.

Then, upon Mg doping using the S2021-4 sputtering target, we observe a slight improvement of the material conductivity as previously mentioned in the literature as well as a net degradation of the thin film transparency. These observations were also associated to the reduction of the Mg content in the film in contrast to the sputtering target content as reported in the literature. In addition, following the co-incorporation of Mg and N, as the nitrogen flow increases, we observe a drastic decrease of the film crystallinity. And, the nitrogen flow range associated to the sample amorphisation corresponds to the flow range at which a high incorporation of nitrogen is reported (more than 4 times higher than in the Mg undoped thin films).

This high incorporation was also accompanied by a degradation of the electrical properties (for flow values above 2 SCCM) and a slight improvement of the optical properties. We consequently consider a possible interaction between the N and the Mg in the form of a $(N_2)_{Cu} + I_{Mg}$ cluster defect. Indeed, the incorporation of Mg on the $V_{Cu,split}$ site leads to an increase of the V_{Cu} sites. Incorporation further supported by the stabilisation of the Cu_2O crystalline phase reported for the Mg-doped sputtering target in opposition to the one undoped. And, in the N-doped samples without Mg, these simple copper vacancies were identified as hosts to form $(N_2)_{Cu}$ point defects. Unfortunately the high degree of amorphisation of the N,Mg doped thin films (that could be due to the high nitrogen incorporation) does not allow us to identify these point defects in the Raman measurements.

Further investigations would then be required to obtain a complete picture of the physical phenomena underlined in this work. Among them, the investigation of the deposition plasma pressure between 5 and 15 mTorr is proposed in appendix C. Then, gaining additional control over the oxygen flow would allow us to tune layer stoichiometry. The control of the oxygen flow rate is also reported as essential in the literature as this one affects the impurity concentration as well as the film transmittance [39]. Finally, post-deposition thermal treatments in nitrogen atmosphere would also be interesting, specifically in the case of the (N,Mg)-doped copper oxide layers, in order to improve the sample crystallinity [214]. Finally, as illustrated using Raman spectroscopy, further defect-related investigation techniques are essential to understand the origin of the thin film optoelectrical behaviours. Therefore photoluminescence (PL) and advanced measurements such as positron annihilation spectroscopy (PAS) appear also relevant to strengthen the scientific knowledge in copper oxide layers [196].

CONCLUSION

The objective of this thesis is to **extend the knowledge of the scientific community concerning the role of point defects on the physical properties of Cu_2O and $\text{Cu}_2\text{ZnSnS}_4$ absorber layers and consequently, on the resulting photovoltaic performances.**

In that perspective, in section 2.3, classification and definitions of point defects were introduced. Via a comprehensive analysis of the SRH statistics, we described defect-assisted recombination processes and detailed the microscopic origin of the charge carrier capture coefficients. We also discussed the fundamental relation between recombinations and lattice distortions undergone by the pristine crystal upon defect introduction or charge state variation. Through this initial endeavour, we reached an accurate description concerning the physics of *efficient* non-radiative recombination centres. Moreover, we laid the foundation for the upcoming defect investigations conducted in kesterites and copper oxides. As described, these two earth-abundant Cu-based alloys showcase PV efficiencies that are currently limited by high non-radiative recombination rates.

As reported in the literature, concerning kesterites, the Sn cationic substitution by Ge appeared as an interesting strategy to enhance the material photovoltaic performances. Consequently, to investigate the impact of Ge doping and alloying, combined studies using first-principles calculations, photo-electrical conversion efficiency modelling and defect formation energy predictions based on the supercell methodology were performed in $\text{Cu}_2\text{ZnSnS}_4$ compounds.

First, we reported on the evolution of the structural, optical and electrical properties of $\text{Cu}_2\text{ZnSnS}_4$ following the sequential substitution of Sn by Ge and Si. We observed increasing direct bandgap values of 1.32, 1.89 and 3.06 eV for $\text{Cu}_2\text{ZnSnS}_4$,

$\text{Cu}_2\text{ZnGeS}_4$ and $\text{Cu}_2\text{ZnSiS}_4$, respectively. Moreover, high absorption coefficients of the order of 10^4 cm^{-1} were reported for each compound, confirming their suitability as PV absorber layer. Then, using as data input, the *ab initio* computed material optical properties, the key solar cell parameters were modelled as a function of the non-radiative recombination rate based on a model proposed by Blank *et al.* [87]. For vanishing non-radiative recombination rate, we highlighted maximal efficiency values of 25.71, 19.85 and 3.1 % for Cu_2ZnXS_4 (X=Sn,Ge,Si), respectively. Moreover, based on an optimal $1.15 \mu\text{m}$ absorber thickness value, we emphasised the large room for improvement reported for the Sn- and Ge-based kesterites following the reduction of the non-radiative recombination rate. With respect to state-of-the art performances corresponding to V_{OC} values of 685 mV, the efficiencies of $\text{Cu}_2\text{ZnSnS}_4$ and $\text{Cu}_2\text{ZnGeS}_4$ can be improved by ~ 10 and ~ 5 points, respectively. These results therefore support the possible short-term incorporation of kesterites in tandem approaches as reported in Ref. [16]. Then, following the construction of the phase diagrams of both $\text{Cu}_2\text{ZnSnS}_4$ and $\text{Cu}_2\text{ZnGeS}_4$, we underlined the small area corresponding to a stable kesterite phase free of secondary phases. This observation is further supported by the experimental work reported in appendix B. The important number of distinct secondary phases is directly related to the complex quaternary structure of kesterite compounds and contribute to the high non-radiative recombination rates reported. Therefore, reducing the occurrence of these ones is a key parameter to improve further the cell efficiencies. In that sense, solution based processes offer a convenient growth method (see appendix B). Concerning the behaviour of point defects, $\text{Cu}_2\text{ZnSnS}_4$ and $\text{Cu}_2\text{ZnGeS}_4$ present both a p-type conductivity attributed to the low formation energies of V_{Cu} and Cu_{Zn} acceptor defects. Then, we also confirm the detrimental behaviour of Sn_{Zn} featuring all characteristics of an *efficient* recombination centre as presented in section 2.3. Finally, following the introduction of Ge, the lowest formation energy is reported for the Ge_{Sn} substitution induced by the electronic similarities between Sn and Ge. In addition, upon Ge doping and alloying, Ge_{Zn} is identified as a possible recombination centre in both $\text{Cu}_2\text{ZnSnS}_4$ and $\text{Cu}_2\text{ZnGeS}_4$. This substitution presents low formation energy as well as ionisation levels within the centre of the material bandgap. Furthermore, it appeared that the lattice distortion induced by the formation of X_{Zn} defects or by variation of their charge states is reduced for the Ge_{Zn} in comparison to its Sn counterpart. This result hints at a less detrimental defect behaviour to be ascribed to Ge_{Zn} with respect to Sn_{Zn} . As a consequence, we point out both the decreased concentration and the reduction of lattice distortion of the detrimental defect X_{Zn} (X=Sn,Ge) as possible sources of the V_{OC} improvement reported in the literature upon Ge incorporation.

The research work conducted in kesterites shed the light on the open circuit voltage V_{OC} limitation imputed to point defects that act as efficient non-radiative recombination centres within the bulk absorber layer. And, the identification of the positive impact of Ge doping and alloying with respect to the Ge_{Zn} defect offer a piece of explanation for the V_{OC} improvement reported. Furthermore, as under-

lined in chapter 2, doping, the intentional introduction of an extrinsic defect in the pristine crystal lattice, can also be used to improve the material optoelectrical properties. That mechanism is of specific interest to improve both V_{OC} and FF photovoltaic parameters in copper oxide based solar cells. Moreover, the experimental study of point defects in another Cu-based material used for PV applications allow us to highlight the similar relevance of defect investigations. Based on state-of-the-art theoretical predictions concerning points defects in Cu_2O , we experimentally studied the (N,Mg) co-doping strategy of copper oxide thin films synthesised using RF magnetron sputtering at room temperature. The use of vacuum-based deposition method without any thermal treatment was motivated by the search for a low cost synthesis process. Moreover, the defined objective of this investigation was to correlate defect concentrations and crystalline structure variations to the evolution of the thin film properties. To do so, a battery of characterisation techniques was exploited.

Starting from a CuO crystalline phase, we unveil a possible synthesis mechanism for N-doped Cu_2O layers attributed to oxygen losses. We believe that this crystalline transition is attributed to a reduction of the oxygen inside the synthesised layer due to the lack of control of the O flow during the RF sputtering deposition. In addition, the nitrogen doping lead to a drastic improvement of both electrical and optical properties with resistivity and transparency enhancements from 192 to 1.15 Ωcm and from 17.02 to 33.74%, respectively. This electrical improvement is mainly attributed to a charge carrier concentration increase from $7.7\text{E}16\text{ cm}^{-3}$ to a maximal value of $4.4\text{E}20\text{ cm}^{-3}$. Concerning point defects, in the literature, both $(\text{N}_2)_{\text{Cu}}$ and N_{O} were identified as possible candidates to be ascribed to the thin film electrical enhancements. Indeed, these two substitutions feature low formation energies and acceptor like behaviours. However, from optical characterisation results, in this work, no N_{O} related absorption subband between 1 and 2 eV were reported for any of the samples. Furthermore, DFT predictive studies reported that N_{O} could not be the source of the charge carrier concentration increase as the associated acceptor level is too deep in the material bandgap. In contrast, using Raman spectroscopy, as the nitrogen incorporation increases, we report an increased activity of the Raman band located around 2280 cm^{-1} , associated to the $(\text{N}_2)_{\text{Cu}}$ substitution. We therefore deduced that the thin film electrical improvement is attributed to the increased concentration of N_2 on Cu sites. Consistent with the established literature, we also confirm the improvement of the sample optoelectrical properties as Mg is introduced within split copper vacancy sites $V_{\text{Cu,split}}$. Enhancement that is limited with respect to the impact of the nitrogen doping. Conversely, we demonstrate that co-doping with Mg and N degrades the material crystallinity, leading to a reduction in thin film conductivity, likely due to high nitrogen incorporation. Finally, the good experimental reproducibility of the study was underlined. From this co-doping investigation, we therefore confirm and highlight possible microscopic mechanisms that contribute to the improvement of the material optoelectrical behaviour.

A main conclusion that can be drawn from the research conducted for both

kesterites and copper oxides is the following one. In order to improve the efficiency of the application considered, it is essential to understand the physical mechanisms underlying the macroscopic material properties. In that sense, concerning PV absorber layers, defects (point defects, secondary phases, *etc.*) play a crucial role in both material properties improvement and limitation. Their understanding is therefore crucial to push further the efficiency of the technology under study. This statement is also true for any applications involving solid-state materials. Based on that conclusion, we would like to detail several perspectives concerning further investigations of kesterites and copper oxides.

Regarding kesterites, as described in appendix B, solution-based processes offer a convenient route to tune the precursor stoichiometry and as a result the synthesised layer after S,Se annealing [57,66,175]. Indeed, the solution growth procedure allows the control of the Sn oxidation state and therefore the selection of the +4 configuration. Furthermore, as presented in chapter 5, the lattice deformation associated to the $\text{Sn}_{\text{Zn}}^{+2}$ substitution (charge state +2 corresponding to Sn in oxidation state +4) is "close" to the one of the pristine crystal therefore reducing the detrimental behaviour of the defect in contrast to the large lattice distortion reported for Sn_{Zn}^0 (charge state 0 corresponding to Sn in oxidation state +2). Observations that corroborate the results presented in Refs. [73,109]. As a consequence, this route should be further investigated in order to synthesise absorber layer with limited secondary phases (see appendix B) and reduced amount of detrimental defects, both leading to a reduction of the V_{OC} deficit. Moreover, in combination with other strategies such as bandgap grading [215], post-annealing [66] and Ag doping [57], new breakthroughs and efficiency records should be in reach. The improvement of the synthesis conditions should also be conducted in parallel with further defect predictions using *ab initio* approaches, such complex defects investigations [216] or charge carrier capture coefficients computations [73,109,191]. Finally, prediction confirmations using advanced characterisation methods such as transient electrical characterisations [66] on bare absorber layers or complete solar cell structures should offer a complete picture of the fundamental physical mechanisms. This last point also emphasises the need for strong collaborations between research groups with distinct expertise such as thin film synthesis, advanced characterisation methods and sophisticated material predictions.

Then, concerning copper oxide materials, the pursue of the (N,Mg) co-doping investigation should be considered in order to gain further insights concerning the interaction between N and Mg inside the Cu_2O layers. Study that can again be supported by *ab initio* predictions of possible complex defects [42]. In addition, a possible refinement of the synthesis parameters could be considered notably for the N_2 flow. In that perspective, the control of the oxygen flow during the thin film synthesis is considered as a crucial ingredient to tune both copper oxide crystalline phases and defect concentrations (impurities being closely related to the transmittance value as reported by Shibasaki *et al.* in Ref. [39]). Then, following the optimisation of

the synthesis conditions, post-deposition thermal treatments in nitrogen atmosphere would also be interesting in order to improve the sample crystallinity [214]. Finally, as illustrated using Raman spectroscopy, defect-related investigation techniques are vital to understand the origin of the thin film optoelectrical behaviours. Therefore, as presented by Sekkat *et al.*, photoluminescence (PL) and advanced measurements such as positron annihilation spectroscopy (PAS) appear relevant to strengthen the scientific knowledge in copper oxide layers [196]. From these additional investigations, absorber layers showcasing improved electrical and optical properties should result in enhanced solar cell short circuit current density J_{SC} and fill factor FF , which were the two PV parameters highlighted as limiting factors for copper oxide solar cells. Naturally, parallel works focused on the optimisation of the remaining parts of the cell architecture, as well as on interface defects, are also desirable [217].

COMMENTS ON *AB INITIO* CALCULATIONS

A



The purpose of this appendix is to provide the reader a description of the methodology employed to compute the *ab initio* results obtained using the Vienna Ab Initio Simulation Package (VASP). First, the ionic and electronic relaxations are presented including \mathbf{k} -points and cutoff energy convergences. These relaxations allow us to gather the total energy of the system. Quantity required to compute the defect formation energy (see Eq.(3.43)). Then, we present the method used to compute the density of states (DOS) and the band structure as well as to calculate the material dielectric tensor. In addition, as presented in chapter 3 (see Eq.(3.3)), a section is dedicated to the Hartree energy used to scale the many-body Schrödinger equation in condensed matter. Finally, in relation to chapter 5, the kesterite formation energies and associated chemical potential values are reported in the last section.

A.1 VASP PRACTICAL FEATURES

A.1.1 Ionic and electronic relaxations

In this section, we present the methodology used to compute the ground state energy of the crystal under consideration using VASP software¹. The ground state is obtained through the ionic and electronic relaxations. To achieve these ones, 4 initial files are required:

¹<https://www.vasp.at/> visited on the 2nd of November 2023.

POSCAR: This first file contains the lattice vectors describing the primitive cell under consideration, as well as the positions of each chemical species within the primitive cell.

```

1  Cu_2 Zn Sn S_4
2  1.0000000000000000
3      6.6115909555381087    0.0199297216888466    -0.0000000675610566
4      2.1801647744171460    6.2418277542984084    -0.0000000463891245
5      -4.3958773490867715    -3.1308783835407774    3.8193448334043834
6      Sn      Zn      Cu      S
7      1      1      2      4
8  Direct
9      0.2499999733612270    0.7499999560400923    0.4999999735386780
10     0.5000000175570989    0.5000000001148734    -0.0000000000000000
11     0.7500000130355673    0.249999923791023    0.4999999735386780
12     -0.0000000000000000    -0.0000000000000000    -0.0000000000000000
13     0.1141324715965275    0.1382348166809158    0.4933560019255824
14     0.8617651094684552    0.3551211712349666    0.9758975944866803
15     0.3792235897333764    0.8858674811233904    0.0241023295591434
16     0.6448788073327839    0.6207764711553114    0.5066439452276952
17
18     0.00000000E+00    0.00000000E+00    0.00000000E+00
19     0.00000000E+00    0.00000000E+00    0.00000000E+00
20     0.00000000E+00    0.00000000E+00    0.00000000E+00
21     0.00000000E+00    0.00000000E+00    0.00000000E+00
22     0.00000000E+00    0.00000000E+00    0.00000000E+00
23     0.00000000E+00    0.00000000E+00    0.00000000E+00
24     0.00000000E+00    0.00000000E+00    0.00000000E+00
25     0.00000000E+00    0.00000000E+00    0.00000000E+00

```

POTCAR: This file provides the pseudopotential associated to each atomic species (with their specific number of valence electrons). It is important to note that the exchange-correlation functional used to compute the pseudopotential has to match the one used in the upcoming calculation (see section 3.2).

KPOINTS: This file contains information concerning the \mathbf{k} -space meshing of the first Brillouin zone (see section 3.2). The convergence of this \mathbf{k} -point mesh has to be performed correctly prior to the electronic relaxation.

```

1 Automatic mesh
2 0 ! number of k-points = 0 ->automatic generation scheme
3 Gamma
4 6 6 6
5 0 0 0

```

INCAR: This file contains all the flags required to properly describe the calculation that the user wants to perform on the crystal (described in **POSCAR** and **POTCAR**) and at each \mathbf{k} -point contained in **KPOINTS**. Besides describing the electronic or ionic relaxations to be done, the **INCAR** file specifies also the exchange-correlation functional used as well as the converged value of the cutoff energy (**ENCUT**) (see section 3.2). Furthermore, one can specify whether the calculation starts from scratch (**ISTART**), from an initial charge density (**ICHARG**) or from an initial wavefunction (**INIWAV**). Finally, some writing flags list the outputs to be saved at the end of the calculation.

One can also decide to perform both ionic and electronic relaxations or to fix the atomic positions and perform only the electronic relaxation. For each ionic relaxation step (each atomic movement), a complete series of electronic relaxations is performed. The ionic relaxation can be performed using a criterion of energy, of force, or a number of steps (**EDIFFG**). Once the convergence criterion selected, the

cell is relaxed accordingly by respecting some degrees of freedom (atomic positions, cell volume, and/or cell shape) fixed by the **ISIF** flag. In addition, the **ISYM** parameter can be specified if one wishes VASP to treat the system symmetry. Between each ionic relaxation step, a complete electronic relaxation is performed based on an energy criterion fixed by the **EDIFF** flag.

Finally, at the end of the relaxations, the output files are written. Among them, one can cite the relaxed atomic positions (**CONTCAR**), the electronic wavefunction (**WAVECAR**), and the electronic charge density (**CHGCAR**). Most importantly, the **OUTCAR** file contains all the information concerning the convergence of the calculation² (forces, pressure, energy, *etc.*). Concerning the calculation of the defect formation energy, the total system energy can be found here.

Once the ground state of the system has been obtained, further calculations can be realised starting from the **CONTCAR**, **WAVECAR** and **CHGCAR** files for continuation jobs. We emphasize that thorough convergences of the cutoff energy E_{cutoff} and the **k**-point grid meshing are required.

A.1.2 Band structure and density of states (DOS)

The material band structure or the DOS can be computed by restarting the electronic relaxation from the continuation files obtained as a result of the ground state calculation.

First, concerning the density of states, an electronic relaxation including a higher number of points (**NEDOS**) is required to obtain a smooth distribution. Furthermore, the DOS can be computed on the same **k**-points grid as the ground state calculation (uniform meshing of the first Brillouin zone). In contrast, the band structure calculation implies to set properly the path that the user wants to follow in the reciprocal space. To do so, additional **k**-points have to be added to the existing uniform meshing used for the ground state calculation.

A.1.3 Optical properties

Finally, to extract the optical properties of the material, the dielectric tensor must be calculated (see section 2.2). To do so, using the converged **k**-points uniform mesh and restarting from the ground state, the dielectric matrix is computed using the flag **LOPTICS**. Furthermore, as the calculation of this tensor implies a summation over filled bands (valence bands) and empty bands (conduction bands), one must ensure the setting a sufficient number of conduction band states using the flag **NBANDS**.

²The specific information stored in this file depends on the writing flags defined in INCAR.

A.2 HARTREE ENERGY

In this section, the energy quantity)à used to scale the many-body Schrödinger equation (see Eq.(3.3)) is detailed.

Looking at electrostatic interactions, the simplest system that can be considered is the coulombic interaction within the hydrogen atom. The potential energy between the electron and the proton at an average distance $a_0 = 0.529 \text{ \AA}$ (Bohr radius) can be defined as such:

$$E_{\text{Hartree}} = \frac{e^2}{4\pi\epsilon_0 a_0} = 4.36 \times 10^{-18} \text{ J} = 1 \text{ Ha} \quad (\text{A.1})$$

Consequently, in condensed matter, the typical scale of the potential energy related to the coulomb interaction between two elementary charges is of the order of 1 Ha.

Furthermore, as expressed in Eq.(A.2), based on some considerations, one can establish a balance between the centrifugal force experienced by the electron and the coulomb interaction. To do so, we consider the semi-classical theory of Bohr that describes the electron trajectories based on quantified angular momentum: $m_e v a_0 = n\hbar$.

$$m_e \frac{v^2}{a_0} = \frac{e^2}{4\pi\epsilon_0 a_0^2} \xrightarrow{(\text{A.1})} m_e v^2 = \frac{e^2}{4\pi\epsilon_0 a_0} \quad (\text{A.2})$$

Consequently, the kinetic energy is also of the order of magnitude of the Hartree energy. Therefore, the established Schrödinger equation presented in Eq.(3.3) can be expressed by scaling the total energy by the Hartree energy: $\frac{E_{\text{tot}}}{E_{\text{Ha}}}$. The coulomb energy contributions can be rescaled by a factor

$$E_{\text{Ha}} = \frac{e^2}{4\pi\epsilon_0 a_0}, \quad (\text{A.3})$$

and the kinetic contributions can be rescaled using the electron angular momentum quantification:

$$E_{\text{Ha}} = \frac{\hbar^2}{m_e a_0^2} \quad (\text{A.4})$$

As a result, the many-body Schrödinger equation is expressed as such

$$\left[-\sum_{i=1}^N \frac{a_0^2}{2} \nabla_i^2 - \sum_{I=1}^M \frac{a_0^2}{2(M_I/m_e)} \nabla_I^2 + \frac{1}{2} \sum_{I \neq J}^M Z_I Z_J \frac{a_0}{|\mathbf{R}_I - \mathbf{R}_J|} - \sum_{i,I}^{N,M} Z_I \frac{a_0}{|\mathbf{r}_i - \mathbf{R}_I|} + \frac{1}{2} \sum_{i \neq j}^N \frac{a_0}{|\mathbf{r}_i - \mathbf{r}_j|} \right] \Psi(\mathbf{r}_1, \dots, \mathbf{r}_N, \mathbf{R}_1, \dots, \mathbf{R}_M) = \frac{E_{tot}}{E_{Ha}} \Psi(\mathbf{r}_1, \dots, \mathbf{r}_N, \mathbf{R}_1, \dots, \mathbf{R}_M) \quad (\text{A.5})$$

In chapter 3, the Hartree atomic unit system is used. The energies are expressed in Ha (Hartree $\simeq 4.359 \times 10^{-18}$ J), distances in a_0 (Bohr radius $\simeq 0.529 \text{ \AA}$) and masses in m_e (electron mass $\simeq 9.109 \times 10^{-31}$ kg). In addition, the electron charge will be taken as $e = 1$.

A.3 KESTERITE SECONDARY PHASES

In this section, specific quantities related to defect formation energies in kesterites are provided. First, the pristine kesterite formation energies calculated are:

- $\Delta H_F(\text{Cu}_2\text{ZnSnS}_4) = -4.572 \text{ eV}$
- $\Delta H_F(\text{Cu}_2\text{ZnGeS}_4) = -4.573 \text{ eV}$

Then, we present in **Tab.A.1**, the secondary phases formation energies computed in both kesterites.

$\text{Cu}_2\text{ZnSnS}_4$ secondary phases	ΔH_F [eV]	$\text{Cu}_2\text{ZnGeS}_4$ secondary phases	ΔH_F [eV]
Cu_2SnS_3	-2.496	Cu_2GeS_3	-2.497
Cu_7S_4	-2.941	Cu_7S_4	-2.941
CuS	-0.493	CuS	-0.493
CuS_2	-0.215	CuS_2	-0.215
SnS	-0.847	GeS	-0.441
SnS_2	-1.237	GeS_2	-1.186
ZnS	-1.897	ZnS	-1.897
ZnS_2	-1.422	ZnS_2	-1.422
Cu_2GeS_3	-2.496	/	/
Cu_3Ge	-0.145	/	/
GeS	-0.441	/	/
GeS_2	-1.190	/	/
SnGeS_3	-2.065	/	/

Table A.1: Formation energies of the secondary phases computed in both $\text{Cu}_2\text{ZnSnS}_4$ and $\text{Cu}_2\text{ZnGeS}_4$ as $\Delta H_F(A_i B_j) = E_{A_i B_j} - n_i E_A - n_j E_B$.

In **Tab.A.2**, we present the chemical potential values corresponding to the stoichiometry points labelled in **Fig.5.1**.

Chemical potentials	$\text{Cu}_2\text{ZnSnS}_4$					$\text{Cu}_2\text{ZnGeS}_4$			
	μ_{Cu} [eV]	μ_{Zn} [eV]	μ_{Sn} [eV]	μ_{S} [eV]	μ_{Ge} [eV]	μ_{Cu} [eV]	μ_{Zn} [eV]	μ_{Ge} [eV]	μ_{S} [eV]
A	-0.27	-1.25	-0.202	-0.64	-0.31	-0.27	-1.10	0	-0.73
B	-0.27	-1.52	-0.29	-0.55	-0.58	-0.27	-1.34	0	-0.67
C	-0.27	-1.82	-1.18	-0.26	-1.46	-0.27	-1.82	-1.17	-0.19
D	-0.27	-1.64	-1.36	-0.26	-1.46	-0.27	-1.64	-1.36	-0.19
E	-0.55	-1.56	-0.56	-0.34	-0.79	-0.55	-1.51	-0.40	-0.32
F	-0.55	-1.92	-0.92	-0.16	-1.21	-0.55	-1.87	-0.75	-0.14
G	-0.55	-2.08	-1.50	-0.05	-1.85	-0.55	-2.08	-1.49	-0.05
H	-0.55	-1.91	-1.68	-0.05	-1.85	-0.55	-1.90	-1.68	-0.05
I	-0.82	-2.00	-1.54	0	-1.87	-0.82	-1.97	-1.39	-0.02

Table A.2: Chemical potential values corresponding to the labelled point in the kesterite phase diagrams (see **Fig.5.1**).

COMMENTS ON THE SULPHURISATION OF KESTERITE SAMPLES

B

The purpose of this appendix is to comment on the physical and chemical synthesis of kesterite layers. In a first section, as part of the "Focus on Reviews in Kesterite Thin Film Photovoltaics" commanded by the Journal of Physics: Energy, we present from the historical CIGS-based method, the evolution of the physical routes concerning the growth of kesterite samples. Then, in a second section, we detail the chemical pathway identified during the experimental growth of kesterite layers. The synthesis process implies first the e-beam deposition of a metallic precursor stack and, second, the precursor sulphurisation in an Annealsys system using H₂S as sulphur source. We report on the multiple secondary phases observed as well as on the difficulty to obtain homogenise void-free thin films using this technique. Finally, the last section comment on the advantages of solution-based processes as experienced during a laboratory visit in Edgardo Saucedo's research group at UPC (Barcelona) in July 2023.

B.1 PHYSICAL ROUTES FOR KESTERITE SYNTHESIS

This section is based on the following work:

Ratz, T., Brammertz, G., Caballero, R., León, M., Canulescu, S., Schou, J., ... & Vermang, B, *Physical routes for the synthesis of kesterite*, Journal of Physics: Energy, **1(4)**, 042003 (2019).

Historically, based on the similarities between kesterite and chalcopyrite compounds, the standard device structure adopted for $\text{Cu}(\text{In,Ga})(\text{S,Se})_2$ (CIGSSe) was directly extended to CZTSSe, by simply replacing the CIGSSe absorber layer with a p-type CZTSSe thin film. Therefore, CZTSSe solar cells are typically produced using a soda-lime glass (SLG) substrate coated with a sputtered Mo layer acting as rear metallic contact. Then, Cadmium sulfide (CdS) is normally used as the buffer (n-type) layer of the PN junction. The so-called window layer consists of an intrinsic ZnO and a transparent conducting oxide (TCO) layer (indium tin oxide or aluminum zinc oxide). Finally, a metallic Al, Ni or Ni/Al grid is deposited as front contact of the cell. Ultimately, the complete structure of the device is Al-Ni/TCO/ZnO/CdS/CZT(S,Se)/Mo(S,Se)₂/Mo/SLG.

Concerning the synthesis of the kesterite layer itself, a historical change from a one-step to a two-step procedure was initiated around 2010. First, one-step processes were based on co-evaporation of single elements onto pre-heated substrates. However, using the one-step coevaporation approach, the most important obstacle for high-efficiency kesterite is probably the volatility of Sn-(S,Se) species. This has limited in large extent the further development of these methodologies, requiring the inclusion of an additional step at high temperature and under chalcogen and Sn atmosphere, which normally helps to correct possible stoichiometric deviations, and improves the growth of crystal grains. Now used as a benchmark, two-step processes are the most widely used for the growth of kesterite absorbers. These experimental procedures consist in (i) a first deposition of a precursor film containing all (or part of) the chemical elements necessary for the kesterite phase formation, followed by (ii) a thermal annealing treatment under S (sulphurisation) or Se (selenisation) containing atmosphere, necessary to convert the precursor in a kesterite film and to promote the grain growth. This method has demonstrated devices with comparable efficiencies than those reported by chemical routes thanks to a better control of the grain growth and the limitation of Sn(S,Se) losses and secondary phases formation. These elemental losses are known to cause a V_{OC} deficit through the formation of deep defects within the bandgap.

In the two-step approach, the kesterite absorber layer can be deposited using various physical routes such as: sequential or co-sputtering, sequential e-beam evaporation and pulsed laser deposition (PLD).

Moreover as presented in chapter 1, it is worth mentioning that efficiency progresses cannot simply be ascribed to the optimisation of the absorber layer synthesis procedure alone. Indeed, beneficial effects from post-deposition annealing, buffer layer optimisation and interfaces passivation have also contributed to the solar cell efficiency enhancement over the years. Finally, compared to CVD processes, the synthesis of kesterite absorber layers using PVD routes offers safer (as far as environmental issues are concerned) and more reproducible scale-up procedures and is beneficial in terms of high throughput.

B.2 SULPHURISATION USING ANNEALSYS

In this section, we comment on the poor homogeneity as well as the high number of secondary phases encountered during the synthesis of kesterite absorber layers. The physical process used includes an e-beam deposited metallic precursor stack sulphurised in an Annealsys AS-One RTP chamber using H_2S gas as sulphur source. The metallic stack considered, aiming at a Cu-poor and Zn-rich kesterite stoichiometry, is composed as such : Mo/Cu(1)/Sn(300)/Zn(135)/Cu(155) (thickness indicated in nm).

After few studies aiming at the optimisation of the sulphurisation parameters: alloying and annealing time, temperature and gas conditions (injection time, pressure and flow), the two-step recipe was set as presented in **Fig.B.1**. This one consists in, first, alloying at 260°C under nitrogen atmosphere for 20 min followed by annealing at 470°C during 15 min under 700 mbar of H_2S . As illustrated in **Fig.B.2(d)**, higher annealing temperatures result in the deterioration of the thin film. Details concerning the XRD and Raman characterisations presented in the following can be found in section 6.2.

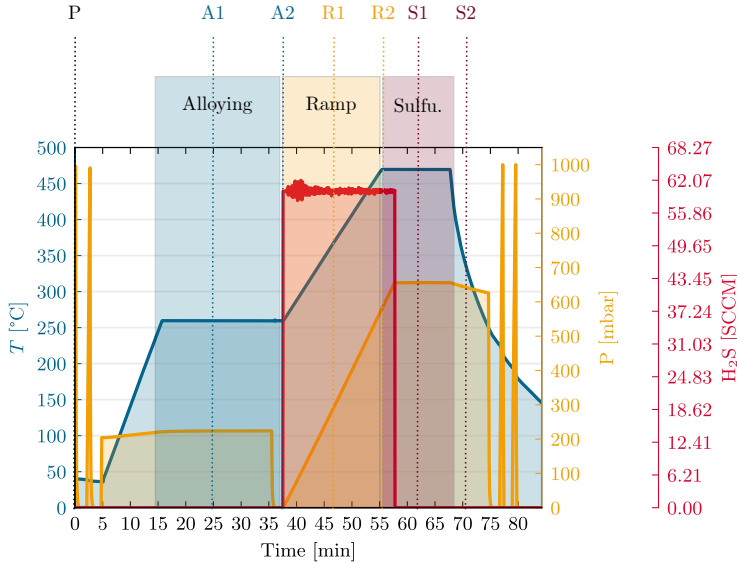


Figure B.1: Representation of the process data acquired during the kesterite sulphurisation in the Annealsys: temperature T [$^\circ\text{C}$], chamber pressure P [mbar] and H_2S gas flow [SCCM]. As illustrated, the process is divided in three sequences. Starting with the alloying phase at 260°C in N_2 atmosphere followed by a temperature ramp in H_2S reaching 470°C for the sulphurisation phase.

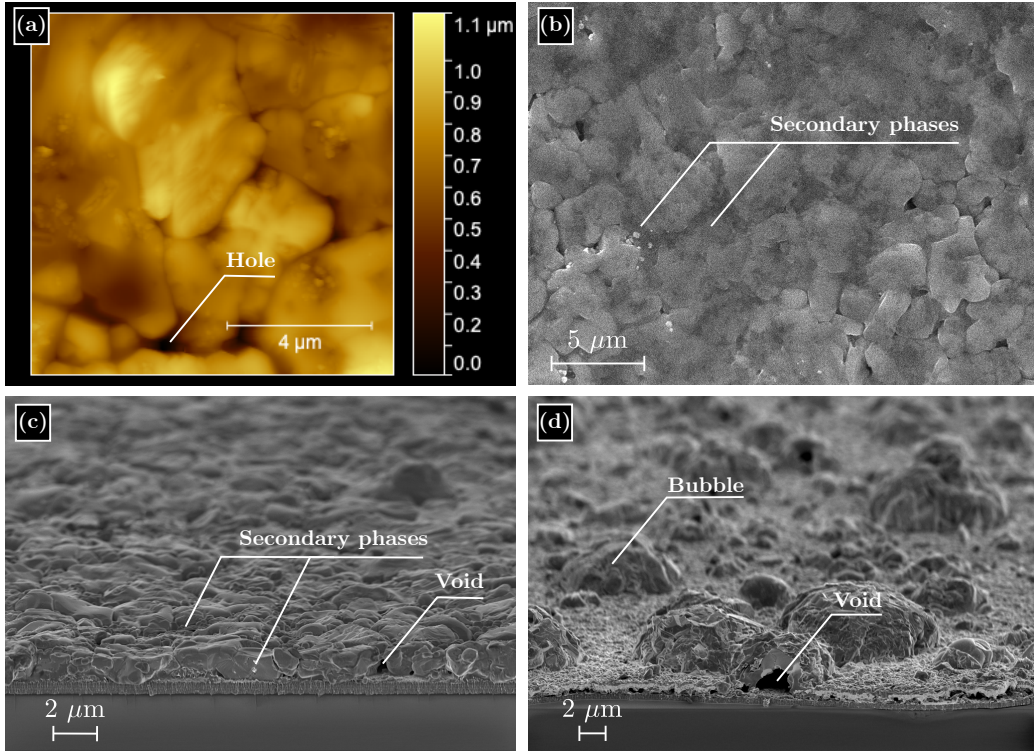


Figure B.2: (a) AFM characterisation of the kesterite sample surface highlighting the presence of μm -size grains and holes. As depicted in (b) and (c), we present the top and cross section SEM observations of the synthesised kesterite layer. In both cases, secondary phases can be observed as dark and bright patches. (d) Cross section SEM observation of a kesterite sample sulphurised at high temperature (above 500°C). Bubble-like structure and voids can be observed. These features could be ascribed to the elemental decomposition of the kesterite layer and the high volatility of SnS species [52].

The synthesised thin film highlights the complex nature of kesterite and the multiple secondary phases that occur using this physical process. As presented in **Fig.B.1(b)**, black patches and white points can be observed as secondary phases while **Fig.B.1(d)** highlights the voids and bubble like structures that occur for too high annealing temperatures. Moreover, the reported holes inside the absorber layer (see **Fig.B.1(a)**) lead to the short circuit of the PN junction (electrical contact between the Mo rear metallic contact and the deposited n-type layer (CdS)).

The material uniformity and composition were then further investigated using Raman spectroscopy (532 nm laser) as presented in **Fig.B.3**. Using optical microscopy, bright and dark areas were identified and confirmed the poor uniformity of the thin film. In **Fig.B.3(a)**, we report on the Raman measurements of both types of zones. In the dark zone, the CZTS phase was identified along with multiple secondary phases such as Cu_xS , ZnS, SnS and Cu_2SnS_3 . In addition, strong bands associated to the

MoS₂ were also reported. These observations suggest an incomplete formation of the kesterite and, possibly, a lower thickness of the layer at these locations indicated by the presence of MoS₂. In contrast, in the bright zones, an increase CZTS activity was reported along with a decrease, however not a suppression, of the bands associated to secondary phases. The layer poor uniformity is then further highlighted using a Raman cartography as presented in **Fig.B.3(b)**. This map corresponds to the intensity of the main CZTS band located at 337 cm⁻¹ on a 20×20 μm² area with 100 measured points [69].

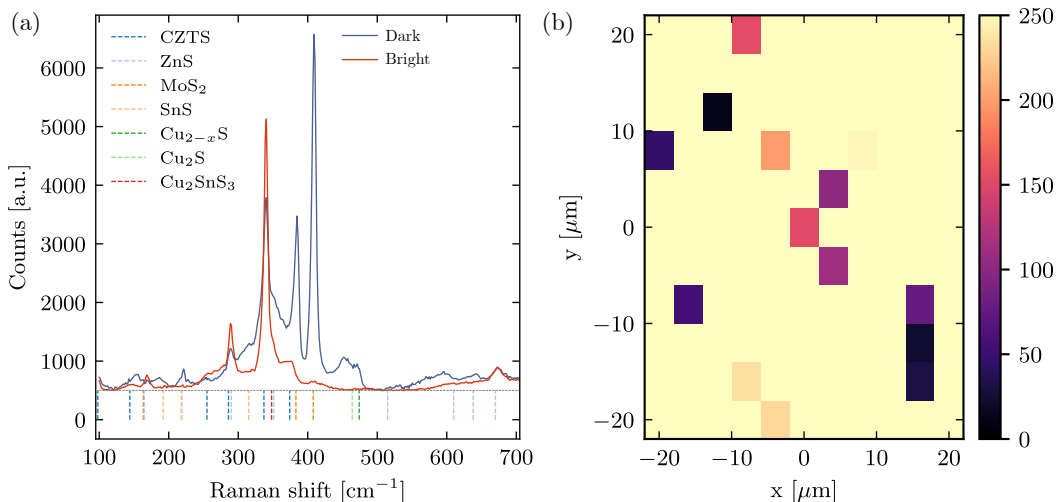
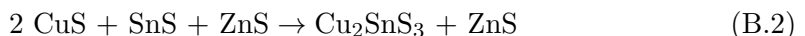
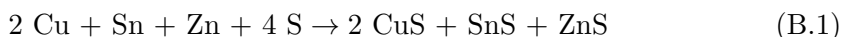


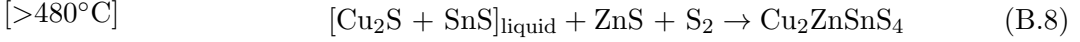
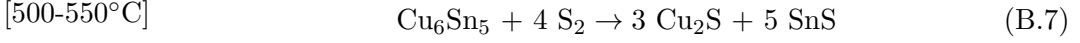
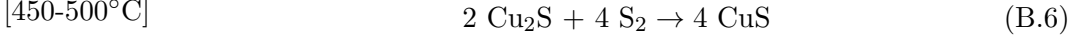
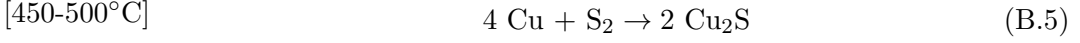
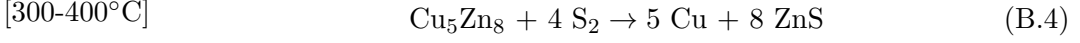
Figure B.3: (a) Raman characterisation of the synthesised kesterite sample at two different locations corresponding respectively to a dark and a bright area on the optical microscope. In addition, known Raman activity related to secondary phases are depicted [69]. (b) Cartographic Raman characterisation of Cu₂ZnSnS₄ main band located at 337 cm⁻¹. The measurement was repeated using a 10×10 meshing between -20 and 20 μm in each space direction. Each measurement corresponds to a scanned surface of 1μm².

Then, we investigated the possible reaction pathway undergone during the kesterite synthesis to understand the occurrence of the secondary phases observed. First, in 2009, several works reported on the possible reaction pathway as described in Eqs.(B.1-B.3) [218, 219].



However this first reaction hypothesis does not take into account low temperature inter metallic phases [69]. Then, in 2013, Fairbrother *et al.* proposed another reaction path for the formation of CZTS as presented in Eqs.(B.4-B.8). Using XRD

and Raman characterisations, the authors reported that above 480°C, the $\text{Cu}_2\text{S}+\text{SnS}$ compounds melt and act as a liquid flux that accelerates the reaction between the solid binary phases and the sulphur gas in the atmosphere.



As depicted in **Fig.B.1**, using XRD, thin films were sequentially characterised at various process stages, starting from the precursor layer and reaching the final sulphurised sample ($\text{P} \rightarrow \text{S}_2$). It is also relevant to note that in the XRD characterisation, the main CZTS peak is very close to those of Cu_2SnS_3 and ZnS . Therefore, it is difficult to establish a clear distinction between these phases.

Secondary phase	2θ peak [°]	Intensity [a.u.]	P	A1	A2	R1	R2	S1	S2
Cu	43.46	37.93	X	↘	↘	o	o	o	o
Zn									
Sn	30.61	47.41	X	↘	↘	↘	o	o	o
Mo	40.52	79.04	X	X	X	X	↘	↘	↘
Cu_3Sn									
Cu_6Sn_5	42.97	73.04	o	↗	X	↘	o	o	o
Cu_5Zn_8	43.19	263.82	o	↗	X	↘	o	o	o
Cu_2S	37.77	13.89	o	o	o	X	o	o	o
CuS	31.78	13.96	o	o	o	o	X	o	o
SnS	27.47	7.65	o	o	o	o	X	o	o
SnS_2	32.12	26.29	o	o	o	X	↘	o	o
ZnS	28.52	445.84	o	o	o	↗	X	X	X
MoS_2									
Cu_2SnS_3	28.541	339.11	o	o	o	↗	X	X	X
$\text{Cu}_2\text{ZnSnS}_4$	28.451	591.14	o	o	o	↗	X	X	X

Table B.1: Results of the main Cu, Zn, Sn and S phases detected using XRD characterisation of kesterite samples. Elemental, binary, ternary and quaternary phases are reported according to their main XRD peak location and intensity. In grey, some undetected secondary phases are highlighted. The characterised samples correspond to layers obtain following different stages in the sulphurisation process presented in **Fig.B.1**. Starting from the precursor layer (P) to the alloying stage (A1,A2), reaching the temperature ramp (R1,R2) and, finally, proceeding to the sample sulphurisation (S1,S2). The "X" indicates the presence of the phase, the "↗" and "↘" arrows correspond respectively to the increase or the decrease of the phase and the "o" represents the absence of the compound.

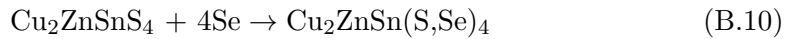
From this crystallographic investigation, the main material phases observed are reported in **Tab.B.1**. First, the e-beam stacked precursor layer presents the Cu, Sn and Mo elemental phases. Then, during the alloying stage (from A_1 to A_2), we report a reduction of the Cu and Sn elemental phase and the formation of the binary Cu_6Sn_5 and Cu_5Zn_8 metallic compounds. Following the temperature ramp (from R_1 to R_2) and the introduction of S through the H_2S flow, a reduction of the metallic binary phases is observed in favour of both binary (Cu_xS , SnS_x and ZnS) and ternary (Cu_2SnS_3) sulphur-based secondary phases. Finally, during the last sulphurisation phase (from S_1 to S_2), the remaining detected secondary phases are ZnS and Cu_2SnS_3 . From R_1 to S_2 , we also report on the crystallisation of the desired CZTS material along with the reduction of the Mo peak intensity that could be ascribed to the increase thickness of the processed layer. Indeed, from the precursor stack to the final kesterite layer the thin film thickness increases from around ~ 590 nm to ~ 1.5 μm . The observed secondary phases can also be put into perspective with the kesterite phase diagrams reported in **Fig.5.1**.

The reaction pathway undergone during the sulphurisation process seems to corresponds first to the decomposition of the binary metallic phases Cu_5Zn_8 and Cu_6Sn_5 formed during the alloying sequence (see Eqs.(B.4) to (B.7)). However, during the ramp stage (R_1 to R_2), in contrast to the pathway proposed by Faribrother *et al.* [69], we observe the formation of the ternary Cu_2SnS_3 alloy that remains as secondary phase in the processed layer. As a result, this observation would corresponds to an incomplete reaction as expressed in Eq.(B.3).

From the XRD characterisation, the synthesised kesterite layers present a main CZTS phase but with the occurrence of at least both ZnS and Cu_2SnS_3 secondary phases. In addition to the incomplete kesterite crystallisation, the holes reported in the SEM observations lead to inefficient solar cell due to low shunt resistances. We believe that the uncontrol of the kesterite reaction pathway as well as the technical impossibility to saturate the kesterite precursor with S during the sulphurisation might be the two possible culprits to assign to these observations.

B.3 SOLUTION-BASED PROCESSES

In addition, as presented by Gong *et al.*, the reaction pathway depends on the oxidation state of Sn ($2+$ or $4+$) within the precursor layer [175]. In their work, the authors presented the selenisation of a Sn^{2+} precursor with similar reactions as expressed in Eqs.(B.1-B.3) resulting in defective surface with multiple secondary phases. In contrast, the Sn^{4+} precursor's reaction pathway is more direct and avoid the intermediate formation of secondary phases (see Eqs.(B.9) and (B.10)). As a result the V_{OC} of the Sn^{4+} based precursor is improved with respect to the Sn^{2+} counterpart.



Solution-based processes offer a direct control of oxidation state of Sn within the kesterite precursor [175]. Indeed, as proposed by Gong *et al.*, kesterite absorber layer fabricated from a dimethylsulfoxide (DMSO) along with zinc acetate $\text{Zn}(\text{CH}_3\text{CO}_2)_2$ and Sn chloride SnCl_4 results in a kesterite precursor solution with Sn in the convenient Sn^{4+} state. This process allowed the recent breakthrough concerning kesterite-based solar cell with a record efficiency of 14.9% [57, 66].

PLASMA PRESSURE EFFECT ON (N,Mg)-DOPED COPPER OXIDE LAYERS

C

In this appendix, we discuss the results obtained concerning the (N,Mg)-doping of copper oxide thin films deposited using two sputtering pressures, 5 mTorr (as presented in Chapter 6) and 15 mTorr. Then, in a second section, we provide detailed information concerning the various thin film depositions performed.

C.1 RESULTS AND DISCUSSION

In this section, we present N-doping and (N,Mg)-doping of copper oxide thin films deposited at two deposition pressure, 5 mTorr (with the sputtering targets S2023-0 and S2021-4) and 15 mTorr (with the sputtering targets S2018-0 and S2021-4).

In **Fig.C.1**, the thin film optoelectrical characterisations (resistivity, bandgap and mean transparency) are presented. Concerning the material resistivity, for low nitrogen flow rate (2 SCCM) and independently of the Mg-content or the plasma pressure (see **Fig.C.1(a)**), a systematic decrease is observed. In order to confirm this trend, an additional investigation should be conducted by increasing the parameter resolution for low N₂ flow. Then, for increased nitrogen flows, a stabilisation of the resistivity values are reported for the 15 mTorr deposited samples in contrast to the 5 mTorr investigations.

Then, concerning the thin film optical properties, constant bandgap values of 2.5 eV are reported for both 0Mg studies at 5 and 15 mTorr. However, at 15 mTorr, we observe a higher thin film transparency for nearly each nitrogen flow. This observation can be put into perspective with the thin film material phase observed through the increase of the nitrogen flow as reported in **Fig.C.3**. Concerning the 5mTorr-0Mg study (S2023-0 sputtering target), we report a crystalline transition from Cu_4O_3 to Cu_2O while in the case of the 15mTorr-0Mg study (S2018-0 sputtering target), a constant Cu_2O material phase is observed. Then, upon Mg doping a reduction of the material bandgap is observed with transparency values lower than 20 %.

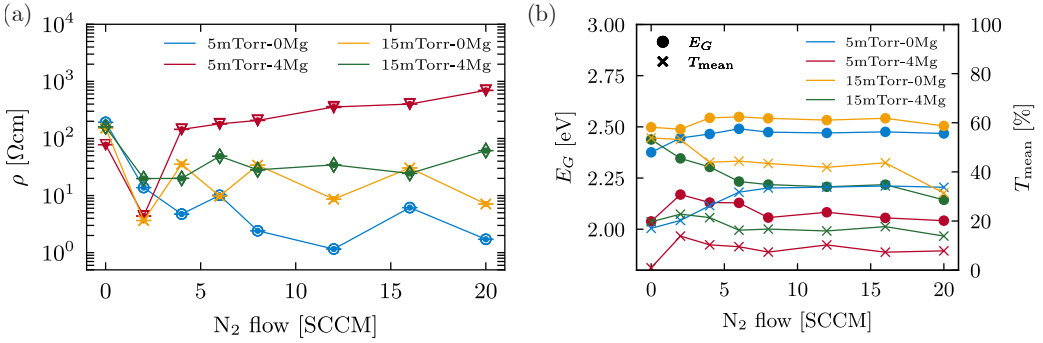


Figure C.1: Plasma pressure investigation for deposition pressures of 5 and 15 mTorr on sputtering targets S2023-0 (0Mg) and S2021-4 (4Mg). The thin film resistivity as well as the bandgap values and average transparencies are presented respectively in the insets (a) and (b). The extracted bandgap values have an error margin of 0.05 eV.

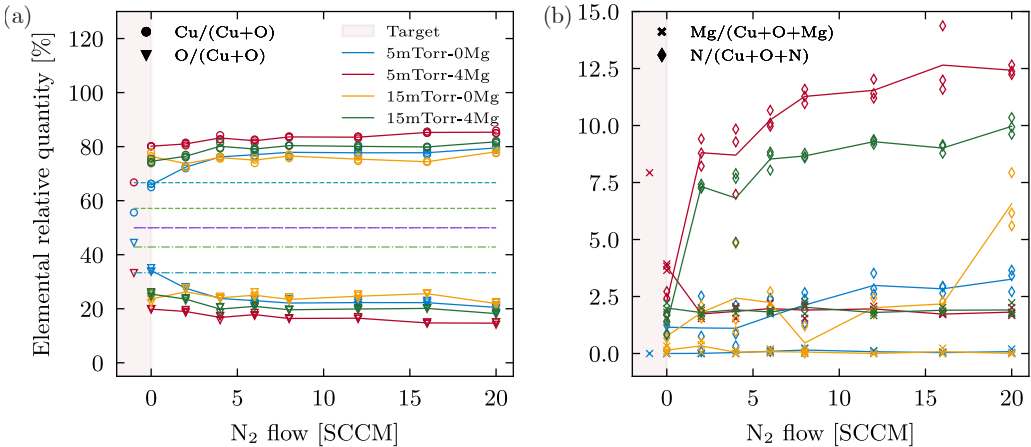


Figure C.2: EDX characterisation of copper oxide thin films deposited at plasma pressures of 5 and 15 mTorr using the sputtering targets S2023-0 (0Mg) and S2021-4 (4Mg).

Finally, in **Figs.C.2** and **C.3**, the EDX, XRD and Raman thin film characterisations are presented. Very similar trends between the 5 and 15 mTorr studies can be

observed. First, concerning the Mg undoped samples (see **Fig.C.3(a)**), Cu_2O material phases are reported for N_2 flows above 4 SCCM. Below this value, depending on the initial sputtering target used (S2023-0 (CuO) or S2018-0 (Cu_2O)), a crystalline transition to an oxygen poor phase is reported for samples produced based on the S2023-0 sputtering target. In **Fig.C.3(b)**, concerning the Mg-doped thin films, an amorphisation is reported for both deposition pressures. In addition, high nitrogen incorporation are reported for both Mg-containing studies.

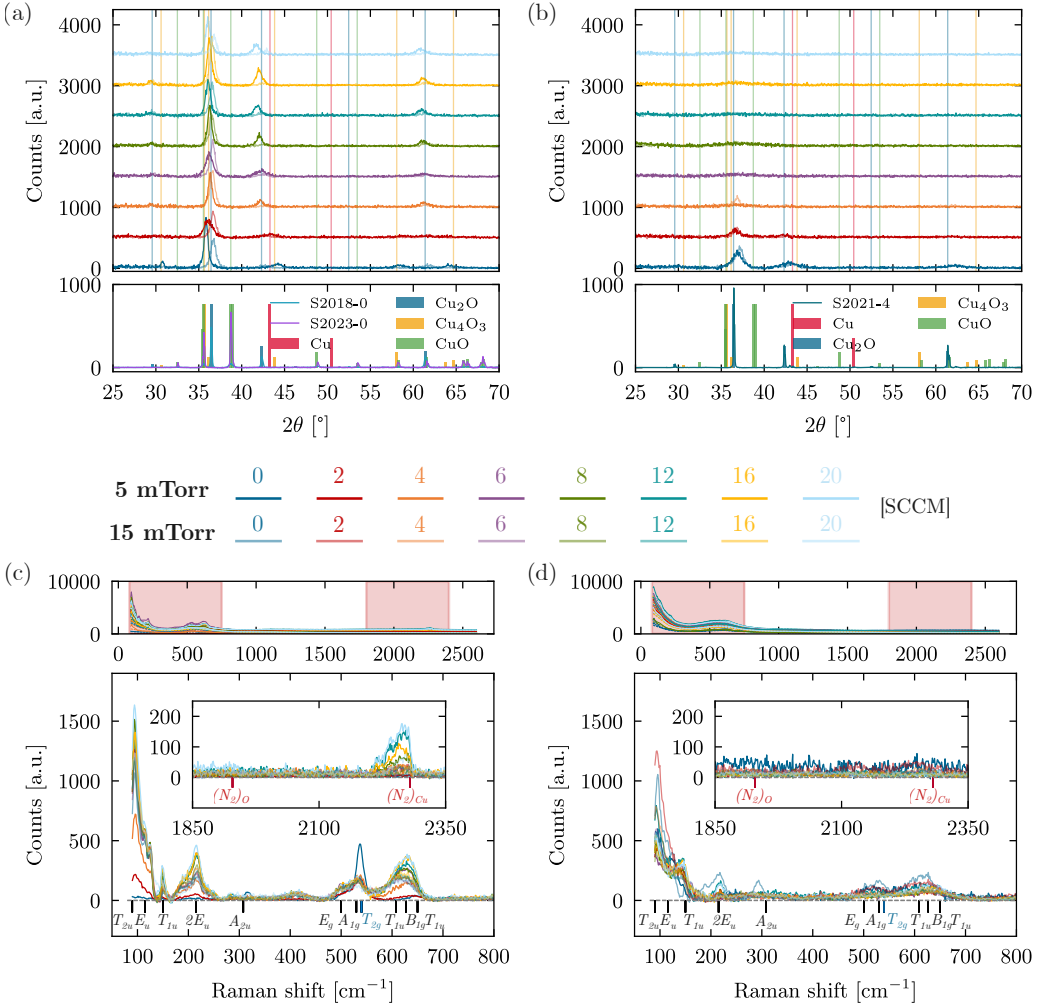


Figure C.3: (a) XRD and (b) Raman characterisation of copper oxide thin films deposited at plasma pressures of 5 and 15 mTorr using the sputtering targets S2023-0 (0Mg) and S2021-4 (4Mg).

C.2 DEPOSITION PARAMETERS

In **Tab.C.1**, we detail the deposition parameters of the processed samples.

Target	ID	P_{Base} [Torr]	\mathcal{P} [W]	R [nm/s]	P_{Plasma} [mTorr]	Ar <i>flow</i> [SCCM]	N ₂ <i>flow</i> [SCCM]	t [nm]
S2021-0	21-0Mg-5-0	1.40E-7	63	0.025	5	20	0	200
	21-0Mg-5-3	1.07E-7	63	0.027	5	20	3	200
	21-0Mg-5-6	1.14E-7	63	0.027	5	20	6	200
	21-0Mg-5-9	1.28E-7	63	0.025	5	20	9	200
	21-0Mg-5-12	1.01E-7	63	0.025	5	20	12	200
	21-0Mg-5-15	8.08E-8	63	0.025	5	20	15	200
	21-0Mg-5-18	9.8E-8	63	0.026	5	20	18	200
	21-0Mg-5-21	7.59E-8	63	0.026	5	20	21	200
S2023-0	23-0Mg-5-0	5.12E-8	69	0.024	5	20	0	218
	23-0Mg-5-2	1.05E-7	63	0.025	5	20	2	200
	23-0Mg-5-4	4.15E-8	69	0.025	5	20	4	215
	23-0Mg-5-6	8.70E-8	63	0.027	5	20	6	204
	23-0Mg-5-8	9.84E-8	69	0.025	5	20	8	237
	23-0Mg-5-12	7.27E-8	69	0.025	5	20	12	211
	23-0Mg-5-16	1.36E-7	69	0.023	5	20	16	227
	23-0Mg-5-20	1.07E-7	69	0.024	5	20	20	221
S2021-4	21-0Mg-5-0	9.88E-8	69	0.028	5	20	0	250
	21-0Mg-5-2	1.46E-7	63	0.029	5	20	2	255
	21-0Mg-5-4	1.15E-7	69	0.025	5	20	4	256
	21-0Mg-5-6	1.51E-7	63	0.027	5	20	6	250
	21-0Mg-5-8	8.60E-8	69	0.026	5	20	8	254
	21-0Mg-5-12	7.20E-8	63	0.026	5	20	12	239
	21-0Mg-5-16	9.20E-8	69	0.026	5	20	16	256
	21-0Mg-5-20	9.38E-8	69	0.026	5	20	20	250
S2018-0	18-0Mg-5-0	9.80E-8	69	0.033	5	20	0	247
	18-0Mg-5-12	1.23E-7	63	0.029	5	20	12	244
S2018-0	18-0Mg-15-0	6.20E-8	69	0.03	15	20	0	120
	18-0Mg-15-2	7.50E-8	69	0.028	15	20	2	113
	18-0Mg-15-4	9.50E-8	69	0.028	15	20	4	142
	18-0Mg-15-6	1.15E-7	69	0.028	15	20	6	181
	18-0Mg-15-8	8.70E-8	69	0.027	15	20	8	177
	18-0Mg-15-12	9.60E-8	69	0.026	15	20	12	195
	18-0Mg-15-16	8.50E-8	69	0.025	15	20	16	205
	18-0Mg-15-20	1.07E-7	69	0.025	15	20	20	202
S2021-4	21-0Mg-15-0	9.58E-8	69	0.013	15	20	0	203
	21-0Mg-15-2	1.62E-7	69	0.013	15	20	2	182
	21-0Mg-15-4	1.05E-7	69	0.012	15	20	4	194
	21-0Mg-15-6	1.17E-7	69	0.013	15	20	6	178
	21-0Mg-15-8	1.02E-7	69	0.013	15	20	8	185
	21-0Mg-15-12	1.19E-7	69	0.012	15	20	12	197
	21-0Mg-15-16	1.81E-7	69	0.012	15	20	16	198
	21-0Mg-15-20	8.60E-8	63	0.012	15	20	20	195

Table C.1: Thin film deposition parameters: chamber base pressure P_{Base} [Torr] prior to the deposition, sputtering power \mathcal{P} [W], deposition rate R [nm/s], plasma pressure P_{Plasma} [mTorr] during the deposition and the corresponding Ar and N₂ gas *flows*. The deposited sample label and the corresponding sputtering target are also provided with the sample thickness t as measured using AFM.

BIBLIOGRAPHY

- [1] H. Ritchie, M. Roser, and P. Rosado, *Energy*, Our World in Data (2022).
- [2] H. Lee *et al.*, *IPCC, 2023: AR6 synthesis report: Climate Change 2023*, (2023).
- [3] D. Gielen *et al.*, *World energy transitions outlook: 1.5° C pathway*, (2021).
- [4] D. Gielen *et al.*, *Global energy transformation: a roadmap to 2050*, (2019).
- [5] International Renewable Energy Agency, *Future of solar photovoltaic: deployment, investment, technology, grid integration and socio-economic aspects*, (2019).
- [6] European Commission and Directorate: General for Communication, *European green deal : delivering on our targets*, (2021).
- [7] The Shift Project, *Climat, crises: Le plan de transformation de l'économie française*, (2022).
- [8] International Energy Agency, *The role of critical minerals in clean energy transitions* (OECD Publishing, 2021).
- [9] L. Gregoir *et al.*, *Metals for clean energy: pathways to solving Europe's raw materials challenge*, Eurometaux, KU Leuven (2022).
- [10] P. C. K. Vesborg and T. F. Jaramillo, *Addressing the terawatt challenge: scalability in the supply of chemical elements for renewable energy*, RSC Adv. **2**, 7933 (2012).
- [11] Fraunhofer Institute For Solar Energy Systems ISE, *Photovoltaics Report*, (2022).
- [12] M. A. Green *et al.*, *Solar cell efficiency tables (Version 63)*, Progress in Photovoltaics: Research and Applications **32**, 3 (2024).

- [13] D. Lincot, *The new paradigm of photovoltaics: From powering satellites to powering humanity*, Comptes Rendus Physique **18**, 381 (2017).
- [14] U. P. Singh, *Recent Advances in Thin Film Photovoltaics* (Springer Nature, 2022).
- [15] B. Vermang *et al.*, *Wide band gap kesterite absorbers for thin film solar cells: potential and challenges for their deployment in tandem devices*, Sustainable Energy & Fuels **3**, 2246 (2019).
- [16] A. Jimenez-Arguijo *et al.*, *Setting the baseline for the modelling of Kesterite solar cells: The case study of tandem application*, Solar Energy Materials and Solar Cells **251**, 112109 (2023).
- [17] J. Li *et al.*, *Emergence of flexible kesterite solar cells: Progress and perspectives*, npj Flexible Electronics **7**, 16 (2023).
- [18] *Communication from the Commission to the European Parliament, the Council, the European Economic and Social Committee and the Committee of the Regions on the 2017 list of Critical Raw Materials for the EU*, 2017, Accessed: 2020-11-18.
- [19] T. K. Wong, S. Zhuk, S. Masudy-Panah, and G. K. Dalapati, *Current status and future prospects of copper oxide heterojunction solar cells*, Materials **9**, 271 (2016).
- [20] S. Lany, *Band-structure calculations for the 3 d transition metal oxides in GW*, Physical Review B **87**, 085112 (2013).
- [21] Y. Wang *et al.*, *Electronic structures of Cu_2O , Cu_4O_3 , and CuO : A joint experimental and theoretical study*, Physical Review B **94**, 245418 (2016).
- [22] M. Nolan and S. D. Elliott, *The p-type conduction mechanism in Cu_2O : a first principles study*, Physical Chemistry Chemical Physics **8**, 5350 (2006).
- [23] L. Y. Isseroff and E. A. Carter, *Importance of reference Hamiltonians containing exact exchange for accurate one-shot GW calculations of Cu_2O* , Physical Review B **85**, 235142 (2012).
- [24] K. H. Zhang, K. Xi, M. G. Blamire, and R. G. Egdell, *P-type transparent conducting oxides*, Journal of Physics: Condensed Matter **28**, 383002 (2016).
- [25] G. Hautier, A. Miglio, G. Ceder, G.-M. Rignanese, and X. Gonze, *Identification and design principles of low hole effective mass p-type transparent conducting oxides*, Nature communications **4**, 2292 (2013).
- [26] B. Meyer *et al.*, *Binary copper oxide semiconductors: From materials towards devices*, physica status solidi (b) **249**, 1487 (2012).

- [27] A. Lakshmanan, Z. C. Alex, and S. Meher, *Recent advances in cuprous oxide thin film based photovoltaics*, Materials Today Sustainability **20**, 100244 (2022).
- [28] W. Shockley and H. J. Queisser, *Detailed balance limit of efficiency of p-n junction solar cells*, Journal of Applied Physics **32**, 510 (1961).
- [29] S. Rühle, *Tabulated values of the Shockley–Queisser limit for single junction solar cells*, Solar energy **130**, 139 (2016).
- [30] J. Herion, E. Niekisch, and G. Scharl, *Investigation of metal oxide/cuprous oxide heterojunction solar cells*, Solar energy materials **4**, 101 (1980).
- [31] H. Tanaka, T. Shimakawa, T. Miyata, H. Sato, and T. Minami, *Electrical and optical properties of TCO–Cu₂O heterojunction devices*, Thin solid films **469**, 80 (2004).
- [32] A. Mittiga, E. Salza, F. Sarto, M. Tucci, and R. Vasanthi, *Heterojunction solar cell with 2% efficiency based on a Cu₂O substrate*, Applied physics letters **88**, 163502 (2006).
- [33] T. Minami, Y. Nishi, T. Miyata, and J.-i. Nomoto, *High-efficiency oxide solar cells with ZnO/Cu₂O heterojunction fabricated on thermally oxidized Cu₂O sheets*, Applied physics express **4**, 062301 (2011).
- [34] Y. Nishi, T. Miyata, and T. Minami, *Effect of inserting a thin buffer layer on the efficiency in n-ZnO/p-Cu₂O heterojunction solar cells*, Journal of Vacuum Science & Technology A **30**, 04D103 (2012).
- [35] T. Minami, Y. Nishi, and T. Miyata, *High-efficiency Cu₂O-based heterojunction solar cells fabricated using a Ga₂O₃ thin film as n-type layer*, Applied Physics Express **6**, 044101 (2013).
- [36] T. Minami, Y. Nishi, and T. Miyata, *Impact of incorporating sodium into polycrystalline p-type Cu₂O for heterojunction solar cell applications*, Applied Physics Letters **105**, 212104 (2014).
- [37] T. Minami, T. Miyata, and Y. Nishi, *Relationship between the electrical properties of the n-oxide and p-Cu₂O layers and the photovoltaic properties of Cu₂O-based heterojunction solar cells*, Solar energy materials and solar cells **147**, 85 (2016).
- [38] T. Minami, Y. Nishi, and T. Miyata, *Efficiency enhancement using a Zn_{1-x}Ge_xO thin film as an n-type window layer in Cu₂O-based heterojunction solar cells*, Applied Physics Express **9**, 052301 (2016).
- [39] S. Shibasaki *et al.*, *Highly transparent Cu₂O absorbing layer for thin film solar cells*, Applied Physics Letters **119**, 242102 (2021).

- [40] L. Olsen, R. Bohara, and M. Urie, *Explanation for low-efficiency Cu_2O Schottky-barrier solar cells*, Applied physics letters **34**, 47 (1979).
- [41] M. Nolan and S. D. Elliott, *Tuning the transparency of Cu_2O with substitutional cation doping*, Chemistry of Materials **20**, 5522 (2008).
- [42] L. Y. Isseroff and E. A. Carter, *Electronic structure of pure and doped cuprous oxide with copper vacancies: suppression of trap states*, Chemistry of Materials **25**, 253 (2013).
- [43] A. Živković, A. Roldan, and N. H. de Leeuw, *Tuning the electronic band gap of Cu_2O via transition metal doping for improved photovoltaic applications*, Physical Review Materials **3**, 115202 (2019).
- [44] M. Nyborg, A. Azarov, K. Bergum, and E. Monakhov, *Deposition and characterization of lithium doped direct current magnetron sputtered Cu_2O films*, Thin Solid Films **722**, 138573 (2021).
- [45] J. Resende, C. Jiménez, N. D. Nguyen, and J.-L. Deschanvres, *Magnesium-doped cuprous oxide ($\text{Mg}:\text{Cu}_2\text{O}$) thin films as a transparent p-type semiconductor*, physica status solidi (a) **213**, 2296 (2016).
- [46] J. Li *et al.*, *Probing defects in nitrogen-doped Cu_2O* , Scientific reports **4**, 7240 (2014).
- [47] S. S. K. Jacob *et al.*, *Enhanced optoelectronic properties of Mg doped Cu_2O thin films prepared by nebulizer pyrolysis technique*, Journal of Materials Science: Materials in Electronics **30**, 10532 (2019).
- [48] G. Lai, Y. Wu, L. Lin, Y. Qu, and F. Lai, *Low resistivity of N-doped Cu_2O thin films deposited by rf-magnetron sputtering*, Applied surface science **285**, 755 (2013).
- [49] C. Malerba *et al.*, *Nitrogen doped Cu_2O : A possible material for intermediate band solar cells?*, Solar energy materials and solar cells **105**, 192 (2012).
- [50] M. Grossberg *et al.*, *The electrical and optical properties of kesterites*, Journal of Physics: Energy **1**, 044002 (2019).
- [51] G. Brammertz *et al.*, *Correlation between physical, electrical, and optical properties of $\text{Cu}_2\text{ZnSnSe}_4$ based solar cells*, Applied Physics Letters **102**, 013902 (2013).
- [52] T. Ratz *et al.*, *Physical routes for the synthesis of kesterite*, Journal of Physics: Energy **1**, 042003 (2019).
- [53] T. Todorov *et al.*, *Solution-based synthesis of kesterite thin film semiconductors*, Journal of Physics: Energy **2**, 012003 (2020).

- [54] M. Green *et al.*, *Solar cell efficiency tables (version 57)*, Progress in Photovoltaics: Research and Applications **29**, 3 (2021).
- [55] M. Nakamura *et al.*, *Cd-free Cu(In,Ga)(Se,S)₂ thin-film solar cell with record efficiency of 23.35%*, IEEE Journal of Photovoltaics **9**, 1863 (2019).
- [56] S. Giraldo *et al.*, *Progress and perspectives of thin film kesterite photovoltaic technology: a critical Review*, Advanced Materials **31**, 1806692 (2019).
- [57] J. Zhou *et al.*, *Control of the phase evolution of kesterite by tuning of the selenium partial pressure for solar cells with 13.8% certified efficiency*, Nature Energy **8**, 526 (2023).
- [58] H. Katagiri *et al.*, *Preparation and evaluation of Cu₂ZnSnS₄ thin films by sulfurization of EB evaporated precursors*, Solar Energy Materials and Solar Cells **49**, 407 (1997).
- [59] H. Katagiri *et al.*, *Enhanced conversion efficiencies of Cu₂ZnSnS₄-based thin film solar cells by using preferential etching technique*, Applied physics express **1**, 041201 (2008).
- [60] M. Kauk *et al.*, *Effects of sulphur and tin disulphide vapour treatments of Cu₂ZnSnSSe₄ absorber materials for monograin solar cells*, Energy Procedia **10**, 197 (2011).
- [61] K. Sun *et al.*, *Over 9% efficient kesterite Cu₂ZnSnS₄ solar cell fabricated by using Zn_{1-x}Cd_xS buffer layer*, Advanced Energy Materials **6**, 1600046 (2016).
- [62] M. Altosaar *et al.*, *Cu₂ZnSnSe₄ monograin powders for solar cell application*, in *2006 IEEE 4th World Conference on Photovoltaic Energy Conference*, volume 1, pp. 468–470, IEEE, 2006.
- [63] M. Altosaar *et al.*, *Cu₂Zn_{1-x}Cd_xSn(Se_{1-y}S_y)₄ solid solutions as absorber materials for solar cells*, physica status solidi (a) **205**, 167 (2008).
- [64] D. A. R. Barkhouse, O. Gunawan, T. Gokmen, T. K. Todorov, and D. B. Mitzi, *Device characteristics of a 10.1% hydrazine-processed Cu₂ZnSn(Se,S)₄ solar cell*, Progress in Photovoltaics: Research and Applications **20**, 6 (2012).
- [65] W. Wang *et al.*, *Device characteristics of CZTSSe thin-film solar cells with 12.6% efficiency*, Advanced Energy Materials **4**, 1301465 (2013).
- [66] Y. Gong *et al.*, *Elemental de-mixing-induced epitaxial kesterite/CdS interface enabling 13%-efficiency kesterite solar cells*, Nature Energy **7**, 966 (2022).
- [67] Y. Li *et al.*, *Suppressing Element Inhomogeneity Enables 14.9% Efficiency CZTSSe Solar Cells*, Advanced Materials , 2400138 (2024).

- [68] *International cooperation for the development of cost-efficient kesterite/c-Si thin film next generation tandem solar cells*, 2023, Accessed: 2024-05-23.
- [69] A. Fairbrother *et al.*, *On the formation mechanisms of Zn-rich $\text{Cu}_2\text{ZnSnS}_4$ films prepared by sulfurization of metallic stacks*, *Solar Energy Materials and Solar Cells* **112**, 97 (2013).
- [70] S. Chen, A. Walsh, X.-G. Gong, and S.-H. Wei, *Classification of lattice defects in the kesterite $\text{Cu}_2\text{ZnSnS}_4$ and $\text{Cu}_2\text{ZnSnSe}_4$ earth-abundant solar cell absorbers*, *Advanced Materials* **25**, 1522 (2013).
- [71] A. Wang, M. He, M. A. Green, K. Sun, and X. Hao, *A Critical Review on the Progress of Kesterite Solar Cells: Current Strategies and Insights*, *Advanced Energy Materials* **13**, 2203046 (2023).
- [72] S. Kim, J.-S. Park, and A. Walsh, *Identification of killer defects in kesterite thin-film solar cells*, *ACS Energy Letters* **3**, 496 (2018).
- [73] S. Kim, J.-S. Park, S. N. Hood, and A. Walsh, *Lone-pair effect on carrier capture in $\text{Cu}_2\text{ZnSnS}_4$ solar cells*, *Journal of Materials Chemistry A* **7**, 2686 (2019).
- [74] Y. E. Romanyuk *et al.*, *Doping and alloying of kesterites*, *Journal of Physics: Energy* **1**, 044004 (2019).
- [75] M. Jyothirmmai, H. Saini, N. Park, and R. Thapa, *Screening of suitable cationic dopants for solar absorber material CZTS/Se: A first principles study*, *Scientific reports* **9**, 15983 (2019).
- [76] J. Li, D. Wang, X. Li, Y. Zeng, and Y. Zhang, *Cation substitution in Earth-abundant kesterite photovoltaic materials*, *Advanced Science* **5**, 1700744 (2018).
- [77] S. Giraldo *et al.*, *How small amounts of Ge modify the formation pathways and crystallization of kesterites*, *Energy & Environmental Science* **11**, 582 (2018).
- [78] S. Kim, K. M. Kim, H. Tampo, H. Shibata, and S. Niki, *Improvement of voltage deficit of Ge-incorporated kesterite solar cell with 12.3% conversion efficiency*, *Applied Physics Express* **9**, 102301 (2016).
- [79] M. Neuschitzer *et al.*, *Revealing the beneficial effects of Ge doping on $\text{Cu}_2\text{ZnSnSe}_4$ thin film solar cells*, *Journal of Materials Chemistry A* **6**, 11759 (2018).
- [80] M. S. Kumar, S. P. Madhusudanan, and S. K. Batabyal, *Substitution of Zn in Earth-Abundant $\text{Cu}_2\text{ZnSn}(S,Se)_4$ based thin film solar cells—A status review*, *Solar Energy Materials and Solar Cells* **185**, 287 (2018).
- [81] S. Hadke *et al.*, *Effect of Cd on cation redistribution and order-disorder transition in $\text{Cu}_2(\text{Zn,Cd})\text{SnS}_4$* , *Journal of Materials Chemistry A* **7**, 26927 (2019).

- [82] W.-C. Huang, S.-Y. Wei, C.-H. Cai, W.-H. Ho, and C.-H. Lai, *The role of Ag in aqueous solution processed (Ag,Cu)₂ZnSn(S,Se)₄ kesterite solar cells: antisite defect elimination and importance of Na passivation*, Journal of Materials Chemistry A **6**, 15170 (2018).
- [83] L. Choubrac *et al.*, *7.6% CZGSe solar cells thanks to optimized CdS chemical bath deposition*, Physica Status Solidi (a) **215**, 1800043 (2018).
- [84] M. He *et al.*, *Kesterite solar cells: insights into current strategies and challenges*, Advanced Science **8**, 2004313 (2021).
- [85] C. Platzer-Björkman *et al.*, *Back and front contacts in kesterite solar cells: state-of-the-art and open questions*, Journal of Physics: Energy **1**, 044005 (2019).
- [86] T. Ratz, J.-Y. Raty, G. Brammertz, B. Vermang, and N. D. Nguyen, *Opto-electronic properties and solar cell efficiency modelling of Cu₂ZnXS₄ (X= Sn,Ge,Si) kesterites*, Journal of Physics: Energy **3**, 035005 (2021).
- [87] B. Blank, T. Kirchartz, S. Lany, and U. Rau, *Selection metric for photovoltaic materials screening based on detailed-balance analysis*, Physical Review Applied **8**, 024032 (2017).
- [88] T. Ratz, N. D. Nguyen, G. Brammertz, B. Vermang, and J.-Y. Raty, *Relevance of Ge incorporation to control the physical behaviour of point defects in kesterite*, Journal of Materials Chemistry A **10**, 4355 (2022).
- [89] T. Ratz *et al.*, *Correlation between material properties, crystalline transitions, and point defects in RF sputtered (N,Mg)-doped copper oxide thin films*, under submission process (2024).
- [90] T. Sander *et al.*, *Correlation of intrinsic point defects and the Raman modes of cuprous oxide*, Physical Review B **90**, 045203 (2014).
- [91] K. W. Böer and U. W. Pohl, *Semiconductor physics* (Springer Nature, 2023).
- [92] C. Kittel, P. McEuen, and P. McEuen, *Introduction to solid state physics* (Wiley New York, 1996).
- [93] H. Ibach and H. Lüth, *Solid-state physics: an introduction to principles of materials science* (Springer Science & Business Media, 2009).
- [94] F. Giustino, *Materials Modelling Using Density Functional Theory* (Oxford University Press, United Kingdom, 2014).
- [95] R. d. L. Kronig and W. G. Penney, *Quantum mechanics of electrons in crystal lattices*, Proceedings of the royal society of London. series A, containing papers of a mathematical and physical character **130**, 499 (1931).

- [96] J. I. Pankove, *Optical processes in semiconductors* (Courier Corporation, 1975).
- [97] S. Adachi, *Properties of semiconductor alloys: group-IV, III-V and II-VI semiconductors* (John Wiley & Sons, 2009).
- [98] A. H. Smets, K. Jäger, O. Isabella, R. A. Swaaij, and M. Zeman, *Solar Energy: The physics and engineering of photovoltaic conversion, technologies and systems* (UIT Cambridge, 2015).
- [99] B. Das, I. Aguilera, U. Rau, and T. Kirchartz, *What is a deep defect? Combining Shockley-Read-Hall statistics with multiphonon recombination theory*, Physical Review Materials **4**, 024602 (2020).
- [100] K. W. Böer, *Survey of Semiconductor Physics: Volume II Barriers, Junctions, Surfaces, and Devices* (Springer Science & Business Media, 2012).
- [101] R. De Souza and G. Harrington, *Revisiting point defects in ionic solids and semiconductors*, Nature Materials **22**, 794 (2023).
- [102] W. Cai and W. D. Nix, *Imperfections in crystalline solids* (Cambridge University Press, 2016).
- [103] W. Shockley and W. Read Jr, *Statistics of the recombinations of holes and electrons*, Physical review **87**, 835 (1952).
- [104] R. N. Hall, *Electron-hole recombination in germanium*, Physical review **87**, 387 (1952).
- [105] B. Das, Z. Liu, I. Aguilera, U. Rau, and T. Kirchartz, *Defect tolerant device geometries for lead-halide perovskites*, Materials advances **2**, 3655 (2021).
- [106] N. J. Turro, V. Ramamurthy, and J. C. Scaiano, *Principles of molecular photochemistry: an introduction* (University science books, 2009).
- [107] B. K. Ridley, *Quantum processes in semiconductors* (Oxford University Press, USA, 2013).
- [108] D. Dexter, C. Klick, and G. Russell, *Criterion for the occurrence of luminescence*, Physical Review **100**, 603 (1955).
- [109] J. Li, Z.-K. Yuan, S. Chen, X.-G. Gong, and S.-H. Wei, *Effective and non-effective recombination center defects in $\text{Cu}_2\text{ZnSnS}_4$: Significant difference in carrier capture cross sections*, Chemistry of Materials **31**, 826 (2019).
- [110] M. Becquerel, *Mémoire sur les effets électriques produits sous l'influence des rayons solaires.*, Comptes rendus hebdomadaires des séances de l'Académie des sciences **9**, 561 (1839).
- [111] C. Fritts, *On a New Form of Selenium Photocell*, American J. of Science **26**, 465 (1883).

- [112] A. Chodos, *April 25, 1954: Bell labs demonstrates the first practical silicon solar cell*, APS News-This month in Physics history (2009).
- [113] M. Riordan and L. Hoddeson, *Origins of the pn junction*, IEEE spectrum **34**, 46 (1997).
- [114] D. M. Chapin, C. S. Fuller, and G. L. Pearson, *A new silicon p-n junction photocell for converting solar radiation into electrical power*, Journal of applied physics **25**, 676 (1954).
- [115] A. Cuevas, *The recombination parameter J_0* , Energy Procedia **55**, 53 (2014).
- [116] A. G. Milnes, *Heterojunctions and metal semiconductor junctions* (Elsevier, 2012).
- [117] L. C. Hirst and N. J. Ekins-Daukes, *Fundamental losses in solar cells*, Progress in Photovoltaics: Research and Applications **19**, 286 (2011).
- [118] R. M. Martin, *Electronic structure: basic theory and practical methods* (Cambridge university press, 2020).
- [119] P. Hohenberg and W. Kohn, *Inhomogeneous electron gas*, Physical review **136**, B864 (1964).
- [120] W. Kohn and L. J. Sham, *Self-consistent equations including exchange and correlation effects*, Physical review **140**, A1133 (1965).
- [121] C. Freysoldt *et al.*, *First-principles calculations for point defects in solids*, Reviews of modern physics **86**, 253 (2014).
- [122] S. Lany and A. Zunger, *Assessment of correction methods for the band-gap problem and for finite-size effects in supercell defect calculations: Case studies for ZnO and GaAs*, Physical Review B **78**, 235104 (2008).
- [123] C. Persson, Y.-J. Zhao, S. Lany, and A. Zunger, *n-type doping of CuInSe₂ and CuGaSe₂*, Physical Review B **72**, 035211 (2005).
- [124] J. S. Park, S. Kim, Z. Xie, and A. Walsh, *Point defect engineering in thin-film solar cells*, Nature Reviews Materials **3**, 194 (2018).
- [125] T. Ogawa, A. Taguchi, and A. Kuwabara, *An extended computational approach for point-defect equilibria in semiconductor materials*, npj Computational Materials **8**, 79 (2022).
- [126] C. G. Van de Walle and J. Neugebauer, *First-principles calculations for defects and impurities: Applications to III-nitrides*, Journal of applied physics **95**, 3851 (2004).

- [127] M. Dimitrievska, A. Fairbrother, E. Saucedo, A. Pérez-Rodríguez, and V. Izquierdo-Roca, *Secondary phase and Cu substitutional defect dynamics in kesterite solar cells: impact on optoelectronic properties*, Solar Energy Materials and Solar Cells **149**, 304 (2016).
- [128] R. B. Wexler, G. S. Gautam, and E. A. Carter, *Exchange-correlation functional challenges in modeling quaternary chalcogenides*, Physical Review B **102**, 054101 (2020).
- [129] S. Lany and A. Zunger, *Accurate prediction of defect properties in density functional supercell calculations*, Modelling and simulation in materials science and engineering **17**, 084002 (2009).
- [130] C. Freysoldt, J. Neugebauer, and C. G. Van de Walle, *Fully ab initio finite-size corrections for charged-defect supercell calculations*, Physical review letters **102**, 016402 (2009).
- [131] J. Heyd, J. E. Peralta, G. E. Scuseria, and R. L. Martin, *Energy band gaps and lattice parameters evaluated with the Heyd-Scuseria-Ernzerhof screened hybrid functional*, The Journal of Chemical Physics **123**, 174101 (2005).
- [132] P. Deák, A. Gali, B. Aradi, and T. Frauenheim, *Accurate gap levels and their role in the reliability of other calculated defect properties*, physica status solidi (b) **248**, 790 (2011).
- [133] A. Walsh, *Correcting the corrections for charged defects in crystals*, npj Computational Materials **7**, 72 (2021).
- [134] A. Crovetto and O. Hansen, *What is the band alignment of $\text{Cu}_2\text{ZnSn}(\text{S},\text{Se})_4$ solar cells ?*, Solar Energy Materials and Solar Cells **169**, 177 (2017).
- [135] C. Tablero, *Electronic and optical properties of substitutional V, Cr and Ir impurities in $\text{Cu}_2\text{ZnSnS}_4$* , Solar Energy Materials and Solar Cells **125**, 8 (2014).
- [136] M. Buffière *et al.*, *Physical characterization of $\text{Cu}_2\text{ZnGeSe}_4$ thin films from annealing of Cu-Zn-Ge precursor layers*, Thin Solid Films **582**, 171 (2015).
- [137] S. Khelifi *et al.*, *The path towards efficient wide band gap thin-film kesterite solar cells with transparent back contact for viable tandem application*, Solar Energy Materials and Solar Cells **219**, 110824 (2021).
- [138] S. Chen *et al.*, *Wurtzite-derived polytypes of kesterite and stannite quaternary chalcogenide semiconductors*, Physical Review B **82**, Part (2010).
- [139] S. Zamulko, R. Chen, and C. Persson, *Investigation of the structural, optical and electronic properties of $\text{Cu}_2\text{Zn}(\text{Sn},\text{Si}/\text{Ge})(\text{S}/\text{Se})_4$ alloys for solar cell applications*, Physica Status Solidi (b) **254**, 1700084 (2017).

- [140] H.-R. Liu *et al.*, *First-principles study on the effective masses of zinc-blend-derived $\text{Cu}_2\text{ZnIVVI}_4$ ($\text{IV}=\text{Sn, Ge, Si}$ and $\text{VI}=\text{S, Se}$)*, Journal of Applied Physics **112**, 093717 (2012).
- [141] C. Dun, N. Holzwarth, Y. Li, W. Huang, and D. L. Carroll, *$\text{Cu}_2\text{ZnSn}(\text{S}_x\text{O}_{(1-x)})_4$ and $\text{Cu}_2\text{ZnSn}(\text{S}_x\text{Se}_{(1-x)})_4$: First principles simulations of optimal alloy configurations and their energies*, Journal of Applied Physics **115**, 193513 (2014).
- [142] A. Walsh, S. Chen, S.-H. Wei, and X.-G. Gong, *Kesterite thin-film solar cells: Advances in materials modelling of $\text{Cu}_2\text{ZnSnS}_4$* , Advanced Energy Materials **2**, 400 (2012).
- [143] J. Jiang *et al.*, *Inserting an intermediate band in Cu- and Ag-based Kesterite compounds by Sb doping: A first-principles study*, Materials Science and Engineering: B **264**, 114937 (2021).
- [144] J. Paier, R. Asahi, A. Nagoya, and G. Kresse, *$\text{Cu}_2\text{ZnSnS}_4$ as a potential photovoltaic material: a hybrid Hartree-Fock density functional theory study*, Physical Review B **79**, 115126 (2009).
- [145] Y. Zhang *et al.*, *Structural properties and quasiparticle band structures of Cu-based quaternary semiconductors for photovoltaic applications*, Journal of Applied Physics **111**, 063709 (2012).
- [146] G. K. Gupta, R. Chaurasiya, and A. Dixit, *Theoretical studies on structural, electronic and optical properties of kesterite and stannite $\text{Cu}_2\text{ZnGe}(\text{S/Se})_4$ solar cell absorbers*, Computational Condensed Matter **19**, e00334 (2019).
- [147] J. Heyd, G. E. Scuseria, and M. Ernzerhof, *Hybrid functionals based on a screened Coulomb potential*, The Journal of Chemical Physics **118**, 8207 (2003).
- [148] G. Kresse and J. Furthmüller, *Efficiency of ab-initio total energy calculations for metals and semiconductors using a plane-wave basis set*, Computational Materials Science **6**, 15 (1996).
- [149] G. Kresse and D. Joubert, *From ultrasoft pseudopotentials to the projector augmented-wave method*, Physical Review B **59**, 1758 (1999).
- [150] J. P. Perdew, K. Burke, and M. Ernzerhof, *Generalized gradient approximation made simple*, Physical Review Letters **77**, 3865 (1996).
- [151] J. Sun, A. Ruzsinszky, and J. P. Perdew, *Strongly constrained and appropriately normed semilocal density functional*, Physical Review Letters **115**, 036402 (2015).
- [152] J. Sun *et al.*, *Accurate first-principles structures and energies of diversely bonded systems from an efficient density functional*, Nature Chemistry **8**, 831 (2016).

- [153] D. Fritsch and S. Schorr, *Climbing Jacob's ladder: A density functional theory case study for $Ag_2ZnSnSe_4$ and $Cu_2ZnSnSe_4$* , Journal of Physics: Energy **3**, 015002 (2020).
- [154] Q. Guo, H. W. Hillhouse, and R. Agrawal, *Synthesis of Cu_2ZnSnS_4 nanocrystal ink and its use for solar cells*, Journal of the American Chemical Society **131**, 11672 (2009).
- [155] S. Levchenko, V. Tezlevan, E. Arushanov, S. Schorr, and T. Unold, *Free-to-bound recombination in near stoichiometric Cu_2ZnSnS_4 single crystals*, Physical Review B **86**, 045206 (2012).
- [156] K. Lisunov *et al.*, *Features of the acceptor band and properties of localized carriers from studies of the variable-range hopping conduction in single crystals of $p-Cu_2ZnSnS_4$* , Solar Energy Materials and Solar Cells **112**, 127 (2013).
- [157] J. Chen, W. Li, C. Yan, S. Huang, and X. Hao, *Studies of compositional dependent $Cu_2Zn(Ge_xSn_{1-x})S_4$ thin films prepared by sulfurizing sputtered metallic precursors*, Journal of Alloys and Compounds **621**, 154 (2015).
- [158] S. Schorr, H.-J. Hoebler, and M. Tovar, *A neutron diffraction study of the stannite-kesterite solid solution series*, European Journal of Mineralogy **19**, 65 (2007).
- [159] K. Tsuji, T. Maeda, and T. Wada, *Optical properties and electronic structures of Cu_2ZnSnS_4 , Cu_2ZnGeS_4 , and $Cu_2Zn(Ge,Sn)S_4$ and $Cu_2Zn(Ge,Sn)Se_4$ solid solutions*, Japanese Journal of Applied Physics **57**, 08RC21 (2018).
- [160] D. B. Khadka and J. Kim, *Study of structural and optical properties of kesterite Cu_2ZnGeX_4 ($X = S, Se$) thin films synthesized by chemical spray pyrolysis*, CrystEngComm **15**, 10500 (2013).
- [161] M. Courel, T. Sanchez, N. Mathews, and X. Mathew, *Cu_2ZnGeS_4 thin films deposited by thermal evaporation: the impact of Ge concentration on physical properties*, Journal of Physics D: Applied Physics **51**, 095107 (2018).
- [162] M. Hamdi *et al.*, *Crystal chemistry and optical investigations of the $Cu_2Zn(Sn,Si)S_4$ series for photovoltaic applications*, Journal of Solid State Chemistry **220**, 232 (2014).
- [163] S. Levchenko *et al.*, *Polarization-dependent electrolyte electroreflectance study of Cu_2ZnSiS_4 and $Cu_2ZnSiSe_4$ single crystals*, Journal of Alloys and Compounds **509**, 7105 (2011).
- [164] J. C. Slater, *Atomic radii in crystals*, The Journal of Chemical Physics **41**, 3199 (1964).

- [165] C. P. Heinrich, T. W. Day, W. G. Zeier, G. J. Snyder, and W. Tremel, *Effect of Isovalent Substitution on the Thermoelectric Properties of the $\text{Cu}_2\text{ZnGeSe}_{4-x}\text{S}_x$ Series of Solid Solutions*, Journal of the American Chemical Society **136**, 442 (2014).
- [166] S. Ikeda *et al.*, *Photocathode characteristics of a spray-deposited $\text{Cu}_2\text{ZnGeS}_4$ thin film for CO_2 reduction in a CO_2 -saturated aqueous solution*, ACS Applied Energy Materials **2**, 6911 (2019).
- [167] E. Garcia-Llamas *et al.*, *Wide band-gap tuning $\text{Cu}_2\text{ZnSn}_{1-x}\text{Ge}_x\text{S}_4$ single crystals: Optical and vibrational properties*, Solar Energy Materials and Solar Cells **158**, 147 (2016).
- [168] M. Vishwakarma, D. Varandani, S. Shivaprasad, and B. Mehta, *Structural, optical, electrical properties and energy band diagram of $\text{Cu}_2\text{ZnSiS}_4$ thin films*, Solar Energy Materials and Solar Cells **174**, 577 (2018).
- [169] S. Kim, J. A. Márquez, T. Unold, and A. Walsh, *Upper limit to the photovoltaic efficiency of imperfect crystals from first principles*, Energy & Environmental Science **13**, 1481 (2020).
- [170] I. El Radaf and H. Al-Zahrani, *Facile Synthesis and Structural, Linear and Nonlinear Optical Investigation of p-type $\text{Cu}_2\text{ZnGeS}_4$ Thin Films as a Potential Absorber Layer for Solar Cells*, Journal of Electronic Materials **49**, 4843 (2020).
- [171] K. Pal, P. Singh, A. Bhaduri, and K. B. Thapa, *Current challenges and future prospects for a highly efficient ($> 20\%$) kesterite CZTS solar cell: A review*, Solar Energy Materials and Solar Cells **196**, 138 (2019).
- [172] S. Schorr *et al.*, *Point defects, compositional fluctuations, and secondary phases in non-stoichiometric kesterites*, Journal of Physics: Energy **2**, 012002 (2019).
- [173] T. Gokmen, O. Gunawan, T. K. Todorov, and D. B. Mitzi, *Band tailing and efficiency limitation in kesterite solar cells*, Applied Physics Letters **103**, 103506 (2013).
- [174] K. Biswas, S. Lany, and A. Zunger, *The electronic consequences of multivalent elements in inorganic solar absorbers: Multivalency of Sn in $\text{Cu}_2\text{ZnSnS}_4$* , Applied Physics Letters **96**, 201902 (2010).
- [175] Y. Gong *et al.*, *Identifying the origin of the V_{OC} deficit of kesterite solar cells from the two grain growth mechanisms induced by Sn^{2+} and Sn^{4+} precursors in DMSO solution*, Energy & Environmental Science **14**, 2369 (2021).
- [176] A. Crovetto *et al.*, *Assessing the defect tolerance of kesterite-inspired solar absorbers*, Energy & Environmental Science **13**, 3489 (2020).

- [177] Q. Tian and S. F. Liu, *Defect suppression in multinary chalcogenide photovoltaic materials derived from kesterite: progress and outlook*, Journal of Materials Chemistry A **8**, 24920 (2020).
- [178] Z.-K. Yuan *et al.*, *Engineering solar cell absorbers by exploring the band alignment and defect disparity: the case of Cu-and Ag-based kesterite compounds*, Advanced Functional Materials **25**, 6733 (2015).
- [179] M. H. Sharif, T. Enkhbat, E. Enkhbayar, and J. Kim, *Control of defect states of kesterite solar cells to achieve more than 11% power conversion efficiency*, ACS Applied Energy Materials **3**, 8500 (2020).
- [180] R. B. Wexler, G. S. Gautam, and E. A. Carter, *Optimizing kesterite solar cells from $\text{Cu}_2\text{ZnSnS}_4$ to $\text{Cu}_2\text{CdGe}(\text{S},\text{Se})_4$* , Journal of Materials Chemistry A **9**, 9882 (2021).
- [181] L. Choubrac *et al.*, *Sn substitution by Ge: strategies to overcome the open-circuit voltage deficit of kesterite solar cells*, ACS Applied Energy Materials **3**, 5830 (2020).
- [182] S. Giraldo *et al.*, *Large efficiency improvement in $\text{Cu}_2\text{ZnSnSe}_4$ solar cells by introducing a superficial Ge nanolayer*, Advanced Energy Materials **5**, 1501070 (2015).
- [183] Y. Du *et al.*, *Defect Engineering in Earth-Abundant $\text{Cu}_2\text{ZnSn}(\text{S},\text{Se})_4$ Photovoltaic Materials via Ga^{3+} -Doping for over 12% Efficient Solar Cells*, Advanced Functional Materials **31**, 2010325 (2021).
- [184] Y. Deng *et al.*, *Adjusting the SnZn defects in $\text{Cu}_2\text{ZnSn}(\text{S},\text{Se})_4$ absorber layer via Ge4+ implanting for efficient kesterite solar cells*, Journal of Energy Chemistry **61**, 1 (2021).
- [185] J. Fu *et al.*, *Ag, Ge dual-gradient substitution for low-energy loss and high-efficiency kesterite solar cells*, Journal of Materials Chemistry A **8**, 22292 (2020).
- [186] M. He *et al.*, *Systematic Efficiency Improvement for $\text{Cu}_2\text{ZnSn}(\text{S},\text{Se})_4$ Solar Cells By Double Cation Incorporation with Cd and Ge*, Advanced Functional Materials **31**, 2104528 (2021).
- [187] H. Nishihara, T. Maeda, A. Shigemi, and T. Wada, *First-principles study of defect formation in the photovoltaic semiconductors Cu_2GeS_3 and $\text{Cu}_2\text{ZnGeS}_4$ for comparison with Cu_2SnS_3 , $\text{Cu}_2\text{ZnSnS}_4$, and CuInSe_2* , Japanese Journal of Applied Physics **56**, 04CS08 (2017).
- [188] J. Just *et al.*, *Secondary phases and their influence on the composition of the kesterite phase in CZTS and CZTSe thin films*, Physical Chemistry Chemical Physics **18**, 15988 (2016).

- [189] S. Ma *et al.*, *Origin of band-tail and deep-donor states in $\text{Cu}_2\text{ZnSnS}_4$ solar cells and their suppression through Sn-poor composition*, The journal of physical chemistry letters **10**, 7929 (2019).
- [190] G. Rey *et al.*, *On the origin of band-tails in kesterite*, Solar Energy Materials and Solar Cells **179**, 142 (2018).
- [191] A. Alkauskas, Q. Yan, and C. G. Van de Walle, *First-principles theory of nonradiative carrier capture via multiphonon emission*, Physical Review B **90**, 075202 (2014).
- [192] G. Paul, Y. Nawa, H. Sato, T. Sakurai, and K. Akimoto, *Defects in Cu_2O studied by deep level transient spectroscopy*, Applied physics letters **88**, 141901 (2006).
- [193] H. Raebiger, S. Lany, and A. Zunger, *Origins of the p-type nature and cation deficiency in Cu_2O and related materials*, Physical Review B **76**, 045209 (2007).
- [194] D. O. Scanlon, B. J. Morgan, G. W. Watson, and A. Walsh, *Acceptor levels in p-type Cu_2O : rationalizing theory and experiment*, Physical review letters **103**, 096405 (2009).
- [195] A. Wright and J. Nelson, *Theory of the copper vacancy in cuprous oxide*, Journal of Applied Physics **92**, 5849 (2002).
- [196] A. Sekkat *et al.*, *Chemical deposition of Cu_2O films with ultra-low resistivity: correlation with the defect landscape*, Nature Communications **13**, 5322 (2022).
- [197] A. Sekkat *et al.*, *Open-air printing of Cu_2O thin films with high hole mobility for semitransparent solar harvesters*, Communications Materials **2**, 78 (2021).
- [198] J. T-Thienprasert and S. Limpijumnong, *Identification of nitrogen acceptor in Cu_2O : First-principles study*, Applied Physics Letters **107**, 221905 (2015).
- [199] Z. Zhao *et al.*, *First-principles study on the doping effects of nitrogen on the electronic structure and optical properties of Cu_2O* , RSC advances **3**, 84 (2013).
- [200] K. Reimann and K. Syassen, *Raman scattering and photoluminescence in Cu_2O under hydrostatic pressure*, Physical Review B **39**, 11113 (1989).
- [201] J. Resende *et al.*, *Resilience of cuprous oxide under oxidizing thermal treatments via magnesium doping*, The Journal of Physical Chemistry C **123**, 8663 (2019).
- [202] N. Sliti, E. Fourneau, T. Ratz, S. Touihri, and N. D. Nguyen, *Mg-doped Cu_2O thin films with enhanced functional properties grown by magnetron sputtering under optimized pressure conditions*, Ceramics International **48**, 23748 (2022).
- [203] S. Ishizuka, S. Kato, T. Maruyama, and K. Akimoto, *Nitrogen doping into Cu_2O thin films deposited by reactive radio-frequency magnetron sputtering*, Japanese Journal of Applied Physics **40**, 2765 (2001).

- [204] A. Mudhaffar, B. Sultan, E. Shalaan, and H. Al-Jawhari, *Switching Enhancement in Copper Oxide Thin-Film Transistors via Molybdenum Trioxide Buffering and Nitrogen Doping*, Journal of Electronic Materials **52**, 3446 (2023).
- [205] M. Ahmadi, M. Asemi, and M. Ghanaatshoar, *Mg and N co-doped CuCrO_2 : A record breaking p-type TCO*, Applied Physics Letters **113** (2018).
- [206] M. Querry, *Optical Constants, contractor report*, US Army Chemical Research, Development and Engineering Center (CRDC), Aberdeen Proving Ground, MD **418** (1985).
- [207] J. C. Russ, *Fundamentals of energy dispersive X-ray analysis: Butterworths monographs in materials* (Butterworth-Heinemann, 2013).
- [208] C. Almazán *et al.*, *Cu_4O_3 thin films deposited by non-reactive rf-magnetron sputtering from a copper oxide target*, Revista mexicana de física **67**, 495 (2021).
- [209] R. Tadjine, A. Houimi, M. M. Alim, and N. Oudini, *Oxygen flow rate effect on copper oxide thin films deposited by radio frequency magnetron sputtering*, Thin Solid Films **741**, 139013 (2022).
- [210] M. A. M. Patwary *et al.*, *Nitrogen doping effect in Cu_4O_3 thin films fabricated by radio frequency magnetron sputtering*, physica status solidi (b) **257**, 1900363 (2020).
- [211] L. Debbichi, M. Marco de Lucas, J. Pierson, and P. Kruger, *Vibrational properties of CuO and Cu_4O_3 from first-principles calculations, and Raman and infrared spectroscopy*, The Journal of Physical Chemistry C **116**, 10232 (2012).
- [212] Y. Wang *et al.*, *Tuning the structure and preferred orientation in reactively sputtered copper oxide thin films*, Applied Surface Science **335**, 85 (2015).
- [213] Y. Wang *et al.*, *Room temperature self-assembled growth of vertically aligned columnar copper oxide nanocomposite thin films on unmatched substrates*, Scientific reports **7**, 11122 (2017).
- [214] M. Umar *et al.*, *Morphological and stoichiometric optimization of Cu_2O thin films by deposition conditions and post-growth annealing*, Thin Solid Films **732**, 138763 (2021).
- [215] R. Scaffidi *et al.*, *Ge-alloyed kesterite thin-film solar cells: previous investigations and current status - a comprehensive review*, Journal of Materials Chemistry A **11**, 13174 (2023).
- [216] K. Zhao, H. Xiang, R. Zhu, C. Liu, and Y. Jia, *Passivation principle of deep-level defects: a study of Sn_{Zn} defects in kesterites for high-efficient solar cells*, Journal of Materials Chemistry A **10**, 2849 (2022).

- [217] A. Zivković, G. Mallia, H. E. King, N. H. de Leeuw, and N. M. Harrison, *Mind the Interface Gap: Exposing Hidden Interface Defects at the Epitaxial Heterostructure between CuO and Cu₂O*, ACS Applied Materials & Interfaces **14**, 56331 (2022).
- [218] A. Weber, R. Mainz, T. Unold, S. Schorr, and H.-W. Schock, *In-situ XRD on formation reactions of Cu₂ZnSnS₄ thin films*, Physica status solidi C **6**, 1245 (2009).
- [219] S. Schorr, A. Weber, V. Honkimäki, and H.-W. Schock, *In-situ investigation of the kesterite formation from binary and ternary sulphides*, Thin Solid Films **517**, 2461 (2009).

ABOUT THE AUTHOR

Personal data

First name Thomas
Last name Ratz
Date of birth August 8th, 1995
Nationality Belgian
Contact thomas_ratz@outlook.com



Education

- 2018-2024 PhD. Thesis in Science (Physics), University of Liège, Q-MAT.
*Defects in earth-abundant photovoltaic materials:
spotlight on kesterites and copper oxides*
Supervisor: Prof. Dr. Ngoc Duy Nguyen
- 2013-2016 Master's degree in physics, University of Liège
*Electrical and optical characterisation of $\text{Cu}_2\text{O}:\text{Mg}/\text{AZO}$
transparent heterojunctions grown by RF magnetron sputtering*
- 2013-2016 Bachelor's degree in physics, University of Liège